

Nichtlineare Photoemission an Metalloberflächen unter Einfluss der Spin-Bahn-Kopplung

Habilitationsschrift

zur Erlangung des akademischen Grades
Dr. rer. nat. habil.

vorgelegt der
Mathematisch-Naturwissenschaftlich-Technischen Fakultät
der Martin-Luther-Universität Halle-Wittenberg

von Herrn Dr. rer. nat. Aimo Winkelmann
geb. am 24. März 1973 in Waren

Gutachter:

1. Prof. Dr. Jürgen Kirschner
2. Prof. Dr. Wolf Widdra
3. Prof. Dr. Martin Weinelt

Halle(Saale), verteidigt am 6. Juni 2012, Probevorlesung am 27. Juni 2012

Inhaltsverzeichnis

1	Einleitung	1
1.1	Spin-Bahn-Kopplung in der elektronischen Struktur von Festkörpern	3
1.2	Winkelaufgelöste Photoemission mit Spin-Analyse	8
1.2.1	Photoemission	8
1.2.2	Spin-Analyse der Photoelektronen	9
1.3	Ultrakurze optische Anregungen und spinaufgelöste nichtlineare Photoemission . .	13
2	Spinaufgelöste Nichtlineare Photoemission	19
2.1	Femtosekunden-Lasersystem	20
2.2	Elektronen-Spin-Analysator	21
2.3	Impulsmikroskop	22
3	Ausgewählte Ergebnisse	24
3.1	Elektronische Bandstrukturinformation über kohärente Mehrphotonen-Resonanzen	24
3.2	Optische Steuerung der spin-polarisierten Photoemission von Cu(001)	33
3.3	Rashba-Effekt in unbesetzten Zuständen von Bi/Cu(111)	39
3.4	Magnetischer Dichroismus von angeregten Quantentopfzuständen in Co/Cu(001) .	42
4	Zusammenfassung und Ausblick	49
	Literaturverzeichnis	50
5	Originalveröffentlichungen	63
5.1	Resonant coherent three-photon photoemission from Cu(001)	65
5.2	Band structure effects in surface second harmonic generation: The case of Cu(001)	75
5.3	Angle-dependent study of a direct optical transition in the sp bands of Ag(111) by one- and two-photon photoemission	83
5.4	Higher Order Photoemission from Metal Surfaces	95
5.5	High efficiency electron spin polarization analyzer based on exchange scattering at Fe/ W(001)	115
5.6	Ultrafast Spin Injection into Image potential states	121
5.7	Interferometric Control of Spin-Polarized Electron Populations at a Metal Surface Observed by Multiphoton Photoemission	125
5.8	Spin-polarized multi-photon photoemission and surface electronic structure of Cu(001)	129
5.9	Unconventional spin topology in surface alloys with Rashba-type spin splitting . . .	143
5.10	Magnetic Dichroism from Optically Excited Quantum Well States	149
5.11	Spin-orbit coupling in unoccupied quantum well states: Experiment and theory for Co/Cu(001)	153

1 Einleitung

Die Photoelektronenspektroskopie ist eine der wichtigsten experimentellen Methoden der Festkörperphysik, weil sie einen sehr direkten Zugriff auf die elektronischen Zustände von Festkörpern und ihrer Oberflächen ermöglicht. Über die Ausnutzung des Photoeffekts kann die elektronische Struktur dabei heutzutage mit Hilfe von Strahlung aus Laborquellen und Synchrotrons bei nahezu beliebigen Bindungsenergien analysiert werden. Als besondere Strahlungsquellen für Photoemissionsexperimente stehen ultrakurze Laserpulse im Mittelpunkt der vorliegenden Arbeit. Mit diesen hochintensiven Laserpulsen werden die Photoelektronen nicht nur in Zustände angeregt, die der Energieübertragung durch einzelne Photonen entsprechen, sondern es können auch Vielfache der Einzelphotonenenergien auf die Elektronen übertragen werden. In diesen nichtlinearen Prozessen spielen die optisch angeregten, im Grundzustand ursprünglich unbesetzten Zwischenzustände eine große Rolle. Mehrphotonen-Photoemission (mPPE) bietet auch deswegen einen einzigartigen Zugang zu diesen Zuständen, weil über die eingesetzten ultrakurzen Laserpulse mit Zeitdauern im Femtosekundenbereich zusätzlich auch dynamische Prozesse analysierbar sind.

Die angeregten Photoelektronen sind nicht nur durch ihren Impuls und ihre Energie, sondern auch durch den Spin charakterisiert. Durch die direkte Verknüpfung eines magnetischen Moments mit dem Elektronenspin ist dieser Freiheitsgrad naturgemäß für die Untersuchung ferromagnetischer Proben außerordentlich relevant. Der Elektronenspin ist aber nicht nur eine Schlüsseleigenschaft für die verschiedenen magnetischen Ordnungsprozesse, sondern er ist ebenfalls bestimmend für die chemische Bindung und elektronische Struktur in Festkörpern überhaupt. Ganz generell wird durch das Pauli-Prinzip und die elektromagnetischen Wechselwirkungen zwischen den Elektronen eine Vielzahl von korrelierten Effekten in aktuell relevanten Forschungsrichtungen der Festkörperphysik direkt oder indirekt auch vom Elektronenspin beeinflusst. Dies macht die Wichtigkeit eines experimentellen Zugangs zum Elektronenspin in Festkörpern deutlich.

Optische Felder herkömmlicher Ultrakurzpuls laser wechselwirken jedoch nicht direkt mit Spins, da die magnetischen Anteile dieser Pulse normalerweise dafür nicht stark genug sind. Jedoch kann über die Kopplung des Spins eines Elektrons mit seiner Bahnbewegung im Mechanismus der Spin-Bahn-Kopplung ein indirekter Zugriff auf den Spinfreiheitsgrad über die Anregung der Elektronenorbitale erfolgen. Zum Beispiel können mittels zirkular polarisierter Strahlung die Dipol-Auswahlregeln für optische Übergänge zwischen verschiedenen Elektronenzuständen genutzt werden, um gezielt Elektronen mit einer bestimmten Spinausrichtung aus einem insgesamt unpolarisierten Ensemble anzuregen.

In Verbindung dieser verschiedenen Ideenstränge beschäftigt sich die vorliegende Arbeit mit der Untersuchung des Einflusses der Spin-Bahn-Wechselwirkung in der optischen Mehrphotonenanregung von spin-polarisierten Photoelektronen an nichtmagnetischen und magnetischen Metalloberflächen. Dabei werden drei relevante Systeme untersucht:

1. Die optische Anregung spin-polarisierter Elektronen über Drei-Photonen-Photoemission (3PPE) aus d -Bändern von (nichtmagnetischem) Kupfer in Oberflächenzustände oberhalb des Fermi-niveaus
2. Die Auswirkungen der Spin-Bahn-Kopplung in unbesetzten Zuständen von nichtmagnetischen Oberflächenlegierungen von Wismut auf Cu(111)-Oberflächen (Rashba-Effekt)
3. Die magnetisierungsabhängige Photoemissionsintensität in Zwei-Photonen-Photoemission (2PPE) durch Spin-Bahn-Kopplung in unbesetzten Quantentopf-Zuständen von ferromagnetischen Kobalt-Filmen auf Cu(001)-Oberflächen (Magnetischer Dichroismus)

Die im Rahmen dieser Arbeit untersuchten Themengebiete werden in den folgenden Abschnitten näher vorgestellt. Dazu wird in Abschnitt [1.1](#) die allgemeine Bedeutung der Spin-Bahn-Kopplung in der elektronischen Struktur von Festkörpern erläutert. Dies geschieht in Bezug zu potentiellen technischen Anwendungen der grundlegenden spin-abhängigen Effekte in Kristallen und an ihren Oberflächen. Es folgt in Abschnitt [1.2](#) die Vorstellung der herkömmlichen Photoemissionsspektroskopie mit Spin-Analyse. In Abschnitt [1.3](#) werden dann die besonderen Vorteile der nichtlinearen Photoemission mit ultrakurzen Pulsen herausgearbeitet. Die experimentelle Voraussetzungen zu den in Kapitel [3](#) vorgestellten Ergebnissen werden in Kapitel [2](#) behandelt. Eine Zusammenfassung gibt einen Ausblick auf weitere Arbeiten. Die für diese Arbeit relevanten Originalpublikationen sind in Kapitel [5](#) zusammengestellt. Auf diese Veröffentlichungen wird jeweils mit [AW [5.1](#)] ... [AW [5.11](#)] im Text Bezug genommen.

1.1 Spin-Bahn-Kopplung in der elektronischen Struktur von Festkörpern

Die elektronischen Zustände in Atomen, Molekülen und Festkörpern sind durch die Bewegung der negativ geladenen Elektronen in den dort vorliegenden elektrischen Feldern bestimmt. Zusätzlich zu seiner Ladung, Masse und Geschwindigkeit besitzt das Elektron den „Spin“ als einen relativistisch begründeten intrinsischen Drehimpuls, welcher mit einem magnetischen Moment verknüpft ist. Die Wirkung eines elektrischen Feldes \mathbf{E} auf ein bewegtes Elektron mit Geschwindigkeit \mathbf{v} kann nun im Ruhesystem des Elektrons auch als ein effektives Magnetfeld \mathbf{B} gesehen werden. Wenn dieses effektive Feld $\mathbf{B}(\mathbf{v}, \mathbf{E})$ auf das mit dem Spin $\boldsymbol{\sigma}$ verknüpfte magnetische Dipolmoment $\mathbf{m}(\boldsymbol{\sigma})$ des Elektrons wirkt, ergibt sich somit auch eine entsprechende Energiedifferenz für Zustände mit gleichem Geschwindigkeitsvektor, aber entgegengesetzter Spinorientierung $\pm \mathbf{m}(\boldsymbol{\sigma})$ in einem elektrischen Feld. Dies ist der Mechanismus der Spin-Bahn-Kopplung, der die besondere Wirkung von relativistischen Effekten auf elektronische Zustände verdeutlicht. Die Kopplung der Bahnbewegung \mathbf{v} mit dem Spin des Elektrons trägt somit zur Energie des Systems über einen eigenen Anteil H_{SOC} im Hamiltonian bei [1]:

$$H_{SOC} = -\mathbf{m}(\boldsymbol{\sigma}) \cdot \mathbf{B}(\mathbf{v}, \mathbf{E}) = \frac{\mu_B}{2c^2} \boldsymbol{\sigma} \cdot (\mathbf{v} \times \mathbf{E}) = \frac{\hbar^2}{4im^2c^2} \boldsymbol{\sigma} \cdot (\nabla V \times \nabla) \quad (1.1)$$

wo $\boldsymbol{\sigma}$ der Paulische Spin-Operator ist, ∇V ist der Gradient des Potentials und ∇ wirkt auf den Ortsanteil der Wellenfunktion. Für die Zwecke der vorliegenden Arbeit wird die Form von H_{SOC} hier durch die eingehenden Erläuterungen motiviert und als gegeben betrachtet, H_{SOC} kann aus der relativistischen Elektronentheorie abgeleitet werden [2].

Die zentrale Rolle im Mechanismus der Spin-Bahn-Kopplung spielt, wie in Gleichung (1.1) zu erkennen, der Potentialgradient ∇V und das damit verbundene elektrische Feld. Aus der räumlichen Struktur dieses Potentialgradienten in einem betrachteten spezifischen System resultieren ebenso spezifische Auswirkungen auf die Kopplung zwischen dem Spin und dem Geschwindigkeitsvektor. Nach ihren unterschiedlichen, symmetriebedingten Spin-Bahn-Kopplungseffekten kann man zum Beispiel das kugelsymmetrische Potentiale freier Atome, das dreidimensional periodische Potential im Volumen von Festkörpern sowie die Potentiale an Grenz- und Oberflächen von Festkörpern unterscheiden.

In der Atomphysik führt die Spin-Bahn-Kopplung dazu, dass der Bahndrehimpuls \mathbf{l} und der Spin \mathbf{s} zum Gesamtdrehimpuls \mathbf{j} verknüpft sind [3]. Wegen der Kugelsymmetrie des Potentials gilt $\nabla V = (\mathbf{r}/r)dV/dr$ und der Spin-Bahn-Hamiltonian (1.1) kann explizit als eine Kopplung von \mathbf{l} und \mathbf{s} geschrieben werden:

$$H_{SOC} = \frac{1}{2m^2c^2} \frac{1}{r} \frac{dV}{dr} (\mathbf{s} \cdot \mathbf{l}) \quad (1.2)$$

mit $\mathbf{s} = \frac{1}{2}\hbar\boldsymbol{\sigma}$ und $\mathbf{l} = \mathbf{r} \times \mathbf{p} = -i\hbar\mathbf{r} \times \nabla$. Für die durch diese Kopplung entstehenden Wellenfunk-

tionen beschreiben die Clebsch-Gordan-Koeffizienten den Anteil der jeweiligen m_l und m_s für Zustände mit einem zu j gehörigen m_j . Für die beiden möglichen atomaren $|p_{1/2}; m_j = \pm 1/2\rangle$ Zustände ergeben sich zum Beispiel die Kombinationen [4] :

$$|p_{1/2}; m_j = \pm \frac{1}{2}\rangle = \mp \sqrt{\frac{2}{3}} |m_l = 1\rangle |m_s = -\frac{1}{2}\rangle \pm \sqrt{\frac{1}{3}} |m_l = 0\rangle |m_s = +\frac{1}{2}\rangle \quad (1.3)$$

Die beiden Zustände $|p_{1/2}; m_j = \pm 1/2\rangle$ sind ohne Magnetfeld entartet und insgesamt liegt keine Spinpolarisation bei der Energie dieser Zustände vor. Wie man aber an den Vorfaktoren in (1.3) sieht, enthält ein spezifischer m_j Zustand keine Gleichverteilung der Spinkomponenten m_s und ist somit potentiell zur Erzeugung einer Spinpolarisation nutzbar. Unter Anregung eines Atoms mit zirkular polarisiertem Licht zum Beispiel können je nach der Helizität des Lichtes gezielt Übergänge mit einer Änderung von $\Delta m_j = +1$ oder $\Delta m_j = -1$ angeregt werden. Aus s -Ausgangszuständen mit $m_j = \pm 1/2$ können also $p_{1/2}$ Endzustände mit festgelegtem m_j adressiert werden. Über diesen Effekt kann man eine Spin-Polarisation von optisch gepumpten Atomen erzeugen („Optical Spin Orientation“ [5]). In Festkörpern ist die Kugelsymmetrie des Atoms gebrochen, so daß dort entsprechend modifizierte Clebsch-Gordan-Koeffizienten benutzt werden müssen, um die Mischung von Spin- und Ortskomponenten in den elektronischen Zuständen zu beschreiben. Der wesentliche, auf der Symmetrie der elektronischen Zustände beruhende Mechanismus bleibt aber bestehen [4]. Als sehr wichtige Anwendung ist hier die optisch spin-selektive Anregung von Photoelektronen aus GaAs zur Erzeugung von spinpolarisierten Elektronenstrahlen zu nennen [6, 7]. Analog zur Bildung des $p_{1/2}$ - $p_{3/2}$ Spin-Bahn-Dubletts in Atomen spalten zum Beispiel auch in Kupferkristallen die d -Bänder mit Δ_5 -Symmetrie in der Nähe des X -Punktes in zwei Bänder auf, deren Symmetrie mit Δ_6 und Δ_7 bezeichnet wird (siehe die Ergebnisse in Abschnitt 3.2 über spinpolarisierte Photoemission von Cu(001)).

Wenn man von der nichtrelativistischen Schrödinger-Gleichung ohne ein zusätzliches angelegtes Magnetfeld ausgeht, sind die elektronischen Zustände in Atomen und in Festkörpern jeweils doppelt mit Elektronen unterschiedlichen Spins besetzt. Diese Entartung kann im Prinzip durch den spinabhängigen Anteil H_{SOC} im Hamiltonian aufgehoben werden, wodurch Zustände mit verschiedenem Spin auch unterschiedliche Energien hätten. Im Festkörper wie im Atom wird dies jedoch durch symmetriebedingte Restriktionen eingeschränkt [8, 9]. Das Vorliegen einer Zeitumkehr-Invarianz im System führt zur zweifachen Entartung (Kramersche Entartung) jedes Energieniveaus: $E^a(+\mathbf{k}, \uparrow) = E^a(-\mathbf{k}, \downarrow)$. Dabei bezeichnen (\uparrow, \downarrow) die beiden Spin-Eigenzustände zu einem gegebenen Blochvektor \mathbf{k} im Kristall, welche nicht notwendigerweise auch Eigenzustände z.B. des Spin-Operators σ_z für eine fest gewählte z -Komponente des Elektronenspins sein müssen (das bedeutet, dass die Quantisierungsachse des Spins im Allgemeinen von \mathbf{k} abhängen kann). Die Zeitumkehr-Invarianz fordert ebenso für Zustände mit dem selben \mathbf{k} , aber dem anderen Spin-Eigenzustand: $E^b(+\mathbf{k}, \downarrow) = E^b(-\mathbf{k}, \uparrow)$, was aber im allgemeinen *nicht* heißt, dass auch $E^a = E^b$. Dies kann an einzelnen hochsymmetrischen \mathbf{k} -Punkten der Fall sein, wird jedoch für einen beliebigen \mathbf{k} -Punkt erst bei Inversionssymmetrie des Potentials gefordert. Wenn die Operation $+\mathbf{r} \rightarrow -\mathbf{r}$

eine Symmetrieoperation des Systems ist (Inversionssymmetrie, Zentrosymmetrie), folgt auch: $E(+\mathbf{k}, \uparrow) = E(-\mathbf{k}, \uparrow)$. Damit ergibt sich bei Zeitumkehrinvarianz und Inversionssymmetrie insgesamt: $E(\mathbf{k}, \uparrow) = E(\mathbf{k}, \downarrow)$, so dass die Energie der elektronischen Zustände in zentrosymmetrischen nichtmagnetischen Kristallen nicht vom Spin abhängt. Dies bedeutet zum Beispiel für die Volumenzustände der fcc-Kristalle von Cu, Ag und Au, dass jedes Band doppelt entartet bezüglich des Spins ist. Wie wir oben am Beispiel der Spin-Bahn-Kopplung in Atomen gesehen haben, verbietet dies aber nicht, das Spin- und Bahnmoment auf bestimmte Weise gekoppelt sind, sondern bestimmt nur, dass in einem Energieniveau keine Gesamtpolarisation vorliegen kann. Dies war auch in Gleichung (1.3) für ein $p_{1/2}$ -Niveau zu sehen: wenn man die beiden entarteten $m_{\pm 1/2}$ -Anteile bei einer Energie zusammen betrachtet, liegt keine Spinpolarisation vor. Im Gegensatz zu zentrosymmetrischen Elementkristallen können zum Beispiel bei GaAs, das nicht zentrosymmetrisch ist, auch im Volumen spin-aufgespaltene Zustände vorkommen [10–13]. Wegen der immer noch vorliegenden Zeitumkehr-Invarianz in diesem nichtmagnetischen Kristall gibt es wegen $E(+\mathbf{k}, \uparrow) = E(-\mathbf{k}, \downarrow)$ für ein $(+\mathbf{k}, -\mathbf{k})$ -Paar von Elektronen mit entgegengesetzten Wellenzahlvektoren keine Gesamtpolarisation des Grundzustandes.

Die Inversionssymmetrie ist notwendigerweise auch an der Oberfläche von Kristallen gebrochen, was dann prinzipiell erlaubt, dass für ein \mathbf{k} die beiden Eigenzustände unterschiedliche Energie besitzen: $E(\mathbf{k}, \uparrow) \neq E(\mathbf{k}, \downarrow)$. Die Potentialänderung an der Oberfläche wirkt sich über die Spin-Bahn-Kopplung weiterhin auch in einer im allgemeinen spin-abhängigen Transmission der Oberfläche für Elektronen aus [14, 15]. Die durch Spin-Bahn-Kopplung bewirkte Spinstruktur von bestimmten Oberflächenzuständen spielt ebenso eine Rolle bei den neuartigen Effekten die bei den sogenannten „topologischen Isolatoren“ (topological insulators) oder Quanten-Spin-Hall-Systemen beobachtet werden [16, 17]. Ein grundlegender Mechanismus von Spin-Bahn-Kopplungseffekten an Oberflächen kann über das Rashba-Bychkov-Modell verstanden werden [18]: Wenn der Potentialgradient in Gleichung (1.1) in der z -Richtung der Oberflächennormale angenommen wird, $\nabla V = \mathbf{e}_z \cdot dV/dz$, mit dem Einheitsvektor \mathbf{e}_z , dann ist die durch die Richtung des effektiven Magnetfelds bestimmte Quantisierungsachse nach Gleichung (1.1) über $(\nabla V \times \nabla) = -i\hbar(\nabla V \times \mathbf{p})$ sowohl senkrecht zu \mathbf{e}_z als auch zur Richtung des Impulses \mathbf{p} eines Elektrons in einem Oberflächenzustand. Die dann durch H_{SOC} bewirkte Energieaufspaltung hängt damit nach (1.1) linear von dem Anteil von \mathbf{p} ab, welcher zu \mathbf{e}_z senkrecht, also parallel zur Oberfläche ist: $|\mathbf{p}_{||}| = |\hbar\mathbf{k}_{||}|$. Eine solche Situation liegt zum Beispiel für die Spin-Bahn-Kopplung im Shockley-Oberflächenzustand von Au(111) vor [19]. Als weitere prototypische Systeme für den Rashba-Effekt an Oberflächen haben insbesondere Strukturen von schweren Atomen (Bi, Pb, Sb) auf (111)-Oberflächen von Silber und Kupfer Bedeutung erlangt, weil sie große spin-abhängige Energieaufspaltungen zeigen (siehe die Ergebnisse in Abschnitt 3.3 über Wismut-Oberflächenlegierungen auf Cu(111)).

Aufgrund der Verknüpfung des Elektronenspins mit einem magnetischen Moment spielt der Spin eine zentrale Rolle in Fragestellungen des Magnetismus. In magnetischen Festkörpern ist die Zeitumkehrinvarianz durch die Magnetisierung \mathbf{M} gebrochen und führt zu einer spin-

abhängigen elektronischen Struktur. Die *Magnetisierungsrichtung* kann bevorzugt an bestimmte *Kristallrichtungen* gekoppelt sein (magnetokristalline Anisotropie). Dieser Effekt wird wiederum durch die Spin-Bahn-Kopplung vermittelt [20]. Wie oben in Gleichung (1.1) prinzipiell zu sehen, ist eine Energie-Anisotropie bzgl. der Richtung der Geschwindigkeiten in den elektronischen Zuständen mit der Ausrichtung der Spins gekoppelt. Zur Minimierung der Gesamtenergie kann also eine bestimmte feste Ausrichtung der Magnetisierung bezüglich der den räumlichen Anteil der elektronischen Zustände bestimmenden Kristallstruktur bevorzugt sein. Dies ist insbesondere an Oberflächen und in ultradünnen Filmen wichtig, wo die gegenüber dem Volumen veränderte Struktur auch die magnetische Anisotropie beeinflusst [21–23]. Umgekehrt können Veränderungen der Magnetisierung über die Spin-Bahn-Wechselwirkung auf die elektronische Struktur und auf die Kristallstruktur zurückwirken.

Diese vielfältigen Wechselwirkungen sind insbesondere auch bei ultraschnellen Prozessen von Bedeutung, bei denen magnetische Proben mittels optischer Femtosekundenpulse angeregt werden und eine Magnetisierungsänderung im Bereich weniger zehn Femtosekunden stattfinden kann [24, 25]. Dies ist für die Frage der prinzipiell möglichen Schreibgeschwindigkeit magnetischer Informationen von fundamentalem Interesse. Die mikroskopischen Details der komplexen Wechselwirkungen zwischen den elektronischen Zuständen, den Spins und den phononischen Anregungen sind dabei teilweise noch nicht vollständig verstanden und unterscheiden sich in ihrer Bedeutung zum Teil für Metalle, Isolatoren oder ferromagnetische Halbleiter [26–36]. Die Spin-Bahn-Kopplung in den angeregten Zuständen ist einer der Mechanismen, welche bei diesen schnellen Entmagnetisierungsprozessen eine Rolle spielen [36]. Es stellt sich heraus, dass durch die Spin-Bahn-Kopplung in magnetischen Systemen die Absorption polarisierter Strahlung von der vorliegenden Magnetisierungsrichtung abhängig ist. Dies ist die Grundlage des *magnetischen Dichroismus*, den man zum Beispiel in der Absorption von Röntgenstrahlung [37, 38] und in spin- und winkelaufgelöster Photoemission [39, 40] beobachten kann. Der quantitative Zugang zum relativen Anteil von magnetischem Orbitalmoment und dem durch den Spin bewirkten Beitrag zum magnetischen Moment in elektronischen Rumpfniveauständen wird zum Beispiel über Summenregeln für den Dichroismus in der Absorption zirkular polarisierter Strahlung (X-ray magnetic circular dichroism, XMCD) ermöglicht [41]. In Kombination mit ultrakurzen Laserpulsen ermöglicht der Effekt des magnetischen Dichroismus die Analyse der Dynamik von Spin- und Orbitalmoment bis hinab zur Femtosekundenskala [42, 43], was Einblicke in Fragen des optisch angeregten Nichtgleichgewichtsmagnetismus erlaubt. Weil angeregte Zustände generell eine Schlüsselrolle in optisch gesteuerten spin-abhängigen Prozessen spielen können, ist es deshalb von großem Interesse, die Spin-Bahn-Kopplung in diesen angeregten Zuständen zu charakterisieren. Dazu werden klare spektroskopische Informationen benötigt, die insbesondere mittels einer Kombination von magnetischem Dichroismus und Zweiphotonen-Photoemission von magnetischen Proben erhalten werden können, mit den optisch angeregten Zuständen als Zwischenzuständen (siehe die Ergebnisse in Abschnitt 3.4 über optisch angeregte Quantentopfzustände in Kobaltfilmen).

Wir sehen, dass die Spin-Bahn-Kopplung einen fundamentalen Wechselwirkungsmechanismus in elektronischen Systemen beschreibt, über den sich der Freiheitsgrad des Spins in verschiedenen physikalischen Effekten auswirkt. Über die magnetische Datenspeicherung hinausgehend, ist die Nutzung des Elektronenspins in technischen Bauelementen ein Ziel der sogenannten „Spintronik“ [44], die potentiell auf den räumlichen Skalen der Nanotechnologie, mit höheren Verarbeitungsgeschwindigkeiten und mit weniger elektrischen Verlusten als die herkömmliche Elektronik arbeiten würde. Nicht zuletzt für die Realisierung solcher Technologien sind genaue Kenntnisse der spinabhängigen elektronischen Struktur von Festkörpern und der möglichen Kopplungs- und Steuermechanismen von Spins von großer Bedeutung.

1.2 Winkelaufgelöste Photoemission mit Spin-Analyse

1.2.1 Photoemission

Die Photoelektronenspektroskopie (PES) ist eine leistungsfähige Methode zur Analyse der elektronischen Struktur von Festkörpern und ihrer Oberflächen [45–47]. Sehr allgemein betrachtet, bestimmt man in dieser Methode, wieviele Elektronen mit einer bestimmten Energie die bestrahlte Probe in festgelegte Richtungen verlassen. Da die Anregungsphotonen bei den verwendeten Wellenlängen nur einen vernachlässigbar kleinen Impuls übertragen können, läßt der außerhalb der Probe beobachtete Elektronenimpuls Rückschlüsse auf den Zusammenhang zwischen Impuls und Energie der Elektronen im Ausgangszustand zu. Dies reicht von den Rumpfniveaus mit Bindungsenergien im Röntgenbereich bis zu den Valenzelektronen, die mittels kurzwelliger UV-Strahlung erreichbar sind. In grundlegende festkörperphysikalische Effekte wie Supraleitung [48], Metall-Isolator-Übergänge [49], die elektronische Struktur von Graphen [50–52], topologische Isolatoren [16, 17], und niedrigdimensionale Systeme [53–55] können mit Photoelektronenspektroskopie Einblicke erhalten werden.

Der Photoemissionsstrom J resultiert in einer vereinfachten theoretischen Beschreibung im Einteilchenbild aus photoinduzierten Übergängen zwischen besetzten ($|\psi_i\rangle, E_i, \mathbf{k}_i$) und unbesetzten ($|\psi_f\rangle, E_f, \mathbf{k}_f$) Zuständen (für eine Diskussion von Mehrteilcheneffekten in der Photoemission siehe z.B. [56]). Diese Einteilchenzustände besitzen einen Energieunterschied $E_f - E_i$, welcher der einfallenden Photonenenergie $h\nu$ entspricht. Es wird angenommen, dass nach dem Übergang das Photoelektron sofort vom übrigen System entkoppelt ist („sudden approximation“). Der durch die einfallende Strahlung bewirkte Übergang wird mittels eines Wechselwirkungsoperators \hat{V}_I beschrieben. Im sogenannten „three-step-model“ werden dann (I) die Anregung des Photoelektrons im Festkörper, (II) der Transport zur Oberfläche und (III) der Durchgang durch die Oberfläche als unterscheidbare Phasen im Gesamtprozess betrachtet, denen separate Effekte auf das Photoemissionssignal zugeordnet werden können [46]. In einer vollständigen theoretischen Beschreibung sind die drei Schritte im allgemeinen nicht trennbar und werden als ein zusammenhängender kohärenter Prozess betrachtet („one-step-model“). Der Endzustand des Photoelektrons kann im Festkörper und an seiner Oberfläche gestreut werden und entspricht am Detektor einer auslaufenden ebenen Welle („inverser LEED-Zustand“) [57]. Der Photostrom J bei der kinetischen Energie E_{kin} und der Parallelkomponente des Wellenzahlvektors im Vakuum \mathbf{k}_{\parallel}^V ergibt sich als

$$J(E_{kin}, \mathbf{k}_{\parallel}^V) \propto \sum_{i,f,\mathbf{G},\mathbf{g}_{\parallel}} |M_{fi}(\mathbf{k}_f, \mathbf{k}_i)|^2 \cdot \delta(E_f - E_i - h\nu) \cdot \delta(\mathbf{k}_f - \mathbf{k}_i - \mathbf{G}) \quad (1.4)$$

$$\cdot \delta(E_{kin} - E_f + \Phi) \cdot \delta(\mathbf{k}_{\parallel}^V - \mathbf{k}_{f\parallel} - \mathbf{g}_{\parallel})$$

Die Deltafunktionen in der ersten Zeile von Gleichung (1.4) beschreiben eine ideale Energie- und Impulserhaltung (modulo eines reziproken Gittervektors \mathbf{G}) des Übergangs im Festkörper, sowie

in der zweiten Zeile eine ideale energie- und winkelaufgelöste Detektion, wobei beim Übergang nur der Impuls \mathbf{k}_{\parallel}^V parallel zur Oberfläche modulo eines reziproken Oberflächengittervektors \mathbf{g}_{\parallel} erhalten bleibt. Die kinetische Energie $E_{kin} = E_f - \Phi$ ergibt sich dabei aus der Differenz der Endzustandsenergie und dem Vakuumniveau Φ . Die Photoemission wird im wesentlichen durch das Übergangsmatrixelement M_{fi} gesteuert [58]:

$$M_{fi} = \langle \psi_f | \hat{V}_I | \psi_i \rangle \quad (1.5)$$

$$\hat{V}_I = \frac{-e}{mc} [\mathbf{A}(\mathbf{r}) \cdot \mathbf{p} + \mathbf{p} \cdot \mathbf{A}(\mathbf{r})] + \frac{e^2}{2mc^2} |\mathbf{A}(\mathbf{r})|^2 \quad (1.6)$$

Im Wechselwirkungsoperator \hat{V}_I wird häufig der Term $\mathbf{p} \cdot \mathbf{A}(\mathbf{r})$ auf Null gesetzt (Coulomb-Eichung im Volumen), und der quadratische Term wird ebenfalls vernachlässigt (dies ist bei hohen Laserintensitäten nicht mehr zulässig [59]). Im verbleibenden Term $\mathbf{A}(\mathbf{r}) \cdot \mathbf{p}$ kann durch $\mathbf{A}(\mathbf{r}) = A_0 \mathbf{e}$ die Dipolnäherung durchgeführt werden, wobei das Vektorpotential $\mathbf{A}(\mathbf{r})$ der einfallenden Strahlung als konstant angenommen wird, mit dem Polarisationsvektor \mathbf{e} . Diese Näherungen werden z.B. in [58] detailliert beschrieben. In der Dipolnäherung reduziert sich dann das Matrixelement auf:

$$M_{fi} \propto A_0 \langle \psi_f | \mathbf{e} \cdot \mathbf{r} | \psi_i \rangle \quad (1.7)$$

Im Rahmen der in der vorliegenden Arbeit untersuchten Effekte ist als wichtige Eigenschaft des Matrixelementes (1.7) festzuhalten, dass der Spin des Ausgangszustandes und des Endzustandes nicht explizit im Wechselwirkungsoperator vorkommen und dass damit der Spin durch die optische Anregung nicht verändert wird. Aus (1.7) folgen jedoch auch die optischen Auswahlregeln für Dipolübergänge, insbesondere für atomare Zustände auch die Auswahlregeln für zirkular polarisierte Strahlung $j_f = j_i \pm 1$ und $m_f = m_i \pm 1$. Diese Auswahlregel ist für die oben erwähnte optische Anregung spinpolarisierter Elektronen unter Einfluss der Spin-Bahn-Wechselwirkung relevant, wenn entweder $|\psi_i\rangle$ oder auch $|\psi_f\rangle$ eine (1.3) analoge Zusammensetzung haben. Eine Verallgemeinerung dieser Auswahlregeln auf elektronische Zustände in Kristallen findet sich in [60, 61]. Die Anregung mit zirkular polarisiertem Licht in einer chiralen experimentellen Geometrie kann das Matrixelement (1.7) zu richtungsabhängigen Interferenzeffekten bei der gleichzeitigen Anregung von verschiedenen Orbitalen führen. Dieser Effekt wird als zirkularer Dichroismus in der winkelaufgelösten Photoemission (circular dichroism in the angular distribution, CDAD) [62] bezeichnet. Mit einer zusätzlich vorliegenden Magnetisierung entsteht über die Transformationseigenschaften der Spin-Wellenfunktion in analoger Weise der verallgemeinerte Effekt des magnetischen Dichroismus [63].

1.2.2 Spin-Analyse der Photoelektronen

Das Ziel der Photoelektronenspektroskopie ist die zuverlässige Charakterisierung aller Eigenschaften von Photoelektronen. Neben der kinetischen Energie und dem Impuls der Elektronen

gehört dazu potentiell natürlich auch ihr Spin [14, 64, 65]. Spinpolarisierte Photoströme können durch verschiedene Effekte entstehen [66–68]. Die Spinpolarisation kann (a) schon im elektronischen Grundzustand vorliegen, (b) im Anregungsprozess nach Matrixelement (1.7) zwischen Grundzustand und Endzustand entstehen und (c) durch spinabhängige Streuprozesse im Endzustand, z.B. bei der Transmission durch die Oberfläche [15] produziert werden. Diese Anteile können im allgemeinen Fall nicht notwendigerweise voneinander getrennt werden. Wenn die optisch angeregten Elektronen jedoch ihren Spin während des Photoemissionsprozesses nicht ändern, können die Photoelektronenspektren direkt die Majoritäts- und Minoritätsbänder von magnetischen System widerspiegeln [14, 69, 70].

Wegen der elektrischen Ladung des Elektrons und der damit verbundenen zusätzlichen Lorentzkraft kann man den Spin eines freien Elektrons nicht wie in einem Stern-Gerlach-Experiment durch die Ablenkung in einem inhomogenen Magnetfeld messen [64]. Das Arbeitsprinzip von Spin-Analysatoren für freie Elektronen beruht deswegen auf spinabhängigen Streuprozessen, wobei man an Prozessen mit möglichst unterschiedlichen Streuquerschnitten für Elektronen mit entgegengesetzten Projektionen des Spins ($+\frac{\hbar}{2} \rightarrow I^{\uparrow\uparrow}$ oder $-\frac{\hbar}{2} \rightarrow I^{\uparrow\downarrow}$) auf eine durch das Streuexperiment festgelegte Quantisierungsachse z interessiert ist.

Aus den experimentell gemessenen Intensitäten für parallele ($I^{\uparrow\uparrow}$) und antiparallele ($I^{\uparrow\downarrow}$) Ausrichtung wird die experimentelle Asymmetrie A_z und daraus die Polarisation P_z bezüglich der gewählten Quantisierungsachse mit Hilfe der Spinsensitivität S berechnet. Die anderen Komponenten P_x und P_y müssen in unabhängigen Experimenten mit entsprechend angepasster Quantisierungsachse bestimmt werden [71]. Die Spinsensitivität (auch Sherman-Funktion genannt) gibt dabei an, welche Spin-Asymmetrie für 100% polarisierte Elektronen gemessen werden würde.

$$A_z = \frac{I^{\uparrow\uparrow} - I^{\uparrow\downarrow}}{I^{\uparrow\uparrow} + I^{\uparrow\downarrow}} \quad (1.8)$$

$$P_z = A_z/S \quad (1.9)$$

Aus der Gesamtintensität I können die Partialspektren I^+ , I^- der beiden Spinkomponenten berechnet werden:

$$I = I^{\uparrow\uparrow} + I^{\uparrow\downarrow} \quad (1.10)$$

$$I^+ = \frac{I}{2}(1 + P) \quad (1.11)$$

$$I^- = \frac{I}{2}(1 - P) \quad (1.12)$$

Die Effektivität eines Spinpolarisationsanalysators wird durch eine Gütezahl F („figure of merit“) gemessen. Dabei gibt $1/F$ an, wieviel mal mehr Ereignisse man in einer spinaufgelösten Messung zählen muss, um den gleichen statistischen Fehler wie eine nicht-spinaufgelöste Messung zu erreichen (für die Fehlerrechnung bei der Bestimmung der Spinpolarisation aus den gezählten Er-

eignissen $I^{\uparrow\uparrow}$ und $I^{\uparrow\downarrow}$ siehe [64, 72]). In die Gütezahl F geht die Reflektivität I/I_0 für die einfallende Intensität I_0 linear ein, und die Spinsensitivität S quadratisch [64]:

$$F = S^2 \cdot I/I_0 \quad (1.13)$$

Ein systematischer Vergleich von verschiedenen Typen von Spin-Analysatoren findet sich in [73] und [74], [75]. Eine große Gruppe von Spin-Analysatoren nutzt den Einfluss der Spin-Bahn-Kopplung im Mott-Streuquerschnitt aus, was z.B. zu einer Links-Rechts-Asymmetrie im Streuprozess für spin-polarisierte Elektronen führt. In den meisten Fällen dominiert jedoch die Coulomb-Streuung den Streuquerschnitt im Vergleich Spin-Bahn-Kopplung. Das bedeutet, dass man, damit die Spin-Bahn-Kopplung relevant wird, experimentell solche Streubedingungen wählen muss, unter denen die Coulomb-Streuung relativ klein ist. Dies geht notwendigerweise mit einer Verringerung der Zählrate um ein bis zwei Größenordnungen einher [64]. Typischerweise resultieren insgesamt Faktoren in der Größenordnung $1/F \approx 10^4$. Dies verdeutlicht auf der einen Seite die Erhöhung des Zeitaufwands, der für spin-aufgelöste Photoemissionsmessungen nötig ist, auf der anderen Seite illustriert dieser Faktor das Potential, welches Verbesserungen in der Spinanalyse freier Elektronen für den weiträumigeren Einsatz in spinaufgelösten elektronenspektroskopischen Methoden haben.

Ein weiterer Typ von spinabhängigen Wechselwirkungen besteht in der Austauschwechselwirkung in magnetischen Systemen. Die entsprechende Wechselwirkungsenergie ist in der Größenordnung von 2 eV in ferromagnetischem Eisen. Diese Energie ist signifikant im Vergleich zu Streuenergien von sehr niederenergetischen Elektronen (< 20 eV) an Oberflächen und es kann deshalb erwartet werden, dass die Streuquerschnitte merklich durch die spin-abhängige Austauschenergie beeinflusst werden können. Magnetische Oberflächen können zum Beispiel spin-abhängige Bandlücken besitzen, was dazu führt, dass Elektronen mit unterschiedlichem Spin entweder Zustände im Kristall besetzen können oder nicht, also auch eine spin-abhängige Reflektivität für die beiden möglichen Spinkomponenten vorliegt. Wenn die Streuenergie niedrig genug ist, sind außerdem keine gebeugten Strahlen erlaubt, in welche zusätzliche Intensität verloren gehen könnte. Dies führt dann zu einer hohen über den Spin gemittelten Reflektivität. Ferromagnetische Eisenoberflächen sind hier von besonderem Interesse, da für sie eine große Streu-Asymmetrie bei gleichzeitiger hoher Streueffektivität vorhergesagt [76] und auch gemessen wurde [77, 78]. Auf der Basis dieser Beobachtungen wurde der für die hier vorgestellten Arbeiten eingesetzte Spinanalysator am MPI Halle durch J. Kirschner entwickelt. Die technischen Parameter sind in Abschnitt 2.2 zusammengestellt.

Im Gegensatz zur explizit spinaufgelösten Photoelektronenspektroskopie erfordert die Beobachtung des Effekts des *magnetischen Dichroismus* keinen zusätzlichen Spinanalysator. Dies ist gegenüber spin-aufgelösten Methoden einerseits experimentell von Vorteil, andererseits aber ist wegen des Fehlens der expliziten Spinanalyse für quantitative Rückschlüsse oftmals eine Kombinati-

on mit entsprechenden theoretischen Rechnungen notwendig [63]. Wenn keine quantitative Spinanalyse erforderlich ist, bildet der magnetische Dichroismus zum Beispiel eine effektive Möglichkeit zur Abbildung magnetischer Domänen im Photoelektronenemissionsmikroskop (PEEM) [79].

Völlig analog zur spinabhängigen Asymmetrie A_z in Gleichung (1.8) benutzt man zur Quantifizierung des magnetischen Dichroismus die normalisierte Intensitätsänderung bei Umschalten der Magnetisierung (M^+ , M^-) bzw. bei Änderung der Polarisation der anregenden Strahlung (π^+ , π^-):

$$A^M = \frac{I^{M^+} - I^{M^-}}{I^{M^+} + I^{M^-}} \quad (1.14)$$

$$A^\pi = \frac{I^{\pi^+} - I^{\pi^-}}{I^{\pi^+} + I^{\pi^-}} \quad (1.15)$$

Der magnetische Dichroismus in der Photoemission ist im wesentlichen ein Interferenzeffekt zwischen verschiedenen möglichen Anregungspfaden und spiegelt damit den Spin nur indirekt wieder, da zusätzlich die spezifischen Eigenschaften des Anregungsprozesses (Matrixelemente, Photonenergie, Geometrie von Magnetisierung und Photoelektronenimpuls) den Interferenzeffekt quantitativ bestimmen [63]. In einem spinaufgelösten Photoemissionsexperiment mit magnetischem Dichroismus kann die gemessene Intensität aber natürlich zusätzlich durchaus noch nach dem Spin der Photoelektronen analysiert werden. Dann ergibt sich ein Datensatz von insgesamt 8 möglichen Photoelektronenspektren $I^{\pm s, M^\pm, \pi^\pm}$, zwischen denen bestimmte Symmetriebeziehungen bestehen müssen [80]. Hieraus lassen sich wertvolle Informationen über den relativen Anteil der Austausch- und der Spin-Bahn-Wechselwirkung in dem jeweiligen System erhalten [81].

1.3 Ultrakurze optische Anregungen und spinaufgelöste nichtlineare Photoemission

Der bekannte äußere photoelektrische Effekt kann durch die Energieübertragung einzelner Lichtquanten auf die Elektronen erklärt werden [82]. Die Möglichkeit von Prozessen bei denen nicht nur ein einzelnes Photon, sondern gleichzeitig zwei oder mehrere Quanten ausgetauscht werden, wurde durch M. Göppert-Mayer [83, 84] schon Anfang der 1930iger Jahre beschrieben. Wegen der niedrigen Wahrscheinlichkeit dieser Mehrquantenprozesse und der dafür notwendigen Strahlungsintensitäten wurden solche Prozesse jedoch erst mit der Erfindung des Lasers regelmäßig beobachtbar. Die ersten Messungen nichtlinearer Photoemission wurden von Teich *et al.* [85] berichtet. Laser liefern aber nicht nur hohe Intensitäten, sondern ermöglichen über die Erzeugung kurzer Lichtpulse auch den Zugang zu dynamischen Prozessen. Durch die Entwicklung der Femtosekundenlaser als „Blitzlicht“ seit den 1980er Jahren ist die Zeitskala von chemischen Reaktionen zwischen 10 fs und 10 ps direkt in der Zeitdömane zugänglich geworden [86]. Die kürzesten Laserpulse sind heutzutage nur noch wenige optische Zyklen lang [87]. Diese Pulse sind der Ausgangspunkt zum Erreichen der Attosekundenzeitskala (10^{-18} s), mit der ein direkter Zugang zur Elektronendynamik in Atomen und Festkörpern prinzipiell in Reichweite gekommen ist [88]. Die direkte Kontrolle über niederenergetische *kollektive* Anregungen in Festkörpern ermöglichen heutzutage starke Femtosekundenpulse im THz-Frequenzbereich, womit auch kollektive magnetische Anregungen [89] steuerbar sind.

In nichtlinearen Photoemissionsprozessen spielen die besetzten Ausgangszustände, die anfänglich unbesetzten Zwischenzustände und die photoemittierten Endzustände eine zentrale Rolle, sowie die durch die ultrakurzen, hochintensiven optischen Pulse erzeugte Kopplung zwischen diesen Zuständen. Die Besonderheit von Mehrphotonenprozessen liegt in der Möglichkeit, über Messungen mit verzögerten Pulsen direkt Zugang zum zeitlichen Verhalten des angeregten Systems zu bekommen („pump-probe“ Experimente). Hier hat insbesondere die Zweiphotonenphotoemission (2PPE) bedeutende Einblicke in die Zerfalls- und Dekohärenzzeiten angeregter Elektronen an Oberflächen ermöglicht [90–92]. Eine große Gruppe von Experimenten untersuchte dabei Bildpotentialzustände an Metalloberflächen. Diese Zustände zeigen wegen ihrer weitgehenden Entkopplung von den Volumenzuständen relative lange Lebensdauern und sie sind wegen ihres physikalisch klaren Bildungsmechanismus [93] wichtige Modellsysteme für Elektronendynamik an nichtmagnetischen und magnetischen Festkörperoberflächen [90, 91, 94–97].

Gegenüber der linearen Photoemission spielen in der Mehrphotonenphotoemission auf der einen Seite die Zwischenzustände eine zentrale Rolle, auf der anderen Seite muss auch die zeitliche quantenmechanische Entwicklung der Anregung durch ultrakurze Pulse direkt in Betracht gezogen werden. Eine Beschreibung nach Fermis Goldener Regel wie in (1.4) reicht deswegen im Allgemeinen nicht aus. Eine allgemeine Methode für die Beschreibung der Zeitentwicklung quantenmechanischer Systeme in Wechselwirkung mit externe Freiheitsgraden ist der Dichtematrix-

formalismus [98–101]. Damit ist es möglich, die Kopplungen zwischen elektronischen Zuständen und dem optischen Anregungsfeld, sowie die Wechselwirkung mit den zusätzlichen externen Umweltfreiheitsgraden explizit zeitabhängig in Betracht zu ziehen [91, 102–107]. Für nichtlineare Photoemissionsexperimente wird in vielen Fällen eine semiklassische Behandlung genutzt, bei der die elektronischen Zustände quantisiert sind, aber die Strahlung als klassisches elektrisches Feld betrachtet wird.

Für die Klärung der später benutzten Nomenklatur soll als einfachstes Beispiel der 2PPE-Prozess dienen, an dem drei Zustände beteiligt sind. Eine verallgemeinerte Diskussion für 3PPE findet sich in den Ergebnissen in [AW 5.1]. Das betrachtete System besteht aus drei orthonormalisierten Zuständen ($\langle a|b\rangle = \delta_{ab}$), welche jeweils den Ausgangszustand $|i\rangle$, den Zwischenzustand $|m\rangle$ und den Endzustand $|f\rangle$ repräsentieren, die bei den Energien $\epsilon_{i,m,f}$ liegen. Der Dichteoperator $\hat{\rho}$ eines Dreiniveausystems ist:

$$\hat{\rho} = \begin{pmatrix} \rho_{ii} & |i\rangle\langle i| & \rho_{im} & |i\rangle\langle m| & \rho_{if} & |i\rangle\langle f| \\ \rho_{mi} & |m\rangle\langle i| & \rho_{mm} & |m\rangle\langle m| & \rho_{mf} & |m\rangle\langle f| \\ \rho_{fi} & |f\rangle\langle i| & \rho_{fm} & |f\rangle\langle m| & \rho_{ff} & |f\rangle\langle f| \end{pmatrix} \quad (1.16)$$

$$\rho_{ii}(t = -\infty) = 1$$

Die Diagonalelemente beschreiben dabei die Besetzungen der jeweiligen Zustände, die Nichtdiagonalelemente beschreiben Überlagerungen von Zuständen, welche für Interferenzeffekte verantwortlich sind [98]. Das Matrixelement ρ_{ii} ist dabei dunkelgrau unterlegt, um seine Rolle als einziger besetzter Ausgangszustand zu betonen, mit $\rho_{ii} = 1$ ohne Laserpuls zur Anfangszeit $t = -\infty$. Die beobachteten Photoelektronen $N(\epsilon_f)$ bei der Energie des Endzustandes werden im Dichtematrixformalismus über die Spurbildung nach Anwendung eines der Observable entsprechenden Operators \hat{F} und der Integration über die Zeit (Pulsdauer) beschrieben:

$$N(E_f) = \int_{-\infty}^{+\infty} dt \text{Tr}\{\hat{F}\hat{\rho}(t, E_f)\} \quad (1.17)$$

Die explizite Form des Operators \hat{F} ist hier relativ einfach, da wir im Prinzip nur ρ_{ff} messen wollen: $\hat{F} = |f\rangle\langle f|$. Diese Besetzung kann letztendlich nur aus dem Ausgangszustand kommen. Dies passiert während der Zeitentwicklung des Systems unter Einwirkung der einfallenden Strahlung. Die entsprechende Entwicklung des Dichteoperators ist durch die Liouville - von Neumann Gleichung gegeben [91, 99, 103, 104, 106]:

$$\frac{d\rho_{ab}}{dt} = -\frac{i}{\hbar} \langle a | [\hat{H}_S + \hat{V}_I, \hat{\rho}] | b \rangle - \Gamma_{ab} \rho_{ab} \quad (1.18)$$

$(a, b = i, m, f)$

Dabei ist \hat{H}_S der Hamiltonoperator des ungestörten Systems und \hat{V}_I der Wechselwirkungsoperator (vgl. (1.5)), der die optischen Kopplungen liefert und letztendlich Intensität von einem Dichtematrixelement zu einem anderen transferiert. Die Dipolnäherung für \hat{V}_I führt zu den Dipolmatrixelementen μ_{ab} welche die Stärke der Kopplung zwischen zwei Zuständen $|a\rangle$ und $|b\rangle$ durch ein klassisches elektrisches Feld mit Amplitude $E(t)$ angeben. In einem Festkörper wird das interne elektrische Feld, das zur Anregung der Photoemission führt, durch die kollektive optische Antwort des Systems zeitabhängig beeinflusst, was durch z.B. eine komplexe frequenzabhängige Antwortfunktion berücksichtigt werden kann [108].

In Gleichung (1.18) sind Γ_{ab} phänomenologische Parameter, welche die zeitliche Relaxation des Systems zurück zum Gleichgewicht durch Energie- und Impulsaustausch mit externen Freiheitsgraden beschreiben. Die Diagonalelemente Γ_{aa} beschreiben den Zerfall der Besetzungszahl von Zuständen, während die Nichtdiagonalelemente Γ_{ab} den zeitlichen Zerfall von Überlagerungen (Kohärenzen) zwischen Zuständen berücksichtigen. Es sind gerade die Parameter Γ und die ihnen entsprechenden Lebensdauern und Zerfallszeiten, die z.B. in zeitaufgelösten 2PPE-Experimenten ermittelt werden sollen.

Aus Gleichung (1.18) ergibt sich durch Einsetzen der entsprechenden Operatormatrixelemente ein System gekoppelter Differentialgleichungen für die Dichtematrixelemente ρ_{ab} , welches numerisch gelöst werden kann [91]. Analytische Lösungen sind für 2PPE von Dreineiveausystemen unter kontinuierlicher Anregung bekannt [109]. Physikalisch transparent ist eine störungstheoretische Entwicklung von $\hat{\rho}$ nach der Anzahl der Wechselwirkungen mit dem elektrischen Feld. Dies erlaubt es, die Entwicklung endlicher Werte in den ursprünglich unbesetzten Matrixelementen ρ_{ab} als Sequenzen zu visualisieren, bei denen die Kommutatoren $[\hat{H}_S + \hat{V}_I, \hat{\rho}]$ in Gleichung (1.18) rekursiv bis zu einer bestimmten Ordnung entwickelt werden. Diese Entwicklung kann über sogenannte doppelseitige Feynmandiagramme symbolisiert werden, welche sowohl die Zeitentwicklung der Populationen (Diagonalelemente von $\hat{\rho}$) als auch die der Superpositionen der Zustände (Nichtdiagonalelemente von $\hat{\rho}$) berücksichtigen [99]. Ein weiterer sehr nützlicher Typ von graphischen Visualisierungen der möglichen Kopplungen zwischen beliebigen Elementen ρ_{ab} und ρ_{cd} der Dichtematrix sind Liouville-Pfade (Liouville space pathways) [99]. Aus den Liouville-Pfaden wird erkennbar, dass eine einzelne Wechselwirkung mit dem elektromagnetischen Feld jeweils nur horizontal oder vertikal benachbarte Elemente der Dichtematrix koppelt [106]. Damit sind mehrteilige Photoemissionspfade möglich, die eine explizite Besetzung des Zwischenzustandes ρ_{mm} umgehen und welche für die kohärenten Photoemissionseffekte verantwortlich sind, die in [AW 5.1] beschrieben werden.

Im Vergleich zum Photostrom werden elektromagnetische Signale direkt von der im System induzierten Polarisation \vec{P} und damit letztendlich von Erwartungswerten des Dipoloperators $\hat{\mu}$ bestimmt: $\vec{P} = \text{Tr}[\hat{\mu}\hat{\rho}]$. Die relevanten Dichtematrixelemente sind vom Typ $|b\rangle\langle a|$, also nichtdiagonal [99]. Damit wird ein Vorteil des Dichtematrixformalismus klar, nämlich dass sowohl die Photoemission als auch die nichtlinear-optischen Signale des beobachteten Systems in einem vereinigten Bild über gemeinsame Parameter behandelt werden können. Wie in [AW 5.2] gezeigt ist, können solche kombinierten Experimente zusätzliche Informationen über die optisch angeregten Zustände geben.

Elektronische Bandstrukturen in realen Festkörpern können nur in seltenen Fällen durch ein Dreiniveausystem angenähert werden. Eine Verallgemeinerung auf bandartige Zustände kann zum Beispiel durch Einführung von \mathbf{k} -abhängigen Drei- oder Mehrniveausystemen erfolgen [110]. Dabei muss zusätzlich die Kopplung von Zuständen bei verschiedenen E und \mathbf{k} durch elastische und inelastische Streuprozesse berücksichtigt werden. Hieraus resultiert die extrem steigende Komplexität einer *ab-initio* Behandlung der nichtlinearen Photoemission in Festkörpern gegenüber der linearen Photoemission.

Ebenso vernachlässigt wurde in der obigen Beschreibung der Spin in den betrachteten Zuständen, welcher ja prinzipiell durch einen spin-abhängigen Wechselwirkungsoperator \hat{V}_I , spinabhängige Matrixelemente $\langle a|V_I|b\rangle$ oder spinabhängige Streuprozesse Γ_{ab} beeinflusst werden könnte. Im allgemeinen Fall muss eine Kopplung zwischen beiden Spinreservoirs berücksichtigt werden, da Streuprozesse mit Spinumkehr ein angeregtes Elektron im Zwischenzustand von einer Gruppe in die andere transferieren können [72, 111]. Dazu zählt eine mögliche Aufüllung eines Zustands $|a\rangle$ durch inelastische spinabhängige Streuprozesse aus einem anderen Zustand $|b\rangle$. Damit können die Dynamiken der Populationen mit unterschiedlichem Spin miteinander auf komplexe Weise verbunden sein, was die Notwendigkeit einer theoretischen Beschreibung und Modellierung verdeutlicht.

Spinaufgelöste 2PPE wurde bis jetzt vorwiegend zur Aufklärung der spinabhängigen elektronischen Struktur und Dynamik an ferromagnetischen Oberflächen eingesetzt. Erste energie- und zeitaufgelöste Untersuchungen dazu erfolgten 1997 von Aeschlimann *et al.* für die Lebensdauern von Volumenzuständen in fcc Kobaltfilmen auf Cu(001) [112]. Die spin-integrierten Lebensdauern waren dabei näherungsweise zu $1/(E - E_{Fermi})^2$ proportional, was aus der Theorie der Fermi-Flüssigkeiten erwartet wird [113]. Aus der größeren unbesetzten Zustandsdichte und der dadurch erhöhten Anzahl von Zerfallskanälen wird in Ferromagneten allgemein für Minoritätselektronen eine kürzere Lebensdauer im Vergleich zu den Majoritätselektronen erwartet [114, 115]. In den erwähnten spinaufgelösten 2PPE-Messungen [112] wurde damit übereinstimmend ein Verhältnis von Majoritäts- zu Minoritätslebensdauern in Co von ≈ 2 für Elektronen mit einer Energie von 1 eV über dem Fermi-niveau gefunden, das sich bei 0.6 eV auf ≈ 1.3 reduziert, mit ähnlichen Werten auch für Eisen- und Nickelfilme [116]. Die Erzeugung von Sekundärelektronen in Austauschstreuprozessen beeinflusst dabei die gemessenen Lebensdauern bei Energien näher am

Fermi-Niveau [117]. Mögliche Verbindungen von Spin-flip Prozessen und der Magnetisierungsdynamik wurden ebenfalls für Messungen an Kobaltfilmen diskutiert [118]. Durch Experimente an verschiedenen Heusler-Legierungen wurde weiterhin der Einfluss der elektronischen Struktur auf die spinabhängigen Lebensdauern untersucht [119].

Eine weitere Gruppe von spinaufgelösten 2PPE-Experimenten von Weinelt *et al.* [72,96,120] nutzte die durch die Austauschwechselwirkung spin-aufgespaltene Bildpotentialzustände [121]. Das Bild der kürzeren Lebensdauern für Minoritätselektronen gilt auch für diese Zustände, und wegen des gegenüber Volumenzuständen reduzierten Phasenraumes können die entsprechenden Streuprozesse sehr definiert untersucht werden. Für die Bildpotentialzustände an Eisen- und an Kobaltoberflächen wurden dabei ähnliche Lebensdauer $verhältnisse$ gefunden, wie schon für die Volumenzustände [72,96]. Die Erzeugung von Magnonen wurde für spinabhängige quasi-elastische Streuung und daraus folgende höhere Dephasierungsraten für Minoritäts-Bildpotentialzustände von Fe/Cu(001) verantwortlich gemacht [72,120]. Ebenso wurde Magnonenerzeugung auf der fs-Zeitskala für spinabhängige inelastische Intrabandstreuung diskutiert [111]. Da die Bildpotentialzustände an die Volumenbandstruktur gekoppelt sind, können sie als Sensor für die Oberflächen- und Volumenmagnetisierung dienen, zum Beispiel über die Analyse der Spinpolarisation in Abhängigkeit von der Photonenenergie und der Polarisation der anregenden Strahlung [122]. Spin-Bahn-Kopplungseffekte in *besetzten* elektronischen Zuständen waren in diesen Experimenten ebenfalls messbar [123].

Weitere Systeme die mit spinaufgelöster 2PPE untersucht worden sind, beinhalten organische Schichten auf ferromagnetischen Oberflächen. Hier wurde der spinabhängige Transport von Photoelektronen durch die Grenzfläche analysiert [124]. Mit Bezug zur Magnetisierungsdynamik unter optischer Anregung untersuchten Scholl *et al.* Nickelfilme auf Ag(001) [125], allerdings ohne Energieauflösung spezifischer elektronischer Zustände. Für das wichtige Modellsystem der Alkali-Adsorption sind spinabhängige Lebensdauern für Adsorbate auf ferromagnetischen Oberflächen zu erwarten und wurden für Cs/Fe(110) theoretisch vorhergesagt [126].

Im Vergleich zu 2PPE Experimenten haben Prozesse höherer Ordnung und spin-aufgelöste nicht-lineare Photoemissionsprozesse an nichtmagnetischen Festkörperoberflächen bisher vergleichsweise weniger Aufmerksamkeit erfahren. Dies liegt in der hohen benötigten Anregungsintensität und in den niedrigen Photoemissionsintensitäten begründet, welche zum Beispiel durch Raumladungseffekte von Photoelektronen der Prozesse niedrigerer Ordnung überlagert und verwischt werden können [127–137]. Weiterhin können selbst durch relativ niedrige Laserintensitäten schon nicht-photoelektrische Prozesse über Plasmonenanregung und mögliche Tunnelemission verursacht werden, die zu einer direkten Beschleunigung von Elektronen durch das elektrische Feld auf mehrere hundert Elektronenvolt führen [130,138]. Deswegen sind die Mechanismen der nichtlinearen Photoemission höherer Ordnung an Festkörperoberflächen bisher wenig untersucht worden, insbesondere in welchem Ausmaß diese Effekte durch die elektronische Bandstruktur des Festkörpers und seiner Oberfläche beeinflusst sind. Diese offenen Fragestellungen werden mit

den vorliegenden Arbeiten erforscht, und insbesondere werden die Untersuchungen auf spinabhängige Prozesse höherer Ordnung fokussiert.

2 Spinaufgelöste Nichtlineare Photoemission

In diesem Kapitel werden die experimentellen Grundlagen für die hier vorgestellten Arbeiten erläutert. Es handelt sich im wesentlichen um ein Femtosekunden-Lasersystem, welches mit einer Ultrahochvakuum-Oberflächenanalyseanlage zur Probenpräparation und für spinaufgelöste Photoemissionsmessungen gekoppelt ist. Die UHV-Kammer beinhaltet eine Ar-Ionen-Sputterquelle, einen Auger-Analysator (Staib), sowie ein LEED-System (low energy electron diffraction, Omicron SpectraLEED) und einen Phosphorschirm für die Beobachtung von Elektronenbeugung bei streifendem Einfall (medium energy electron diffraction, MEED) zur Kontrolle des Schichtwachstums ultradünner Filme. Die Photoelektronenspektren werden mit einem elektrostatischen Energieanalysator gemessen (Focus CSA 300), der sich in der gleichen Kammer befindet. Dies ermöglicht es, Photoemissions- und nichtlinear-optische Messungen direkt bei zeitabhängigen Wachstums- oder Adsorptionsprozessen durchzuführen.

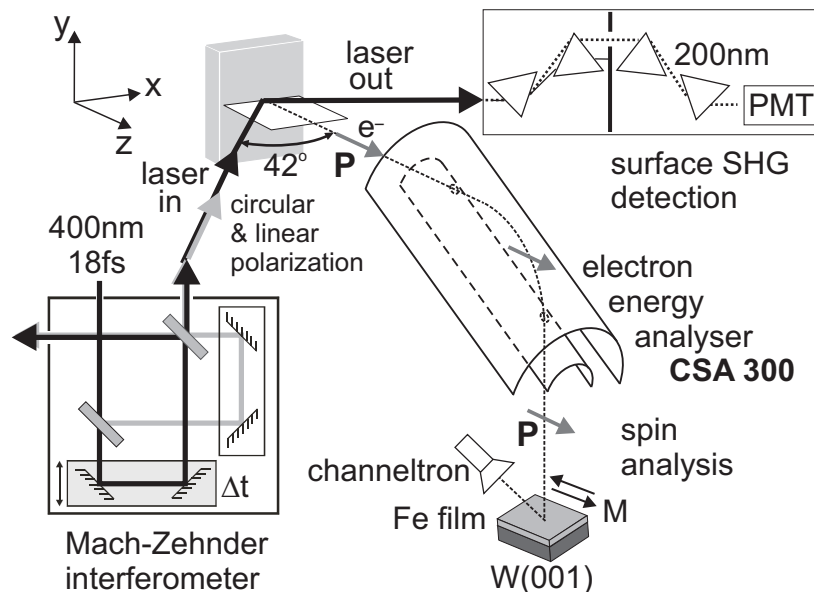


Abbildung 2.1: Prinzipskizze des experimentellen Aufbaus zur spinpolarisierten Mehrphotonen-Photoemission und nichtlinearer Optik. Pulse mit einer Zentralwellenlänge von 400 nm (≈ 3 eV) und einer Dauer von ≈ 18 fs können mittels eines Mach-Zehnder-Interferometers zueinander verzögert werden. Polarisationsoptik ermöglicht die Nutzung zirkular oder linear polarisierter Laserstrahlung an der Probe. Die emittierten Photoelektronen werden mittels eines elektrostatischen Energieanalysators (CSA 300) gemessen. Über Streuung an einem magnetischen Fe-Film auf W(001) erfolgt die Spin-Analyse der Photoelektronen. Gezeigt ist die Analyse der z -Komponente des Elektronenspins. Durch Drehen des W(001)-Kristalls um 90° kann die Spin-Quantisierungsrichtung auch entlang der x -Richtung parallel zur Probenoberfläche gewählt werden. Die reflektierten Photonen nach Erzeugung der zweiten Harmonischen bei 200 nm (surface second harmonic generation, SSHG) werden über einen Prismenfilter und Photovervielfacher (PMT) simultan mit den Photoelektronen detektiert.

2.1 Femtosekunden-Lasersystem

Femtosekundenlaser als Lichtquelle für Photoemissionsexperimente liefern eine sehr hohe Intensität auf einer ultrakurzen Zeitskala und können damit nichtlineare Prozesse induzieren. Die laserbasierte Photoemission ist aber nicht nur wegen der Möglichkeit zur Beobachtung dieser nichtlinearen Prozesse interessant, sondern können auch für konventionelle (lineare, 1PPE) winkelaufgelöste Photoemissionsmessungen große Vorteile bieten. Dies liegt daran, dass der Laser auf eine kleine Fokusfläche mit hoher Photonenintensität in einer relativ schmalen Bandbreite fokussiert werden kann und die Polarisation von Licht bei optischen Wellenlängen kann leicht mittels entsprechender $\lambda/2$ - und $\lambda/4$ -Verzögerungsplatten auf vorgegebene Werte eingestellt werden. Es zeigt sich, dass Intensitäten erreicht werden können, die mit modernen Synchrotrons vergleichbar sind [139, 140]. Die hohe Brillanz ist insbesondere für lokale Messungen mit dem Impulsmikroskop (siehe unten) von Vorteil.

Das genutzte Lasersystem (Abb. 2.1) besteht aus einem Titan-Sapphir Oszillator, dessen Laserpulse eine Zentralwellenlänge um 790nm und eine Zeitdauer unter 10fs haben. Die mittlere Leistung bei 81MHz Repetitionsrate beträgt ≈ 1 W. Die Photonenenergie der Ausgangspulse wird in einem β -BaB₂O₄ (BBO) Kristall über den nichtlinear-optischen Effekt der Erzeugung der zweiten Harmonischen verdoppelt. Die zentrale Photonenenergie der so entstandenen Pulse kann von etwa $h\nu = 2.99$ eV bis 3.15 eV durch Änderung des Phasenanpassungswinkels des BBO-Kristalls verändert werden. Durch einen weiteren Frequenzverdopplungsschritt können dann auch Photonenenergien nahe 6.0 eV für 1PPE-Messungen erzeugt werden. Die Kombination von 2PPE bei 3 eV mit 1PPE bei 6 eV erlaubt systematische Untersuchungen zum Einfluss des Zwischenzustandes in 2PPE im Vergleich zum 1PPE-Prozess ohne diese Zustände (siehe [AW 5.3, AW 5.10]). Für Untersuchungen mit zeitverzögerten Pulsen wurde ein Mach-Zehnder-Interferometer (Abb. 2.1) eingesetzt. Zur Detektion der Photonen, die durch Erzeugung der zweiten Harmonischen (surface second harmonic generation, SHG) von 400 nm zu 200 nm an der Probenoberfläche entstehen, wurde ein Filteraufbau aus vier CaF₂ Prismen genutzt, in welchem die Lichtwellenlängen räumlich dispersiv getrennt und blockiert werden können so dass nur noch die Photonen bei 200 nm mit einem Photoelektronenvervielfacher detektiert werden. Bei der Photonenenergie von $h\nu = 3.07$ eV war die Pulslänge an der Oberfläche ≤ 20 fs. Die Spitzenintensität der Laserpulse auf der Probenoberfläche liegt in der Größenordnung von 10 GW/cm², und die gemessenen Probenströme etwa bei 1 nA, was weniger als 100 emittierten Elektronen pro Puls entspricht. Raumladungseffekte können bei den mit dem Laseraufbau produzierbaren Intensitäten durchaus signifikant sein. In den jeweiligen Experimenten wurde deswegen immer sichergestellt, dass diese Effekte die Photoelektronenspektren nicht messbar beeinflussen.

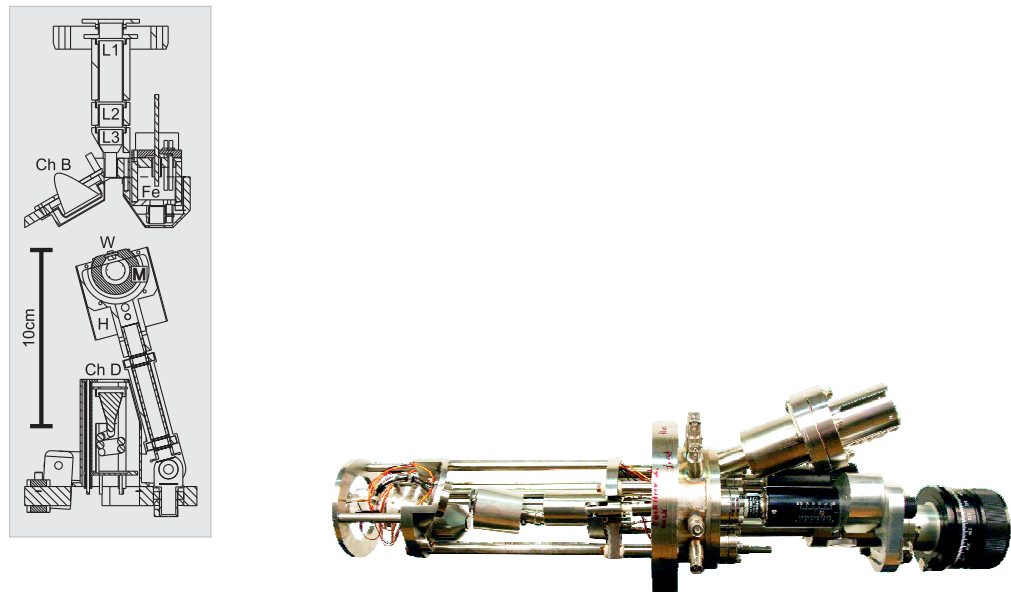


Abbildung 2.2: Links: Zeichnung der Hauptteile des Spinanalysators. (L1,L2,L3) elektrostatische Linsen, (W) W(001) Kristall, (M) Elektromagnet, (H) Halter (rotier- und kippbar) für W, M und das Heizfilament, (Ch B) Channeltron für die von W reflektierten Elektronen, (Ch D) Channeltron für nicht-spinaufgelöste Messungen mit H in der Position unter der Eisenquelle (Fe). Rechts: Foto des Spinanalysators im ausgebauten Zustand

2.2 Elektronen-Spin-Analysator

Originalveröffentlichung: [AW 5.5]

Die spinabhängige Reflexion an Eisenoberflächen wurde wegen ihrer außergewöhnlich hohen Effektivität zur Nutzung in Spin-Analysatoren vorgeschlagen und in der Folge wurden von verschiedenen Gruppen entsprechende Polarimeter konstruiert: Ein Typ basiert auf Fe(001)-Filmen (Dicke $> 3000\text{\AA}$) auf MgO(001) [141, 142], ein anderer auf ultradünnen Fe(001)-Filmen auf Ag(001) [143, 144].

Wegen der relativ einfachen Präparationsmethode von Wolfram W(001)-Substraten durch kurzzeitiges Heizen auf hohe Temperaturen von etwa 2000°C wurde am MPI Halle der Weg über Fe-Filme auf dieser Unterlage gewählt. Der Detektor wurde so entworfen, dass er an einen kommerziellen Elektronen-Energieanalysator angeschlossen werden kann. Dabei handelt es sich um einen zylindrischen Sektoranalysator *Focus CSA300*, der zu einer Ablenkung der Elektronen um 90° führt, was die Detektion der Spinkomponente senkrecht zur Oberfläche der Probe (z -Richtung in Abb. 2.1) sowie einer weiteren Komponente parallel zur Oberfläche ermöglicht (x -Richtung in Abb. 2.1). Die Energieauflösung in den hier vorgestellten spinaufgelösten Experimenten lag bei 100 meV . Die Quantisierungsachse des Spin-Analysators ist durch die Richtung der Magnetisierung M des

Eisenfilms gegeben. Der streuende Kristall und damit die Quantisierungsrichtung kann mechanisch über eine Drehdurchführung justiert werden. Die Kalibrierung des Spindetektors erfolgte über Vergleichsmessungen an bekannten Systemen von ferromagnetischen Filmen.

Die Dimensionen des Analysators betragen etwa $20 \times 20 \times 60 \text{ cm}^3$, damit ist das Gerät leicht in bestehende UHV-Aufbauten zu integrieren. Außer für die Elektronenstoßheizung wird keine Hochspannung benötigt. Die statistische Gütezahl F des Spinanalysators wurde als 0.002 abgeschätzt, was eine wesentliche Verbesserung gegenüber anderen Typen von Spindetektoren bedeutet. In der Zwischenzeit wurde ein weiterer Fe(001)-Spindetektor mit sogar noch besserem F von etwa 0.02 von Okuda *et al.* [145] vorgestellt, was das Potential dieses Systems verdeutlicht. Eine weitere Gruppe nutzt die Austauschstreuung an Co/W(110) in einem Flugzeitspektrometer [146].

Ein wesentlicher Vorteil des hier benutzten Spinanalysators ist seine lange Standzeit, die durch die chemisch inaktive O/Fe(001)-Oberfläche gewährleistet wird. Spinaufgelöste Messungen sind damit über einen Zeitraum von mindestens 2 Wochen ohne Neupräparierung des Fe-Films und ohne wesentliche Änderung der Spinsensitivität möglich.

2.3 Impulsmikroskop

In Photoemissionsexperimenten basiert ein wesentlicher Informationsgehalt auf der möglichst hochaufgelösten Detektion der Energie und der Emissionsrichtung der Photoelektronen. Insbesondere spiegeln sich in der Winkelverteilung der emittierten Photoelektronen diejenigen Effekte wieder, welche mit der Symmetrie der relevanten elektronischen Zustände unter dem Einfluss der Polarisation der anregenden Strahlung zusammenhängen. Die entsprechenden Experimente profitieren somit sehr von einer Paralleldetektion von Elektronen bei verschiedenen Emissionswinkeln und/oder verschiedenen kinetischen Energien. Dies wird in herkömmlichen hemisphärischen Analysatoren meistens durch die zweidimensionale Elektronendetektion mittels eines Multichannelplates (MCP) realisiert, wobei eine Richtung energie- und die andere winkeldispersiv (\vec{k}_{\parallel}) arbeitet. Damit bildet man eine skalierte $E(\vec{k}_{\parallel})$ -Dispersion der Photoelektronen in einem mehr oder weniger ausgedehnten E und \vec{k}_{\parallel} -Bereich ab. Aktuelle hemisphärische Analysatoren erreichen hier einen detektierten Öffnungswinkel von bis zu 60° bei einer Auflösung von wenigen meV (z.B. Scienta EW4000 [147], SPECS PHOIBOS 150 WAL [148]). Andere elektrostatische Ansätze können ausgedehnte zweidimensionale Winkelverteilungen abbilden („Display-type“ Analysatoren) [149, 150].

Eine andere sehr effektive Methode besteht in der Kopplung eines Photoelektronen-Emissionsmikroskops mit nachfolgender Energieanalyse [152]. Das Arbeitsprinzip des PEEM mit einer hohen Absaugspannung im Bereich mehrerer kV bringt eine mögliche Detektion quasi aller in den Halbraum über der Probe emittierten Elektronen mit sich. Die Elektronenoptik eines PEEM kann eine Ortsabbildung mit Auflösungen bis in den Bereich weniger Nanometer reali-

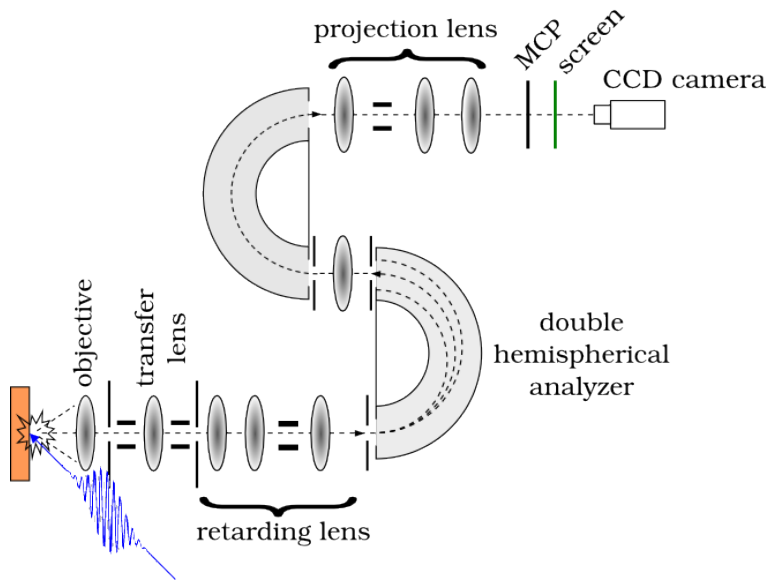


Abbildung 2.3: Prinzipskizze des Impulsmikroskops zur Messung von energiegefilterten Winkelverteilungen emittierter Photoelektronen [151].

sieren. Bildet man jedoch die Fourier-Ebene des Objektivs ab, erhält man eine direkte Messung der relativen Intensität der zum Bild beitragenden Elektronen nicht im Ortsraum $I(x, y)$, sondern im Impulsraum $I(k_x, k_y)$ der Wellenzahlvektoren parallel zur Oberfläche. Dies ist die wesentliche Idee hinter dem *Impulsmikroskop* [151, 153, 154], dessen Aufbau in Abbildung 2.3 schematisch gezeigt ist. Das Impulsmikroskop arbeitet dabei besonders gut in Kombination mit einem Laser als Anregungsquelle für die Photoelektronen zusammen, da das Anregungslicht sich sehr genau in den begrenzten Analysebereich (Durchmesser $\approx 100\mu\text{m}$) fokussieren lässt und somit eine effiziente Detektion fast aller überhaupt bei einer gewählten Energie (Energieauflösung $\approx 100\text{ meV}$) emittierten Photoelektronen möglich ist. Die Energieanalyse der Photoelektronen erfolgt dabei nach dem Durchlaufen der PEEM-Optik über zwei hintereinander geschaltete hemisphärische Analysatoren, wobei der erste zur eigentlichen Energiefilterung dient, während der zweite die dabei entstehenden Abbildungsfehler korrigiert. Im Rahmen dieser Arbeit wurde das Impulsmikroskop benutzt, um die Ergebnisse der bisherigen Studien durch zusätzliche Messungen in einem weiten (k_x, k_y) -Bereich zu komplementieren (siehe Abschnitt 3.3).

3 Ausgewählte Ergebnisse

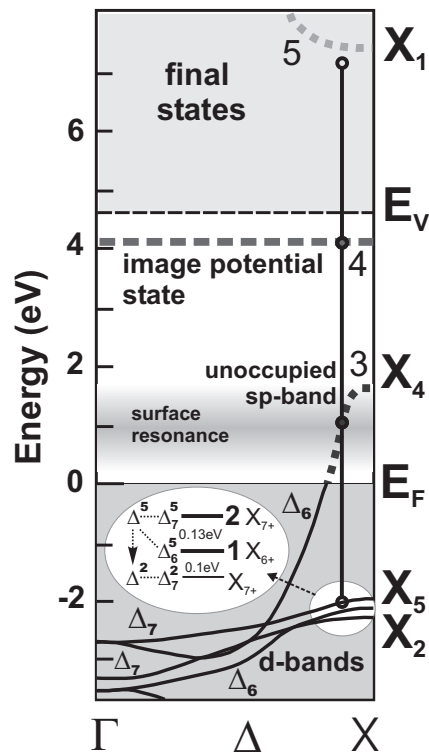
3.1 Elektronische Bandstrukturinformation über kohärente Mehrphotonen-Resonanzen

Originalveröffentlichungen: [AW 5.1], [AW 5.2], [AW 5.3], [AW 5.4]

Nichtlineare optische Anregungen an Festkörperoberflächen hängen sehr empfindlich von der vorliegenden elektronischen Struktur des untersuchten Systems ab. Entsprechende Experimente können daher wertvolle Einsichten über die relevanten elektronischen Zustände liefern. Insbesondere die Cu(001) Oberfläche bietet hier besondere Bedingungen, da im Bereich der Photonenenergie von 3 eV starke Kopplungen zwischen ganz bestimmten Zuständen stattfinden, wie unten gezeigt wird. Dies ist experimentell sehr vorteilhaft, da 3 eV als zweite Harmonische von Ti:Sa Lasern eine relativ leicht zugängliche Photonenenergie ist.

Viele der in dieser Arbeit vorgestellten Ergebnisse wurden an Cu(001)-Oberflächen erhalten. Kupfer ist eines der am besten mit herkömmlichen Photoemissionsmessungen und theoretischen Rechnungen untersuchten Materialien, was für die Analyse der hier erhaltenen neuen Resultate wichtig ist. Die elektronische Bandstruktur von Cu(001) ist in Abbildung 3.1 gezeigt. Dort sieht man die Möglichkeit einer Drei-Photonen-Resonanz, welche von den besetzten *d*-Bändern ausgeht, über unbesetzte *sp*-Zustände und den Bildpotentialzustand. Eine solche Kombination von

Abbildung 3.1: Relativistische Bandstruktur [155] von Cu(001) für Normalemission entlang $\Gamma - X$. Eine mögliche Drei-Photonen-Resonanz bei einer Photonenenergie nahe 3 eV ist durch senkrechte Linien nahe des X -Punktes gezeigt. Zusätzlich liegen der $n = 1$ Bildpotentialzustand bei 4.04 eV [91] und eine unbesetzte Oberflächenresonanz bei 1 eV [156] vor. Die Nomenklatur Δ_6^5 beschreibt Zustände mit Δ_6 Doppelgruppensymmetrie, deren räumlicher Anteil Δ_5 -Symmetrie besitzt.



Volumenzuständen, die in einem nichtlinearen Photoemissionsprozess mit Oberflächenzuständen gekoppelt sind, stellt wegen der verschiedenen Eigenschaften der involvierten Zustände ein interessantes Modellsystem dar, welches in mehreren der folgenden Untersuchungen analysiert wurde.

In Abbildung 3.2 werden Multiphotonen-Photoemissionsspektren für Cu(001)- und Cu(111)-Oberflächen verglichen. Es wurden Elektronen gemessen, welche durch zwei, drei oder vier Photonen angeregt wurden. Die Energieskala ist auf das Fermi-Niveau E_F bezogen. Die niederenergetische Seite der Spektren ist durch die Austrittsarbeit von 4.6 eV für Cu(001) und 4.9 eV für Cu(111) [91] bestimmt. Die höchsten Energien, welche durch Elektronen vom Fermi-niveau durch Absorption von zwei, drei oder vier Photonen (2PPE, 3PPE, 4PPE) erreicht werden können, sind als vertikale Linien eingezeichnet.

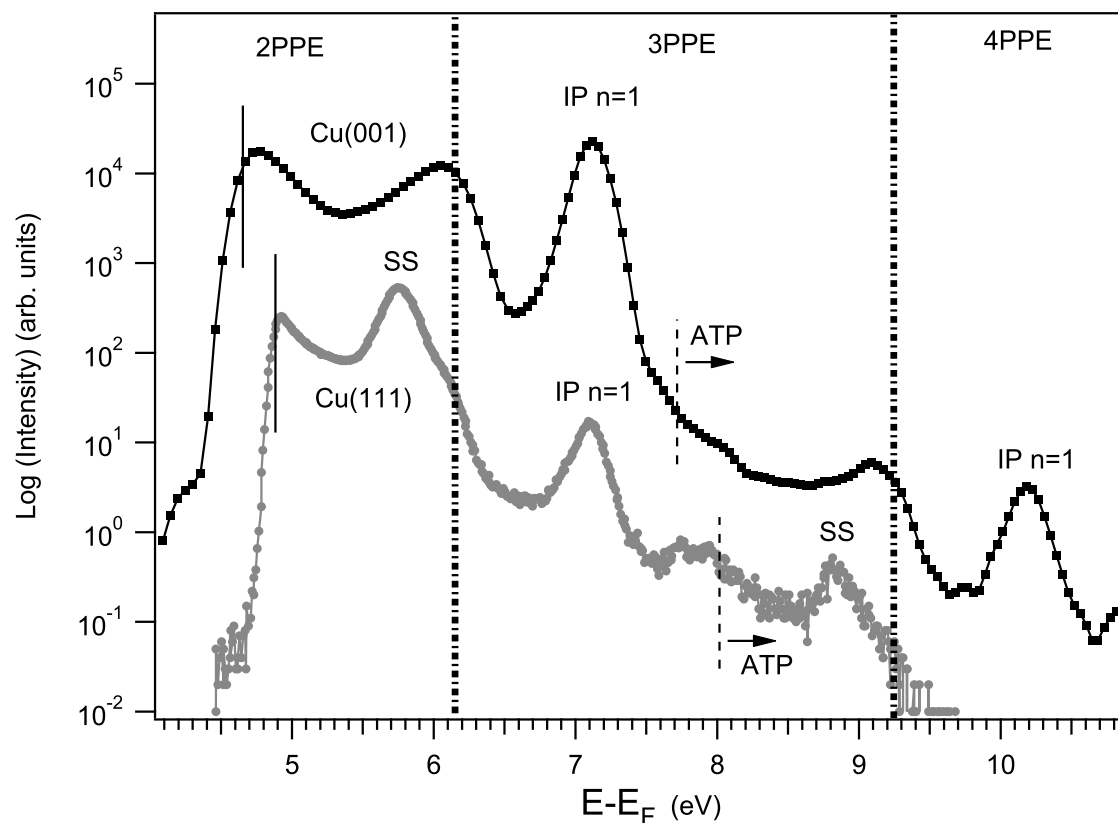


Abbildung 3.2: Nichtlineare Photoemissionsspektren von Cu(001) (schwarze Quadrate) und Cu(111) (graue Punkte). Emission senkrecht zur Oberfläche, Photonenergie $h\nu = 3.07$ eV, p -polarisiertes Licht. Markiert sind Regionen die von den besetzten Zuständen aus mit jeweils 2, 3 oder 4 Photonen erreicht werden können. Es können die Multi-Photonen-Replikate des $n = 1$ Bildpotentialzustandes (IP) und des Cu(111) Shockley-Zustandes (SS) unterschieden werden. Above-Threshold-Prozesse werden bei Energien beobachtet, die größer sind als die Austrittsarbeit (schwarze vertikale Linien) plus eine weitere Photonenenergie $h\nu$ (ATP). Die Energieauflösung war ≈ 100 meV. Die beiden Spektren sind nicht zueinander normalisiert.

In der 2PPE-Region von Cu(111), kann der bekannte Shockley Oberflächenzustand (SS) bei $E_F - 0.4$ eV gesehen werden, während das Cu(001)-Spektrum keine solchen auffallenden Merkmale zeigt. Im 3PPE-Teil beider Oberflächen sieht man den $n=1$ Bildpotentialzustand (IP) bei einer Endzustandsenergie von 7.1 eV. Die Bindungsenergie der $n=1$ Zustände relativ zum Vakuumniveau sind 0.59 eV für Cu(001) und 0.84 eV für Cu(111) [91]. Wegen des Unterschieds von 0.3 eV in der Austrittsarbeit zwischen beiden Oberflächen befinden sich damit die $n=1$ Bildpotentialzustände bei etwa der gleichen Energie relativ zum Fermi-niveau.

Bei Energien höher als die der Bildpotentialzustände sind die Positionen des Vakuumniveaus plus einer Photonenenergie als „ATP“ eingezeichnet. Diese Elektronen haben eine kinetische Energie, die größer ist als eine einzelne Photonenenergie und könnten die Probe prinzipiell also schon mit Absorption eines Photons weniger verlassen. Deswegen wird dieser Effekt als „above threshold photoemission“ (ATP) bezeichnet. Der 3PPE-Peak des Cu(111) Oberflächenzustandes bei 8.8 eV zeigt dies besonders klar: diese Elektronen können ja auch mit 2PPE bei 5.7 eV photoemittiert werden. Ein ähnlicher Prozess findet zwischen dem 4PPE Bildpotentialzustand und seiner 3PPE-Kopie bei Cu(001) statt.

Der wichtigste Effekt jedoch kann in der Intensität des 3PPE Peaks von Cu(001) relativ zu Cu(111) gesehen werden: Das 3PPE-Signal von Cu(001) am Bildpotentialzustand hat eine höhere Intensität als der 2PPE-Teil des Spektrums und ist auch um Größenordnungen höher als das 3PPE-Signal von Cu(111). Im folgenden wird analysiert, wie die Cu(001) Bandstruktur einen solch effektiven 3PPE-Prozess unterstützen kann.

Um das starke 3PPE-Signal von Cu(001) zu erklären, ist in Abbildung 3.1 die relativistische Bandstruktur für Photoemission senkrecht zur Cu(001)-Oberflächenebene (Δ -Linie von Γ to X) gezeigt (Eckardt *et al.* [155]). In Abbildung 3.1 ist ein Drei-Photonen-Prozess für Photonenenergien nahe 3 eV gezeigt, der von den Cu d -Bändern über die unbesetzten sp -Bänder und den $n = 1$ Bildpotentialzustand abläuft [157]. Bei einer ausreichenden Photonenintensität ist dieser resonante 3PPE-Prozess effektiver als der nichtresonante 2PPE-Prozess. Als besondere Beobachtung kommt hinzu, dass der 3PPE-Peak in zwei Teilpeaks aufgespalten ist, deren relative Höhe von der Photonenenergie abhängt [158]

Eine theoretische Bandstruktur wie in Abbildung 3.1 kann normalerweise zwar die Lage experimenteller Photoemissionspeaks nicht quantitativ beschreiben [159, 160], jedoch kann man annehmen, dass die Band-Dispersion näherungsweise korrekt wiedergegeben wird, bei an das Experiment anzupassender Lage der kritischen Punkte an den Brillouinzonengrenzen. Dann sucht man nach k -erhaltenden (senkrechten) Resonanzen als Funktion der Photonenenergie. Graphisch kann dies durch Verschieben der jeweiligen Bänder erfolgen, wobei um das jeweilige Vielfache der Photonenenergie verschoben wird, mit dem der Endzustand erreicht wird. Eine exakte Mehrphotonen-Resonanz liegt dann vor, wenn sich die Bänder in einem einzigen Punkt kreuzen [161]. Wegen der Dispersion der Bänder erzeugt dies erhebliche Restriktionen für den relativen

Abstand der involvierten Zustände, auf den damit durch Resonanz-Experimente zurückgeschlossen werden kann.

Das Ergebnis einer solchen Analyse ist in Abbildung 3.3 gezeigt. Es wurde angenommen, daß die beobachtete spektrale Struktur vorwiegend vom Bildpotentialzustand bei 4.04 eV [91] in Kombination mit d -Band-Ausgangszuständen mit reduzierter k_{\perp} -Dispersion in der Nähe des X -Punktes hervorgerufen wird. Deswegen wird in Abbildung 3.3 nach einer Zwei-Photonen-Resonanz zwischen $n = 1$ Bildpotentialzustand und den d -Bändern gesucht. Zusätzlich können die unbesetzten sp -Bänder Zwischenzustände bereitstellen, die gleichzeitig mit d -Bändern und dem Bildpotentialzustand in Ein-Photonen-Resonanz sind.

Eine gute Übereinstimmung mit unseren Experimenten ergibt sich mit bekannten Literaturwerten für die Lage der d -Bänder mit X_5 bei -1.99eV und mit X_2 bei -2.18eV [159], welche mittels konventioneller ARPES-Messungen erhalten wurden. Aufgrund der Spin-Bahn-Kopplung, spaltet das d -Band mit räumlicher Δ^5 Symmetrie in zwei Bänder mit relativistischer Δ_7^5 und Δ_6^5 Symmetrie auf, mit beobachteten experimentellen Aufspaltungen zwischen 100meV [162] und 170meV [163] nahe des X -Punktes. Zum Vergleich beträgt der theoretische Wert 160meV [159] direkt am X -Punkt. Das obere sp -Band lag mit X_1 bei 7.67eV [159] und kann deswegen mit den hier benutzten Photonenenergien nicht resonant erreicht werden. In Abbildung 3.3 findet man zwei Dreiphotonenresonanzen für leicht unterschiedliche Photonenenergien $h\nu = 2.97eV$ (links) und $h\nu = 3.08eV$ (rechts). Da diese Photonen gleichzeitig in den ultrakurzen Pulsen mit breitem Frequenzspektrum vorhanden sind, werden beide Resonanzen auch zusammen im Spektrum beobachtet, wenn es mit ausreichender Energieauflösung gemessen wird, wie man im grau unterlegten experimentellen Spektrum in Abb. 3.3 sieht.

Die Resultate in Abb. 3.3 beweisen den Resonanzmechanismus in 3PPE von Cu(001). Die beiden Teile von Abb. 3.3 zeigen, dass sich bei Photonenenergien von 2.97 eV und 3.08 eV drei Bänder nahezu schneiden. Da diese Photonenenergien 110 meV Abstand besitzen, können sie vom Spektrum der Laserpulse mit etwa 170 meV Bandbreite gleichzeitig angeregt werden. Der Überlapp von drei Bändern in Abb. 3.3 bedeutet, dass nicht nur eine Zwei-Photonen-Resonanz zwischen den d -Bändern und dem Bildpotentialzustand vorliegt, sondern dass zusätzlich ein Bereich der unbesetzten sp -Bänder in gleichzeitiger Ein-Photonen-Resonanz sowohl zu d -Band-Zuständen als auch zum Bildpotentialzustand IP ist. Bei Vorliegen einer solchen Situation sind die in Abb. 3.3 identifizierten k -spezifischen Drei-Photonen-Prozesse sehr bevorzugt, da in ihnen die Energieerhaltung für die Anregungsschritte $d \rightarrow sp \rightarrow IP$ sowohl für die Ein-Photonen-Übergänge mit $h\nu$ als auch für die Zwei-Photonen-Übergänge mit $2h\nu$ näherungsweise erfüllt ist. Die beiden separaten Resonanzen sind durch A und B in den experimentellen 3PPE-Spektren in Abb. 3.3 markiert. In Betrachtung des relativ einfachen Modells, das auf der Band-Dispersion und der möglichst guten Energieerhaltung in Einzelschritten basierte, ergibt sich eine akzeptable Übereinstimmung mit den gemessenen Werten für die Separation von A und B und den bei der Formierung von A und B wirksamen Photonenenergien. Die Doppelpeakstruktur in 3PPE bei A und B in Abb.

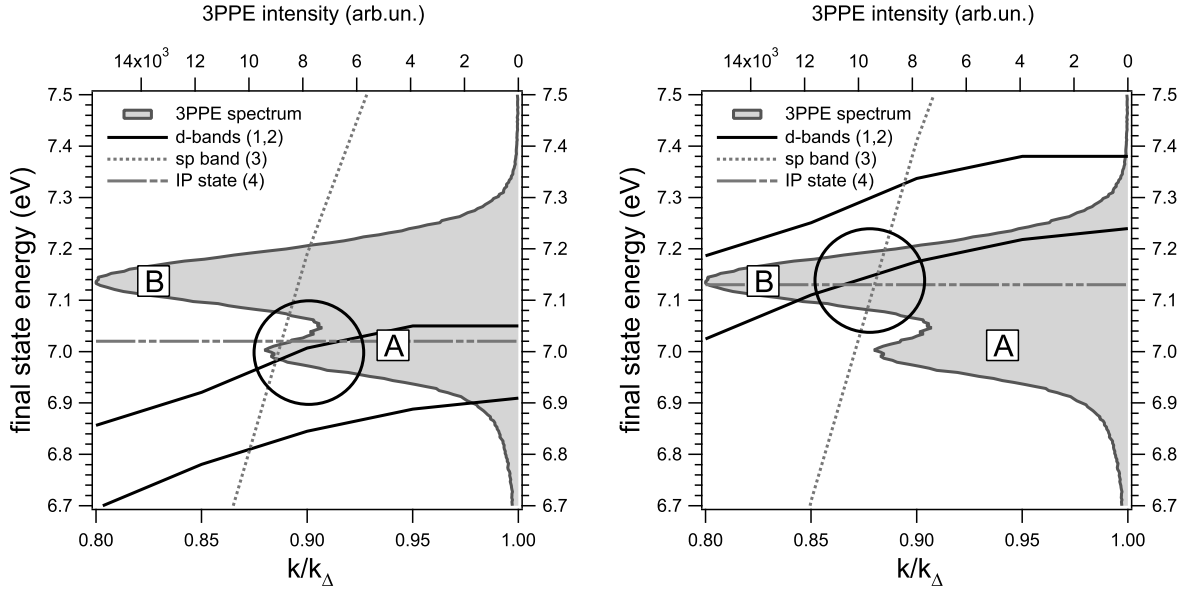


Abbildung 3.3: Analyse der möglichen Resonanzbedingungen zwischen den d -Band-Ausgangszuständen (schwarz), den sp -Band-Zwischenzuständen (gepunktet) und dem Bildpotentialzustand (strich-punkt-punkt). Die Bänder sind wie in Abb. 3.1 nummeriert. Die d -Band-Ausgangszustände werden um 3 Photonenergien $h\nu$ nach oben verschoben, die sp -Band-Zwischenzustände um $2 h\nu$, und der $n = 1$ Bildpotentialzustand um $h\nu$ zur Endzustandsenergie. Eine Überschneidung aller Bänder würde gleichzeitige Zwei-Photonen- und zwei Ein-Photonen-Resonanzen bedeuten. Aufgrund des breiten Pulsspektrums ($\approx 170\text{meV}$), können zwei separate Resonanzen beobachtet werden, welche von den beiden spin-Bahn-aufgespaltenen d -Bändern ausgehen und für $h\nu = 2.97\text{eV}$ (links) und $h\nu = 3.08\text{eV}$ (rechts) als Peaks A und B im experimentellen Spektrum (grau gefüllt, für 3.04eV mittlerer Photonenergie) gleichzeitig beobachtet werden. Energieauflösung $\approx 50\text{meV}$.

3.3 durch die Summe zweier Gauss-Peaks mit Breiten (FWHM) von 110meV für (A) und 130meV für (B) angepasst werden, mit der Separation von 150meV (gegenüber den im Modell abgeschätzten 110meV). Peak A ist bei einer Endzustandsenergie von 6.95eV und Peak B bei 7.15eV .

In Betracht der Breite des Anregungsspektrums von 170meV ist es bemerkenswert, dass die Breite der Peaks im 3PPE-Spektrum deutlich unter der Anregungsbreite ist [158]. Bei näherer Betrachtung wird eine weitere sehr interessante Eigenschaft der diskutierten Multiphotonenresonanzen deutlich, nämlich, dass diese über den *selben* Bildpotentialzustand verlaufen müssen, aber in den Endzuständen eine Doppelpeakstruktur aufgrund der verschiedenen Ausgangszustände zeigen. Für ein Elektron, das vor dem Übergang im Bildpotentialzustand ist und von dort aus durch ein Spektrum von 170meV Breite photoemittiert wird, sollte sich ein einziger Endzustandspeak mit einer minimalen Breite des Anregungsspektrums (170meV) ergeben, aber nicht zwei Peaks, welche auch noch schmalere als dieses Spektrum sind. Das weist auf den Einfluss von solchen Mehrphotonenprozessen hin, welche nicht als schrittweise Übergänge von Elektronen von einem Niveau zum nächsten erklärt werden können, in welchen die Information über die vorherigen Anregung-

schritte verloren gehen würde. Diese *kohärenten* Anregungen können zur Analyse der elektronischen Bandstruktur genutzt werden.

Der Mechanismus, welcher der Bildung der Doppelppeakstruktur und der beobachteten Peakbreiten in Abb. 3.3 unterliegt, kann mittels des Dichtematrixformalismus (Abschnitt 1.3) näher analysiert werden, in dem die Populationen und die Superpositionen (Kohärenzen) zwischen elektronischen Zuständen gemeinsam berücksichtigt werden können, jeweils in den Diagonal- (ρ_{aa}) und Nichtdiagonalelementen (ρ_{ab}) der Dichtematrix ρ [91, 103–107].

Dazu muss man annehmen, dass der relevante Bereich der Cu Bandstruktur durch ein Vierniveausystem angenähert werden kann. Dies ist näherungsweise dadurch erfüllt, dass die Übergänge nur in einem sehr eng begrenzten \mathbf{k} -Bereich stattfinden können. Der ungestörte Hamiltonian \hat{H}_S des Systems wird in der Basis von vier orthonormalisierten Zuständen ($\langle a|b\rangle = \delta_{ab}$) geschrieben, welche jeweils die besetzten Ausgangszustände der d -band Bänder $|i_{1,2}\rangle$, die unbesetzten sp -Zustände $|s\rangle$, den Bildpotentialzustand $|m\rangle$ und den Photoemissionsendzustand $|f\rangle$ an den dazugehörigen Energieniveaus $\epsilon_{i,s,m,f}$ repräsentieren. Diese Vereinfachung vernachlässigt (a) die Dispersion der elektronischen Zustände mit \mathbf{k} welche ein bedeutender inhomogener Beitrag zu nichtresonanten 2PPE-Spektren sein kann [105] und (b) die verschiedenen Inter- und Intra-band-Relaxationsmechanismen welche Teil eines quantitativen Modells in einem kristallinen Festkörper sein müssten. Dieses Problem könnte zum Beispiel durch die Einführung eines Satzes von \mathbf{k} -abhängigen Mehrniveausystemen gelöst werden, in denen die oben erwähnten Prozesse über entsprechenden Kopplungsterme berücksichtigt werden [105, 110]. Weiterhin wird angenommen, dass die Störung durch den Laserpuls insgesamt als schwach beschrieben werden kann und dass die 3PPE-Prozesse unabhängig von zwei verschiedenen d -Bandzuständen $|i_{1,2}\rangle$ ausgehen. Der Dichtoperator $\hat{\rho}$ eines solchen vereinfachten Vierniveausystems ist:

$$\hat{\rho} = \begin{pmatrix} \rho_{ii} & |i\rangle\langle i| & \rho_{is} & |i\rangle\langle s| & \rho_{im} & |i\rangle\langle m| & \rho_{if} & |i\rangle\langle f| \\ \rho_{si} & |s\rangle\langle i| & \rho_{ss} & |s\rangle\langle s| & \rho_{sm} & |s\rangle\langle m| & \rho_{sf} & |s\rangle\langle f| \\ \rho_{mi} & |m\rangle\langle i| & \rho_{ms} & |m\rangle\langle s| & \rho_{mm} & |m\rangle\langle m| & \rho_{mf} & |m\rangle\langle f| \\ \rho_{fi} & |f\rangle\langle i| & \rho_{fs} & |f\rangle\langle s| & \rho_{fm} & |f\rangle\langle m| & \rho_{ff} & |f\rangle\langle f| \end{pmatrix} \quad (3.1)$$

$$\rho_{ii}(t = -\infty) = 1$$

Das Matrixelement ρ_{ii} ist dabei dunkelgrau unterlegt, um seine Rolle als besetzter (d -band) Ausgangszustand zu betonen, es ist das einzige Matrixelement welches im Grundzustand zur Zeit $t = -\infty$ ungleich Null ist.

Das andere, hellgrau unterlegte Matrixelement ρ_{ff} bestimmt das Signal, welches im Experiment

gemessen wird: die (sehr kleine) Population die in den Endzustand angeregt wird während der Wechselwirkung mit dem Laserpuls. Vor dem Laserpuls ist $\rho_{ff} = 0$, und es erreicht einen nichtverschwindenden Wert durch die optische Kopplung über das elektrische Feld des Pulses $\mathbf{E}(t)$ zum Ausgangszustand über die Zwischenzustände. Wir nehmen hierbei an, dass die stärksten Kopplungen zwischen denjenigen Zuständen bestehen, welche etwa eine Photonenergie $\hbar\omega_p$ voneinander im Energieniveauschema entfernt sind:

$$|i\rangle \xleftrightarrow{\hbar\omega_p} |s\rangle \xleftrightarrow{\hbar\omega_p} |m\rangle \xleftrightarrow{\hbar\omega_p} |f\rangle \quad (3.2)$$

Beginnend bei $t = -\infty$ für nur $\rho_{ii} \neq 0$, bewirkt der Wechselwirkungsoperator \hat{V}_I (siehe Gleichung (1.6)) die Entwicklung von endlichen Werten in den anderen Matrixelementen während der zeitlichen Entwicklung des Dichteoperators $\hat{\rho}$. Diese Zeitentwicklung wird durch die entsprechende Liouville - von Neumann Gleichung (1.18) beschrieben. Neben der sequentiellen Besetzung von Populationen von einem Zustand zum nächsten (vgl. Relation (3.2)):

$$\rho_{ii} \rightarrow \rho_{ss} \rightarrow \rho_{mm} \rightarrow \rho_{ff} \quad (3.3)$$

existieren auch andere Beiträge, die nach ρ_{ff} nur über die Nichtdiagonalelemente verlaufen:

$$\rho_{ii} \rightarrow \rho_{is} \rightarrow \rho_{im} \rightarrow \rho_{if} \rightarrow \rho_{ff}, \quad (3.4)$$

Die letzteren Beiträge produzieren keine Population im Zwischenzustand $|m\rangle$ (einer Observable $N_m = \text{Tr}[|m\rangle\langle m| \hat{\rho}]$ entsprechend), da ja die ρ_{mm} (sowie ρ_{ss}) gar nicht von diesen Prozessen beeinflusst werden. Dabei muss betont werden, dass die Zwischenzustände selbst natürlich eine Rolle in diesem Anteil der Übergänge spielen, aber nur durch ihre quantenmechanische Überlagerung mit anderen Zuständen (Dipolmoment) und nicht dadurch, dass man eine Population in ihnen mit der Observable N_m messen könnte. Diese Interpretation zeigt, dass in den experimentellen Daten der Anteil der *kohärenten* Kopplung der d -Bandzustände an den Bildpotentialzustand die zwei *Ausgangszustandspeaks* im Photoelektronenspektrum $\rho_{ff}(E)$ bewirkt.

Auch die reduzierte Peakbreite kann über das Dichtematrixmodell erklärt werden. Die Forderung der Energieerhaltung muss streng nur für den Gesamtprozess in 3PPE erfüllt werden, bei dem der Ausgangszustand um $\hbar\omega_{03}$ vom Endzustand entfernt ist. Alle Drei-Photonen-Prozesse mit $\hbar\omega_{03} = \hbar\omega_{01} + \hbar\omega_{12} + \hbar\omega_{23}$ sind im Prinzip erlaubt (mit i.a. unterschiedlichen Einzelphotonenenergien $\hbar\omega_{01,12,23}$). Wenn jedoch die Anregungsenergie zusätzlich in Einphotonenresonanz $\hbar\omega_R \approx \hbar\omega_{01} \approx \hbar\omega_{12} \approx \hbar\omega_{23}$ zwischen Niveaus in der Bandstruktur ist (vgl. Abb. 3.3), dann besteht auch Energieerhaltung für die Zwischenschritte. Die entsprechenden Übergänge sind damit auch wahrscheinlicher, da die Energie-Zeit-Unschärferelation den Zeitraum nicht beschränkt, in der ein Zwischenzustand bei einer bestimmten Energie existieren kann. Insgesamt werden damit diejenigen Photonenergien $\hbar\omega_R$ aus einem breiten Spektrum herausgefiltert, welche gleichzeitig Ein-, Zwei-, und Drei-Photonenresonanzen $\hbar\omega_{03} = \hbar(\approx \omega_R) + \hbar(\approx \omega_R) + \hbar(\approx \omega_R)$ im nichtlinearen

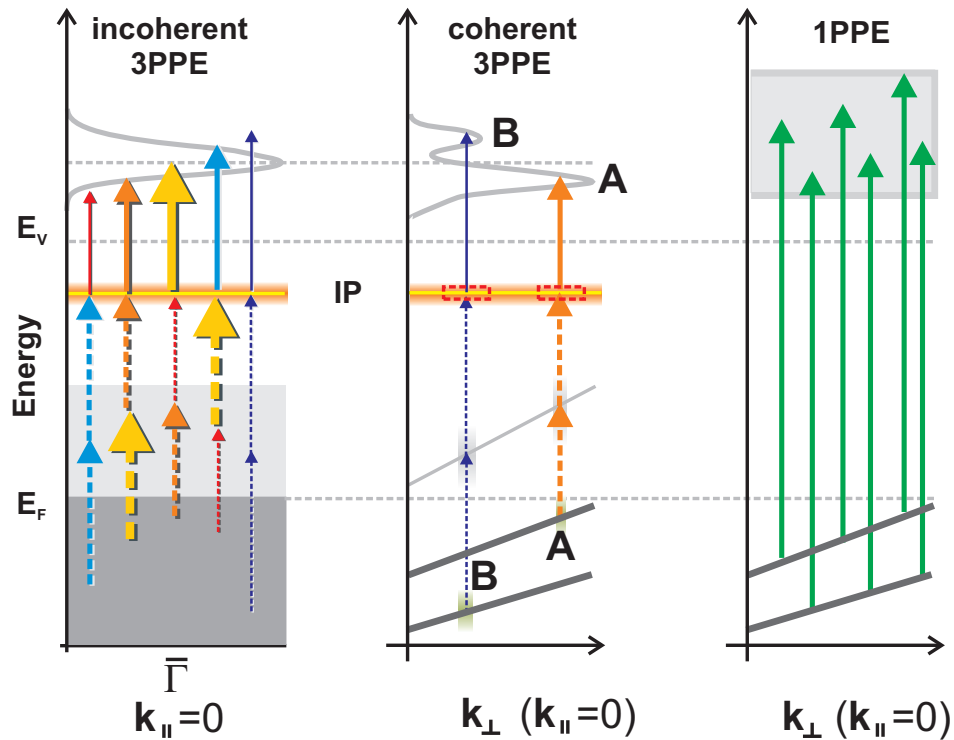


Abbildung 3.4: Prinzip zur Detektion von kohärenten Bandstrukturresonanzen in 3PPE über Bildpotentialzuständen an Cu(001)-Oberflächen [AW 5.4].

Links: nichtresonante k_{\perp} -unspezifische Anregung des Bildpotentialzustandes in senkrechter Emission ($k_{\parallel} = 0$). Die Farben des Pfeile repräsentieren verschiedene Photonenfrequenzen im Anregungspuls, und deren Dicke dem jeweiligen spektralen Anteil. Die Photonen wechselwirken in beliebiger Reihenfolge in schrittweisen Anregungsschritten. Der Bildpotentialpeak ist durch die Zentralwellenlänge des Pulses bestimmt und seine Breite durch die Breite des Anregungsspektrums.

Mitte: Kohärente 3PPE-Resonanzen zum Bildpotentialzustand produzieren die k_{\perp} -spezifische Peaks A und B. Eine feste Photonenfrequenz bestimmt den einen jeweiligen resonanten Anregungspfad. Die Breite von A und B ist nicht durch die Pulsbreite bestimmt.

Rechts: Der analoge 1PPE-Prozess im gleichen Niveauschema mit Photonenenergie $3h\nu$ ist nicht k_{\perp} -selektiv wenn keine Resonanz zu einem Endzustand vorliegt. Der 1PPE-Prozess ist durch die Symmetriebrechung an der Oberfläche beeinflusst.

Anregungsprozess bewirken.

Aus der Beobachtung zweier getrennter Peaks lassen sich weitere Schlüsse über die Dynamik der Kohärenz (Dephasierungsraten) zwischen involvierten Zuständen ziehen. Dazu kann man nach dem Model von Wolf *et al.* [109] die analytische Lösung für eine Dreiniveausystem anwenden. Es stellte sich dabei heraus [AW 5.4], dass für sehr schnelle Dephasierung zwischen Bildpotentialzustand und den d -Band-Ausgangszuständen nur ein einzelner Peak zu beobachten ist (wie dies nach der Diskussion oben für sequentielle Anregungen zu erwarten wäre). Um eine Doppelpeakstruktur zu beobachten, muss die Dephasierungszeit der Ausgangszustände im Bereich von etwa 10 bis 20 fs liegen, bei Annahme einer dazu im Vergleich sehr großen Dephasierungszeit im Bildpotenti-

alzustand. Dies ist in guter Übereinstimmung mit direkt zeitabhängigen Experimenten, in denen Cu d -Band Dephasierungszeiten von > 20 fs in der d -Band-Region nahe des X -Punktes beobachtet wurden [164].

Die in diesem Abschnitt vorgestellten Studien von 3PPE an Cu(001)-Oberflächen sind relevant für die Anwendung der nichtlinearen Photoemission in der Analyse der elektronischen Struktur mittels hochintensiver Labor-Laserquellen und beschleunigerbasierter Freie-Elektronen-Laser. Es wurde z.B. theoretisch vorhergesagt [161], dass resonante Zwei-Photonen-Photoemission den Abstand zwischen elektronischen Zuständen in zwei Volumenbändern mit einer Genauigkeit liefern könnte, die nur durch die intrinsische Energie- und Impulsverbreiterung der gekoppelten Zustände begrenzt wäre. Ein bedeutender Vorteil solcher Zwei-Photonen-Messungen ist, dass der optische Anregungsschritt zwischen dem Ausgangszustand und dem Zwischenzustand nicht durch die Symmetriebrechung an der Oberfläche beeinflusst ist [165] und damit der senkrechte k_{\perp} -Vektor exakt erhalten wäre. Dies würde genauere Analysen optisch angeregter Volumenbänder ermöglichen [166]. Die Erweiterung dieser Idee auf 3PPE ist in Abb. 3.4 gezeigt, wo der qualitative Unterschied zwischen unspezifischen inkohärenten Volumen Anregungen im Vergleich zu \mathbf{k} -abhängigen Resonanzen gezeigt ist. Dabei ist eine Generalisierung auf die Nutzung verschiedener, variabler Photonenenergien impliziert, mit denen man systematisch nach Einzelphotonenresonanzen im Mehrphotonenprozess suchen kann. Die Nutzung von Mehrphotonenresonanzen bei spezifischen \mathbf{k} -Positionen ist ebenfalls für zeitaufgelöste Messungen relevant [92], zum Beispiel zur Analyse von *band*-aufgelöster Elektronendynamik, da man gezielt auf verschiedene d -Bänder zugreifen kann. Die hier demonstrierte kohärente Kopplung von Volumenlektronen an Oberflächenzustände verbessert auch die Steuermöglichkeiten von Elektronenströmen an Oberflächen mittels interferometrischer Methoden, da dabei die Erhaltung der Kohärenz von elektronischen Zuständen und deren Interferenzmöglichkeit von zentraler Bedeutung ist [167, 168].

3.2 Optische Steuerung der spin-polarisierten Photoemission von Cu(001)

Originalveröffentlichungen: [AW 5.6], [AW5.7], [AW 5.5], [AW5.8]

Die im vorhergehenden Abschnitt 3.1 diskutierten spezifischen Mehrphotonenresonanzen können zur Steuerung der Spinpolarisation von angeregten Elektronen genutzt werden, weil die Ausgangszustände in den involvierten d -Bändern durch die Spin-Bahn-Wechselwirkung beeinflusst sind und damit spin-abhängig auf eine Anregung mit zirkular polarisiertem Licht reagieren.

Wie oben gezeigt, sind die d -Bänder in der Nähe des X-Punktes in Δ_6 und Δ_7 Symmetrien aufgespalten, mit einer Energiedifferenz in der Größe von etwa 150meV. Die spin-abhängigen Photoemissionsintensitäten können dann anhand von optischen Auswahlregeln für elektronische Zustände unter Spin-Bahn-Kopplung analysiert werden [169]. Wenn sowohl die Photoemission als auch der Strahlungseinfall senkrecht zur Oberfläche stattfinden, müssen die Endzustände die Symmetrie Δ_6^1 haben¹. In diese Zustände werden durch rechts-zirkular polarisiertes Licht unterschiedlich spin-polarisierte Elektronen aus den beiden Ausgangszustandssymmetrien angeregt (entsprechend umgekehrt für links-zirkular polarisiertes Licht) [169]:

$$|\uparrow\rangle : \Delta_7^5 \rightarrow \Delta_6^1 \quad (3.5)$$

$$|\downarrow\rangle : \Delta_6^5 \rightarrow \Delta_6^1 \quad (3.6)$$

Diese Auswahlregeln bleiben für die hier untersuchten Fälle auch für nicht-senkrechten Lichteinfall und nicht-senkrechte Emission näherungsweise bestehen [170].

Im Rahmen der vorliegenden Arbeit wurde untersucht, wie die mittels zirkular polarisierten Lichts angeregte Spin-Polarisation in Drei-Photonen-Photoemission experimentell gesteuert werden kann. Die durchgeführten Experimente lassen sich dabei in drei Gruppen unterteilen, die in Abbildung 3.5 anhand von schematisch vereinfachten Bandstrukturen gezeigt sind:

1. Prinzip A: Änderung der Anregungs-Photonenenergie zur Steuerung der Kopplung an unterschiedliche d -Band-Zustände,
2. Prinzip B: Verschiebung des Energieniveaus des Bildpotentialzustandes durch Änderung der Austrittsarbeit über Cs-Adsorption.
3. Prinzip C: Detektion für nicht-senkrechte Emission ($k_{\parallel} > 0$) unter Ausnutzung der Dispersion der beteiligten Zustände.

¹Die Nomenklatur Δ_6^1 beschreibt Zustände mit Δ_6 Doppelgruppensymmetrie, deren räumlicher Anteil Δ_1 -Symmetrie besitzt [169].

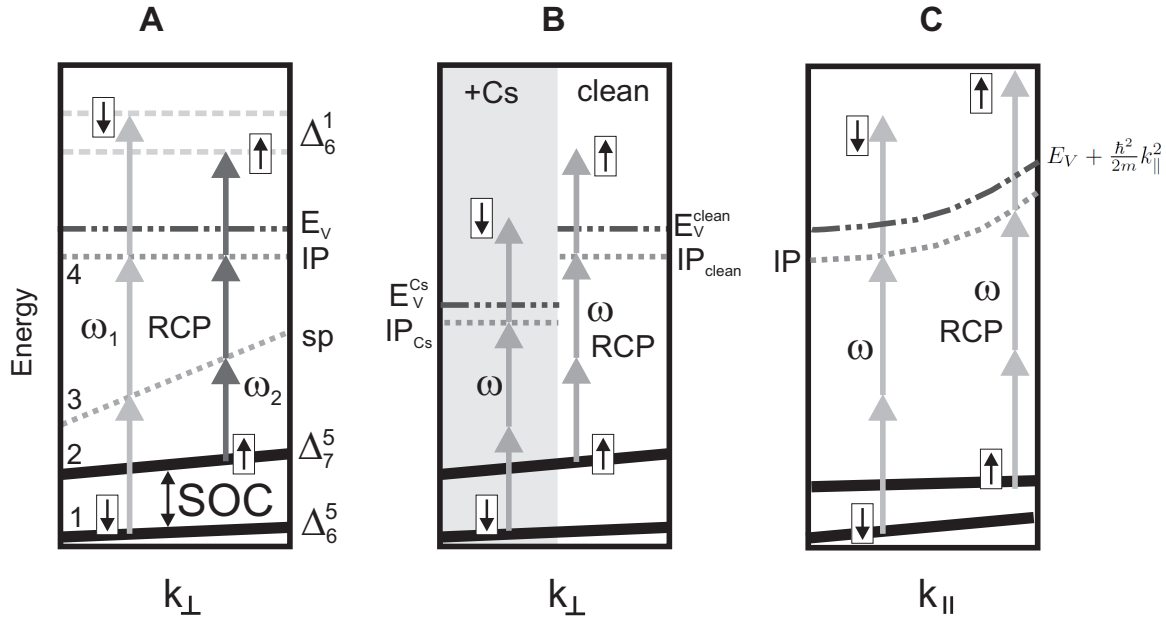


Abbildung 3.5: Prinzipien der optischen Anregung spin-polarisierter Elektronen in der Bandstruktur von Cu(001) [AW 5.8]

(A): Änderung der Anregungs-Photonenenergie zur Steuerung der Kopplung an unterschiedliche d -Band-Zustände,

(B): Verschiebung des Energieniveaus des Bildpotentialzustandes durch Änderung der Austrittsarbeit über Cs-Adsorption.

(C): Detektion für nicht-senkrechte Emission ($k_{\parallel} > 0$) unter Ausnutzung der Dispersion der beteiligten Zustände.

In allen drei Teilabbildungen symbolisieren die Pfeile an den Ausgangszustandsbändern den spin-selektiven Anregungsprozess mit zirkular polarisiertem Licht und *nicht* eine etwaige vorhandene Spinpolarisation dieser Bänder.

Die erste Gruppe von Experimenten (Prinzip A) nutzt die Photonenenergieabhängigkeit der Mehrphotonenresonanzen auf einer reinen Cu(001)-Oberfläche. Dies ist in Abb. 3.5A gezeigt, wo man sieht, dass für zirkular polarisiertes Licht eine Umkehrung der Spinpolarisation stattfinden kann, weil die Mehrphotonenresonanz für kleinere Photonenenergien von den besetzten d -Band-Zuständen mit Δ_7^5 und dann für größere Photonenenergien zu den Δ_6^5 bei größeren Bindungsenergien wechselt und damit nach den Auswahlregeln (3.5) und (3.6) entgegengesetzte Spinkomponenten ausgewählt werden. Die experimentellen Untersuchungen in [AW 5.6] bestätigen diese theoretischen Erwartungen. Als Beispiel ist dazu im linken Teil von Abb. 3.6 gezeigt, dass sich bei Umkehrung der Photonenhelizität das spin-polarisierte 3PPE-Signal ebenfalls umkehrt, wie dies nach den optischen Auswahlregeln zu erwarten ist. Im Spektrum links in Abb. 3.6 erkennt man zusätzlich, dass das 2PPE-Signal gegenüber dem 3PPE-Peak keine messbare Spinpolarisation zeigt. Für das 2PPE-Signal sind nämlich die sp -Bänder nahe des Fermi-Niveaus als Ausgangszustände wirksam, und diese zeigen keine relevanten Spin-Bahn-Kopplungseffekte. Im rechten Teil von Abb. 3.6 ist gezeigt, wie bei Änderung der Photonenenergie um nur 140 meV von 3.14 eV zu 3.00 eV

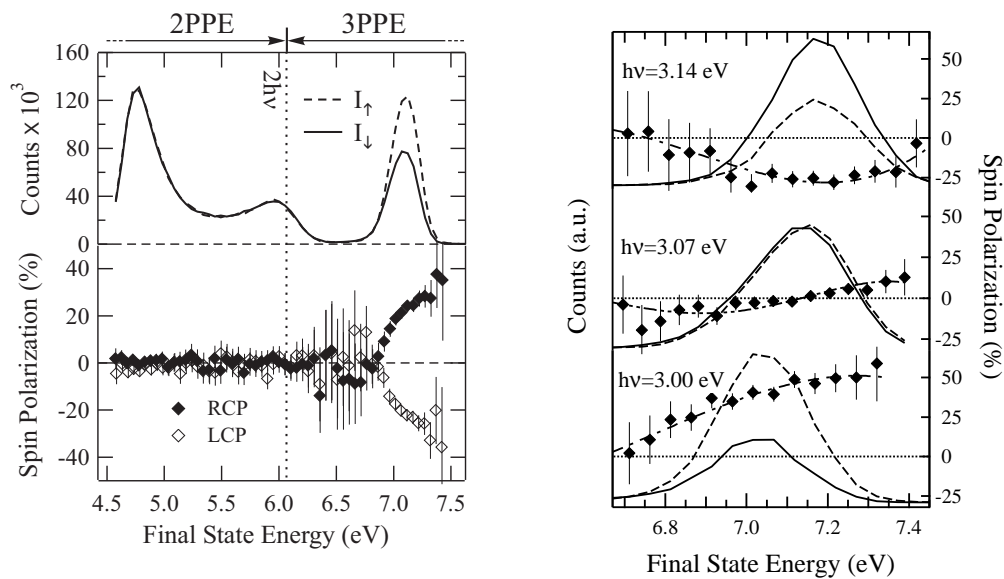


Abbildung 3.6: Optische Anregung spin-polarisierter Elektronen in 3PPE von Cu(001) [AW 5.6]

Links: Partialspektren in 2PPE und 3PPE, $h\nu=3.02$ eV, rechts-zirkular polarisiertes Licht (oben) und Spinpolarisation in Abhängigkeit von der Photonenhelizität (unten). Umkehrung der Helizität führt zur Umkehrung der erzeugten Spinpolarisation. Wegen der vernachlässigbaren Spin-Bahn-Wechselwirkung in den sp -Ausgangszuständen entsteht in 2PPE keine messbare Spinpolarisation.

Rechts: Spinpolarisation des 3PPE-Signals in Abhängigkeit von der Photonenenergie für rechts-zirkular polarisiertes Licht. Durch Kopplung and verschiedene d -Bänder wechselt die Spinpolarisation das Vorzeichen.

die diskutierte energieabhängige Umkehrung der Spinpolarisation tatsächlich stattfindet.

Das Anregungsspektrum für den 3PPE-Prozess kann sehr spezifisch über die Interferenz zweier zueinander verzögerter optischer Pulse gesteuert werden. Ultrakurze Pulse enthalten ein verbreitertes Spektrum an Photonenenergien und die Interferenz beeinflusst gleichzeitig den zeitlichen Verlauf und das resultierende Frequenzspektrum des resultierenden optischen Feldes. Dies führt zum Beispiel dazu, dass bei einer relativen Phasenänderung um π zwischen zwei optischen Pulsen jeweils der höher- oder der niederenergetische Teil des Frequenzspektrums destruktiv interferiert. Damit ist eine Steuerung der spinpolarisierten 3PPE über die Kontrolle der Pulsverzögerung möglich. Dies ist in Abb. 3.7 gezeigt. Im linken oberen Teil sieht man, wie die beobachtete Spinpolarisation als Funktion der Pulsverzögerung variiert. Im Extremfall kehrt sich die Spinpolarisation nahe einer Verzögerung von etwa 15 fs innerhalb eines optischen Zyklus von -20% auf +40% um. Für eine Phasenänderung von 10.75 zu 11.25 optischen Zyklen ist im unteren Teil von Abb. 3.7 gezeigt, wie sich das nichtspinaufgelöste Photoemissionssignal gegenüber einer Verzögerung von Null zwischen den Pulsen ändert. Dies führt zu einer Änderung der Spinpolarisation nach dem photonenergieabhängigen Mechanismus von Abb. 3.5A.

Über Prinzip B in Abb. 3.5 kann man die Abhängigkeit der elektronischen Struktur an der Cu(001)-

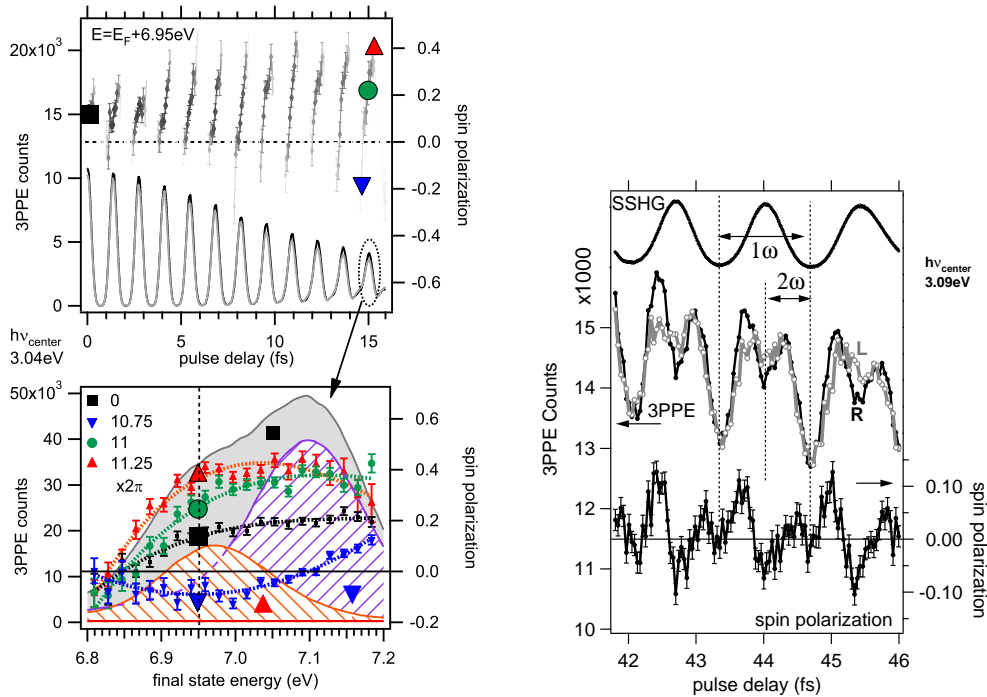


Abbildung 3.7: Interferometrische Steuerung der Anregung spin-polarisierter Elektronen in 3PPE von Cu(001) [AW 5.7]

Links: Interferenz zweier gegeneinander verzögerter optischer Pulse steuert das Frequenzspektrum der 3PPE-Anregung und führt zur Betonung jeweils entgegengesetzt spin-polarisierter Resonanzen für eine relative Phasenänderung von π (unten: 10.75 gegenüber 11.25 optischen Zyklen). **Rechts:** Signatur der Elektronendynamik im zeitaufgelösten 3PPE-Signal. Gegenüber dem optischen Signal (surface SHG, oben) zeigt die interferometrische Korrelationskurve für die 3PPE-Anregung (Mitte) einen klar verstärkten Anteil der verdoppelten Fundamentalfrequenz, was sich auf die Verzögerungsabhängigkeit beobachteten Spinpolarisation (unten) auswirkt.

Oberfläche von z.B. einer Adsorbatbedeckung ausnutzen. Durch Adsorption von Cs wird die Austrittsarbeit verringert, womit sich das Referenzniveau für die Bildpotentialzustände zu geringeren Energien relativ zum Fermienergielevel verschiebt. Bei konstanter Photoenergie erlaubt dies, die Mehrphotonenresonanz von den d -Bändern bei geringerer Bindungsenergie zu denjenigen in größerem Abstand zum Fermienergielevel zu verschieben. Damit einher geht folgerichtig eine Umkehrung der Spinpolarisation der emittierten Photoelektronen im 3PPE-Peak, wie im oberen Teil von Abb. 3.8b zu sehen ist [AW 5.11].

Im unteren Teil von Abb. 3.8b ist das Resultat von Experimenten nach Prinzip C gezeigt: die Ausnutzung der Dispersion der elektronischen Zustände mit der Parallelkomponente des winkelaufgelösten detektierten Elektronenimpulses. Dabei verhalten sich die Bildpotentialzustände wie nahezu freie Elektronen mit einer in \vec{k}_{\parallel} quadratischen Dispersion, während die d -Bänder eine deutlich weniger ausgeprägte Dispersion zeigen. Für Winkel, die nahe der Normalemission sind, lässt sich in erster Ordnung die Dispersion der d -Bänder vernachlässigen und damit führt bei fester Photonenenergie die Dispersion des Bildpotentialzustandes zu höheren Energien wiederum zu

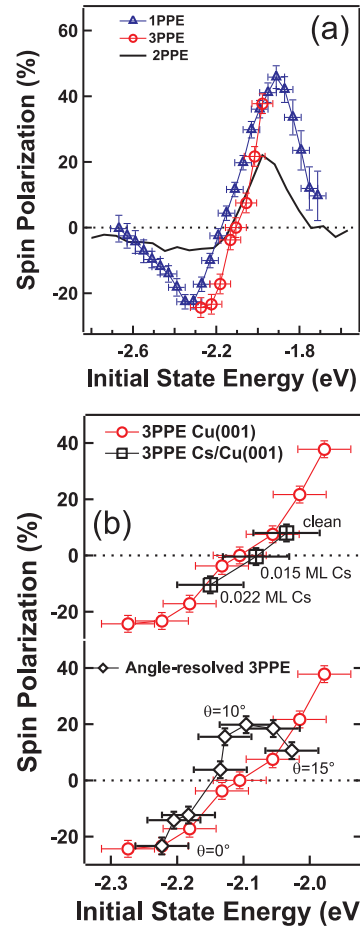


Abbildung 3.8: Vergleich verschiedener Methoden zur Anregung spinpolarisierter Photoelektronen an Cu(001)-Oberflächen [AW 5.8]

(a): Die Abhängigkeit der erzeugten Spinpolarisation für 1PPE, 2PPE und 3PPE in Normalemission zeigt einen sehr ähnlichen spektralen Verlauf als Funktion der Ausgangszustandsenergie.

(b): Cs-Adsorption erzeugt Spinpolarisationsänderungen, die einer Änderung der Photonenenergie äquivalent sind (oben). Für steigende Abweichung von der Normalemission an der reinen Cu(001)-Oberfläche entsteht eine Kopplung an andere Ausgangszustände mit einer veränderten resultierenden Spinpolarisation (unten).

einem Wechsel der Mehrphotonenresonanz, diesmal vom niedrigeren zum höheren d -Band [AW 5.8]. Die effektiven Ähnlichkeiten der Resultate nach Prinzip A,B,C sind in Abb. 3.8b im Vergleich zur reinen Cu(001)-Oberfläche in Normalemission gezeigt. Man erkennt dort auch, dass größere Abweichungen für die winkelabhängige Spinpolarisation für Winkel $> 10^\circ$, was durch die entsprechend größere Änderung der Bandstruktur mit dem detektierten Impulsvektor plausibel ist.

In den für diese Arbeit durchgeführten Untersuchungen wird die zentrale Rolle der Ausgangszustände für die produzierte Spinpolarisation deutlich. Demzufolge sollten sich unabhängig von der Anzahl der Photonen, die für die Anregung relevant ist, auch ähnliche Spinpolarisationswerte ergeben. Dies ist in Abb. 3.8a für 1,2, und 3PPE gezeigt. Die 1PPE-Resultate betreffen Messungen von Schneider *et al.* mit einer Photonenenergie von 11 eV, die 2PPE-Messungen wurden für Cu(001)-Oberflächen mit einer erhöhten Cs-Bedeckung gemacht, bei der die d -Bänder schon in 2PPE emittiert werden. Man erkennt deutlich den annähernd gleichen spektralen Verlauf der Spinpolarisation in allen drei Messungen als Funktion der Ausgangszustandsenergie. Dabei muss in 3PPE die Spinpolarisation an der Resonanzposition des Bildpotentialzustandes bestimmt werden, um diese Übereinstimmung zu erhalten. Wegen der Mischung von verschiedenen Übergängen in den 3PPE-Prozessen entsteht außerhalb der Bildpotentialresonanz eine komplexere Abhängigkeit der Spinpolarisation, die nicht allein durch die Polarisation der Ausgangszustände sondern durch die

relative Gewichtung resonanter und nichtresonanter Übergänge bestimmt ist [AW 5.8].

3.3 Rashba-Effekt in unbesetzten Zuständen von Bi/Cu(111)

Originalveröffentlichung: [AW 5.9]

An Oberflächen von Festkörpern ist wegen der dort vorhandenen Brechung der Symmetrie des Volumenkristalls und unter dem Einfluss der Spin-Bahn-Kopplung die Entstehung von speziell geordneten Spinstrukturen auch in nichtmagnetischen Systemen möglich. Die zu beobachtenden Effekte sind dabei für schwere Elemente besonders ausgeprägt und zeigen sich zum Beispiel in einer \vec{k} -abhängigen Aufspaltung des Au(111) Shockley-Oberflächenzustandes [19]. Die resultierende Spin-Polarisation der Au(111) Oberflächenzustände wurde mit spinaufgelöster ARPES untersucht [171] und durch theoretische Rechnungen bestätigt [172, 173]. Ähnliche Effekte treten zum Beispiel auch bei W(110)-(1x1)H Oberflächen auf [174], an Wismut-Oberflächen [175–177] und in Au und Ag-Filmen auf W(110) [178, 179]. In magnetischen Systemen tritt eine Kombination aus Spin-Bahn- und Austauschwechselwirkung auf, wie für Gd(0001) gezeigt wurde [180]. Potentielle Effekte der Spin-Bahn-Kopplung in Graphen [181, 182] wurden ebenfalls mit spin-aufgelöster ARPES untersucht [183–185]. Die nahezu 100%ige Spinpolarisation der durch den Rashba-Effekt beeinflussten Oberflächenzustände auf Au(111) kann praktisch zum Beispiel zur Kalibrierung von Spin-Detektoren genutzt werden [186].

Das Bychkov-Rashba-Modell [18] für ein 2D-Elektronengas beschreibt die Auswirkung der Spin-Bahn-Kopplung auf die Dispersion der elektronischen Zustände in einem unmagnetischen System. Dabei zeigen die Zustände für Elektronen der effektiven Masse m^* eine Aufspaltung, welche linear von $|k|$ abhängt und deren Größe durch den Parameter α_R bestimmt ist:

$$E(k) = \frac{\hbar^2}{2m^*} k^2 + \alpha_R |k| \quad (3.7)$$

Die Spin-Quantisierungsachse liegt in diesem Modell senkrecht zu $\vec{k}_{||}$ in der Oberflächenebene. Für eine feste Energie ergibt sich eine Spinstruktur wie in Abbildung 3.10a gezeigt ist: zwei konzentrische Kreise, auf denen die Spins entgegengesetzt und jeweils senkrecht zu $\vec{k}_{||}$ orientiert sind.

Besonders intensiv sind auch die Oberflächenstrukturen von Bi, Pb und Sb an Cu(111), Ag(111) und Si(111) Oberflächen mit ARPES und spinaufgelöster ARPES untersucht worden [187, 188]. Diese Experimente sind nur für die besetzten Zustände empfindlich. Nach diesen vorhergehenden Studien konnte im System Bi/Cu(111) das Vorhandensein von unbesetzten Zuständen vermutet werden, die durch den Rashba-Effekt beeinflusst sind und welche in einem Energiebereich liegen würden, der in unserem Experiment mit Photonen von 3 eV zugänglich ist. In der Folge fanden wir in experimentellen 2PPE-Messungen von Bi/Cu(111) entsprechende Signaturen unbesetzter Zustände [AW 5.9]. Dies ist in der Abb. 3.9 durch Vergleich von 1PPE-Messungen bei 6 eV mit 2PPE-Messungen bei 2×3.1 eV gezeigt. In den 2PPE-Messungen zeigen sich dort bei niedrigen kinetischen Energien Zustände, deren Dispersion durch zwei entlang der $\vec{k}_{||}$ -Achse verschobene

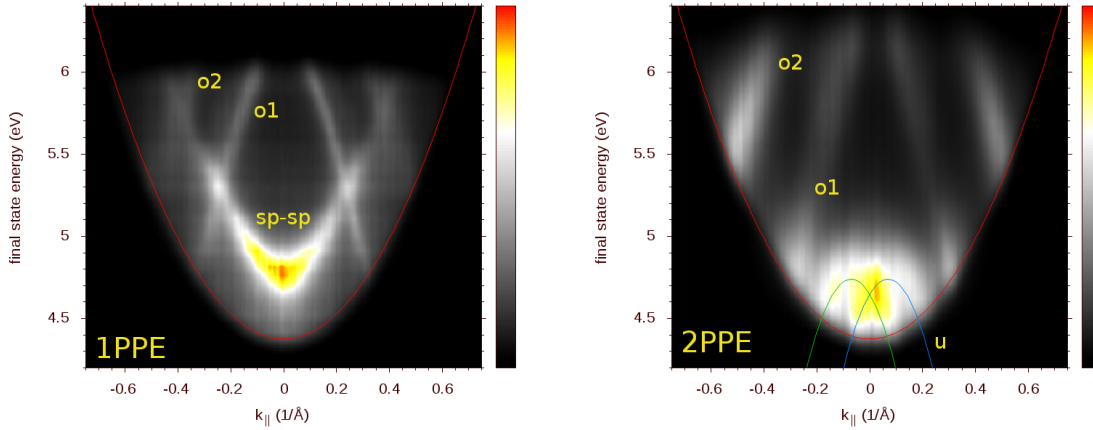


Abbildung 3.9: Identifizierung unbesetzter Zustände für Bi/Cu(111) durch Vergleich der Photoemission in 1PPE ($h\nu = 6$ eV, links) und 2PPE ($2h\nu = 6.2$ eV, rechts) im Impulsmikroskop. Gezeigt ist die Intensität als Funktion von $k_{||}$ im $\bar{\Gamma}\bar{M}$ -Azimuth senkrecht zur optischen Ebene, Anregung p -polarisiert, Einfallswinkel 65° . In 1PPE ist ein $sp - sp$ Volumenübergang sowie die besetzten Bi/Cu(111)-Zustände (o) gekennzeichnet. In 2PPE erscheinen unbesetzte Zustände (u), die durch zwei in k verschobene Parabeln angenähert werden können [AW 5.9]. Die einhüllenden Parabeln kennzeichnen die Dispersion für freie Elektronen, ausgehend von der Energie die um die Austrittsarbeit höher liegt als das Fermi-niveau.

Parabeln angenähert werden kann. Diese Zustände sind in den 1PPE-Resultaten nicht sichtbar, was darauf hinweist, dass sie unbesetzt sind und damit für den 1PPE-Prozess keine Rolle spielen. Dafür spricht auch die in den 1PPE-Messungen zusätzlich zu erkennende parabelartige Intensitätsverteilung, die durch einen sp - sp -Übergang in der Volumenbandstruktur von Cu(111) hervorgerufen wird [158, 189]. Dieser Volumen-Übergang ist in den 2PPE-Messungen nicht mehr dominant, was durch den Einfluss unbesetzter Zwischenzustände an der Oberfläche und einer damit einher gehenden wesentlich erhöhten Effizienz der Oberflächen-2PPE-Prozesse gegenüber von Volumen-2PPE-Prozessen erklärt werden kann. Neben unserer ersten Beobachtung von unbesetzten, durch den Rashba-Effekt beeinflussten Zuständen in Oberflächenlegierungen von Bi/Cu(111) wurden ein ähnlicher Effekt auch für unbesetzte Quantentopfzustände in dickeren Bi-Filmen auf Cu(111) gemessen [190].

Eine theoretische Analyse der unbesetzten Zustände in Bi/Cu(111) erfolgte in Zusammenarbeit mit H. Mirhosseini und J. Henk [AW 5.9]. Dabei konnten die entsprechenden unbesetzten Zustände in Bi/Cu(111) identifiziert werden. In den Rechnungen wurde ebenfalls der Spincharakter dieser Zustände analysiert. Hier ergab sich die Voraussage einer veränderten Spinstruktur in den unbesetzten Zuständen durch Hybridisierung mit niederenergetischen Zuständen. Die resultierende Anordnung der Spins ist in Abb. 3.10b im Vergleich zum Standard-Rashba-Modell daneben in Abb. 3.10a gezeigt. In der vorhergesagten „unkonventionellen“ Anordnung sind die Spins für \vec{k} -Vektoren in gleiche Richtungen gleich ausgerichtet, d.h. es stehen bei dem umgekehrten Vektor $-\vec{k}$ keine Zustände des gleichen Spins zur Verfügung und Streuung in diese Zustände könnte

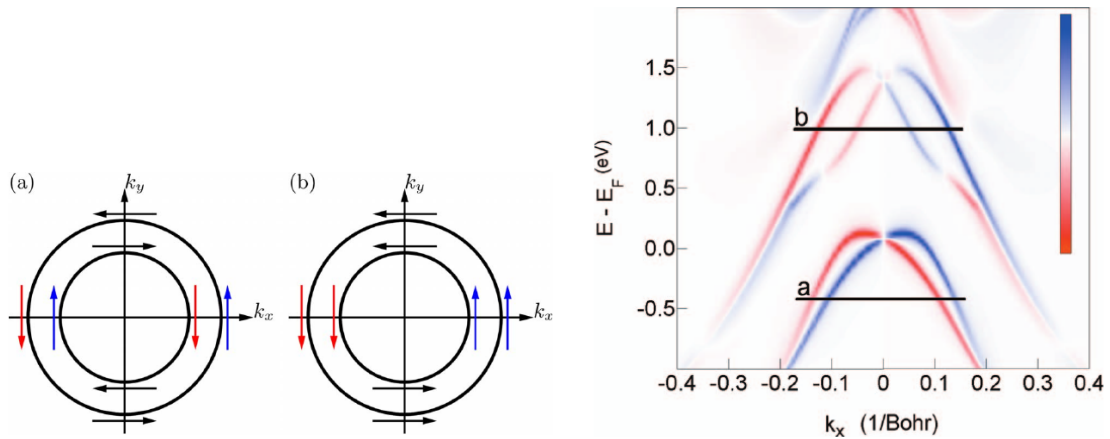


Abbildung 3.10: Bi/Cu(111) Theorie. Rechts: Mögliche Spinstrukturen bei konstanter Energie (a) konventionelles Rashba-Modell, (b) durch Hybridisierung veränderte Spinstruktur. Links: k_{\parallel} -Bandstruktur für Bi/Cu(111), mit den Fällen (a) und (b) für besetzte (a) und unbesetzte (b, und Abb. 3.9) Zustände. (5.9, [191])

nur durch einen Prozess mit Spin-Umkehr stattfinden. Dies könnte für die Elektronendynamik in diesen Zuständen von Bedeutung sein. Außerdem beruhen Vorschläge für spintronische Bauelemente u.a. direkt auf dem Vorhandensein der konventionellen Rashba-Struktur [192], was bedeutet, dass die Möglichkeit einer veränderten Spinstruktur im jeweils vorliegenden System explizit in Betracht gezogen werden muss. Die Wichtigkeit einer spin-aufgelösten Analyse der elektronischen Zustände wird dadurch unterstrichen, dass die beiden verschiedenen Fälle die gleiche nicht-spinaufgelöste Struktur aus zwei Kreisen bei einer konstanten Energie zeigen können, wie in Abb. 3.10 zu sehen ist. Die Verifizierung dieser theoretischen Vorhersage zur Spinanordnung durch spin-aufgelöste 2PPE-Messungen ist ein Ziel zukünftiger Untersuchungen.

3.4 Magnetischer Dichroismus von angeregten Quantentopfzuständen in Co/Cu(001)

Originalveröffentlichungen: [AW 5.10], [AW5.11]

Weil angeregte Zustände eine Schlüsselrolle in optisch gesteuerten spinabhängigen Prozessen spielen, ist es von großer Wichtigkeit, die Spin-Bahn-Kopplung in diesen angeregten Zuständen charakterisieren zu können. Die dazu notwendigen spektroskopischen Informationen können insbesondere mittels einer Kombination von magnetischem Dichroismus und Zweiphotonen-Photoemission von magnetischen Proben erhalten werden können, mit spezifischen optisch angeregten Zuständen als Zwischenzuständen.

In 2PPE-Experimenten wurden bis zu den hier vorgestellten Arbeiten sowohl magnetischer linearer Dichroismus [123] also auch Zirkulardichroismus [193] von zwei anderen Gruppen beobachtet. Dabei konnten jedoch die magnetisierungsabhängigen Intensitäten *nicht* mit spezifischen angeregten elektronischen Zuständen in Zusammenhang gebracht werden. Im ersten Fall beobachteten Pickel et al. [123] dichroische Signale von bis zu 20%, welche mit *besetzten*, von der Spin-Bahn-Wechselwirkung beeinflussten Zuständen in ultradünnen Kobaltfilmen in Verbindung standen. Im zweiten Falle von Hild et al. [193] handelte es sich um Experimente an Heusler-Legierungen mit einem Signal von 0.35% in nichtspektroskopischen total-yield Messungen, welche keine Identifizierung der Zwischenzustände ermöglichen.

In den Veröffentlichungen [AW 5.10], [AW5.11] wird von uns dazu im Vergleich erstmals demonstriert, dass magnetischer Dichroismus auch zu spezifischen optisch angeregten Zuständen zugeordnet werden kann. Dazu dienen uns gut charakterisierte unbesetzte Quantentopfzustände in Kobaltfilmen auf Cu(001) [194, 195], welche hier als Zwischenzustände in 2PPE-Prozessen beobachtet werden. Über die gezielte Änderung der Polarisation des einfallenden Lichtes können wir das gemeinsame Prinzip demonstrieren, welches sowohl den linearen als auch den Zirkulardichroismus bestimmt: die Interferenz zweier optischer Anregungspfade, welche durch zwei zueinander orthogonale Feldkomponenten gekoppelt sind. Die experimentellen und theoretischen Daten, die in den Studien [AW 5.10], [AW5.11] erhalten wurden, ermöglichen die Zuordnung der Spin-Bahn-Kopplung in den Quantentopfzuständen als Ursache des beobachteten magnetischen Dichroismus. Dies wird im Folgenden näher erläutert.

Die für die Entstehung der betrachteten Quantentopfzustände relevanten Bandstrukturen von Kupfer und Kobalt entlang der Richtung der Cu(001)-Oberflächennormalen sind in Abb. 3.11 gezeigt. Man erkennt für Kobalt einen Bereich mit elektronischen Zuständen, die in Kupfer keine erlaubten Wellenzahlvektoren bei derselben Energie besitzen, also räumlich auf den Kobaltfilm beschränkt sind. Die dadurch entstehenden quantisierten Zustände sind ebenfalls in Abb. 3.11 eingezeichnet, sie sind das Resultat einer theoretischen Rechnung von J. Henk für tetragonale Kobaltfilme auf Cu(001) [196]. In der ferromagnetischen Kobaltschicht sind durch die spin-aufgespaltene

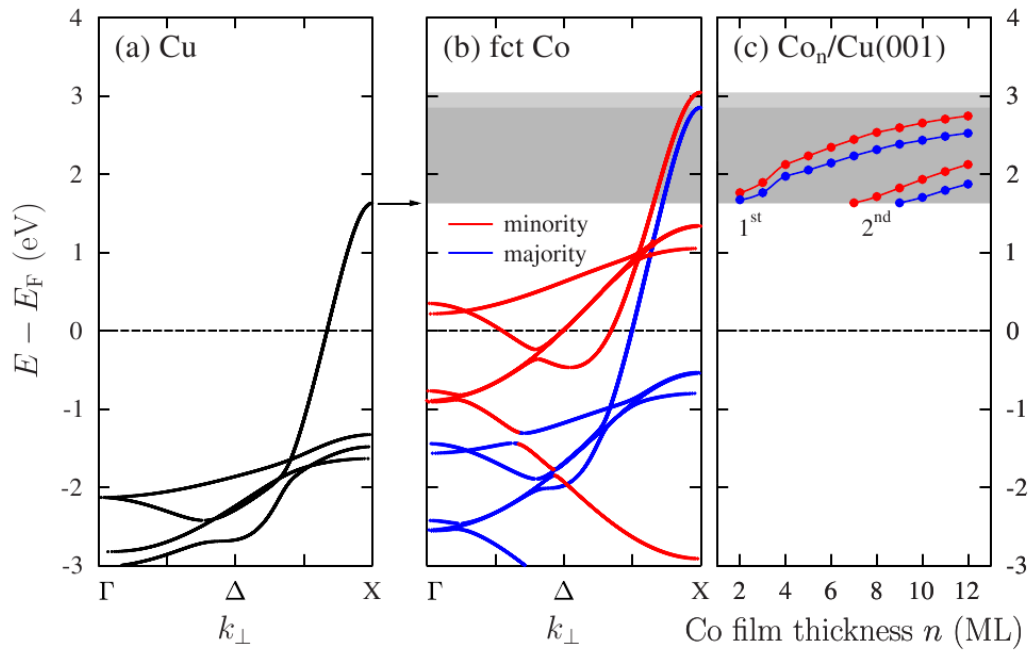


Abbildung 3.11: Elektronische Bandstrukturen von fcc Cu (a) und tetragonalem Co (b) zur Bildung der unbesetzten Quantentopfzustände von Co/Cu(001) (c) [AW 5.11].

Im grau unterlegten Energiebereich können sich quantisierte Zustände durch stehende Elektronenwellen im Kobaltfilm formieren, da im diesem Bereich in Kupfer eine Bandlücke entlang der Δ -Linie vorliegt.

Bandstruktur Majoritäts- und Minoritäts-Quantentopfzustände unterscheidbar, die sich im Energiebereich zwischen etwa 1.8 eV und 3 eV über dem Fermi-Niveau befinden.

Die energieaufgelösten 1PPE- und 2PPE-Intensitäten, die während des Wachstums der Co-Schichten auf Cu(001) gemessen wurden, sind in Abbildung 3.12 gezeigt. Beim Vergleich der jeweiligen 1PPE und 2PPE-Spektren erkennt man in 2PPE eine zusätzliche Struktur, die sich mit zunehmender Filmdicke von den niedrigsten kinetischen Energien zum Fermi-niveau bewegt. Ab ca. 10ML Co ist der Beginn eines zweiten, in ähnlicher Weise dickenabhängigen Zustandes zu sehen. Diese Strukturen können als Beiträge von unbesetzten Quantentopfzuständen als Zwischenzustände identifiziert werden, da die Ausgangs- und Endzustände für 1PPE bei einer Photonenenergie von $h\nu$ und 2PPE bei $2 * h\nu/2$ übereinstimmen. Der Energiebereich und die charakteristische Energiedispersion der beobachteten Zwischenzustände mit der Filmdicke sind mit den Quantentopfzuständen im unbesetzten sp -Band von Co konsistent [194, 195]. Die generell erhöhte Intensität in der Nähe des Fermi-Niveaus im Vergleich zur reinen Kupferoberfläche bei etwa 6.0 and 5.8 eV in 2PPE and 1PPE kann der hohen Zustandsdichte der besetzten Co d -Bänder zugeordnet werden. Weiterhin zeigen die gemessenen Spektren sowohl in 1PPE als auch in 2PPE klare Oszillationen der Gesamtintensität als Funktion der Filmdicke, die mit dem Lagenwachstum der Kobaltfilme korrelieren, mit dem für Co/Cu(001) charakteristischen anfänglichen Doppellagenwachstum [197, 198]. Dabei fällt auf, dass die Intensität im 3PPE-Bereich der gemessenen Spektren in

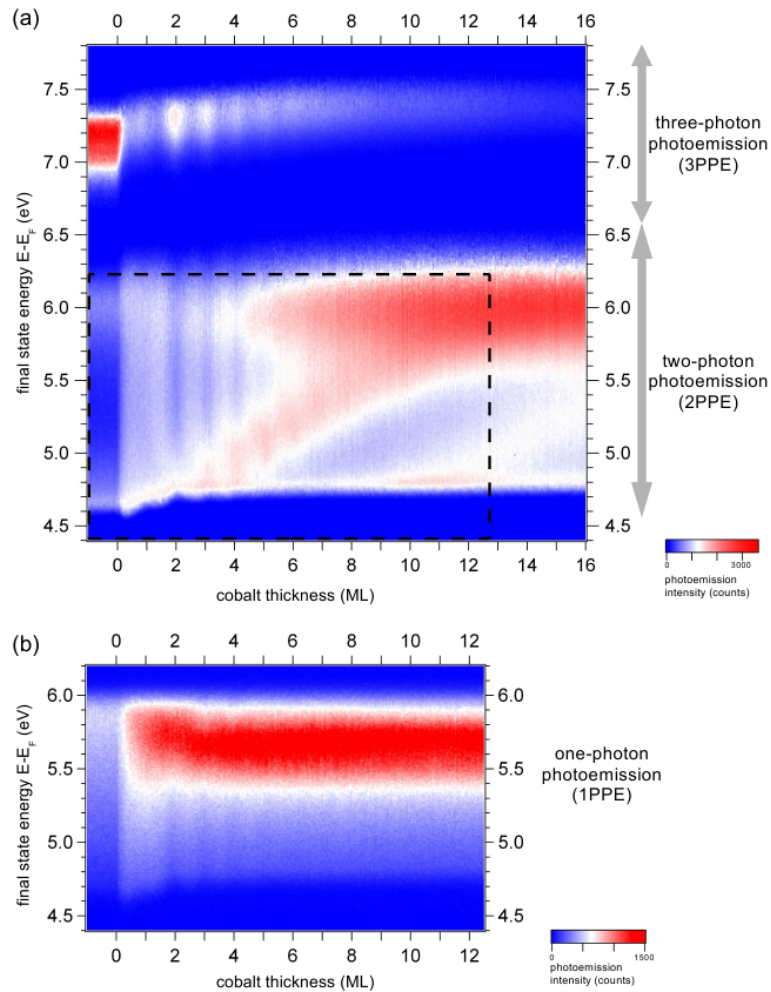


Abbildung 3.12: Experimentelle dickenabhängige Photoemissionsintensitäten während des Wachstums von Co-Filmen auf Cu(001) und gleichzeitiger Messung von 2PPE und 3PPE (oben, $h\nu=3.1$ eV) und dazu im Vergleich in 1PPE (unten, $h\nu=6.0$ eV) [81]. In der 2PPE-Messung ist der Dicken- und Energiebereich für den direkten Vergleich zu 1PPE durch ein gestricheltes Rechteck markiert.

Abb. 3.12 im Vergleich zur lagenabhängigen 2PPE-Intensität *gegenphasig* oszilliert. Dies kann mit dem unterschiedlichen Einfluss der Oberflächenmorphologie auf die relevanten Emissionsprozesse begründet werden: In 2PPE entstehen die höheren Intensitäten durch indirekte Streuprozesse an den nicht vollständigen Monolagen mit vielen zusätzlichen Streuzentren für die in 2PPE angeregten Volumenzustände. Die beobachtete 3PPE-Intensität rührt dagegen vom $n = 1$ Bildpotenzialzustand auf der Co(001)-Oberfläche her. Die Lebensdauer von Elektronen in diesem Oberflächenzustand wird von den Streuzentren in unvollständigen Monolagen verringert [199,200]. Diese gegenläufigen Prozesse führen dann für unvollständige Monolagen zu einem Minimum der Intensität in 3PPE gegenüber einem Maximum in 2PPE. Dies demonstriert die zusätzlichen Informationen über den Einfluss der Oberflächenmorphologie in Mehrphotonenphotoemissionsprozessen die man in *in-situ* Messungen während des Schichtwachstums erhalten kann [81].

Nach der Identifizierung der unbesetzten Quantentopfzustände in 2PPE wurde das Intensitätsverhalten unter Magnetisierungsänderung in der in Abb. 3.13 gezeigten Geometrie untersucht. Abb. 3.13a zeigt dabei das Setup für zirkular polarisiertes und Abb. 3.13b für linear polarisiertes Licht. Die Probenmagnetisierung \mathbf{M} liegt für beide Typen von Messungen in der optischen Ebene, with $\pm\mathbf{M}$ parallel oder anti-parallel zu [110], welche die leichte Magnetisierungsachse der Co-Filme ist. Man beachte, dass die in Abb. 3.13b gezeigte Geometrie nicht der üblicherweise genutzten Anordnung für linearen magnetischen Dichroismus entspricht, bei der \mathbf{M} senkrecht zur optischen Ebene liegt [169]. Das hier benutzte Setup erlaubt aufgrund der experimentell leicht zu steuernden Polarisation des Laserlichts eine systematische Untersuchung der polarisationsabhängigen Effekte, die bei gleicher Lage von \mathbf{M} hervorgerufen werden. Die Polarisationsebene des linear polarisierten Lichts kann dazu kontinuierlich um den Winkel α relativ zur optischen Ebene OP gedreht werden (Abb. 3.13b, p : $\alpha = 0^\circ$, s : $\alpha = 90^\circ$) und die Photoelektronen werden in der Richtung senkrecht zur Cu(001) Oberfläche detektiert.

In Abb. 3.13c und 3.13d sind die Endzustandsenergien der Übergänge durch den Quantentopfzustand und derjenigen vom Fermi-Niveau durch $E_{QW} + hv$ und $E_F + 2hv$ gekennzeichnet. Als Maß des Dichroismus wird die normalisierte Intensitätsänderung A bei der Magnetisierungsänderung $\pm\mathbf{M}$ benutzt, jeweils für linear (MLD) und zirkular polarisiertes Licht (MCD): $A_{MCD,MLD} = (I_{+M} - I_{-M}) / (I_{+M} + I_{-M})$, wobei $I_{\pm M}$ die Photoemissionsintensitäten der beiden Ausrichtungen der Magnetisierung \mathbf{M} sind.

Die 2PPE-Spektren, welche mit linear ($\alpha = 82^\circ$) und zirkular (σ^-, σ^+) polarisiertem Licht gemessen wurden, sind im oberen Teil von Abb. 3.13 gezeigt, mit den dazugehörigen Asymmetriekurven A_{MCD} (links) bzw. A_{MLD} (rechts). Man erkennt für zirkular polarisiertes Licht einen Dichroismus von etwa 5% in der Nähe des Fermi-Niveaus, was mit den Beobachtungen für besetzte Zustände von Pickel *et al.* [123] und Nakagawa *et al.* [201] kompatibel ist. Weiterhin erkennt man einen vorhandenen Dichroismus von etwa 3% an der Position $E_{QW} + hv$ des *unbesetzten* Quantentopfzustandes. Dieses mit dem Quantentopfzustand verbundene Signal wird besonders deutlich in den Messungen mit linear polarisiertem Licht, wo ungefähr 10% Asymmetrie an der Position des Quantentopfzustandes bei einem Winkel von $\alpha \approx 82^\circ$ beobachtet werden. Weitere Messungen für unterschiedlich dicke Co-Schichten zeigen die Korrelation von spektraler Position des Quantentopfzustandes und dichroischem Signal von etwa 10% [AW 5.10]. Dies ist die erste Beobachtung von magnetischem Dichroismus von optisch angeregten Zuständen in 2PPE.

Für nominell p - oder s -polarisiertes Licht beobachten wir keinen Dichroismus. Dieser erscheint nur für eine gekippte Polarisationsebene ($\alpha \neq 0^\circ, \pm 90^\circ, 180^\circ$) in Übereinstimmung mit generellen Symmetrieeorderungen [169], wie im Folgenden gezeigt wird: Da der Photoemissionsstrom eine reelle Größe ist, darf er sich nicht ändern, wenn das gesamte experimentelle Setup nach einer Spiegeloperation an der optischen Ebene in sich selbst überführt wird. Für den Kristall selbst ist das erfüllt, da wie in Abb. 3.13b erkennbar, der Photostrom in einer Spiegelebene des Kristalls liegt. Eine Spiegelung an OP kehrt aber zusätzlich noch die Magnetisierung um, und ändert das Vorzei-

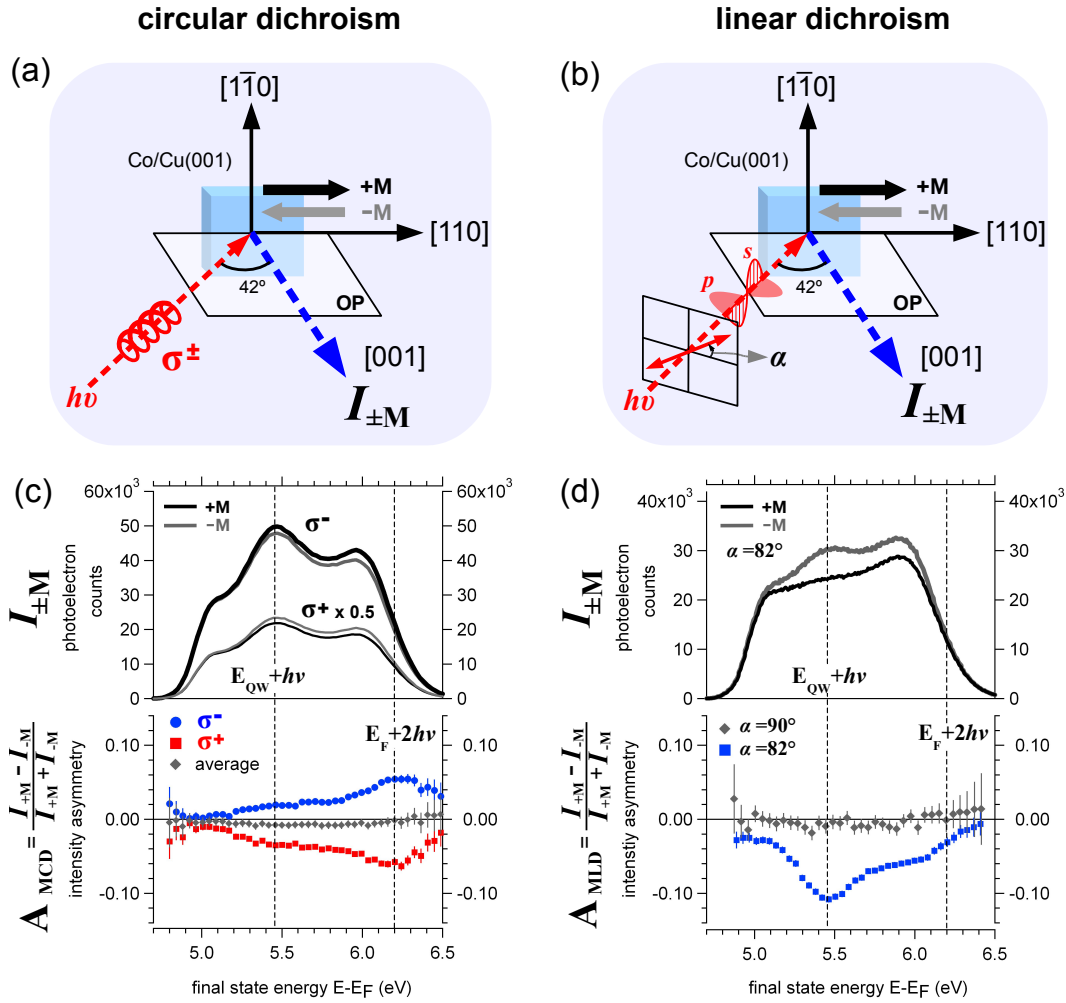


Abbildung 3.13: Messungen des 2PPE-Dichroismus von Co/Cu(001). Experimentelle Anordnung für (a) zirkular und (b) linear polarisiertes Licht. (c,d): Magnetisierungsabhängige Spektren (oben) und Asymmetrie A für zirkularen (c) und linearen (d) Dichroismus. Der zirkulare Dichroismus kehrt sich bei Wechsel der Helizität um (σ^+ , σ^-). Im linearen Fall liegt maximaler Dichroismus bei $\alpha \approx 82^\circ$ vor, bei s - und p -polarisiertem Licht entsteht keine Asymmetrie.

chen der s -Komponente des Lichts während die p -Komponente unverändert bleibt. Die Phase der s -Komponente ändert sich also um 180° gegenüber der p -Komponente durch diese Spiegelung. Das würde einer notwendigen Änderung von α auf $-\alpha$ entsprechen. Im Experiment wird α aber konstant gehalten und nur M geschaltet, so dass eben *nicht* zwei äquivalente experimentelle Setups vorliegen und eine Änderung des Photostroms unter alleiniger Umkehrung von M aus Symmetriegründen nicht verboten ist. Man erkennt, dass das unterschiedliche Verhalten der s - und der p -Komponente des Lichts bezüglich der Spiegelebene für das Vorliegen des magnetischen Dichroismus im Setup von Abb. 3.13 von zentraler Bedeutung ist. Dies gilt in gleicher Weise auch für den zirkularen Dichroismus: hier ändert sich die Phase zwischen s und p ebenfalls um 180° , aber nicht von 0° auf 180° wie im linearen Fall, sondern von 90° auf -90° . Die vorliegenden Experi-

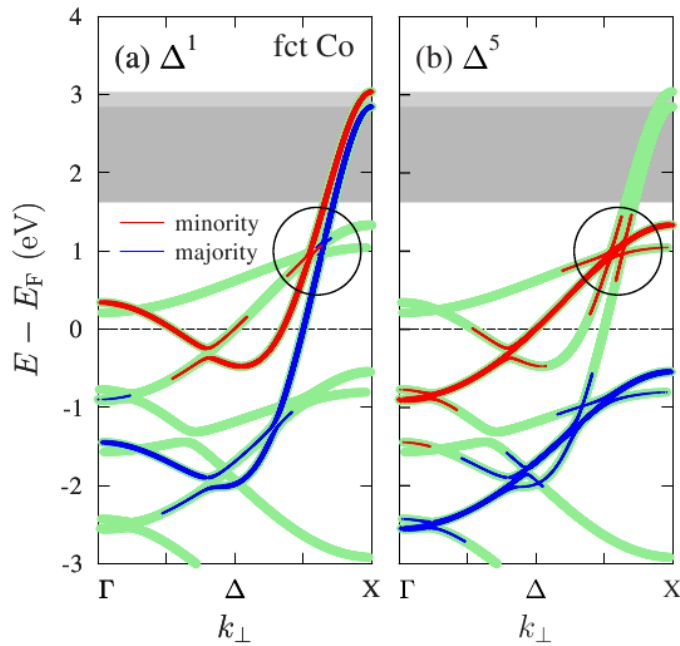


Abbildung 3.14: Symmetrie- und spin-aufgelöste Bandstruktur von tetragonalem Co [AW 5.11]. Die Spin-Bahn-Kopplung mischt Anteile der räumlichen Δ^5 -Symmetrie zu den sp -Zuständen mit vorherrschender Δ^1 -Symmetrie (Kreise). Der in den grau unterlegten Regionen der Co-Quantentopfzustände vorliegende Δ^5 -Anteil (<1%) bewirkt den beobachteten magnetischen Dichroismus in 2PPE.

mente verdeutlichen also einen allgemeinen Fall, bei welchem zwei verschiedene Anteile kohärent zum Photostrom beitragen und die relative Phase zwischen diesen beiden Komponenten um 180° geändert wird, was dann entsprechend zu Interferenzeffekten führen kann. Die Phasenänderung passiert hier effektiv durch Umschalten der Magnetisierung, woraus eine höhere bzw. niedrigere Intensität für \mathbf{M} und $-\mathbf{M}$ resultieren. Andere Möglichkeiten dieser Phasenänderung bestehen in Umschalten der Helizität des Lichts oder der Einstellung der linearen Polarisierung von α auf $-\alpha$ bei konstanter Ausrichtung der Magnetisierung \mathbf{M} .

Die Symmetrieargumente erlauben nur festzustellen, dass der beobachtete Dichroismus prinzipiell erlaubt ist, aber es können keine quantitativen Aussagen gemacht werden. Insbesondere sagen uns diese Symmetrieargumente nichts über die Rolle der unbesetzten Quantentopfzustände für das Zustandekommen des beobachteten Signals. Dies kann nur über theoretische Photoemissionsrechnungen unter Einbezug der elektronischen Struktur geschehen. Aus diesen Rechnungen, die von J. Henk durchgeführt wurden, resultiert ein klares Bild über die jeweiligen Anteile der Quantentopfzustände, welche jeweils auf die s und die p -Polarisationsanteile reagieren. Dabei handelt es sich jeweils um Anteile mit Δ^1 und Δ^5 Symmetrie, welche in der Bandstruktur von Abb. 3.14 gezeigt sind. Während die Δ^1 Symmetrie dominant ist, entsteht ein Anteil von Δ^5 durch Spin-Bahn-Kopplung in der durch Kreise gekennzeichneten Hybridisierungsregion [AW 5.4]. Aus den Rechnungen kann die Größe dieses Anteils als <1% abgeschätzt werden. Dies verdeutlicht die hohe Empfindlichkeit der eingesetzten Methode für Spin-Bahn-Kopplungseffekte in der elektronischen Struktur. Wir haben damit durch die Beobachtung von magnetischem Dichroismus in 2PPE von Co-Quantentopfzuständen gezeigt, dass selbst die relativ schwache Spin-Bahn-Kopplung in diesen optisch angeregten Zuständen nachweisbar ist. Dies ist für zukünftige Untersuchungen von

großer Bedeutung.

4 Zusammenfassung und Ausblick

Die vorliegenden Arbeiten untersuchten verschiedene Manifestationen der Spin-Bahn-Wechselwirkung in der elektronischen Struktur nichtmagnetischer und magnetischer Festkörper in der nichtlinearen Photoemission. Es wurde gezeigt, wie durch spinaufgelöste Photoelektronenspektroskopie zusätzliche Informationen über die Kopplung elektronischer Volumen- und Oberflächenzustände erhalten werden können und wie durch eine Ausnutzung der spinabhängigen Anregungsprozesse die Spinpolarisation der Photoelektronen in Mehrphotonenübergängen gesteuert werden kann. Die nichtlineare Photoemission liefert insbesondere einen Zugang zu Spin-Bahn-Kopplungseffekten in *unbesetzten* elektronischen Zuständen, wie am Beispiel des Rashba-Effekts und des magnetischen Dichroismus von optisch angeregten Zuständen gezeigt wurde.

Die hier vorgestellten Arbeiten bieten einen Ausgangspunkt für weitere Untersuchungen auf verschiedenen Gebieten. Dazu gehört zum Beispiel die Analyse zeitabhängiger Effekte der Spin-Bahn-Kopplung, welche für das Verständnis der Dynamik von Spins in Wechselwirkung mit weiteren Freiheitsgraden wichtig ist. Hier ist zum Beispiel der Impulsvektor der angeregten Photoelektronen interessant, auf den in winkelaufgelösten Experimenten mit dem Impulsmikroskop (Abschnitt 2.3) zugegriffen werden kann. In Kombination mit der schon demonstrierten Möglichkeit zur gleichzeitigen parallelen Spin- und Impulsanalyse mit einem solchen Instrument [202] könnten so zum Beispiel Wege zur räumlich-zeitlichen Steuerung spinpolarisierter Elektronen an Oberflächen untersucht werden.

Literaturverzeichnis

- [1] Schiff, L. I., *Quantum Mechanics*, 3rd ed. (McGraw-Hill Book Company, New York, 1968)
- [2] Rose, E. M., *Relativistic electron theory* (Wiley, New York, 1961) <http://lccn.loc.gov/61005667>
- [3] Haken, H. & Wolf, H. C., *The Physics of Atoms and Quanta*, Advanced Texts in Physics (Springer-Verlag, Berlin/Heidelberg, 2005) ISBN 3-540-20807-0, <http://www.springerlink.com/index/10.1007/3-540-29281-0>
- [4] Meier, E., "Spin Polarized Photoemission by Optical Spin Orientation in Semiconductors," in *Polarized Electrons in Surface Physics* (World Scientific, Singapore, 1985) Chap. 10, pp. 423–466, ISBN 9971-978-49-0
- [5] *Optical Orientation*, edited by Meier, E. & Zakharchenya, B. P. (North-Holland, Amsterdam, 1984)
- [6] Pierce, D., "Direct observation of spin dependent electronic structure of GaAs using spin polarized photoemission," *Phys. Lett. A* **51**, 465–466 (1975)
- [7] Pierce, D. & Meier, E., "Photoemission of spin-polarized electrons from GaAs," *Phys. Rev. B* **13**, 5484–5500 (1976)
- [8] Ziman, J. M., *Prinzipien der Festkörpertheorie* (Harri Deutsch, Thun, 1999) ISBN 3817112556, p. 442, <http://www.worldcat.org/title/prinzipien-der-festkorpertheorie/oclc/246011312>
- [9] Kittel, C., *Quantum theory of solids* (Wiley, New York, 1987) ISBN 0471624128, <http://lccn.loc.gov/86032478>
- [10] Dresselhaus, G., "Spin-Orbit Coupling Effects in Zinc Blende Structures," *Phys. Rev.* **100**, 580–586 (1955)
- [11] Alvarado, S., Riechert, H. & Christensen, N., "Spontaneous Spin Polarization of Photoelectrons from GaAs," *Phys. Rev. Lett.* **55**, 2716–2718 (1985)
- [12] Cardona, M., Christensen, N. & Fasol, G., "Relativistic band structure and spin-orbit splitting of zinc-blende-type semiconductors," *Phys. Rev. B* **38**, 1806–1827 (1988)
- [13] Luo, J.-W., Bester, G. & Zunger, A., "Full-Zone Spin Splitting for Electrons and Holes in Bulk GaAs and GaSb," *Phys. Rev. Lett.* **102**, 056405 (2009)
- [14] *Polarized Electrons in Surface Physics*, edited by Feder, R. (World Scientific, Singapore, 1985) ISBN 9971-978-49-0
- [15] Kirschner, J., Feder, R. & Wendelken, J., "Electron Spin Polarization in Energy- and Angle-Resolved Photoemission from W(001): Experiment and Theory," *Phys. Rev. Lett.* **47**, 614–617 (1981)
- [16] Hsieh, D., Xia, Y., Qian, D., Wray, L., Meier, F., Dil, J., Osterwalder, J., Patthey, L., Fedorov, A., Lin, H., Bansil, A., Grauer, D., Hor, Y., Cava, R. & Hasan, M., "Observation of Time-Reversal-Protected Single-Dirac-Cone Topological-Insulator States in Bi₂Te₃ and Sb₂Te₃," *Phys. Rev. Lett.* **103**, 2–5 (2009)
- [17] Wray, L. A., Xu, S.-Y., Xia, Y., Hor, Y. S., Qian, D., Fedorov, A. V., Lin, H., Bansil, A., Cava, R. J. & Hasan, M. Z., "Observation of topological order in a superconducting doped topological insulator," *Nature Physics* **5**, 1–5 (2010)
- [18] Bychkov, Y. A. & Rashba, E. I., "Oscillatory effects and the magnetic susceptibility of carriers in inversion layers," *J. Phys. C: Solid State Phys.* **17**, 6039 (1984)
- [19] LaShell, S., McDougall, B. & Jensen, E., "Spin Splitting of an Au(111) Surface State Band Observed with Angle Resolved Photoelectron Spectroscopy," *Phys. Rev. Lett.* **77**, 3419–3422 (1996)

- [20] Chikazumi, S., *Physics of Ferromagnetism*, 2nd ed. (Oxford University Press, Oxford, 1997) ISBN 0198517769, <http://lccn.loc.gov/96027148>
- [21] Bruno, P., "Tight-binding approach to the orbital magnetic moment and magnetocrystalline anisotropy of transition-metal monolayers," *Phys. Rev. B* **39**, 865–868 (1989)
- [22] Vaz, C. A. F., Bland, J. A. C. & Lauhoff, G., "Magnetism in ultrathin film structures," *Rep. Prog. Phys.* **71**, 056501 (2008)
- [23] Winkelmann, A., Przybylski, M., Luo, F., Shi, Y. & Barthel, J., "Perpendicular Magnetic Anisotropy Induced by Tetragonal Distortion of FeCo Alloy Films Grown on Pd(001)," *Phys. Rev. Lett.* **96**, 257205 (2006)
- [24] Beaurepaire, E., Merle, J.-C., Daunois, A. & Bigot, J.-Y., "Ultrafast Spin Dynamics in Ferromagnetic Nickel," *Phys. Rev. Lett.* **76**, 4250–4253 (1996)
- [25] Stanciu, C. D., Hansteen, F., Kimel, A. V., Kirilyuk, A., Tsukamoto, A., Itoh, A. & Rasing, T., "All-Optical Magnetic Recording with Circularly Polarized Light," *Phys. Rev. Lett.* **99**, 47601 (2007)
- [26] Bigot, J.-Y., "Femtosecond magneto-optical processes in metals," *Comptes Rendus de l'Academie des Sciences - Series IV - Physics* **2**, 1483–1504 (2001)
- [27] Zhang, G., Hübner, W., Beaurepaire, E. & Bigot, J.-Y., "Laser-Induced Ultrafast Demagnetization: Femtomagnetism, a New Frontier?," in *Spin Dynamics in Confined Magnetic Structures I*, Topics in Applied Physics, Vol. 83, edited by Hillebrands, B. & Ounadjela, K. (Springer Berlin Heidelberg, Berlin, Heidelberg, 2002) pp. 245–290, ISBN 978-3-540-41191-8, <http://www.springerlink.com/index/10.1007/3-540-40907-6>
- [28] Koopmans, B., "Laser-Induced Magnetization Dynamics," in *Spin Dynamics in Confined Magnetic Structures II*, Topics in Applied Physics, Vol. 87, edited by Hillebrands, B. & Ounadjela, K. (Springer Berlin / Heidelberg, 2003) pp. 256–323, ISBN 3-540-46097-7, http://dx.doi.org/10.1007/3-540-46097-7_8
- [29] Hicken, R. J., "Ultrafast nanomagnets: seeing data storage in a new light.." *Philos. Transact. A Math. Phys. Eng. Sci.* **361**, 2827–41 (2003)
- [30] Bennemann, K. H., "Ultrafast dynamics in solids," *J. Phys. Cond. Matter* **16**, R995–R1056 (2004)
- [31] Bennemann, K. H., "Ultra-fast dynamics in solids: non-equilibrium behaviour of magnetism and atomic structure," *Annalen der Physik* **18**, 480–560 (2009)
- [32] Bovensiepen, U., "Coherent and incoherent excitations of the Gd(0001) surface on ultrafast timescales," *J. Phys. Cond. Matter* **19**, 083201 (2007)
- [33] Wang, J., Sun, C., Hashimoto, Y., Kono, J., Khodaparast, G., Cywinski, L., Sham, L. J., Sanders, G. D., Stanton, C. J. & Munekata, H., "Ultrafast magneto - optics in ferromagnetic III - V semiconductors," *J. Phys. Cond. Matter* **18**, R501–R530 (2006)
- [34] Kirilyuk, A., Kimel, A., Hansteen, F., Rasing, T. & Pisarev, R. V., "Ultrafast all-optical control of the magnetization in magnetic dielectrics," *Low Temp. Phys.* **32**, 748 (2006)
- [35] Kimel, A. V., Kirilyuk, A., Hansteen, F., Pisarev, R. V. & Rasing, T., "Nonthermal optical control of magnetism and ultrafast laser-induced spin dynamics in solids," *J. Phys. Cond. Matter* **19**, 043201 (2007)
- [36] Kirilyuk, A., Kimel, A. & Rasing, T., "Ultrafast optical manipulation of magnetic order," *Rev. Mod. Phys.* **82**, 2731–2784 (2010)

- [37] van der Laan, G., Thole, B., Sawatzky, G., Goedkoop, J., Fuggle, J., Esteva, J.-M., Karnatak, R., Remeika, J. & Dabkowska, H., "Experimental proof of magnetic x-ray dichroism," *Phys. Rev. B* **34**, 6529–6531 (1986)
- [38] Schütz, G., Wagner, W., Wilhelm, W., Kienle, P., Zeller, R., Frahm, R. & Materlik, G., "Absorption of circularly polarized x rays in iron," *Phys. Rev. Lett.* **58**, 737–740 (1987)
- [39] Baumgarten, L., Schneider, C., Petersen, H., Schäfers, F. & Kirschner, J., "Magnetic x-ray dichroism in core-level photoemission from ferromagnets," *Phys. Rev. Lett.* **65**, 492–495 (1990)
- [40] Schneider, C., Hammond, M., Schuster, P., Cebollada, A., Miranda, R. & Kirschner, J., "Observation of magnetic circular dichroism in uv photoemission from ferromagnetic fcc cobalt films," *Phys. Rev. B* **44**, 12066–12069 (1991)
- [41] Thole, B., Carra, P., Sette, F. & van der Laan, G., "X-ray circular dichroism as a probe of orbital magnetization," *Phys. Rev. Lett.* **68**, 1943–1946 (1992)
- [42] Stamm, C., Kachel, T., Pontius, N., Mitzner, R., Quast, T., Holldack, K., Khan, S., Lupulescu, C., Aziz, E. E., Wietstruk, M., Dürr, H. a. & Eberhardt, W., "Femtosecond modification of electron localization and transfer of angular momentum in nickel.." *Nature Materials* **6**, 740–3 (2007)
- [43] Braicovich, L. & van der Laan, G., "Rationale for femtosecond magnetism explored with x-ray core-hole excitation," *Phys. Rev. B* **78**, 174421 (2008)
- [44] Zutíć, I., Fabian, J. & Sarma, S. D., "Spintronics: Fundamentals and applications," *Rev. Mod. Phys.* **76**, 323 (2004)
- [45] *Solid-State Photoemission and Related Methods: Theory and Experiment*, edited by Schattke, W. & Van Hove, M. A. (Wiley-VCH Verlag GmbH, Weinheim, Germany, 2003) ISBN 9783527602506, <http://doi.wiley.com/10.1002/9783527602506>
- [46] Hüfner, S., *Photoelectron Spectroscopy* (Springer Verlag, Berlin Heidelberg New York, 1995)
- [47] *Photoemission and the electronic properties of surfaces*, edited by Feuerbacher, B., Fitton, B. & Willis, R. F. (John Wiley & Sons, 1978)
- [48] Damascelli, A., Hussain, Z. & Shen, Z.-X., "Angle-resolved photoemission studies of the cuprate superconductors," *Rev. Mod. Phys.* **75**, 473–541 (2003)
- [49] Yusof, Z., Wells, B., Valla, T., Johnson, P., Fedorov, A., Li, Q., Loureiro, S. & Cava, R., "Angle-resolved photoemission study of the metal-insulator transition in bismuth cobaltates," *Phys. Rev. B* **76**, 165115 (2007)
- [50] Bostwick, A., Emtsev, K. V., Horn, K., Huwald, E. & Ley, L., "Photoemission Studies of Graphene on SiC : Growth , Interface , and Electronic Structure," *Advances in Solid State Physics* **170**, 159–170 (2008)
- [51] Bostwick, A., Ohta, T., McChesney, J. L., Seyller, T., Horn, K. & Rotenberg, E., "Band structure and many body effects in graphene," *The European Physical Journal Special Topics* **148**, 5–13 (2007)
- [52] Seyller, T., Bostwick, A., Emtsev, K. V., Horn, K., Ley, L., McChesney, J. L., Ohta, T., Riley, J. D., Rotenberg, E. & Speck, F., "Epitaxial graphene: a new material," *physica status solidi (b)* **245**, 1436–1446 (2008)
- [53] Barke, I., Zheng, F., Rügheimer, T. K. & Himpfel, F. J., "Experimental Evidence for Spin-Split Bands in a One-Dimensional Chain Structure," *Phys. Rev. Lett.* **97**, 1–4 (2006)
- [54] Crain, J. N., Kirakosian, A., Altmann, K. N., Bromberger, C., Erwin, S. C., McChesney, J. L., Lin, J.-L. & Himpfel, F. J., "Fractional Band Filling in an Atomic Chain Structure," *Phys. Rev. Lett.* **90**, 1–4 (2003)

- [55] Crain, J., Altmann, K., Bromberger, C. & Himpsel, F., "Fermi surfaces of surface states on Si(111)-Ag, Au," *Phys. Rev. B* **66**, 1–8 (2002)
- [56] Mahan, G. D. & Plummer, E. W., "Many-Body Effects in Photoemission," in *Handbook of Surf. Sci. Vol. 2: Electronic Structure*, edited by Horn, K. & Scheffler, M. (Elsevier, Amsterdam, 2000) Chap. 14, ISBN 0-444-89291-5
- [57] Pendry, J., "Theory of photoemission," *Surf. Sci.* **57**, 679–705 (1976)
- [58] Schattke, W., Van Hove, M. A., Garcia De Abajo, F. J., Diez Muino, R. & Mannella, N., "Overview of core and valence photoemission," in *Solid-State Photoemission and Related Methods: Theory and Experiment*, edited by Schattke, W. & Van Hove, M. A. (Wiley-VCH, 2003) Chap. 2, pp. 50–115, ISBN 3-527-40334-5
- [59] Band, Y. B., *Light and matter : electromagnetism, optics, spectroscopy and lasers* (Wiley, 2006) ISBN 978-0-471-89930-3
- [60] Wöhlecke, M. & Borstel, G., "Light-induced electron-spin polarization in cubic crystals," *Phys. Rev. B* **23**, 980 – 985 (1981)
- [61] Borstel, G. & Wöhlecke, M., "Spin polarization of photoelectrons emitted from nonmagnetic solids," *Phys. Rev. B* **26**, 1148–1155 (1982)
- [62] Schönhense, G., "Circular Dichroism and Spin Polarization in Photoemission from Adsorbates and Non-Magnetic Solids," *Physica Scripta* **T31**, 255–275 (1990)
- [63] Henk, J., Scheunemann, T., Halilov, S. V. & Feder, R., "Magnetic dichroism and electron spin polarization in photoemission: analytical results," *J. Phys. Cond. Matter* **8**, 47–65 (1996)
- [64] Kessler, J., *Polarized Electrons* (Springer Verlag, Berlin, 1985)
- [65] Kirschner, J., *Polarized Electrons at Surfaces* (Springer Verlag, Berlin, 1985)
- [66] Johnson, P. D., "Spin-polarized photoemission," *Rep. Prog. Phys.* **60**, 1217–1304 (1997)
- [67] Dil, J. H., "Spin and angle resolved photoemission on non-magnetic low-dimensional systems," *J. Phys. Cond. Matter* **21**, 403001 (2009)
- [68] Schneider, C. M. & Kirschner, J., "Spin- and angle-resolved photoelectron spectroscopy from solid surfaces with circularly polarized light," *Critical Reviews in Solid State and Materials Sciences* **20**, 179–283 (1995)
- [69] Siegmann, H. C., Meier, F., Erbudak, M. & Landolt, M., "Spin-Polarized Electrons in Solid-State Physics," in *Advances in Electronics and Electron Physics Vol. 62*, Vol. Volume 62, edited by Hawkes, P. W. (Academic Press, 1984) pp. 1–99, ISBN 0065-2539, <http://www.sciencedirect.com/science/article/B94TD-4S98HN9-6/2/4548e1bc3c954e098f8ef79fd4f38f0a>
- [70] Schneider, C. M., de Miguel, J. J., Bressler, P., Garbe, J., Ferrer, S., Miranda, R. & Kirschner, J., "Ferromagnetism in epitaxial transition metal films," *Le Journal de Physique Colloques* **49**, 1657–1658 (1988)
- [71] Meier, F., Dil, J. H. & Osterwalder, J., "Measuring spin polarization vectors in angle-resolved photoemission spectroscopy," *New Journal of Physics* **11**, 125008 (2009)
- [72] Weinelt, M., Schmidt, A. B., Pickel, M. & Donath, M., "Spin-Dependent Relaxation of Photoexcited Electrons at Surfaces of 3d Ferromagnets," in *Dynamics at Solid State Surfaces and Interfaces: Current Developments*, Vol. 1, edited by Bovensiepen, U., Petek, H. & Wolf, M. (Wiley-VCH, Weinheim, 2010) pp. 19–22, ISBN 9783527409372

- [73] Pierce, D. T., Celotta, R. J., Kelley, M. H. & Unguris, J., "Electron spin polarization analyzers for use with synchrotron radiation," *Nucl. Instr. Meth. A* **266**, 550–559 (1988)
- [74] Getzlaff, M., Heidemann, B., Bansmann, J., Westphal, C. & Schönhense, G., "A variable-angle electron spin polarization detection system," *Rev. Sci. Instr.* **69**, 3913–3923 (1998)
- [75] Yu, D., Math, C., Meier, M., Escher, M., Rangelov, G. & Donath, M., "Characterisation and application of a SPLEED-based spin polarisation analyser," *Surf. Sci.* **601**, 5803–5808 (2007)
- [76] Tamura, E. & Feder, R., "Theory of Spin-Polarized Secondary-Electron Emission from Ferromagnets," *Phys. Rev. Lett.* **57**, 759–761 (1986)
- [77] Tillmann, D., Thiel, R. & Kisker, E., "Very-low-energy spin-polarized electron diffraction from Fe(001)," *Z. Phys. B* **77**, 1–2 (1989)
- [78] Bertacco, R. & Ciccacci, F., "Oxygen-induced enhancement of the spin-dependent effects in electron spectroscopies of Fe(001)," *Phys. Rev. B* **59**, 4207–4210 (1999)
- [79] Schneider, C. M. & Schönhense, G., "Investigating surface magnetism by means of photoexcitation electron emission microscopy," *Rep. Prog. Phys.* **65**, 1785–1839 (2002)
- [80] Henk, J., Niklasson, A. & Johansson, B., "Multiple-scattering theoretical approach to magnetic dichroism and spin polarization in angle-resolved core-level photoemission," *Phys. Rev. B* **59**, 13986–14000 (1999)
- [81] Chiang, C.-T., *Spin and magnetization dependent two-photon photoemission from ultrathin ferromagnetic cobalt films*, Ph.D. thesis, Martin-Luther-Universität Halle (2011)
- [82] Einstein, A., "Über einen die Erzeugung und Verwandlung des Lichtes betreffenden heuristischen Gesichtspunkt [AdP 17, 132 (1905)]," *Annalen der Physik* **14**, 164–181 (2005)
- [83] Göppert-Mayer, M., "Über Elementarakte mit zwei Quantensprüngen," *Annalen der Physik* **401**, 273–294 (1931)
- [84] Göppert-Mayer, M., "Elementary processes with two quantum transitions," *Annalen der Physik* **18**, 466–479 (2009)
- [85] Teich, M., Schroeder, J. & Wolga, G., "Double-Quantum Photoelectric Emission from Sodium Metal," *Phys. Rev. Lett.* **13**, 611–614 (1964)
- [86] Gruebele, M. & Zewail, A. H., "Ultrafast Reaction Dynamics," *Physics Today* **43**, 24 (1990)
- [87] Brabec, T. & Krausz, F., "Intense few-cycle laser fields: Frontiers of nonlinear optics," *Rev. Mod. Phys.* **72**, 545–591 (2000)
- [88] Krausz, F. & Ivanov, M., "Attosecond physics," *Rev. Mod. Phys.* **81**, 163–234 (2009)
- [89] Kampfrath, T., Sell, A., Klatt, G., Pashkin, A., Mährlein, S., Dekorsy, T., Wolf, M., Fiebig, M., Leitenstorfer, A. & Huber, R., "Coherent terahertz control of antiferromagnetic spin waves," *Nature Photonics* **5**, 31–34 (2011)
- [90] Th. Fauster, "Time Resolved Two-Photon Photoemission," in *Solid-State Photoemission and Related Methods: Theory and Experiment*, edited by Schattke, W. & van Hove, M. (Wiley-VCH, 2003) Chap. 8, pp. 247–268, ISBN 3-527-40334-5
- [91] Weinelt, M., "Time-resolved two-photon photoemission from metal surfaces," *J. Phys. Cond. Matter* **14**, R1099–R1141 (2002)

- [92] Petek, H. & Ogawa, S., "Femtosecond Time-resolved Two-Photon Photoemission Studies of Electron Dynamics in Metals," *Prog. Surf. Sci.* **56**, 239 (1997)
- [93] Echenique, P. M. & Pendry, J. B., "The existence and detection of Rydberg states at surfaces," *J. Phys. C: Solid State Physics* **11**, 2065–2075 (1978)
- [94] Steinmann, W., "Two-Photon Photoemission Spectroscopy of Electronic States at Metal Surfaces," *physica status solidi (b)* **192**, 339–356 (1995)
- [95] Höfer, U., "Time-Resolved Coherent Photoelectron Spectroscopy of Quantized Electronic States on Metal Surfaces," *Science* **277**, 1480–1482 (1997)
- [96] Weinelt, M., Schmidt, A. B., Pickel, M. & Donath, M., "Spin-polarized image-potential-state electrons as ultrafast magnetic sensors in front of ferromagnetic surfaces," *Prog. Surf. Sci.* **82**, 388–406 (2007)
- [97] Fauster, T., "Electron Dynamics in Image Potential States at Metal Surfaces," in *Dynamics at Solid State Surface and Interfaces Vol.1: Current Developments*, Vol. 1, edited by Bovensiepen, U., Petek, H. & Wolf, M. (Wiley, 2010) pp. 53–73, ISBN 978-3-527-40937-2
- [98] Blum, K., *Density Matrix Theory and Applications*, 2nd ed. (Plenum Press, New York, 1996) <http://lccn.loc.gov/96021443>
- [99] Mukamel, S., *Principles of Nonlinear Optical Spectroscopy* (Oxford University Press, New York, 1995) ISBN 0195092783, <http://lccn.loc.gov/94010792>
- [100] Boyd, R., *Nonlinear Optics*, 3rd ed. (Academic Press, Amsterdam Boston, 2008) <http://lccn.loc.gov/2008271820>
- [101] Loudon, R., *The Quantum Theory of Light*, 3rd ed. (Oxford University Press, Oxford, New York, 2000) ISBN 9780198501763, <http://lccn.loc.gov/2001265846>
- [102] Letokhov, V. S. & Chebotayev, V. P., *Nonlinear Laser Spectroscopy* (Springer Verlag, Berlin Heidelberg New York, 1977)
- [103] Knoesel, E., Hotzel, A. & Wolf, M., "Temperature dependence of surface state lifetimes, dephasing rates and binding energies on Cu(111) studied with time-resolved photoemission," *J. Electron Spectr. Rel. Phenom.* **88-91**, 577–584 (1998)
- [104] Ueba, H. & Mii, T., "Theory of energy- and time-resolved two-photon photoemission from metal surfaces - influence of pulse duration and excitation condition," *Appl. Phys. A* **71**, 537–545 (2000)
- [105] Weida, M. J., Ogawa, S., Nagano, H. & Petek, H., "Ultrafast interferometric pump - probe correlation measurements in systems with broadened bands or continua," *J. Opt. Soc. Am. B* **17**, 1443 (2000)
- [106] Ramakrishna, S. & Seideman, T., "Coherence spectroscopy in dissipative media: a Liouville space pathway approach.." *J. Chem. Phys.* **122**, 84502 (2005)
- [107] Pontius, N., Sametoglu, V. & Petek, H., "Simulation of two-photon photoemission from the bulk sp-bands of Ag(111)," *Phys. Rev. B* **72**, 115105 (2005)
- [108] Mershdorf, M., Kennerknecht, C. & Pfeiffer, W., "Collective and single-particle dynamics in time-resolved two-photon photoemission," *Phys. Rev. B* **70**, 193401 (2004)
- [109] Wolf, M., Hotzel, A., Knoesel, E. & Velic, D., "Direct and indirect excitation mechanisms in two-photon photoemission spectroscopy of Cu(111) and CO/Cu(111)," *Phys. Rev. B* **59**, 5926–5935 (1999)

- [110] Meier, T., Thomas, P. & Koch, S. W., *Coherent Semiconductor Optics* (Springer Berlin Heidelberg, Berlin, Heidelberg, 2007) ISBN 978-3-540-32554-3, <http://www.springerlink.com/index/10.1007/978-3-540-32555-0>
- [111] Schmidt, A. B., Pickel, M., Donath, M., Buczek, P., Ernst, A., Zhukov, V., Echenique, P., Sandratskii, L., Chulkov, E. & Weinelt, M., "Ultrafast Magnon Generation in an Fe Film on Cu(100)," *Phys. Rev. Lett.* **105**, 197401 (2010)
- [112] Aeschlimann, M., Bauer, M., Pawlik, S., Weber, W., Burgermeister, R., Oberli, D. & Siegmann, H., "Ultrafast Spin-Dependent Electron Dynamics in fcc Co," *Phys. Rev. Lett.* **79**, 5158–5161 (1997)
- [113] Quinn, J. & Ferrell, R., "Electron Self-Energy Approach to Correlation in a Degenerate Electron Gas," *Phys. Rev.* **112**, 812–827 (1958)
- [114] Echenique, P., "Decay of electronic excitations at metal surfaces," *Surf. Sci. Reports* **52**, 219–317 (2004)
- [115] Zhukov, V. P. & Chulkov, E. V., "The femtosecond dynamics of electrons in metals," *Physics-Uspekhi* **52**, 105–136 (2009)
- [116] Knorren, R., Bennemann, K., Burgermeister, R. & Aeschlimann, M., "Dynamics of excited electrons in copper and ferromagnetic transition metals: Theory and experiment," *Phys. Rev. B* **61**, 9427–9440 (2000)
- [117] Goris, A., Döbrich, K. M., Panzer, I., Schmidt, A. B., Donath, M. & Weinelt, M., "Role of spin-flip exchange scattering for hot-electron lifetimes in cobalt," *Phys. Rev. Lett.* **107**, 026601 (2011)
- [118] Cinchetti, M., Sánchez Albaneda, M., Hoffmann, D., Roth, T., Wüstenberg, J.-P., Krauß, M., Andreyev, O., Schneider, H. C., Bauer, M. & Aeschlimann, M., "Spin-Flip Processes and Ultrafast Magnetization Dynamics in Co: Unifying the Microscopic and Macroscopic View of Femtosecond Magnetism," *Phys. Rev. Lett.* **97**, 177201 (2006)
- [119] Steil, D., Alebrand, S., Roth, T., Krauß, M., Kubota, T., Oogane, M., Ando, Y., Schneider, H., Aeschlimann, M. & Cinchetti, M., "Band-Structure-Dependent Demagnetization in the Heusler Alloy $\text{Co}_{2}\text{Mn}_{1-x}\text{Fe}_{x}\text{Si}$," *Phys. Rev. Lett.* **105**, 17–20 (2010)
- [120] Schmidt, A., Pickel, M., Wiemhöfer, M., Donath, M. & Weinelt, M., "Spin-Dependent Electron Dynamics in Front of a Ferromagnetic Surface," *Phys. Rev. Lett.* **95**, 107402 (2005)
- [121] Thomann, U., Shumay, I., Weinelt, M. & Fauster, T., "Spin splitting of image-potential states on fcc Fe/Cu(100)," *Appl. Phys. B* **68**, 531–536 (1999)
- [122] Schmidt, A. B., Pickel, M., Allmers, T., Budke, M., Braun, J., Weinelt, M. & Donath, M., "Surface electronic structure of fcc Co films: a combined spin-resolved one- and two-photon-photoemission study," *J. Phys. D: Appl. Phys.* **41**, 164003 (2008)
- [123] Pickel, M., Schmidt, A., Giesen, F., Braun, J., Minár, J., Ebert, H., Donath, M. & Weinelt, M., "Spin-Orbit Hybridization Points in the Face-Centered-Cubic Cobalt Band Structure," *Phys. Rev. Lett.* **101**, 66402 (2008)
- [124] Cinchetti, M., Heimer, K., Wüstenberg, J.-P., Andreyev, O., Bauer, M., Lach, S., Ziegler, C., Gao, Y. & Aeschlimann, M., "Determination of spin injection and transport in a ferromagnet/organic semiconductor heterojunction by two-photon photoemission.." *Nature Materials* **8**, 115–9 (2009)
- [125] Scholl, A., Baumgarten, L., Jacquemin, R. & Eberhardt, W., "Ultrafast Spin Dynamics of Ferromagnetic Thin Films Observed by fs Spin-Resolved Two-Photon Photoemission," *Phys. Rev. Lett.* **79**, 5146 LP – 5149 (1997)
- [126] Muiño, R. D., Sánchez-Portal, D., Silkin, V. M., Chulkov, E. V. & Echenique, P. M., "Surface chemistry special feature: Time-dependent electron phenomena at surfaces.." *Proc. Natl. Acad. Sci. USA* **108**, 971–6 (2011)

- [127] Schoenlein, R. W., Fujimoto, J. G., Eesley, G. L. & Capehart, T. W., "Femtosecond Studies of Image-Potential Dynamics in Metals," *Phys. Rev. Lett.* **61**, 2596–2599 (1988)
- [128] Luan, S., Hippler, R., Schwier, H. & Lutz, H. O., "Electron Emission from Polycrystalline Copper Surfaces by Multi-Photon Absorption," *Europhys. Lett.* **9**, 489–494 (1989)
- [129] Fann, W. S., Storz, R. & Bokor, J., "Observation of above-threshold multiphoton photoelectric emission from image-potential surface states," *Phys. Rev. B* **44**, 10980–10982 (1991)
- [130] Irvine, S. E., Dechant, A. & Elezzabi, A. Y., "Generation of {0.4-keV} Femtosecond Electron Pulses using Impulsively Excited Surface Plasmons," *Phys. Rev. Lett.* **93**, 184801 (2004)
- [131] Kinoshita, I., Anazawa, T. & Matsumoto, Y., "Surface and image-potential states on Pt(111) probed by two- and three-photon photoemission," *Chem. Phys. Lett.* **259**, 445–450 (1996)
- [132] Ogawa, S. & Petek, H., "Two-photon photoemission spectroscopy at clean and oxidized Cu(110) and Cu(100) surfaces," *Surf. Sci.* **363**, 313–320 (1996)
- [133] Lehmann, J., Merschdorf, M., Thon, A., Voll, S. & Pfeiffer, W., "Properties and dynamics of the image potential states on graphite investigated by multiphoton photoemission spectroscopy," *Phys. Rev. B* **60**, 17037–17045 (1999)
- [134] Banfi, F., Giannetti, C., Ferrini, G., Galimberti, G., Pagliara, S., Fausti, D. & Parmigiani, E., "Experimental Evidence of Above-Threshold Photoemission in Solids," *Phys. Rev. Lett.* **94**, 37601 (2005)
- [135] Miaja-Avila, L., Yin, J., Backus, S., Saathoff, G., Aeschlimann, M., Murnane, M. & Kapteyn, H., "Ultrafast studies of electronic processes at surfaces using the laser-assisted photoelectric effect with long-wavelength dressing light," *Phys. Rev. A* **79**, 30901 (2009)
- [136] Bisio, F., Winkelmann, A., Lin, W.-C., Chiang, C.-T., Nývlt, M., Petek, H. & Kirschner, J., "Band structure effects in surface second harmonic generation: The case of Cu(001)," *Phys. Rev. B* **80**, 125432 (2009)
- [137] Ferrini, G., Banfi, F., Giannetti, C. & Parmigiani, E., "Non-linear electron photoemission from metals with ultrashort pulses," *Nucl. Instr. Meth. A* **601**, 123–131 (2009)
- [138] Kupersztynch, J., Monchicourt, P. & Raynaud, M., "Ponderomotive Acceleration of Photoelectrons in Surface-Plasmon-Assisted Multiphoton Photoelectric Emission," *Phys. Rev. Lett.* **86**, 5180–5183 (2001)
- [139] Koralek, J. D., Douglas, J. F., Plumb, N. C., Griffith, J. D., Cundiff, S. T., Kapteyn, H. C., Murnane, M. M. & Desauter, D. S., "Experimental setup for low-energy laser-based angle resolved photoemission spectroscopy." *Rev. Sci. Instr.* **78**, 053905 (2007)
- [140] Liu, G., Wang, G., Zhu, Y., Zhang, H., Zhang, G., Wang, X., Zhou, Y., Zhang, W., Liu, H., Zhao, L., Meng, J., Dong, X., Chen, C., Xu, Z. & Zhou, X. J., "Development of a vacuum ultraviolet laser-based angle-resolved photoemission system with a superhigh energy resolution better than 1 meV." *Rev. Sci. Instr.* **79**, 023105 (2008)
- [141] Bertacco, R., Onofrio, D. & Ciccacci, E., "A novel electron spin-polarization detector with very large analyzing power," *Rev. Sci. Instr.* **70**, 3572–3576 (1999)
- [142] Bertacco, R., Marcon, M., Trezzi, G., Duò, L. & Ciccacci, E., "Spin and energy analysis of electron beams: Coupling a polarimeter based on exchange scattering to a hemispherical analyzer," *Rev. Sci. Instr.* **73**, 3867–3871 (2002)
- [143] Jungblut, R., Roth, C., Hillebrecht, F. U. & Kisker, E., "Spin-polarized electron spectroscopy as a combined chemical and magnetic probe," *Surf. Sci.* **269-270**, 615–621 (1992)

- [144] Hillebrecht, F. U., Jungblut, R. M., Wiebusch, L., Roth, C., Rose, H. B., Knabben, D., Bethke, C., Weber, N. B., Manderla, S., Rosowski, U. & Kisker, E., "High-efficiency spin polarimetry by very-low-energy electron scattering from Fe(100) for spin-resolved photoemission," *Rev. Sci. Instr.* **73**, 1229 (2002)
- [145] Okuda, T., Takeichi, Y., Maeda, Y., Harasawa, A., Matsuda, I., Kinoshita, T. & Kakizaki, A., "A new spin-polarized photoemission spectrometer with very high efficiency and energy resolution.." *Rev. Sci. Instr.* **79**, 123117 (2008)
- [146] Jozwiak, C., Graf, J., Lebedev, G., Andresen, N., Schmid, A. K., Fedorov, A. V., El Gabaly, F., Wan, W., Lanzara, A. & Hussain, Z., "A high-efficiency spin-resolved photoemission spectrometer combining time-of-flight spectroscopy with exchange-scattering polarimetry.." *Rev. Sci. Instr.* **81**, 053904 (2010)
- [147] "VGScienta," www.vgscienta.com
- [148] "SPECS GmbH," www.specs.de
- [149] Eastman, D. E., Donelon, J. J., Hien, N. C. & Himpfel, F. J., "An ellipsoidal mirror display analyzer system for electron energy and angular measurements," *Nucl. Instr. Meth.* **172**, 327–336 (1980)
- [150] Nishimoto, H., Daimon, H., Suga, S., Tezuka, Y., Ino, S., Kato, I., Zenitani, F. & Soezima, H., "Simultaneous angle-resolved measurement of the band structure of single crystal graphite by an improved two-dimensional display analyzer," *Rev. Sci. Instr.* **64**, 2857 (1993)
- [151] Krömker, B., Escher, M., Funnemann, D., Hartung, D., Engelhard, H. & Kirschner, J., "Development of a momentum microscope for time resolved band structure imaging.." *Rev. Sci. Instr.* **79**, 053702 (2008)
- [152] Kotsugi, M., Kuch, W., Offi, F., Chelaru, L. I. & Kirschner, J., "Microspectroscopic two-dimensional Fermi surface mapping using a photoelectron emission microscope," *Rev. Sci. Instr.* **74**, 2754 (2003)
- [153] Escher, M., Winkler, K., Renault, O. & Barrett, N., "Applications of high lateral and energy resolution imaging XPS with a double hemispherical analyser based spectromicroscope," *J. Electron. Spec. Rel. Phenom.* **178-179**, 303–316 (2010)
- [154] Renault, O., "High-resolution XPS spectromicroscopy," *Surf. Interf. Anal.* **42**, 816–825 (2010)
- [155] Eckardt, H., Fritsche, L. & Noffke, J., "Self-consistent relativistic band structure of the noble metals," *J. Phys. F: Metal Physics* **14**, 97–112 (1984)
- [156] Thörner, G., Borstel, G., Dose, V. & Rogozik, J., "Unoccupied electronic surface resonance at {Cu(001)}," *Surf. Sci.* **157**, L379 – L383 (1985)
- [157] Bisio, F., Nývlt, M., Franta, J., Petek, H. & Kirschner, J., "Mechanisms of high-order perturbative photoemission from Cu(001)," *Phys. Rev. Lett.* **96**, 87601 (2006)
- [158] Winkelmann, A., Lin, W.-C., Chiang, C.-T., Bisio, F., Petek, H. & Kirschner, J., "Resonant coherent three-photon photoemission from Cu(001)," *Phys. Rev. B* **80**, 155128 (2009)
- [159] Strocov, V., Claessen, R., Aryasetiawan, F., Blaha, P. & Nilsson, P., "Band- and k-dependent self-energy effects in the unoccupied and occupied quasiparticle band structure of Cu," *Phys. Rev. B* **66**, 195104 (2002)
- [160] Strocov, V., Claessen, R., Nicolay, G., Hüfner, S., Kimura, A., Harasawa, A., Shin, S., Kakizaki, A., Starnberg, H., Nilsson, P. & Blaha, P., "Three-dimensional band mapping by angle-dependent very-low-energy electron diffraction and photoemission: Methodology and application to Cu," *Phys. Rev. B* **63**, 205108 (2001)
- [161] Schattke, W., Krasovskii, E. E., Díez Muño, R. & Echenique, P. M., "Direct resolution of unoccupied states in solids via two-photon photoemission," *Phys. Rev. B* **78**, 155314 (2008)

- [162] Schneider, C. M., Demiguel, J. J., Bressler, P., Schuster, P., Miranda, R. & Kirschner, J., "Spin- and angle-resolved photoemission from single crystals and epitaxial films using circularly polarized synchrotron radiation," *J. Electr. Spec. Rel. Phenom.* **51**, 263–274 (1990)
- [163] Courths, R., "Photoemission experiments on copper," *Physics Reports* **112**, 53–171 (1984)
- [164] Petek, H., Nagano, H. & Ogawa, S., "Hole Decoherence of d Bands in Copper," *Phys. Rev. Lett.* **83**, 832 (1999)
- [165] Strocov, V., "Intrinsic accuracy in 3-dimensional photoemission band mapping," *J. Electron. Spec. Rel. Phenom.* **130**, 65–78 (2003)
- [166] Hao, Z., Dadap, J., Knox, K., Yilmaz, M., Zaki, N., Johnson, P. & Osgood, R., "Nonequilibrium Band Mapping of Unoccupied Bulk States below the Vacuum Level by Two-Photon Photoemission," *Phys. Rev. Lett.* **105**, 017602 (2010)
- [167] Gdde, J., Rohleder, M., Meier, T., Koch, S. W. & Hfer, U., "Time-Resolved Investigation of Coherently Controlled Electric Currents at a Metal Surface," *Science* **318**, 1287–1291 (2007)
- [168] Gauyacq, J. P. & Kazansky, A. K., "Modelling of interferometric multiphoton photoemission," *Appl. Phys. A* **89**, 517–523 (2007)
- [169] Kuch, W. & Schneider, C. M., "Magnetic dichroism in valence band photoemission," *Rep. Prog. Phys.* **64**, 147–204 (2001)
- [170] Schneider, C. M., Garbe, J., Bethke, K. & Kirschner, J., "Symmetry-dependent alignment of the electron-spin polarization vector due to electronic band hybridization observed in photoemission from Ag(100)," *Phys. Rev. B* **39**, 1031–1035 (1989)
- [171] Hoesch, M., Muntwiler, M., Petrov, V., Hengsberger, M., Patthey, L., Shi, M., Falub, M., Greber, T. & Osterwalder, J., "Spin structure of the Shockley surface state on Au(111)," *Phys. Rev. B* **69**, 241401 (2004)
- [172] Henk, J., "Spin polarization of the L-gap surface states on Au(111)," *Phys. Rev. B* **68**, 165416 (2003)
- [173] Henk, J., Hoesch, M., Osterwalder, J., Ernst, A. & Bruno, P., "Spin orbit coupling in the L-gap surface states of Au(111): spin-resolved photoemission experiments and first-principles calculations," *J. Phys. Cond. Matter* **16**, 7581–7597 (2004)
- [174] Hochstrasser, M., Tobin, J., Rotenberg, E. & Kevan, S., "Spin-Resolved Photoemission of Surface States of W(110)-(1x1)H," *Phys. Rev. Lett.* **89**, 216802 (2002)
- [175] Koroteev, Y., Bihlmayer, G., Gayone, J., Chulkov, E., Blgel, S., Echenique, P. & Hofmann, P., "Strong Spin-Orbit Splitting on Bi Surfaces," *Phys. Rev. Lett.* **93**, 046403 (2004)
- [176] Hofmann, P., "The surfaces of bismuth: Structural and electronic properties," *Prog. Surf. Sci.* **81**, 191–245 (2006)
- [177] Hirahara, T., Miyamoto, K., Matsuda, I., Kadono, T., Kimura, A., Nagao, T., Bihlmayer, G., Chulkov, E., Qiao, S., Shimada, K., Namatame, H., Taniguchi, M. & Hasegawa, S., "Direct observation of spin splitting in bismuth surface states," *Phys. Rev. B* **76**, 153305 (2007)
- [178] Varykhalov, A., Snchez-Barriga, J., Shikin, A., Gudat, W., Eberhardt, W. & Rader, O., "Quantum Cavity for Spin due to Spin-Orbit Interaction at a Metal Boundary," *Phys. Rev. Lett.* **101**, 256601 (2008)
- [179] Shikin, A., Varykhalov, A., Prudnikova, G., Usachov, D., Adamchuk, V., Yamada, Y., Riley, J. & Rader, O., "Origin of Spin-Orbit Splitting for Monolayers of Au and Ag on W(110) and Mo(110)," *Phys. Rev. Lett.* **100**, 057601 (2008)

- [180] Krupin, O., Bihlmayer, G., Starke, K., Gorovikov, S., Prieto, J., Döbrich, K., Blügel, S. & Kaindl, G., "Rashba effect at magnetic metal surfaces," *Phys. Rev. B* **71**, 201403 (2005)
- [181] Dedkov, Y., Fonin, M., Rüdiger, U. & Laubschat, C., "Rashba Effect in the Graphene/Ni(111) System," *Phys. Rev. Lett.* **100**, 107602 (2008)
- [182] Abdelouahed, S., Ernst, A., Henk, J., Maznichenko, I. & Mertig, I., "Spin-split electronic states in graphene: Effects due to lattice deformation, Rashba effect, and adatoms by first principles," *Phys. Rev. B* **82**, 125424 (2010)
- [183] Varykhalov, A., Sánchez-Barriga, J., Shikin, A., Biswas, C., Vescovo, E., Rybkin, A., Marchenko, D. & Rader, O., "Electronic and Magnetic Properties of Quasifreestanding Graphene on Ni," *Phys. Rev. Lett.* **101**, 157601 (2008)
- [184] Rader, O., Varykhalov, A., Sánchez-Barriga, J., Marchenko, D., Rybkin, A. & Shikin, A., "Is There a Rashba Effect in Graphene on 3d Ferromagnets?," *Phys. Rev. Lett.* **102**, 057602 (2009)
- [185] Varykhalov, A. & Rader, O., "Graphene grown on Co(0001) films and islands: Electronic structure and its precise magnetization dependence," *Phys. Rev. B* **80**, 035437 (2009)
- [186] Cacho, C. M., Vlaic, S., Malvestuto, M., Ressel, B., Seddon, E. A. & Parmigiani, F., "Absolute spin calibration of an electron spin polarimeter by spin-resolved photoemission from the Au(111) surface states.." *Rev. Sci. Instr.* **80**, 043904 (2009)
- [187] Meier, F., Dil, H., Lobo-Checa, J., Patthey, L. & Osterwalder, J., "Quantitative vectorial spin analysis in angle-resolved photoemission: Bi / Ag(111) and Pb/Ag(111)," *Phys. Rev. B* **77**, 165431 (2008)
- [188] Bentmann, H., Forster, F., Bihlmayer, G., Chulkov, E. V., Moreschini, L., Grioni, M. & Reinert, F., "Origin and manipulation of the Rashba splitting in surface alloys," *Europhys. Lett.* **87**, 37003 (2009)
- [189] Hengsberger, M., Baumberger, E., Neff, H., Greber, T. & Osterwalder, J., "Photoemission momentum mapping and wave function analysis of surface and bulk states on flat Cu(111) and stepped Cu(443) surfaces: A two-photon photoemission study," *Phys. Rev. B* **77**, 085425 (2008)
- [190] Mathias, S., Ruffing, A., Deicke, F., Wiesenmayer, M., Sakar, I., Bihlmayer, G., Chulkov, E. V., Koroteev, Y. M., Echenique, P. M., Bauer, M. & Aeschlimann, M., "Quantum-Well-Induced Giant Spin-Orbit Splitting," *Phys. Rev. Lett.* **104**, 066802 (2010)
- [191] Mirhosseini, H., Henk, J., Ernst, A., Ostanin, S., Chiang, C.-T., Yu, P., Winkelmann, A. & Kirschner, J., "Unconventional spin topology in surface alloys with Rashba-type spin splitting," *Phys. Rev. B* **79**, 245428 (2009)
- [192] Datta, S. & Das, B., "Electronic analog of the electro-optic modulator," *Appl. Phys. Lett.* **56**, 665 (1990)
- [193] Hild, K., Maul, J., Schönhense, G., Elmers, H., Amft, M. & Oppeneer, P., "Magnetic Circular Dichroism in Two-Photon Photoemission," *Phys. Rev. Lett.* **102**, 57207 (2009)
- [194] Yu, D., Donath, M., Braun, J. & Rangelov, G., "Spin-polarized unoccupied quantum-well states in ultrathin Co films on Cu(100)," *Phys. Rev. B* **68**, 155415 (2003)
- [195] Ortega, J., Himpfel, F., Mankey, G. & Willis, R., "Quantum-well states and magnetic coupling between ferromagnets through a noble-metal layer," *Phys. Rev. B* **47**, 1540–1552 (1993)
- [196] Chiang, C.-T., Winkelmann, A., Yu, P., Kirschner, J. & Henk, J., "Spin-orbit coupling in unoccupied quantum well states: Experiment and theory for Co/Cu(001)," *Phys. Rev. B* **81**, 115130 (2010)
- [197] Schmid, A. K. & Kirschner, J., "In situ observation of epitaxial growth of Co thin films on Cu(100)," *Ultramicroscopy* **42-44**, 483–489 (1992)

- [198] Navas, E., Schuster, P., Schneider, C. M., Kirschner, J., Cebollada, A., Ocal, C., Miranda, R., Cerda, J. & de Andres, P., "Crystallography of epitaxial face centered tetragonal Co/Cu(100) by low energy electron diffraction," *J. Magn. Magn. Mat.* **121**, 65–68 (1993)
- [199] Hirschmann, M. & Fauster, T., "Scattering of electrons on the Cu(001) surface by Co adatoms," *Appl. Phys. A* **88**, 547–554 (2007)
- [200] Fauster, T., Weinelt, M. & Höfer, U., "Quasi-elastic scattering of electrons in image-potential states," *Prog. Surf. Sci.* **82**, 224–243 (2007)
- [201] Nakagawa, T. & Yokoyama, T., "Magnetic Circular Dichroism near the Fermi Level," *Phys. Rev. Lett.* **96**, 237402 (2006)
- [202] Tusche, C., Ellguth, M., Ünal, A., Chiang, C.-T., Winkelmann, A., Krasnyuk, A., Schönhense, G. & Kirschner, J., "Spin resolved photoelectron microscopy using a two-dimensional spin-polarizing electron mirror," *Appl. Phys. Lett.* **99**, 032505 (2011)

5 Originalveröffentlichungen

5.1 Resonant coherent three-photon photoemission from Cu(001) (Reprinted with permission. Copyright 2009, American Physical Society.)	65
5.2 Band structure effects in surface second harmonic generation: The case of Cu(001) (Reprinted with permission. Copyright 2009, American Physical Society.)	75
5.3 Angle-dependent study of a direct optical transition in the sp bands of Ag(111) by one- and two-photon photoemission (Reprinted with permission. Copyright 2007, American Physical Society.)	83
5.4 Higher Order Photoemission from Metal Surfaces (Reprinted with permission. Copyright 2010, Wiley-VCH.)	95
5.5 High efficiency electron spin polarization analyzer based on exchange scattering at Fe/ W(001) (Reprinted with permission. Copyright 2008, American Institute of Physics.)	115
5.6 Ultrafast Spin Injection into Image potential states (Reprinted with permission. Copyright 2007, American Physical Society.)	121
5.7 Interferometric Control of Spin-Polarized Electron Populations at a Metal Surface Observed by Multiphoton Photoemission (Reprinted with permission. Copyright 2008, American Physical Society.)	125
5.8 Spin-polarized multi-photon photoemission and surface electronic structure of Cu(001) (Reprinted with permission. Copyright 2010, IOP and DPG.)	129
5.9 Unconventional spin topology in surface alloys with Rashba-type spin splitting (Reprinted with permission. Copyright 2009, American Physical Society.)	143
5.10 Magnetic Dichroism from Optically Excited Quantum Well States (Reprinted with permission. Copyright 2009, American Physical Society.)	149
5.11 Spin-orbit coupling in unoccupied quantum well states: Experiment and theory for Co/Cu(001) (Reprinted with permission. Copyright 2010, American Physical Society.)	153

PHYSICAL REVIEW B **80**, 155128 (2009)**Resonant coherent three-photon photoemission from Cu(001)**Aimo Winkelmann,^{1,*} Wen-Chin Lin,¹ Cheng-Tien Chiang,¹ Francesco Bisio,^{2,3} Hrvoje Petek,⁴ and Jürgen Kirschner¹¹Max-Planck Institut für Mikrostrukturphysik, Weinberg 2, D-06120 Halle (Saale), Germany²CNISM, Sede consorziata di Genova, via Dodecaneso 33, I-16146 Genova, Italy³CNR-INFN LAMIA, Corso Perrone 24, I-16152 Genova, Italy⁴Department of Physics and Astronomy, University of Pittsburgh, Pittsburgh, Pennsylvania 15260, USA

(Received 23 July 2009; revised manuscript received 22 September 2009; published 20 October 2009)

We demonstrate the contribution of coherent excitation pathways in three-photon photoemission from Cu(001). We identify separate peaks in the photoelectron spectra as originating from two specific Cu *d* bands that are excited at different *k* points via the *same* unoccupied image-potential state. By model calculations we show that our experimental observations impose lower limits on the relevant Cu *d*-hole dephasing time on the order of 10–20 fs. Our findings suggest extensions to future studies in electronic structure mapping with tunable laboratory and free-electron laser sources, exploiting possible multiphoton resonances between occupied bulk and unoccupied surface states.

DOI: 10.1103/PhysRevB.80.155128

PACS number(s): 79.60.Bm

I. INTRODUCTION

The effect of quantized energy absorption by electrons¹ is at the heart of angle-resolved photoemission spectroscopy (ARPES) as the most general and widely employed method for mapping the occupied electronic structure in solids.^{2,3} In the simplest picture, the incident radiation induces transitions of electrons from occupied to unoccupied single-particle states separated by the photon energy. By invoking the laws of energy and momentum conservation, the photoemission process can be applied to map the occupied band structure of solids by detecting the photoelectrons in final states above the vacuum barrier.

A generalization of the photoelectric effect can be realized by multiphoton processes induced by ultrashort laser pulses of high intensity, where the occupied initial states, the unoccupied intermediate states, and the coupling between them play a central role. Especially the technique of time-resolved two-photon photoemission (2PPE) has been used to gain information on the decay rates of electronic populations and on the survival times of coherent superpositions of states (“dephasing times”).^{4–6} Interferometric 2PPE measurements⁶ have been used to determine dephasing times of quantum coherence at metal surfaces^{7–9} and recently the control of directional surface currents was also demonstrated.¹⁰ Also, interference in 2PPE can be observed directly if several close-lying unoccupied states are excited coherently. The 2PPE yield then can show quantum beats¹¹ and the decay of these beats allows us to investigate the dephasing process between the various states due to intrinsic properties of solids and scattering with the impurities.¹² More indirectly, dephasing can also be estimated from frequency domain measurements via its influence on the measured linewidths.⁵ The decisive role of dephasing processes in 2PPE is also seen by the fact that in the total absence of dephasing, under certain circumstances intermediate surface states should not be observed at all because of destructive interference between different excitation pathways.^{13,14}

As multiphoton photoemission experiments depend sensitively on the wave functions and energy levels of the states that are involved in the excitation, they are expected to provide band-structure information about occupied and unoc-

cupied states in solids with high precision.¹⁵ Because photons in the visible and UV range cannot transfer significant momentum to the electrons, such multiphoton resonances effectively proceed vertically in the electronic $E(\vec{k})$ band-structure (just as optical transitions in conventional ARPES measurements) and thus can be used to determine the separation of electronic bands at specific \vec{k} points by looking for resonances between the multiple states coupled by the incident radiation. The linewidth and intensity of the observed signals depend on the dephasing rates in the relevant states. This is why it is important to examine the implications of coherence in optically excited solid-state systems.

In this paper we report observations of coherent multiphoton photoemission that carries information about the bulk band structure of copper by resonant excitation of electronic bulk states through unoccupied intermediate surface states. In a three-photon photoemission experiment from a Cu(001) surface, we identify separate peaks in the photoelectron spectra as originating from different initial state Cu *d* bands that are resonantly excited at different photon energies via the *same* unoccupied image-potential (IP) state. The image-potential states reside at a fixed energy for a specific surface parallel momentum and thus can provide a reliable reference level. This study builds on our previous investigations where we have demonstrated that at a Cu(001) surface, three- and even four-photon photoemission (3PPE and 4PPE) processes with clear band-structure-related features are in principle observable.¹⁶ Using spin-resolved detection and circularly polarized light for excitation, we also demonstrated that the $n=1$ image-potential state on Cu(001) can be selectively coupled to two spin-orbit split *d* bands belonging to different components of the double-group symmetry¹⁷ and we showed that it is possible to control this process¹⁸ interferometrically. In this contribution, we will analyze the role of phase-preserving multiphoton excitation processes in conveying bulk band-structure information.

II. EXPERIMENTAL DETAILS

The experimental setup is the same as described before.^{16,17} Compared to the previous experiments, we used

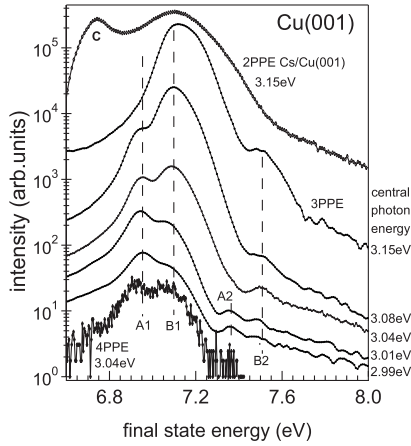
WINKELMANN *et al.*PHYSICAL REVIEW B **80**, 155128 (2009)

FIG. 1. Experimental spectra of the 3PPE resonance as a function of the central energy of the excitation pulse, p -polarized excitation (logarithmic scale). For comparison, the 2PPE spectrum from cesiated Cu(001) is shown shifted upward by $h\nu$ and the 4PPE peak is shifted downward by $h\nu$. Feature C in the 2PPE spectrum near the vacuum edge is due a background of secondary electrons which could not be further decreased. The spectra are displaced vertically for better visibility. They are not normalized with respect to the laser intensity.

the electrostatic electron energy analyzer in a higher energy resolution mode of about 50 meV as was estimated from the low-energy cutoff of the photoelectron spectra. The photoemission experiments were carried out in an ultrahigh-vacuum system (pressure $<5 \times 10^{-11}$ mbar). The ultrashort excitation pulses were provided by the frequency-doubled output of a self-built Ti:sapphire oscillator. The pulse central energy could be continuously varied in the range of $h\nu = 2.99$ – 3.15 eV by tuning the phase-matching angle of the frequency-doubling 80- μm -thick $\beta\text{-BaB}_2\text{O}_4$ crystal. At the energy of $h\nu = 3.07$ eV, the pulse length at the surface was ≤ 20 fs and the pulse energy ~ 1 nJ. A clean and ordered Cu(001) surface was prepared by standard sputtering and annealing procedures. The optical plane was aligned parallel to the [100] direction. All the experiments, unless specified, were carried out at 300 K. The electrons photoemitted along the surface normal were analyzed by a cylindrical sector analyzer (Focus CSA300).

III. RESULTS

In Fig. 1, we show experimental 3PPE spectra taken for different central energies of the exciting pulse using p -polarized excitation. We show for comparison the 2PPE part of the spectrum on top and the 4PPE part at the bottom of Fig. 1.¹⁶ For the 3PPE spectra, four peaks A1, B1, A2, and B2 can be identified. An analysis of the dominating double-peak structure A1 and B1 shows that this part of the spectrum can be fitted by the sum of two Gaussian peaks with widths (full width at half maximum) of 110 meV for (A1) and 130 meV for (B1) and a separation of 150 meV. Peak A1 is located at a final-state energy of 6.95 eV and peak B1 at

7.15 eV. Considering that the optical spectrum of the excitation pulses has a width of 170 meV, the resolution of the 3PPE spectrum well below the excitation linewidth in the three-photon absorption process is striking.

The peaks A1 and B1 obviously do not disperse noticeably with energy but only change their relative intensities. This relative change is connected to an underlying overall shift of intensity, which moves at the same rate as the photon energy $\Delta h\nu$.¹⁷ This shift with $\Delta h\nu$ can be clearly seen from the position of the high-energy wings of the observed peaks. In a (generally nonresonant) three-photon photoemission process involving states with fixed energy (i.e., not dispersing with k_{\perp}), it can be expected that the position of a peak from the initial state tunes with $3\Delta h\nu$, the first intermediate state with $2\Delta h\nu$ and the second intermediate state with $1\Delta h\nu$.¹⁹ In our case, tuning the photon energy causes the disappearance of the A2 peak for photon energies larger than 3.01 eV, by the overwhelming signal from the B1 peak. From the energy separations of 0.41 eV between A1 and A2, as well as between B1 and B2, which do not change with photon energy, we can deduce that these features are related to the $n=1$ and 2 image-potential states, respectively.⁵ As estimated from the final-state energies of peaks A1 and B1 and the known position of the $n=1$ image-potential state at 4.04 eV at $k_{\parallel}=0$,⁵ peaks A1 and B1 correspond to separations of 2.91 and 3.11 eV from the $n=1$ image-potential state, respectively.

To further illustrate the unusual features of the 3PPE spectra, in Fig. 1 we also compare 3PPE spectra with 2PPE and 4PPE spectra, which have been shifted in energy to align the photoemission peaks from the occupied d bands. The top 2PPE spectrum taken from a cesiated Cu(001) surface at 110 K shows only a broad structure without the splitting seen in 3PPE. In a previous 2PPE study of the d bands for Cs/Cu(001) with even higher electron energy resolution (30 meV) and lower temperature (35 K) the distinct splitting found in Fig. 1 could not be resolved.⁹ As will be explained in detail below, this is because 2PPE using photon energies near 3 eV is nonresonant with respect to the image-potential states. The absence of k_{\perp} selectivity that is provided by a resonance causes a reduced energy-filtering effect with respect to the initial d -band states when compared to the resonant 3PPE excitation via an intermediate IP state. In contrast, the bottom 4PPE spectrum clearly displays the spin-orbit splitting with seemingly the same resolution as the 3PPE peaks taking into account the reduced statistics due to a diminished count rate by about four orders of magnitude.¹⁶ This observation is consistent with the fact that the 4PPE process shown proceeds via the same intermediate states as the 3PPE process to which it is compared.

IV. DISCUSSION

A. Electronic band structure of copper

In order to interpret our experimental results, we show in Fig. 2 the relativistic band structure of copper for the k -space line relevant to emission along the surface normal of a Cu(001) surface (Δ line from Γ to X) according to the calculated band structure of Eckardt *et al.*²⁰ We indicate a three-

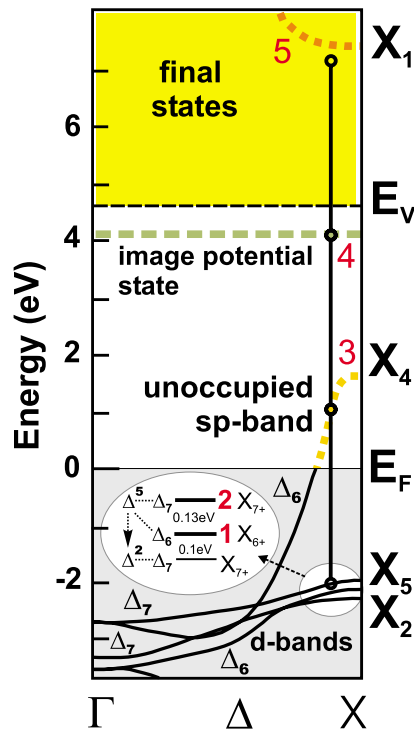


FIG. 2. (Color online) Relativistic band structure (Ref. 20) of Cu(001) with the proposed three-photon resonance for a photon energy near 3 eV. The final photoemitted states correspond to time-reversed low-energy electron diffraction states in the direction of the detector, with complex wave vectors in the band gap (Ref. 21).

photon process for photon energies near 3 eV starting from the Cu d bands via the unoccupied sp band and the $n=1$ image-potential state, which has been demonstrated previously.¹⁶ This process was shown to be very effective, leading to a 3PPE signal higher in intensity than the simultaneously observed 2PPE signal, which occurs through non-resonant pathways.

As is well known, a theoretical band structure such as shown in Fig. 2 usually does not describe experimental photoemission data quantitatively.^{22,23} Because of this, we assume in the following that the calculation still describes the *dispersion* of the bands correctly but we make the absolute values for the critical points adjustable to known experimental data. Then we try to find k -conserving resonances in the band structure as a function of photon energy. In a first approximation this is realized by shifting the involved bands according to the number of photons needed to reach the final-state energy. A strong resonance can be expected when the initial d bands, the intermediate sp bands and the image-potential state cross; this imposes very stringent conditions on the relative energy separation between the involved energy levels.

Adjusting the critical points, we took the position of X_4 at 1.8 eV (Refs. 24 and 25) and the d bands are assumed to have X_5 at -1.99 eV and X_2 at -2.18 eV.²² Due to spin-orbit coupling, the Δ^5 band is split into Δ_7 and Δ_6 bands with reported experimental splittings between 100 (Ref. 26) and

170 meV (Ref. 27) in the region of interest near the X point. For comparison, the theoretical value is 160 meV (Ref. 22) at the X point. The intermediate image-potential states are taken at 4.04 eV for $n=1$ and at 4.45 eV for $n=2$.⁵ The final sp band is assumed with X_1 at 7.67 eV (Ref. 22) and thus cannot be reached resonantly with the photon energies in our experiment. The initial state Δ^2 d band is neglected because of the selection rules for photoemission in the direction of the surface normal. The result of this shifting procedure for two-photon energies is shown in Fig. 3.

The results in Fig. 3 strongly support a resonance mechanism as responsible for the observed double-peak structure. As we show in Fig. 3, two different resonances are present for a pair of photon energies approximately 110 meV apart, at 2.97 and 3.08 eV. The corresponding 3PPE processes involve a two-photon resonance between one of the two d bands and the IP state and both are near one-photon resonance to unoccupied sp -band states. In view of the very simple model, both the photon energies and the separation of the resonances are in good agreement with the measured values. These resonances involve two initial states belonging to spin-orbit split Δ^5 d bands. They both proceed at different k values via the dispersing unoccupied portion of the sp -band states to the image-potential state. The IP state is a surface state which by definition does not show dispersion with momentum in the direction perpendicular to the surface and thus is drawn horizontally in the bulk band structure of Fig. 2. As can be seen by the position of the upper unoccupied sp band in Fig. 3 (dash dotted), a three-photon resonance involving final states from this band can be ruled out.

Our analysis also explains why the observed peaks do not shift according to the number of additional photons necessary to reach the final state when changing the center wavelength of the pulse. In the present case, the relatively broad frequency spectrum of the ultrashort pulse samples a range of resonance conditions. As long as the photon energies of the two most prominent resonance features are supplied by the pulse, there will only be a change in the relative peak amplitudes of the two features as the central photon energy of the pulse is tuned. This obviously shows that features A and B are not a consequence of the presence of the IP state alone but are inherently caused by a nonlinear resonance effect between initial, first intermediate states, and second intermediate (IP) states. Very qualitatively, a memory of its excitation pathway must be imparted on an electron because it starts at a specific energy level (one of the two d bands), then goes through the *same* energy level of the IP state as the other electrons and finally it ends up at a specific energy again. In this sequential picture where only the actual population of the IP state is measured by the third ionizing photon, no initial-state peaks could show up in the photoelectron spectrum if the electrons from different initial states lose memory of their excitation pathway in the IP state before their final ionization. In this respect, the simple observation of two IP-state-related peaks that do not move when the central pulse energy is tuned is a sign of specific nonlinear-optical pathways that cannot be pictured as sequential one-photon transitions but that allow the electron to keep its initial-state information as it is emitted into the vacuum.

The resonance effect also provides an effective energy filter, which would explain why the width of the observed

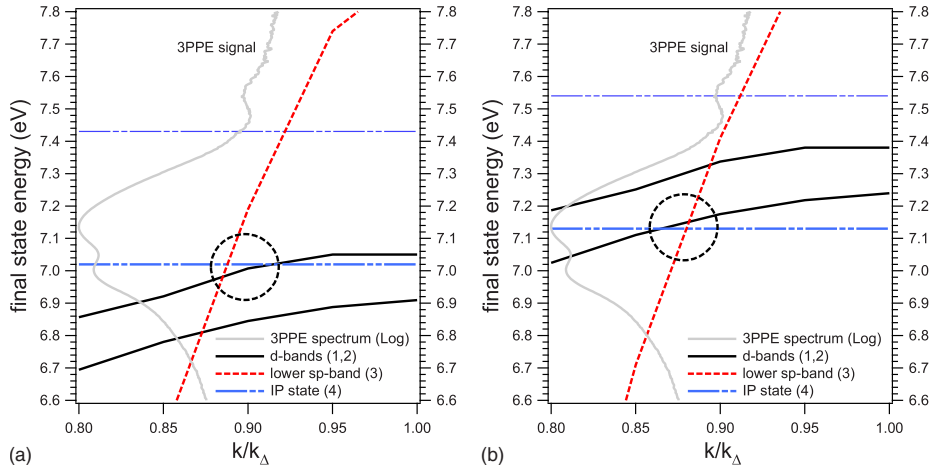


FIG. 3. (Color online) Estimation of resonance conditions for $h\nu=2.97$ eV (left) and $h\nu=3.08$ eV (right) by shifting initial and intermediate states according to the number of necessary photons to reach the final-state energy. The bands are numbered according to Fig. 2. The crossing of initial (solid black), first intermediate (dashed red), and second intermediate (dash-dot-dot blue) state bands indicates simultaneous one-photon and two-photon resonances between one of the two d bands, the sp band, and the $n=1$ image-potential state. Due to the broad pulse spectrum (≈ 170 meV), the separate resonances connected to the two d bands are simultaneously observed in the experimental spectrum (solid gray, experimental data for 3.08 eV central photon energy of the laser pulse, compare with Fig. 1).

peaks A and B is smaller than the optical spectrum of the excitation pulses. Strictly, energy conservation is imposed only on the overall coherent 3PPE process from an initial to a final state that are separated by $\hbar\omega_3$. In principle all three-photon processes that fulfill $\hbar\omega_3 = \hbar\omega_0 + \hbar\omega_1 + \hbar\omega_2$ are allowed. However, if we are additionally near one-photon resonances $\hbar\omega_R$ between dispersing levels (compare Fig. 3), energy conservation is also approximately fulfilled for the intermediate levels. This favors the photon energies near the simultaneous one-photon, two-photon, and three-photon resonances $\hbar\omega_3 = \hbar(\approx\omega_R) + \hbar(\approx\omega_R) + \hbar(\approx\omega_R)$ and thus provides an energy-filtering mechanism.

B. Quantum mechanical model for three-photon photoemission

In order to gain a better insight into the observed three-photon photoemission processes, the above analysis has to be supplemented by a more quantitative theoretical model. Two-photon photoemission has been described in the density-matrix formalism, where the populations of the involved states are described by the diagonal elements ρ_{aa} and the coherences between states by the off-diagonal elements ρ_{ab} of the density matrix ρ .^{5,14,28–31} The application to three-photon photoemission is straightforward but more involved due to the presence of more energy levels in the system. In order to clarify the nomenclature for the various electronic states and processes, we give the following explicit definitions which will be referred to in the discussion below.

We assume that the part of the Cu band structure that is relevant for the observed 3PPE process can be effectively simplified to a four-level system. The unperturbed Hamiltonian of the system is written in the basis of four orthonormalized states ($\langle a|b\rangle = \delta_{ab}$) representing either one of the initially occupied d -band states $|i_{1,2}\rangle$, the intermediate

unoccupied sp -band $|s\rangle$, the image-potential state $|m\rangle$, and the final photoemitted state $|f\rangle$ at the respective energy levels $\epsilon_{i,s,m,f}$. In order to keep the treatment transparent, we also include the zero matrix elements,

$$\hat{H}_S = \begin{pmatrix} \epsilon_i & |i\rangle\langle i| & 0 & |i\rangle\langle s| & 0 & |i\rangle\langle m| & 0 & |i\rangle\langle f| \\ 0 & |s\rangle\langle i| & \epsilon_s & |s\rangle\langle s| & 0 & |s\rangle\langle m| & 0 & |s\rangle\langle f| \\ 0 & |m\rangle\langle i| & 0 & |m\rangle\langle s| & \epsilon_m & |m\rangle\langle m| & 0 & |m\rangle\langle f| \\ 0 & |f\rangle\langle i| & 0 & |f\rangle\langle s| & 0 & |f\rangle\langle m| & \epsilon_f & |f\rangle\langle f| \end{pmatrix}. \quad (1)$$

This simplification disregards the dispersion of the electronic states with crystal momentum \mathbf{k} that is a major inhomogeneous contribution to 2PPE spectra³⁰ and it neglects the various interband and intraband relaxation mechanisms that would need to be part of a quantitative theory for a crystalline solid-state system. This could be handled, e.g., by introducing sets of k -dependent multilevel systems with appropriate couplings that represent the above effects.^{30,32} We also assume weak perturbation of the system by the laser pulse, thereby excluding effects that are typically related to significant population transfers during the action of the pulse such as, e.g., Rabi oscillations.³³ The 3PPE processes proceed independently from either of the two different sets of initial d -band states $|i_{1,2}\rangle$, which are uncorrelated single-particle states. This allows us to treat two uncoupled four-level systems instead of a five-level system with two closely spaced initial states.

The density operator $\hat{\rho}$ of this simplified system explicitly expands as

$$\hat{\rho} = \begin{pmatrix} \rho_{ii} & |i\rangle\langle i| & \rho_{is} & |i\rangle\langle s| & \rho_{im} & |i\rangle\langle m| & \rho_{if} & |i\rangle\langle f| \\ \rho_{si} & |s\rangle\langle i| & \rho_{ss} & |s\rangle\langle s| & \rho_{sm} & |s\rangle\langle m| & \rho_{sf} & |s\rangle\langle f| \\ \rho_{mi} & |m\rangle\langle i| & \rho_{ms} & |m\rangle\langle s| & \rho_{mm} & |m\rangle\langle m| & \rho_{mf} & |m\rangle\langle f| \\ \rho_{fi} & |f\rangle\langle i| & \rho_{fs} & |f\rangle\langle s| & \rho_{fm} & |f\rangle\langle m| & \rho_{ff} & |f\rangle\langle f| \end{pmatrix},$$

$$\rho_{ii}(t = -\infty) = 1. \quad (2)$$

We emphasize that the matrix element ρ_{ii} is the only nonzero element in the ground state at time $t = -\infty$, representing the initial population of the relevant d -band state.

The matrix element ρ_{ff} determines the quantity we measure in the experiment: the (very small) population that is transferred to the final state by the ultrashort optical pulse. Initially, $\rho_{ff} = 0$ and it can only become nonzero due to the

coupling to the initial state via the intermediate states. This coupling is provided by the electric field $E(t)$ of the excitation pulse. For simplicity, we assume here that the most relevant couplings are between those states which are nearly a photon energy $\hbar\omega_p$ apart in the level scheme,

$$|i\rangle \leftrightarrow |s\rangle \leftrightarrow |m\rangle \leftrightarrow |f\rangle. \quad (3)$$

In the density-matrix formalism, this specific coupling is achieved by retaining only the relevant matrix elements in the corresponding interaction Hamiltonian H_{int} , with the dipole moments μ_{ab} describing the relative strength of the coupling of $|a\rangle$ and $|b\rangle$ due to the presence of a classical electric field with amplitude $E(t)$ [polarization effects can be included by vectors $\vec{E}(t)$ and $\vec{\mu}_{ab}$],

$$\hat{H}_{\text{int}}(t) = -E(t) \cdot \begin{pmatrix} 0 & |i\rangle\langle i| & \mu_{is} & |i\rangle\langle s| & 0 & |i\rangle\langle m| & 0 & |i\rangle\langle f| \\ \mu_{is}^* & |s\rangle\langle i| & 0 & |s\rangle\langle s| & \mu_{sm} & |s\rangle\langle m| & 0 & |s\rangle\langle f| \\ 0 & |m\rangle\langle i| & \mu_{sm}^* & |m\rangle\langle s| & 0 & |m\rangle\langle m| & \mu_{mf} & |m\rangle\langle f| \\ 0 & |f\rangle\langle i| & 0 & |f\rangle\langle s| & \mu_{mf}^* & |f\rangle\langle m| & 0 & |f\rangle\langle f| \end{pmatrix}. \quad (4)$$

For a solid-state system, the internal light field that gives rise to photoemission is influenced by the collective optical response of the system, which can be taken into account by a complex response function in the frequency domain.³⁴

Starting at $t = -\infty$ from only $\rho_{ii} \neq 0$, the interaction Hamiltonian allows finite values to develop in the matrix elements during the time evolution of the density operator $\hat{\rho}$. This time evolution is described by the equation of motion for the density matrix (Liouville-von Neumann equation),^{5,14,28,29,35}

$$\frac{d\rho_{ab}}{dt} = -\frac{i}{\hbar} \langle a | [\hat{H}_S + \hat{H}_{\text{int}}, \hat{\rho}] | b \rangle - \Gamma_{ab} \rho_{ab}$$

$$(a, b = i, s, m, f). \quad (5)$$

Straightforward replacement of the definitions (1), (2), and (4) in Eq. (5) results in a set of coupled differential equations for the density-matrix elements ρ_{ab} which in principle can be numerically integrated using standard algorithms.

In Eq. (5), the Γ_{ab} are phenomenological parameters which are introduced to account for the relaxation of the system back to equilibrium by energy and momentum exchange with external degrees of freedom. In our simple picture we assume that the Γ_{ab} are constants, which leads to exponential decay behavior via the structure of Eq. (5) looking like $\dot{\rho} \propto -\Gamma\rho$. Qualitatively, much more complicated dynamics of the excited system can result if the electronic energy levels, the dipole moments, and decay rates themselves are functions of other degrees of freedom coupled to the system.³⁶

The off-diagonal elements, i.e., the coherences ρ_{ab} , decay due to the influence of the population loss rates Γ_{aa} and Γ_{bb} of both involved levels and, in addition, the ρ_{ab} can decay due to the randomization of the relative quantum-mechanical

phase between the states $|a\rangle$ and $|b\rangle$. In general, the coherences ρ_{ab} account for interference effects in the coupling between states $|a\rangle$ and $|b\rangle$, which will be washed out when the phase correlation of the oscillating dipole μ_{ab} between interactions with $E(t)$ at points in time t_1 and t_2 decays to zero.

The integrated dipole moment of an ensemble of dipoles can decay due to disappearance of dipoles from the ensemble (population loss rates Γ_{aa} and Γ_{bb}) but is also destroyed by phase randomization between dipoles that continue with the same strength of the oscillations but with increasingly random phases. On the single dipole level, the required phase jumps can happen if the quantum-mechanical superposition of $|a\rangle$ and $|b\rangle$ that created the dipole is changing its internal phase by, e.g., momentum scattering. The contribution that is solely due to the phase randomization (as opposed to population loss) is assumed to proceed with an exponential decay rate Γ_{ab}^{pd} determined by the interactions with the bath degrees of freedom ("pure dephasing," supposed to be composed of contributions that can be ascribed to both involved states separately like $\Gamma_{ab}^{pd} = \Gamma_a^{pd} + \Gamma_b^{pd}$),

$$\Gamma_{ab} = \Gamma_{ab}^{pd} + \frac{1}{2}(\Gamma_{aa} + \Gamma_{bb}). \quad (6)$$

As stated above, with the above definitions, the nonlinear photoemission signal proportional to ρ_{ff} can in principle be obtained by numerically integrating the coupled differential Eq. (5). We note here that the interaction is completely described by a *classical* electric field $E(t)$ and the notion of "n-photon processes" actually does not appear anywhere directly in the formalism we have discussed. The nonlinearities with respect to the intensity of the incident light appear due

WINKELMANN *et al.*PHYSICAL REVIEW B **80**, 155128 (2009)

to the mathematical properties of a system of coupled differential equations like the system [Eq. (5)] and *not* because any quantization of energy exchange is involved directly anywhere in the formalism.

The photoemission signal $N(E_f)$ at the final-state energy E_f is formally obtained from the population in the final state ρ_{ff} integrated over time (for finite pulse lengths) according to the standard procedure^{14,37} of taking the trace of the operator of the relevant observable $|f\rangle\langle f|$ applied to $\hat{\rho}(t, E_f)$,

$$N(E_f) = \int_{-\infty}^{+\infty} dt \text{Tr}\{|f\rangle\langle f|\hat{\rho}(t, E_f)\}. \quad (7)$$

For comparison, we note that electromagnetic signals observed in purely optical measurements originate from the induced material polarization \vec{P} as a source term in the Maxwell equations. The polarization is related to the expectation value of the dipole operator $\hat{\mu}$: $\vec{P} = \text{Tr}[\hat{\mu}\hat{\rho}]$. Because the dipole operator expands into matrix elements of the type $|b\rangle\langle a|$ (for two generic basis states $|a\rangle$ and $|b\rangle$),³⁵ it probes coherences between states (i.e., it measures the off-diagonal elements ρ_{ab}). The above treatment also illustrates how simultaneous nonlinear-optical and multiphoton photoemission experiments from the same system using the same laser source can be analyzed in a unified manner. Such combined experiments can provide additional information about the optically excited system under investigation.³⁸

The numerical treatment of Eq. (5) is in principle straightforward. However, with respect to the physical interpretation, a perturbative expansion of $\hat{\rho}$ with respect to interactions with the electrical field is useful. Then the order of nonlinearity of the observed quantity as a function of the incident light field $E(t)$ can be determined. Such a perturbative expansion allows us to visualize the induction of non-zero matrix elements ρ_{ab} as a sequence of steps in which the commutators $[H_{\text{int}}, \rho_{ab}]$ in Eq. (5) are recursively expanded up to a specified order. This expansion can be represented by double-sided Feynman diagrams which keep track of both the time development of the population in the involved states as well as the induced coherences between these states that are, respectively, described by the diagonal and off-diagonal elements of the density matrix.³⁵ Another related visualization allows us to show the possible coupling of two generic elements ρ_{ab} and ρ_{cd} of the density matrix as Liouville space pathways.³⁵

These Liouville space pathways show that besides the sequential one-photon pumping of population from one state to the next [compare relation (3)],

$$\rho_{ii} \rightarrow \rho_{ss} \rightarrow \rho_{mm} \rightarrow \rho_{ff}, \quad (8)$$

there are contributions to ρ_{ff} containing only coherences, schematically written like

$$\rho_{ii} \rightarrow \rho_{is} \rightarrow \rho_{im} \rightarrow \rho_{if} \rightarrow \rho_{ff}, \quad (9)$$

which implies that these contributions produce no population in the intermediate states $|m\rangle$ (corresponding to the observable $N_m = \text{Tr}[|m\rangle\langle m|\hat{\rho}]$) due to the fact that the density-matrix components ρ_{mm} are not affected by these processes. It is emphasized that despite the fact that no population in the

intermediate state is involved, these states nevertheless have a decisive role. They contribute via their coherent superposition with the other states. From our experimental data, we see that the coherent coupling of the d -band states to the image-potential state via the sp bands contributes to the initial-state peaks in the photoelectron spectrum $[\rho_{ff}(E)]$. We keep in mind that the pathways (8) and (9) are two particular pathways in a general coherent 3PPE process and occur together with all other pathways and should be added coherently in calculating $\rho_{ff}(E)$.

C. Model calculations

As we discussed above, the theoretical modeling of our spectra requires the treatment of a number of four-level systems at different k points in the Cu band structure. Numerical integration of the corresponding set of Liouville-von Neumann equations would need realistic dipole matrix elements and relaxation rates of the relevant states, including their dispersion and possible intraband and interband interactions. However, the main physics of the effect to be explained is expected to be already present in three-level systems of initial, intermediate, and final states. For these systems, analytical solutions exist for single-frequency interactions in two-photon photoemission.¹³ Assuming that the two initial d -band levels and the intermediate IP state play a dominant role in the mechanism we focus on here, we can simplify our four-level system (3PPE) to a three-level system (2PPE) by artificially moving the two initial d -band states to the original energy level of the first intermediate sp bands, which are neglected in the following. The neglect of the sp bands seems to be justified in this case since they are strongly dispersing and should not contribute significant additional spectral structure by themselves. The validity of this assumption would have to be checked in a quantitative theory since the sp bands can contribute additional intraband relaxation channels. We then apply the model of Wolf *et al.*¹³ to our special simplified system that models 2PPE from two closely spaced, independent initial states via the same intermediate state. We assume a broad continuum of excitation frequencies and analyze how the resonance frequencies can be distinguished in the photoelectron spectrum, similar to transitions in an absorption spectrum using a broadband light source.

For the intermediate state we assumed a constant lifetime of 35 fs and a dephasing rate of 1 meV.⁵ For the final state we assumed infinite population lifetime and 1 meV dephasing rate.⁵ The initial states are separated by 150 meV, at energy levels that reproduce the experimentally observed final-state positions via the intermediate state at 4.04 eV, corresponding to the $n=1$ IP state on Cu(001). We then calculated the resulting 2PPE spectra for a range of initial-state dephasing rates (assuming no population decay in the initial state). The resulting 2PPE spectra in two-dimensional plots for photon energies ranging are shown in Fig. 4. We can distinguish two different linear dispersions, one with a slope of $2\Delta h\nu$, corresponding to the initial states and the other with a slope of $1\Delta h\nu$, corresponding to the intermediate state. Starting with dephasing times between 10 and 20 fs, the two

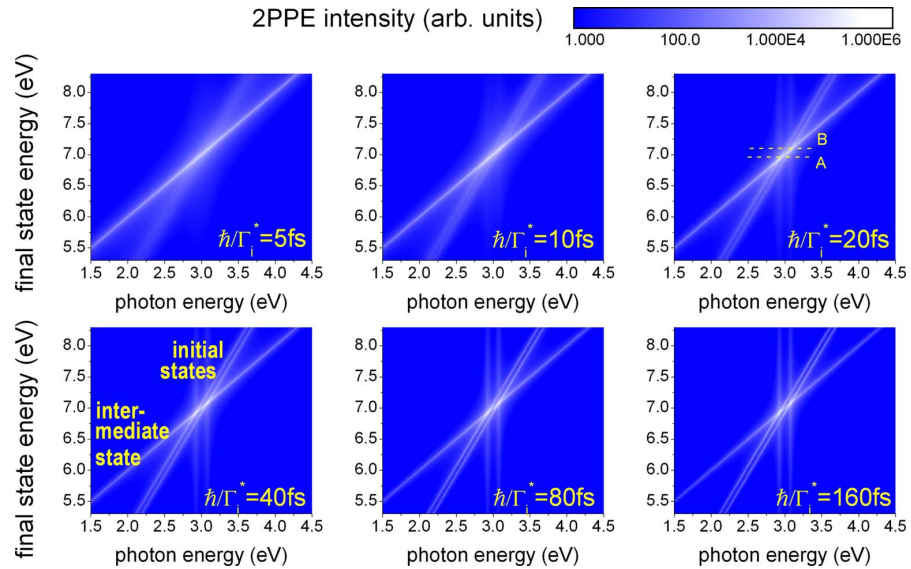


FIG. 4. (Color online) Simulations of one-color 2PPE from two closely spaced initial states via the same intermediate state for a continuous flat excitation spectrum with single-photon energies from 1.5 to 4.5 eV. The panels show the final-state 2PPE yield (logarithmic scale) as a function of the photon energy and final-state energy. The initial and intermediate-state peaks can be distinguished by the change in their final-state energy as a function of the photon energy $h\nu$ (initial state: $2\Delta h\nu$ and intermediate state: $1\Delta h\nu$). The two vertical lines (best visible in the lower panels) indicate the presence of two energy-filtering resonances A and B that increase the *absolute* intensity in the photoelectron spectra for the respective photon energies. The corresponding peak positions in the photoelectron spectrum are shown at A and B. The total photoelectron spectrum for the 3 eV broad continuum of incident light is obtained by integrating over the horizontal axes. With increasing dephasing time, the total photoelectron spectrum evolves from a single broad peak (5 fs) to two separate peaks (>10 fs) (see Fig. 5). In each panel, the assumed initial-state pure dephasing times are indicated. For the intermediate state, a population lifetime of 35 fs and a pure dephasing of 1 meV was assumed. In the final state, we took an infinite population lifetime and pure dephasing rate of 1 meV. The separation of the initial states is 150 meV.

initial states become separately visible. For faster dephasing, only a single peak is present.

Assuming a flat excitation spectrum ranging from 1.5 to 4.5 eV, the partial spectra for each energy were added to simulate the effect of a broad excitation spectrum. The result, corresponding to an average along the horizontal axis of Fig. 4, is shown in Fig. 5. Depending on the initial-state dephasing rate, we can observe a single broad peak or two separate peaks resolving the two initial states. This result for a model 2PPE process shows how the dephasing rate between initial state and intermediate state contributes to the peak width of the transition. If the dephasing rate is high, the two independent transitions from the closely spaced initial states are broadened to an extent that they are not separable anymore and appear as a single peak. With decreasing dephasing, the peak widths of the two resonances become sharp enough to give two peaks in the final-state spectrum. This process can be expected to be of very general character and a similar influence of dephasing is expected to be relevant in the 3PPE experiment. This means that a sufficiently low dephasing rate of the initial states with respect to the intermediate states will be required in any case to distinguish two initial-state peaks in a transition that proceeds via a common intermediate-state level, such as the IP state considered here.

With respect to the 2PPE model calculation, the pure dephasing on one hand is almost totally due to the initial state since image-potential states on perfect surfaces can be

assumed in good approximation to have a nearly zero pure dephasing rate.^{5,12} $\Gamma_b^{pd} \approx 0$. The dephasing due to population decay on the other hand stems solely from the image-potential state since the initial states are assumed not to decay: $\Gamma_{ii} = 0$. In the model calculation, an initial-state dephasing time of at least 10–20 fs is necessary for the observation of the separated peaks. Although this value cannot be taken

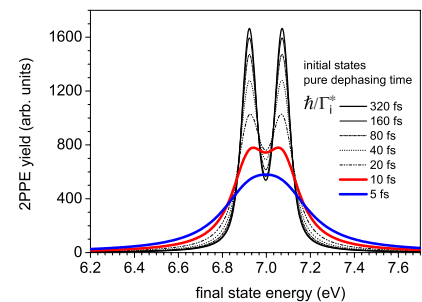


FIG. 5. (Color online) Summation of the spectra from Fig. 4 for all photon energies of the excitation continuum to simulate the total photoelectron spectrum. The presence of two resonances can be clearly distinguished. While the underlying initial and intermediate-state features disperse with photon energy, they strongly change their intensity (logarithmic scale in Fig. 4) to result in the resonance peaks in the total sum spectra shown above. An instrumental broadening of 50 meV was assumed.

WINKELMANN *et al.*

PHYSICAL REVIEW B **80**, 155128 (2009)

as a completely quantitative estimation, nevertheless it compares well with direct time-domain observations of Cu *d*-band hole dephasing times of >20 fs in the observed *d*-band region near the X point.⁹

For ultrashort pulses, the optical frequencies are not independent of each other and this coherent excitation spectrum will additionally have an influence on the observed photoelectron spectra. We assume that a coherent broad pulse spectrum would still tend to broaden the photoelectron peaks rather than to make them narrower in comparison to single-frequency excitation (the actual amount of broadening can be limited by the resonant energy-filtering process discussed above). Other influences such as the dispersion of the involved electronic bands also would lead to an additional broadening. This implies that the observed experimental width of the peaks in the 3PPE spectrum is an upper limit estimation when compared to the results from the simplified 2PPE model. This is why the above estimations based on a single-frequency and continuous-wave approximation should in any case present lower limits on the dephasing times compatible with the observation of two separate peaks in the 3PPE spectrum.

V. CONCLUSION AND SUMMARY

Our observations of the direct influence of coherent excitation pathways in 3PPE from Cu(001) are relevant for applications of nonlinear photoemission in electronic structure investigations, which can be carried out using high-intensity laboratory laser sources and synchrotron-based free-electron lasers. It has been predicted theoretically¹⁵ that resonant two-photon photoemission could give the separation between occupied initial states and unoccupied intermediate *bulk* states within the fundamental limit imposed by the intrinsic energy and momentum widths of the coupled states. The important advantage in such two-photon measurements is that the optical transition from the initial state to the intermediate state would couple bulk states which are not influenced by the symmetry breaking due to the surface³⁹ and the perpendicular crystal momentum k_{\perp} in such a transition would need to be conserved (at negligible photon momentum). The extension of this idea to 3PPE is straightforward and we illustrate in Fig. 6 the qualitative difference between unspecific bulk excitations and coherent resonances which sensitively depend on the band dispersion. It can also be easily imagined that this approach can be generalized to multiple excitation frequencies which can be tuned to search for the simultaneously possible single-photon resonances in a multiphoton process. Furthermore, the use of multiphoton resonances corresponding to very well-defined *k*-space positions should allow improved time-domain investigations⁶ of band-resolved electron dynamics. The demonstrated coherent coupling of bulk states to surface states through a two-photon excitation could also lead to improved possibilities of controlling electron motion at surfaces by interferometric techniques.^{10,40}

In summary, we have demonstrated the clear influence of coherent excitation pathways in three-photon photoemission from Cu(001). Our findings suggest extensions to future

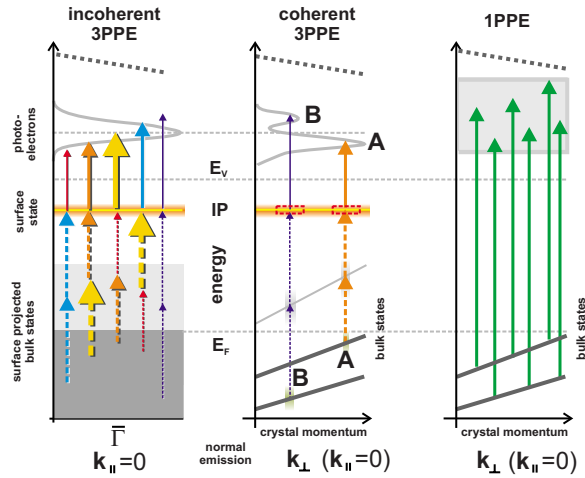


FIG. 6. (Color online) Principle of detecting coherent bulk band-structure resonances in 3PPE via an image-potential state on Cu(001). Left: nonresonant incoherent excitation of the IP state from unspecific bulk bands at normal emission ($k_{\parallel}=0$). The initial states are averaged over k_{\perp} illustrating the loss of k_{\perp} information in the sequential one-photon pathways due to the total lack of a k_{\perp} selection rule in the IP to final-state one-photon transition (k_{\perp} is undefined for surface states). The colors of the arrows correspond to photon frequencies provided by the excitation pulse, their thickness corresponds to the respective spectral weight. The photons can act in any combination for sequential incoherent excitations. The peak position of the IP state is determined by the central photon energy of the pulse (thickest arrow) and the measured width of the IP state is determined by the width of the pulse spectrum. Middle: coherent 3PPE resonances in the bulk band structure coupled to the image-potential state produce specific peaks A and B in the spectrum, providing k_{\perp} information. A fixed photon energy defines each resonant pathway. The width of features A and B is not limited by the spectral pulse width. Right: the corresponding 1PPE process for the same level scheme using a single-photon energy of $\approx 3h\nu_{3\text{PPE}}$ is less k selective if no resonance to a dispersing final-state band is present (e.g., off-resonant transition to final band broadened by absorption).

studies of bulk band structure with tuneable laboratory and free-electron laser sources, exploiting multiphoton resonances for band mapping. If we note that when—in addition to the energy of the exciting radiation—the quantum-mechanical phase relationships between the coupled states and the radiation also become a defining factor in the nonlinear excitation process,⁷ qualitatively different applications as compared to conventional band mapping with one-photon ARPES are expected by exploiting the unique properties of multiphoton transitions between occupied and unoccupied bulk states.

ACKNOWLEDGMENTS

We thank Frank Helbig for invaluable technical support. H.P. is grateful for support by NSF under Grant No. CHE-0650756.

*winkel@mpi-halle.mpg.de

- ¹A. Einstein, *Ann. Phys.* **322**, 132 (1905).
- ²*Solid-State Photoemission and Related Methods: Theory and Experiment*, edited by W. Schattke and M. A. Van Hove (Wiley-VCH, Weinheim, 2003).
- ³S. Hüfner, *Photoelectron Spectroscopy* (Springer-Verlag, Berlin, New York, 1995).
- ⁴Th. Fauster, *Solid-State Photoemission and Related Methods: Theory and Experiment* (Ref. 2), pp. 247–268.
- ⁵M. Weinelt, *J. Phys.: Condens. Matter* **14**, R1099 (2002).
- ⁶H. Petek and S. Ogawa, *Prog. Surf. Sci.* **56**, 239 (1997).
- ⁷H. Petek, A. P. Heberle, W. Nessler, H. Nagano, S. Kubota, S. Matsunami, N. Moriya, and S. Ogawa, *Phys. Rev. Lett.* **79**, 4649 (1997).
- ⁸S. Ogawa, H. Nagano, H. Petek, and A. P. Heberle, *Phys. Rev. Lett.* **78**, 1339 (1997).
- ⁹H. Petek, H. Nagano, and S. Ogawa, *Phys. Rev. Lett.* **83**, 832 (1999).
- ¹⁰J. Güdde, M. Rohleder, T. Meier, S. W. Koch, and U. Höfer, *Science* **318**, 1287 (2007).
- ¹¹U. Höfer, I. L. Shumay, C. Reuss, U. Thomann, W. Wallauer, and T. Fauster, *Science* **277**, 1480 (1997).
- ¹²T. Fauster, M. Weinelt, and U. Höfer, *Prog. Surf. Sci.* **82**, 224 (2007).
- ¹³M. Wolf, A. Hotzel, E. Knoesel, and D. Velic, *Phys. Rev. B* **59**, 5926 (1999).
- ¹⁴S. Ramakrishna and T. Seideman, *J. Chem. Phys.* **122**, 084502 (2005).
- ¹⁵W. Schattke, E. E. Krasovskii, R. Díez Muiño, and P. M. Echénique, *Phys. Rev. B* **78**, 155314 (2008).
- ¹⁶F. Bisio, M. Nývlt, J. Franta, H. Petek, and J. Kirschner, *Phys. Rev. Lett.* **96**, 087601 (2006).
- ¹⁷A. Winkelmann, F. Bisio, R. Ocana, W.-C. Lin, M. Nývlt, H. Petek, and J. Kirschner, *Phys. Rev. Lett.* **98**, 226601 (2007).
- ¹⁸A. Winkelmann, W.-C. Lin, F. Bisio, H. Petek, and J. Kirschner, *Phys. Rev. Lett.* **100**, 206601 (2008).
- ¹⁹W. Steinmann, *Phys. Status Solidi B* **192**, 339 (1995).
- ²⁰H. Eckardt, L. Fritsche, and J. Noffke, *J. Phys. F: Met. Phys.* **14**, 97 (1984).
- ²¹R. Courths, H. Wern, G. Leschik, and S. Hüfner, *Z. Phys. B: Condens. Matter* **74**, 233 (1989).
- ²²V. N. Strocov, R. Claessen, F. Aryasetiawan, P. Blaha, and P. O. Nilsson, *Phys. Rev. B* **66**, 195104 (2002).
- ²³V. N. Strocov, R. Claessen, G. Nicolay, S. Hüfner, A. Kimura, A. Harasawa, S. Shin, A. Kakizaki, H. I. Starnberg, P. O. Nilsson, and P. Blaha, *Phys. Rev. B* **63**, 205108 (2001).
- ²⁴J. E. Ortega, F. J. Himpsel, G. J. Mankey, and R. F. Willis, *Phys. Rev. B* **47**, 1540 (1993).
- ²⁵A. Mugarza, A. Marini, T. Strasser, W. Schattke, A. Rubio, F. J. García de Abajo, J. Lobo, E. G. Michel, J. Kuntze, and J. E. Ortega, *Phys. Rev. B* **69**, 115422 (2004).
- ²⁶C. M. Schneider, J. J. Demiguel, P. Bressler, P. Schuster, R. Miranda, and J. Kirschner, *J. Electron Spectrosc. Relat. Phenom.* **51**, 263 (1990).
- ²⁷R. Courths and S. Hüfner, *Phys. Rep.* **112**, 53 (1984).
- ²⁸E. Knoesel, A. Hotzel, and M. Wolf, *J. Electron Spectrosc. Relat. Phenom.* **88-91**, 577 (1998).
- ²⁹H. Ueba and T. Mii, *Appl. Phys. A: Mater. Sci. Process.* **71**, 537 (2000).
- ³⁰M. J. Weida, S. Ogawa, H. Nagano, and H. Petek, *J. Opt. Soc. Am. B* **17**, 1443 (2000).
- ³¹N. Pontius, V. Sametoglu, and H. Petek, *Phys. Rev. B* **72**, 115105 (2005).
- ³²T. Meier, P. Thomas, and S. W. Koch, *Coherent Semiconductor Optics* (Springer, New York, 2007).
- ³³L. C. Allen and J. H. Eberly, *Optical Resonance and Two-Level Atoms* (Dover, New York, 1988).
- ³⁴M. Mershdorf, C. Kennerknecht, and W. Pfeiffer, *Phys. Rev. B* **70**, 193401 (2004).
- ³⁵S. Mukamel, *Principles of Nonlinear Optical Spectroscopy* (Oxford University Press, New York, 1995).
- ³⁶An example would be the optical excitation electrons at a surface, inducing nuclear motion of an adsorbate atom, leading to shifting *electronic* energy levels and changing wave function overlap, causing changes in the dipole moments and electronic transition rates, and finally feeding back onto the induced *nuclear* motion in the next time step (Ref. 41). Inclusion of such processes would introduce additional nonlinear character into the system of Eq. (5).
- ³⁷H. Ueba and B. Gumhalter, *Prog. Surf. Sci.* **82**, 193 (2007).
- ³⁸F. Bisio, A. Winkelmann, W.-C. Lin, C.-T. Chiang, M. Nývlt, H. Petek, and J. Kirschner, *Phys. Rev. B* **80**, 125432 (2009).
- ³⁹V. N. Strocov, *J. Electron Spectrosc. Relat. Phenom.* **130**, 65 (2003).
- ⁴⁰J. Gauyacq and A. Kazansky, *Appl. Phys. A: Mater. Sci. Process.* **89**, 517 (2007).
- ⁴¹H. Petek, M. J. Weida, H. Nagano, and S. Ogawa, *Science* **288**, 1402 (2000).

Band structure effects in surface second harmonic generation: The case of Cu(001)F. Bisio,^{1,2,*} A. Winkelmann,³ W.-C. Lin,^{3,4} C.-T. Chiang,³ M. Nývlt,⁵ H. Petek,⁶ and J. Kirschner³¹CNISM, Sede Consorzziata di Genova and Dipartimento di Fisica, Università di Genova, via Dodecaneso 33, I-16146 Genova, Italy²CNR-INFM LAMIA, Corso Perrone 24, I-16152 Genova, Italy³Max-Planck-Institut für Mikrostrukturphysik, Weinberg 2, D-06120 Halle (Saale), Germany⁴Department of Physics, National Taiwan Normal University, 88, Section 4, Ting-Chou Road, Taipei 116, Taiwan⁵Faculty of Mathematics and Physics, Institute of Physics, Charles University, Ke Karlovu 5, 12116 Praha 2, Czech Republic⁶Department of Physics and Astronomy, University of Pittsburgh, Pittsburgh, Pennsylvania 15260, USA

(Received 29 June 2009; revised manuscript received 31 August 2009; published 30 September 2009)

We have performed a study of simultaneous nonlinear optical second harmonic generation (SHG) and angle-resolved nonlinear photoemission at the Cu(001) surface excited by fundamental photon energies near 3 eV. At these excitation energies, we identify a dominant contribution to the SHG signal that is determined by a two-photon resonance between the d bands and the $n=1$ image-potential state at the Cu(001) surface. The near-resonant behavior of SHG and nonlinear photoemission is studied via Cs adsorption, which allows to systematically lower the work function and thus the reference vacuum level of the image potential. Comparison of the angle-resolved photoemission signal, arising from a restricted region of electronic momentum space, with the simultaneous optical SHG signal allows to identify an additional contribution of electronic states with nonzero surface-parallel momentum to the SHG signal enhancements. A simple model accounting for the observed behavior is developed and the implications for the quantitative understanding of SHG are discussed.

DOI: [10.1103/PhysRevB.80.125432](https://doi.org/10.1103/PhysRevB.80.125432)

PACS number(s): 73.20.-r, 79.60.-i, 78.68.+m

I. INTRODUCTION

In the nonlinear optical process of second harmonic generation (SHG), optical radiation of frequency ω is coherently converted to radiation at the double frequency 2ω due to the nonlinear response of the electronic subsystem of a material.¹⁻³ In centrosymmetric media and under the electric dipole (ED) approximation, SHG is restricted to the symmetry-breaking surface region.⁴⁻⁶ Due to its surface sensitivity, SHG has been broadly exploited to address a great variety of topics in the fields of surface and interface science, ranging from surface chemistry^{7,8} to magnetism in low-dimensional systems.^{9,10}

The all-optical character of SHG makes the technique applicable to insulators,^{11,12} semiconductors,¹³ and metals.¹⁴ The employment of a purely optical probe allows to address solid-solid,¹⁵ liquid-solid,¹⁶ and air-solid¹⁷ interfaces without encountering the experimental limitations of electron-based methods. Relying on optically induced transitions between electronic states or bands of the investigated medium, SHG is naturally sensitive to the electronic structure of the materials, with enhanced sensitivity to the surface region.¹⁸ This great potential in terms of applicability and sensitivity is however limited by several factors, that can strongly reduce the information yield. Intrinsic to the optical probing of solid-state systems is the lack of selectivity with respect to electron crystal momentum in the SHG process.¹⁹ This appears in strong contrast to photoemission experiments, where the dispersion of electronic states as a function of their crystal momentum k is directly accessed by angle-resolved electron detection.²⁰ Consequently, the interpretation of SHG spectra in solids has to simultaneously take into account all excitations in the whole surface Brillouin zone (BZ), where the eventual presence of strongly dispersing electronic states typically tends to wash out any potentially sharp spectral

features. Independent information about the occupied and unoccupied electronic structure of the material and the extent to which resonances dominate the process has therefore to be available before the SHG yield from a given material can be correctly ascribed to specific electronic transitions,²¹⁻²³ thereby strongly limiting the predictive character of this technique. Moreover, beyond the ground-state band structure and k -resolved transition matrix elements, factors such as excited-state lifetimes, electronic dephasing, and collective electronic excitations (plasmons) can strongly affect SHG²⁴ and need to be known.

In this paper, we report a combined study of SHG and angle-resolved nonlinear photoemission of the Cu(001) surface as a function of the exposure to Cs atoms, performed with fundamental exciting photon energy in the 3 eV range. The SHG and the photoemission were excited by the same laser and were simultaneously recorded. The deposition of Cs provided a mechanism for modifying the surface electronic structure, primarily by shifting the energy position of the surface states of image-potential origin. Angle-resolved two-photon photoemission and three-photon photoemission (2PPE and 3PPE) provided momentum-resolved (k_{\parallel}) information about the electronic structure of the surface in the energy range probed by the SHG signal, allowing to *directly* assess the contribution of the various optically induced transitions in the material. Monitoring the SHG and 3PPE signals as a function of Cs coverage, we observed enhanced photon and electron yields in correspondence with the optically induced resonant transitions between bulk and surface electronic states. A characteristic change in the maximum of the resonant SHG yield as a function of the Cs coverage with respect to the corresponding 3PPE signal measured at $k_{\parallel}=0$ is modeled in terms of the contribution to SHG from electronic transitions with nonzero k_{\parallel} . A simple model for this behavior is developed, providing qualitative agreement with the experimental data.

BISIO *et al.*PHYSICAL REVIEW B **80**, 125432 (2009)

II. EXPERIMENT

A. Apparatus

The experiments were carried out in an ultrahigh vacuum (UHV) system with a base pressure of approximately 5×10^{-11} mbar. Ultrashort excitation pulses with central energy tuneable in the range of $\hbar\omega=2.99\text{--}3.14$ eV were provided by the frequency-doubled output of a self-built Ti:sapphire oscillator. The pulse central energy could be continuously varied by tuning the phase-matching angle of the frequency-doubling 80- μm -thick $\beta\text{-BaB}_2\text{O}_4$ crystal. At the energy of $\hbar\omega=3.07$ eV, the excitation bandwidth was ~ 0.17 eV, the pulse length at the surface was ≤ 20 fs, and the pulse energy was ~ 1 nJ. The laser beam was focused onto the surface at an angle of incidence of 42° . The 2PPE and 3PPE spectra were measured in the normal-emission geometry, with a k_{\parallel} resolution below ± 0.07 \AA^{-1} . The Cu crystal was biased at -3 V to increase the collection efficiency of electrons. The ω and 2ω components of the reflected beam exited the UHV chamber via a CaF_2 optical viewport, and were then spatially separated exploiting the optical dispersion properties of CaF_2 Brewster's angle prisms. In detail, a chain of four such prisms intercalated by adjustable slits allowed to effectively remove any spurious fundamental contribution while maintaining the spectral integrity of a sizeable SHG signal; the detected $2\omega/\omega$ intensity ratio at the detector (Perkin Elmer C922 channel photomultiplier with a CsTe solar-blind photocathode) was better than 10^4 . Linear input polarization could be set to either s_{in} or p_{in} by means of an achromatic half-wave plate placed before the UHV chamber whereas the polarization of the outgoing SHG could be analyzed by means of a MgF_2 Rochon prism. The Cu(001) surface was prepared by standard sputtering and annealing procedures. The optical plane was aligned parallel to the [110] crystallographic direction. Cs was deposited from a commercial getter source. The geometrical arrangement of the apparatus allowed the simultaneous measurement of high-order photoemission in the normal-emission geometry and of SHG. The Cs-coverage dependence of both the SHG and the photoemission curves reported in this paper were measured in real time and simultaneously during the course of Cs evaporations. The background pressure during Cs deposition was lower than 5×10^{-10} mbar. All the experiments were carried out with the sample at 300 K.

B. Nonlinear photoemission spectra

In presenting the experimental data, we chose to start from the multiphoton photoemission spectra since they provide information on the optically coupled occupied/unoccupied electronic states of the sample that are prerequisite for discussing SHG. In Fig. 1, we report two multiphoton spectra measured with p -polarized 3.14 eV photons under normal-emission geometry for a clean Cu(001) surface (gray symbols) and after deposition of ≈ 0.06 monolayer of Cs [where 1 monolayer corresponds to the $(2 \times 2)\text{Cs}/\text{Cu}(001)$ structure, black symbols].^{25–27} The energy scale is referred to the Fermi level E_F . The changes observed in the spectra upon Cs deposition reflect the corresponding variations in the interface electronic structure of the sample. The two-photon

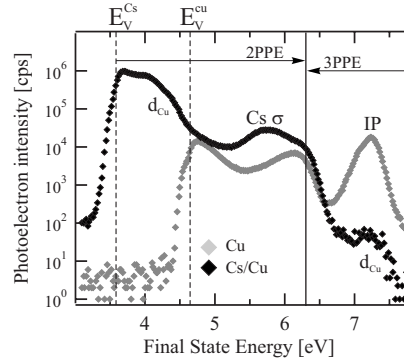


FIG. 1. Multiphoton spectra of the Cu(001) surface, before (gray symbols) and after (black symbols) the deposition of 0.1 monolayer of Cs. The spectra were measured under normal-emission geometry, with 3.14 eV photon energy.

part of the spectra, both clean and cesiated, has been discussed in depth in the literature^{26,28,29} and our spectra agree with the reported data. In detail, we clearly observe the Cs-induced lowering of the work function, that allows the observation, in 2PPE, of the otherwise inaccessible Cu d bands (d_{Cu}) around 4 eV energy above E_F , and the appearance of a Cs adsorbate σ resonance state at a final-state energy of ~ 5.7 eV. The 3PPE part of the spectrum also markedly changes after the Cs deposition. In the clean Cu(001) case, the 3PPE energy range is dominated by an intense peak, ascribed to a near-resonant three-photon transition involving the Cu d bands as initial states, and the unoccupied Cu sp band (sp_{Cu}) and the $n=1$ image-potential state (IP) as intermediate states.³⁰ This peak, which for the clean surface at our laser fluence accounts for more than 95% of the total 3PPE yield in the normal-emission geometry, almost completely disappears after cesiation, leaving only a shoulder in the spectrum. This behavior can be readily interpreted keeping in mind that the IP states maintain, in a first approximation, a constant binding energy with respect to the vacuum energy E_V (Ref. 31) and get broadened upon absorption of alkali atoms.³² Thus, the work-function shift due to Cs detunes the IP state from the resonance condition and broadens it, lowering the corresponding 3PPE yield; the shoulder in the cesiated spectrum accordingly represents the three-photon replica of the large d_{Cu} peak observed in 2PPE at the low-energy end of the spectrum.

C. Second harmonic generation

The Cs-coverage dependence of the SHG yield has been measured for four different combinations of input/output $\omega/2\omega$ polarization, namely, $p_{\text{in}}\text{-}p_{\text{out}}$, $s_{\text{in}}\text{-}p_{\text{out}}$, $p_{\text{in}}\text{-}s_{\text{out}}$, and $s_{\text{in}}\text{-}s_{\text{out}}$. A sizeable SHG signal could be measured in the former two polarization combinations whereas negligible counts were recorded for $p_{\text{in}}\text{-}s_{\text{out}}$ and $s_{\text{in}}\text{-}s_{\text{out}}$ geometries irrespective of the Cs coverage, in agreement with expectations for electric dipole SHG from (001) surfaces and with previous experiments on the system.^{33–35} In general, the $p_{\text{in}}\text{-}p_{\text{out}}$ SHG signal is larger by roughly a factor 5–6 with respect to

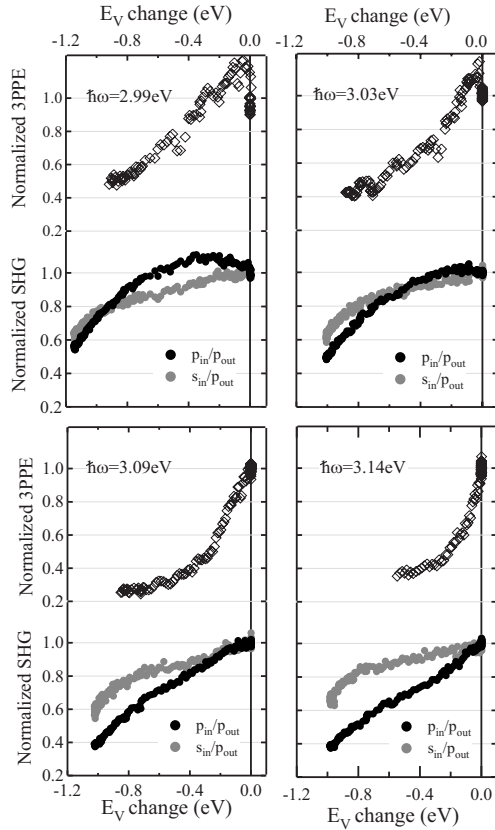


FIG. 2. Normalized total 3PPE yield in normal-emission geometry (open diamonds), normalized $p_{in}-p_{out}$ SHG (black circles), and normalized $s_{in}-p_{out}$ SHG (gray circles) as a function of the Cs-induced change in work function ΔE_V . The excitation energy was 2.99 eV (top left), 3.03 eV (top right), 3.09 eV (bottom left), and 3.14 eV (bottom right).

the $s_{in}-p_{out}$ case. In Fig. 2, we report four sets of SHG measurements in the $p_{in}-p_{out}$ and $s_{in}-p_{out}$ geometries, performed as a function of the Cs coverage for four different excitation wavelengths. The data have been normalized to the respective clean-surface value and have been plotted as a function of the change in the work function ΔE_V with respect to the clean Cu(001), directly deduced from the low-energy cutoff of the spectra. In the top panel of each graph we reported the total 3PPE yield in normal emission normalized to its clean Cu(001) value as a function of ΔE_V .

We begin by describing the 2.99 eV data (top left panel in Fig. 2), subsequently extending the discussion to other energies. For this case, we observe that for decreasing work function the $p_{in}-p_{out}$ measured SHG initially gradually increases, attains a very broad maximum for $\Delta E_V \approx -0.3$ eV and subsequently decreases reaching a value of 60% of the initial yield for $\Delta E_V \approx -1.1$ eV. The corresponding $s_{in}-p_{out}$ SHG instead remains approximately constant up to $\Delta E_V \approx -0.2$ eV and then regularly drops, with constant slope, up to $\Delta E_V \approx -1.0$ eV, somehow steepening its decrease for larger ΔE_V . At the same time the integrated 3PPE signal quickly rises for small Cs coverage, exhibiting a sharp maximum for

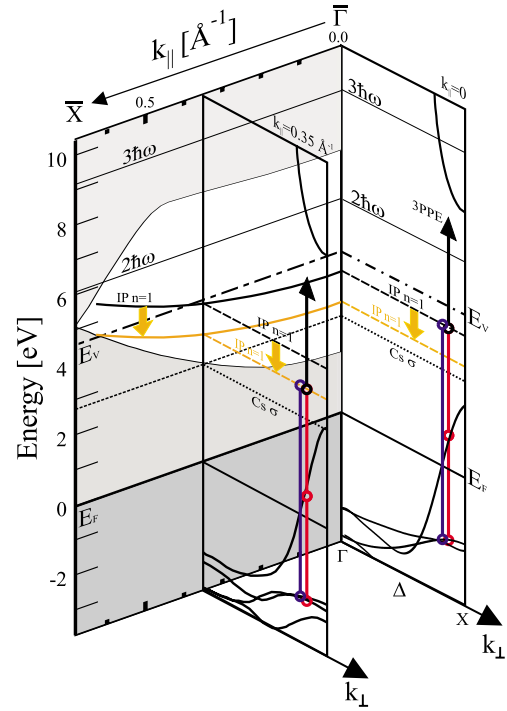


FIG. 3. (Color online) Schematic representation of a section of the surface BZ of a clean and cesiated Cu(001). Background panel: surface-projected bulk band structure (shaded area) along the ΓX direction. The IP state on the clean (cesiated) surface is depicted as the solid black (orange) line. Forefront panels: Cu(001) band structure as a function of perpendicular momentum, after Burdick (Ref. 36) for $k_{\parallel} = 0$ (right) and $k_{\parallel} = 0.35 \text{ \AA}^{-1}$ (center). Possible optically induced transitions at $\omega(2\omega)$ frequency are represented by the red (blue) vertical lines. 3PPE is schematically indicated by stacking a black vertical arrow on top of two 1ω transitions.

$\Delta E_V \approx -0.1$ eV, and subsequently drops with decreasing ΔE_V reaching a value of approximately 50% of the clean Cu(001) for $\Delta E_V \approx -0.9$ eV (Though SHG and photoemission were recorded simultaneously, the 3PPE vs E_V curves are typically displayed in a narrower ΔE_V range because, at large Cs exposure, the possible contribution of 2PPE electrons in the 3PPE range due to space-charge effects cannot be excluded from the data.)

With increasing excitation photon energy, the SHG and 3PPE curves undergo consistent changes. In the 3.03 eV case, the shape of the SHG and 3PPE curves strongly resemble that of the previous case but the maxima of both the $p_{in}-p_{out}$ SHG and 3PPE are shifted toward less negative ΔE_V values; the $p_{in}-p_{out}$ SHG peaks at $\Delta E_V \approx -0.15$ eV whereas the 3PPE maximum seems to occur just off from the $\Delta E_V = 0$ value.

In the 3.09 eV case, no maxima can be seen in any of the curves. The $p_{in}-p_{out}$ SHG is seen around a fairly constant value for ΔE_V within -0.1 eV before starting its drop for ongoing Cs adsorption. The 3PPE curve quickly drops to 40% of its initial value before decreasing its drop rate around $\Delta E_V \approx -0.3$ eV. Finally, for 3.14 eV photon energy, the

BISIO *et al.*PHYSICAL REVIEW B **80**, 125432 (2009)

$p_{\text{in}}p_{\text{out}}$ SHG exhibits a marked decrease beginning from the very early stages of Cs deposition. The 3PPE drops somehow faster than in the 3.09 eV case for small E_V change and also levels off for ΔE_V beyond roughly -0.3 eV.

In general, the $s_{\text{in}}p_{\text{out}}$ SHG for all the investigated photon energies does not show strong and significant variations with respect to the already described 2.99 eV case, as observable in the graphs of Fig. 2.

III. DISCUSSION

In the ED approximation, the SHG yield from a given surface depends on the Fresnel factors at the ω and 2ω frequencies and on the second-order nonlinear susceptibility tensor $\chi_{ijm}^{(2)}$. According to Ref. 19, the dependence of $\chi_{ijm}^{(2)}$ on the electronic structure of the material can be expressed as

$$\chi_{ijm}^{(2)}(2\omega) \propto \sum_{\mathbf{k}, l, l', l''} M_i M_j M_m \left\{ \frac{f(E_{k,l''}) - f(E_{k,l'})}{E_{k,l''} - E_{k,l'} - \hbar\omega + i\hbar\gamma_{l' \rightarrow l''}} - \frac{f(E_{k,l'}) - f(E_{k,l})}{E_{k,l'} - E_{k,l} - \hbar\omega + i\hbar\gamma_{l \rightarrow l'}} \right\}. \quad (1)$$

Here, $M_i = \langle \Psi_{\mathbf{k},l} | p_i | \Psi_{\mathbf{k},l'} \rangle$ is the dipole matrix element between states (\mathbf{k}, l) and (\mathbf{k}, l') (and $M_{j(m)}$, respectively, account for the transitions between the other electronic levels involved). The electronic structure of the material enters through the eigenvalues $E_{k,l}$, which depend on the electron momentum $\mathbf{k} = (k_{\perp}, k_{\parallel})$ and the band index l while $f(E)$ and $\gamma_{l \rightarrow l'}$ represent the Fermi function and the Lorentzian broadening associated with the transitions between the pertinently indexed states, respectively. Equation (1) can be further simplified by assuming the state occupation factors to be $f(E_{k,l'}) = f(E_{k,l''}) \approx 0$ and $f(E_{k,l}) = 1$, for the excited and initial states. The Cs contribution is implicitly included in Eq. (1) by admitting the adsorbate states among the energy eigenvalues $E_{k,l}$. For our specific case, the Cs-coverage dependence of the SHG could arise from either a change in the surface Fresnel factors or a change in $\chi_{ijm}^{(2)}$. For the Cs-coverage range under investigation, we can safely assume that no major change in the Fresnel factors takes place and accordingly proceed to model the observed SHG yield in terms of a variation in the nonlinear susceptibility $\chi_{ijm}^{(2)}$. Furthermore, the weak wavelength dependence of the Fresnel factors would not justify the wavelength-dependent variations in the SHG yields reported in Fig. 2.

We therefore discuss the electronic structure of the Cs/Cu(001) system with the aid of Fig. 3. There, a schematic representation of the system's band structure is reported, in which the electronic states at finite k_{\parallel} are explicitly indicated. In the background panel, the surface-projected band structure of Cu along the ΓX direction is reported, with the parabolically dispersing IP state drawn as the solid black line. The two panels protruding toward the forefront of the picture display the perpendicular-momentum-dependent *bulk* band structure of Cu, after Burdick,³⁶ for two selected values of k_{\parallel} : $k_{\parallel} = 0$ (right) and $k_{\parallel} = 0.35 \text{ \AA}^{-1}$ (center), respectively. Possible electronic transitions at $\omega(2\omega)$ frequency are displayed as red (blue) lines in such panels. The possibility of observing 3PPE from two-photon-excited electronic states is schematically represented by stacking a further black vertical arrow on top of two such red lines. The correlation between SHG and 3PPE is apparent from this diagram since SHG and 3PPE involve the same set of ground, one-photon-excited

and two-photon-excited electronic states, with their related transition matrix elements whereas they notably differ only in the last step. The effect of Cs adsorption will be, in first approximation, represented by the lowering of energy with respect to E_F and broadening of the IP-state (orange lines),³² and by the appearance of the unoccupied, nondispersing, Cs σ resonance which is located, at the maximum coverage we addressed, approximately 2.6 eV above E_F (visible in the cesiated spectrum of Fig. 1).²⁵

We begin our discussion by addressing the $p_{\text{in}}p_{\text{out}}$ SHG and the 3PPE recorded for 2.99 eV photon energy, and subsequently extend it to the other cases. Let us initially focus on the ΔE_V dependence of the integrated 3PPE data, to be discussed based on the $k_{\parallel} = 0$ cross section of the BZ in Fig. 3. From the spectrum of Fig. 1 and the data of Ref. 30, we deduce that the near-resonant transition between d_{Cu} bands, the sp_{Cu} bands and the IP state gives by far the dominant contribution to the 3PPE. The data reported in Fig. 2 show that, as soon as E_V gets lowered by Cs adsorption, the 3PPE intensity increases, sharply peaking at around $\Delta E_V \approx -0.1$ eV. This is due to the fact that on clean Cu(001), the excitation with 2.99 eV photons does not allow the optimum two-photon resonant matching between the d_{Cu} bands and the IP state whereas this is achieved upon decreasing the IP-state energy (i.e., the work function) by Cs of the amount $\Delta E_V \approx -0.1$ eV. Choosing a value for the IP binding energy with respect to E_V at $k_{\parallel} = 0$ of 0.59 eV,³⁷ and a Cu(001) work function $E_V = 4.63$ eV, we deduce that the d_{Cu} bands acting as initial states in the 3PPE process are located $E_{d_{\text{Cu}}} \approx -2.04$ eV below E_F , a value in very good agreement with independent data derived from conventional photoemission experiments.³⁸ The decrease in 3PPE with further Cs deposition can be then assigned to the progressive detuning and broadening of the IP state from resonance occurring upon the further lowering of E_V .

The $p_{\text{in}}p_{\text{out}}$ SHG for 2.99 eV excitation shows two relevant differences with respect to the 3PPE. First of all, the maximum of the SHG vs E_V curve is significantly broader with respect to its 3PPE counterpart; second, it is apparently shifted to lower E_V by approximately 0.2 eV. We can account for this behavior by developing a simple model for SHG

based on the electronic structure in Fig. 3. In order to do this, we have to address the optically induced resonant electronic transitions at ω and 2ω frequency occurring throughout the BZ that go into computing $\chi_{ijm}^{(2)}$ according to Eq. (1). In this respect, the important input that we receive from the 3PPE measurements, thanks to the strong overlap between the electronic states probed by the 3PPE and the SHG, concerns the efficiency of the electronic transitions between states (\mathbf{k}, l) , (\mathbf{k}, l') , and (\mathbf{k}, l'') . From Eq. (1) it can be inferred that the presence of a doubly resonant transition at specific points of the BZ yields a possibly dominant contribution to $\chi_{ijm}^{(2)}$, from the 3PPE data we have the additional information that such doubly resonant transitions can be provided by the two-photon coupling of the d_{Cu} bands with the IP state through the sp_{Cu} bands. The influence of the σ resonance on the SHG yield, which can be very strong under specific excitation conditions,^{25,39,40} can be here considered negligible based on two simple arguments. First, we notice that the Cs σ resonance, according to Fig. 3, can be populated from the sp_{Cu} band only, for which the density of states is much lower with respect to the d_{Cu} bands. To this end, we notice that Cs peak in the 2PPE part of the spectrum of Fig. 1 is smaller by a factor 20 with respect to the corresponding 2PPE d_{Cu} peak. Second, the σ resonance can participate only in photoinduced transitions for which one single step is resonant while no resonance conditions can be met for the other steps. The combination of these two factors is expected to yield a much lower efficiency of this process with respect to the doubly resonant $d_{\text{Cu}} \rightarrow sp_{\text{Cu}} \rightarrow \text{IP}$ transition and hence a much lower SHG. We point out that, on other surfaces, like the Cu(111), resonance conditions between the sp bands and the Cs σ resonance could be more easily met for much broader Cs-coverage ranges, thereby enhancing the role of Cs in SHG at variance with our case.

Based on this observation, the model calculation of the Cs-coverage-dependent $p_{\text{in}}/p_{\text{out}}$ SHG yield can be performed, based on Eq. (1), under the following assumptions: (i) the dominant contribution to SHG is provided by the $d_{\text{Cu}} \rightarrow sp_{\text{Cu}} \rightarrow \text{IP}$ doubly resonant transition and (ii) the matrix elements involved in such transitions are considered constant as a function of both k_{\parallel} and Cs coverage.⁴¹ In this model, the calculation of $\chi_{ijm}^{(2)}$ is performed integrating all over the bulk BZ and not restricted to high-symmetry directions. The integration over k_{\perp} is performed assuming that, for every k_{\parallel} , there exist one (or two, considering momentum directed toward or away from the surface) value of k_{\perp} for which the d_{Cu} and the sp_{Cu} bands are in resonance for our excitation energy (forefront panels of Fig. 3). Then, further integration is performed all over the surface BZ under the assumption that the presence of the $d_{\text{Cu}}-sp_{\text{Cu}}$ resonance occurs throughout the whole surface BZ with initial d_{Cu} states having a binding energy which is constant as a function of k_{\parallel} . With these hypotheses, the doubly resonant contributions to $\chi_{ijm}^{(2)}$ are free to occur at any location in the surface BZ where the IP-state is tied to an energy where it can contribute to the d - sp -IP double resonance.

Thus the initial-state energy $E_{k,l}$ in Eq. (1) is fixed at the energy of the d_{Cu} band region $E_{d_{\text{Cu}}}$ taking part in the resonant process, the intermediate-state energy reads $E_{k,l'} = E_{d_{\text{Cu}}} + \hbar\omega$ and the (k_{\parallel} -dependent) energy of the IP state is $E_{k,l''}$. $E_{k,l''}$ can

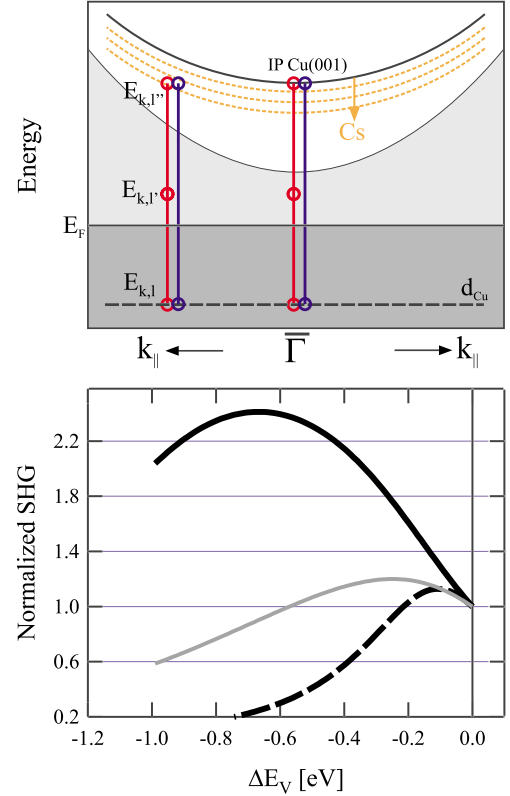


FIG. 4. (Color online) Top panel: energy diagram of the electronic states considered for the model calculation of $\chi_{ijm}^{(2)}$. The Cs-induced shift of the IP-state energy is pictorially represented. Vertical lines represent light-induced electronic transitions for different values of parallel momentum. Bottom panel: calculated dependence of $\chi_{ijm}^{(2)}$ as a function of ΔE_V performed for k -space integration over $k_{x(y)} \in [-0.5, 0.5] \text{ \AA}^{-1}$ (solid black line) and restricted to $\bar{\Gamma}$ (dashed black line). Here $k_{x(y)}$ are the two components of the surface parallel momentum k_{\parallel} . Gray line: calculated value of $\chi_{ijm}^{(2)}$ upon inclusion of a phenomenological adsorbate-induced broadening of the IP state.

in turn be written as $E_{k,l''} = \frac{\hbar^2 k_{\parallel}^2}{2m^*} + E_{\bar{\Gamma}}$, where m^* is the effective mass of the IP state and $E_{\bar{\Gamma}}$ is the Cs-coverage-dependent energy of the IP state at $\bar{\Gamma}$. We point out that since we are merely interested in finding the SHG evolution vs Cs coverage and not its absolute intensity, the value of the matrix elements between all states involved is taken as unity. The energy diagram of the states employed for calculating $\chi_{ijm}^{(2)}$ according to all the above hypothesis is shown with a one-dimensional representation in the top part of Fig. 4. Accordingly, Eq. (1) can be simplified as

$$\chi_{ijm}^{(2)} \propto \int_{k_{\parallel}} \frac{1}{i\hbar \gamma_{l \rightarrow l'}} \cdot \frac{1}{\frac{\hbar^2 k_{\parallel}^2}{2m^*} + E_{\bar{\Gamma}}(E_V) - E_{d_{\text{Cu}}} - 2\hbar\omega + i\hbar \gamma_{l'' \rightarrow l}}. \quad (2)$$

BISIO *et al.*PHYSICAL REVIEW B **80**, 125432 (2009)

In the bottom part of Fig. 4 we report, as the solid black curve, a calculation of the modulus square of $\chi_{ijm}^{(2)}$ (proportional to the SHG intensity) as a function of ΔE_V performed according to our simple model, for 2.99 eV excitation energy. The theoretical curve of Fig. 4 was calculated imposing $m^* = 0.94$,^{30,37} keeping a fixed $\gamma_{p \rightarrow l} = 0.3$ eV (extracted from the effective width of the d bands in 2PPE, as obtained in a low-temperature Cs deposition experiment) and integrating over $k_{\parallel} \in [-0.5, 0.5] \text{ \AA}^{-1}$, an interval more than sufficient to cover the energy range of interest for the IP state. In the same graph, the dashed curve represents the $|\chi_{ijm}^{(2)}(\Delta E_V)|^2$ dependence calculated with the same parameters as for the solid black curve but having limited the k -space integration volume to a narrow region around $\bar{\Gamma}$.

As is clearly seen in the graph, the agreement with the experimental SHG data is not satisfactory under the simple hypothesis made. The calculation of $\chi_{ijm}^{(2)}$ could however be further refined to yield a quantitatively better agreement with the data by explicitly including the adsorbate-induced broadening of the IP state.^{32,42-45} Inserting a Cs-coverage-dependent broadening of $\gamma_{p \rightarrow l}$ with a constant rate of 4.5 eV/ML, a value fully compatible with available experimental and theoretical values,^{32,46} yields in fact the gray curve in the bottom panel of Fig. 4, which reproduces the experimental data significantly better. The good agreement between the experimental data and the model calculations performed under the above simple hypothesis makes us confident about the validity of our assumptions and the capability of capturing the essential physics involved in the nonlinear optical response of the material. Possible refinements involve explicitly addressing the role of single-resonant transitions in the SHG yield, although this would involve the realistic estimation of both the electric dipole matrix elements between the states involved and the phase shifts between the various SHG contributions, a task that goes beyond the scope of the present paper.

One further interesting point can be made from comparing the curves calculated with explicit integration over the whole BZ (black and gray solid curves) and the dashed curve, calculated with $\bar{\Gamma}$ -limited integration. The dashed curve exhibits a ΔE_V dependence very closely resembling the one of the 3PPE signal reported in Fig. 2, peaking at $\Delta E_V \approx -0.1$ eV and quickly decreasing with decreasing E_V . This can be easily understood since the k -space region employed for calculating the dashed curve is the same as the one probed by 3PPE at normal emission. Extending the integration volume to a physically significant portion of the BZ yields a curve which is much smoother and in which the maximum of $\chi_{ijm}^{(2)}$ vs ΔE_V is clearly shifted, two features that are evident from the experimental data. The physical origin for the smoothening of the SHG features and for the ΔE_V shift with respect to 3PPE is, in our view, the variation in k -space volume contributing to the resonant SHG as a function of ΔE_V . At $\bar{\Gamma}$, in fact only one k point in the BZ will contribute to the resonant SHG whereas when resonance conditions are met at $k_{\parallel} \neq 0$, there will be a circle of k points in the surface BZ giving a resonant contribution to $\chi_{ijm}^{(2)}$, thereby increasing the SHG yield.

We can now briefly extend our discussion to the other polarization geometries and photon energies. Starting again

with the 2.99 eV case, we begin by addressing the $s_{\text{in}}-p_{\text{out}}$ geometry. We clearly notice that the ΔE_V dependence of the $s_{\text{in}}-p_{\text{out}}$ SHG mainly differs from the corresponding $p_{\text{in}}-p_{\text{out}}$ case in that the former data do not show any sign of the features that we have ascribed to the IP-state resonance in the latter curve. This can be understood based on ED selection rules, which do not allow a transition induced by s -polarized radiation between the sp_{Cu} bands and the IP state all over the BZ, due to the Δ_1 -type symmetry of the states involved.^{47,48} This can be also viewed as a further confirmation of the dominant role of the $n=1$ IP state in SHG for the $p_{\text{in}}-p_{\text{out}}$ geometry.

Given the absence of a dominating double-resonant transition in the $s_{\text{in}}-p_{\text{out}}$ geometry, the interpretation of the data cannot be reliably performed as for the $p_{\text{in}}-p_{\text{out}}$ case. It is likely that several single-resonant transitions throughout the BZ contribute to the SHG and that the total yield is possibly also influenced by interference effects between such various contributions.^{49,50} Inspecting the band structure of Fig. 3, one single-resonant process is surely represented by the $d_{\text{Cu}}-sp_{\text{Cu}}$ coupling, that is allowed by ED selection rules for s_{in} incoming light and can occur all over the BZ. A further contribution might derive from the population of the Cs σ resonance from the sp_{Cu} bands. Given this, the regular decrease in $s_{\text{in}}-p_{\text{out}}$ SHG can be due to the interference between a roughly coverage-independent contribution to SHG ($d_{\text{Cu}}-sp_{\text{Cu}}$) and a coverage-dependent one ($sp_{\text{Cu}}-\sigma$).

The spectral dependence of the $p_{\text{in}}-p_{\text{out}}$ SHG, as displayed in the panels of Fig. 2, can be qualitatively understood based on the same model previously outlined. In the extreme case of 3.14 eV excitation, both the 3PPE signal and the SHG exhibit a marked decrease starting from the very early stages of Cs absorption. This is because, for larger excitation energy, already for the clean Cu(001) surface the optimum resonance condition for the d_{Cu} to IP transition are met for $k_{\parallel} > 0$. Hence, we observe only the “decreasing” side of the resonant enhancement, due to increased broadening, that was instead observed in its entirety in the 2.99 eV case. For excitation energy between the two limiting cases of 2.99 and 3.14 eV, a gradual crossover from the former to the latter behavior is observed. We point out that the spectral dependence of the SHG is qualitatively reproduced in our calculation (not shown) while keeping all the physical parameters the same as in Fig. 4.

IV. CONCLUSION

In conclusion, we have performed a combined SHG and multiphoton photoemission study of the Cu(001) surface, with ~ 3 eV excitation energy, as a function of the absorption of Cs. We have modeled the SHG response of the material as dominated by a doubly resonant transition between the d_{Cu} band and the image-potential state mediated by the sp_{Cu} band. Due to the additional information directly available from 3PPE we could pinpoint the strong contribution to the total SHG yield due to electronic transitions occurring at nonzero values of parallel momentum k_{\parallel} . Our work therefore emphasizes the limits of analyzing spectroscopic SHG data without explicitly integrating over the relevant k -space vol-

ume while suggesting the possible strong influence of dephasing effects on the SHG yield when there is a strong contribution from surface states. As we have shown, the combination of nonlinear optical and photoemission measurements enhances the potential of either or both techniques as probes of the electronic structure of surfaces.

In this respect, the application of photon energies near 3 eV for performing SHG has represented a substantial advantage for this work. While these energies allowed to cover a broad enough energy range of occupied/unoccupied states of the surface, thereby increasing the information yield, at the same time it was possible to observe nonlinear photoemission using the same excitation light source. This allowed the direct matching of SHG and photoemission data. Furthermore, we point out that performing SHG with 3 eV excitation allows to access the interband excitations that cannot be reached with photons of lower energy. Our results, showing a marked decrease in the SHG yield as a function of the Cs coverage in the submonolayer regime, substantially differ with respect to SHG data gathered with lower excitation energy.³⁹ These latter in fact mostly probe the nonresonant free-electron response of the metal and typically exhibit an increase in the SHG signal upon alkali atom adsorption that

is strictly related to the correspondent increase in the surface polarizability.⁵¹ The occurrence of a resonant interband excitation pathway clearly modifies the material response with respect to what expected from a simple free-electron picture; such a modified response is highlighted in our work by the nonconventional Cs-coverage dependence of the SHG yield. It can be therefore expected that performing SHG with excitation energy near or above 3 eV and coupling it with nonlinear photoemission will prove fruitful in future nonlinear optical studies.

ACKNOWLEDGMENTS

The authors thank Wolfgang Hübner, Ulrich Höfer, and Tony Heinz for stimulating discussion. Technical assistance from F. Helbig is gratefully acknowledged. F.B. acknowledges the CNR-CNISM convention, the Università di Genova (PRA 2008) and the Fondazione Carige for financial support. H.P. acknowledges support from NSF under Grant No. CHE-0650756. W.-C.L. acknowledges support from the National Science Council of Taiwan under Grant No. 96-2112-M-003-015-MY3.

*bisio@fisica.unige.it

¹J. Rudnick and E. A. Stern, *Phys. Rev. B* **4**, 4274 (1971).

²R. W. Boyd, *Nonlinear Optics*, 3rd ed. (Academic, San Diego, 2008).

³*Nonlinear Optics in Metals*, edited by K. H. Bennemann (Clarendon, Oxford, 1998).

⁴O. A. Aktsipetrov, I. M. Baranova, and Y. A. Il'inskiĭ, *Sov. Phys. JETP* **64**, 167 (1986).

⁵P. Guyot-Sionnest, W. Chen, and Y. R. Shen, *Phys. Rev. B* **33**, 8254 (1986).

⁶Y. R. Shen, *Nature (London)* **337**, 519 (1989).

⁷C. K. Chen, T. F. Heinz, D. Ricard, and Y. R. Shen, *Phys. Rev. Lett.* **46**, 1010 (1981).

⁸M. Fuyuki, K. Watanabe, D. Ino, H. Petek, and Y. Matsumoto, *Phys. Rev. B* **76**, 115427 (2007).

⁹H. A. Wierenga, W. de Jong, M. W. J. Prins, T. Rasing, R. Vollmer, A. Kirilyuk, H. Schwabe, and J. Kirschner, *Phys. Rev. Lett.* **74**, 1462 (1995).

¹⁰M. Nývlt, F. Bisio, J. Franta, C. L. Gao, H. Petek, and J. Kirschner, *Phys. Rev. Lett.* **95**, 127201 (2005).

¹¹M. Fiebig, D. Fröhlich, T. Lottermoser, V. V. Pavlov, R. V. Pisarev, and H.-J. Weber, *Phys. Rev. Lett.* **87**, 137202 (2001).

¹²M. Nývlt, F. Bisio, and J. Kirschner, *Phys. Rev. B* **77**, 014435 (2008).

¹³U. Höfer, L. Li, and T. F. Heinz, *Phys. Rev. B* **45**, 9485 (1992).

¹⁴K. J. Song, D. Heskett, H. L. Dai, A. Liebsch, and E. W. Plummer, *Phys. Rev. Lett.* **61**, 1380 (1988).

¹⁵G. Lüpke, D. J. Bottomley, and H. M. van Driel, *Phys. Rev. B* **47**, 10389 (1993).

¹⁶S. Ong, X. Zhao, and K. B. Eisenthal, *Chem. Phys. Lett.* **191**, 327 (1992).

¹⁷J. Xue, C. S. Jung, and M. W. Kim, *Phys. Rev. Lett.* **69**, 474

(1992).

¹⁸M. Y. Jiang, G. Pajer, and E. Burstein, *Surf. Sci.* **242**, 306 (1991).

¹⁹T. A. Luce and K. H. Bennemann, *Phys. Rev. B* **58**, 15821 (1998).

²⁰R. H. Williams, G. P. Srivastava, and I. T. McGovern, *Rep. Prog. Phys.* **43**, 1357 (1980).

²¹K. Giesen, F. Hage, H. J. Riess, W. Steinmann, R. Haight, R. Beigang, R. Dreyfus, Ph. Avouris, and F. J. Himpsel, *Phys. Scr.* **35**, 578 (1987).

²²L. E. Urbach, K. L. Percival, J. M. Hicks, E. W. Plummer, and H. L. Dai, *Phys. Rev. B* **45**, 3769 (1992).

²³G. Lüpke, D. J. Bottomley, and H. M. van Driel, *Phys. Rev. B* **49**, 17303 (1994).

²⁴C. Timm and K. H. Bennemann, *J. Phys.: Condens. Matter* **16**, 661 (2004).

²⁵S. A. Lindgren and L. Walldén, *Phys. Rev. B* **45**, 6345 (1992).

²⁶H. Petek, H. Nagano, and S. Ogawa, *Phys. Rev. Lett.* **83**, 832 (1999).

²⁷V. Sametoglu, Ph.D. thesis, University of Pittsburgh, 2009.

²⁸S. Ogawa and H. Petek, *Surf. Sci.* **363**, 313 (1996).

²⁹J. Zhao, N. Pontius, A. Winkelmann, V. Sametoglu, A. Kubo, A. G. Borisov, D. Sánchez-Portal, V. M. Silkin, E. V. Chulkov, P. M. Echenique, and H. Petek, *Phys. Rev. B* **78**, 085419 (2008).

³⁰F. Bisio, M. Nývlt, J. Franta, H. Petek, and J. Kirschner, *Phys. Rev. Lett.* **96**, 087601 (2006).

³¹V. Dose, W. Altmann, A. Goldmann, U. Kolac, and J. Rogozik, *Phys. Rev. Lett.* **52**, 1919 (1984).

³²X. Y. Wang, R. Paiella, and R. M. Osgood, *Phys. Rev. B* **51**, 17035 (1995).

³³R.-P. Pan, H. D. Wei, and Y. R. Shen, *Phys. Rev. B* **39**, 1229 (1989).

BISIO *et al.*PHYSICAL REVIEW B **80**, 125432 (2009)

- ³⁴G. Petrocelli, S. Martellucci, and R. Francini, *Appl. Phys. A: Mater. Sci. Process.* **56**, 263 (1993).
- ³⁵R. Vollmer, M. Straub, and J. Kirschner, *Surf. Sci.* **352-354**, 684 (1996).
- ³⁶G. A. Burdick, *Phys. Rev.* **129**, 138 (1963).
- ³⁷M. Weinelt, *J. Phys.: Condens. Matter* **14**, R1099 (2002).
- ³⁸J. A. Knapp, F. J. Himpsel, and D. E. Eastman, *Phys. Rev. B* **19**, 4952 (1979).
- ³⁹H. Tom, C. Mate, X. Zhu, J. Crowell, Y. Shen, and G. Somorjai, *Surf. Sci.* **172**, 466 (1986).
- ⁴⁰B. N. J. Persson and L. H. Dubois, *Phys. Rev. B* **39**, 8220 (1989).
- ⁴¹N. Pontius, V. Sametoglu, and H. Petek, *Phys. Rev. B* **72**, 115105 (2005).
- ⁴²Ch. Reuß, I. L. Shumay, U. Thomann, M. Kutschera, M. Weinelt, Th. Fauster, and U. Höfer, *Phys. Rev. Lett.* **82**, 153 (1999).
- ⁴³A. G. Borisov, A. K. Kazansky, and J. P. Gauyacq, *Surf. Sci.* **526**, 72 (2003).
- ⁴⁴T. Fauster, M. Weinelt, and U. Höfer, *Prog. Surf. Sci.* **82**, 224 (2007).
- ⁴⁵S. M. Dounce and H.-L. Dai, *Surf. Sci.* **583**, 310 (2005).
- ⁴⁶A. K. Kazansky, V. M. Silkin, E. V. Chulkov, A. G. Borisov, and J.-P. Gauyacq, *Phys. Rev. B* **75**, 235412 (2007).
- ⁴⁷J. Hermanson, *Solid State Commun.* **22**, 9 (1977).
- ⁴⁸W. Eberhardt and F. J. Himpsel, *Phys. Rev. B* **21**, 5572 (1980).
- ⁴⁹F. Eisert, A. P. Elg, and A. Rosén, *Appl. Phys. A: Mater. Sci. Process.* **60**, 209 (1995).
- ⁵⁰U. Höfer, *Appl. Phys. A: Mater. Sci. Process.* **63**, 533 (1996).
- ⁵¹H. Ishida and A. Liebsch, *Phys. Rev. B* **42**, 5505 (1990).

PHYSICAL REVIEW B **76**, 195428 (2007)

Angle-dependent study of a direct optical transition in the *sp* bands of Ag(111) by one- and two-photon photoemission

Aimo Winkelmann,^{1,2} Vahit Sametoglu,² Jin Zhao,² Atsushi Kubo,^{3,2} and Hrvoje Petek^{2,*}¹Max-Planck-Institut für Mikrostrukturphysik, Weinberg 2, D-06120 Halle, Germany²Department of Physics and Astronomy, University of Pittsburgh, Pittsburgh, Pennsylvania 15260, USA³PRESTO, Japan Science and Technology Agency, 4-1-8 Honcho Kawaguchi, Saitama 332-0012, Japan

(Received 17 July 2007; revised manuscript received 12 September 2007; published 16 November 2007)

We have measured angle-dependent photoemission spectra for one-photon and two-photon excitation from Ag(111). The observed dispersion of the *sp*-band transition of Ag(111) can be reproduced using a nearly-free-electron model for the initial and final states involved. The observed dispersion agrees with the known band structure. We illustrate how the strong refraction of low-energy electrons becomes a limiting factor to obtain quantitative band-structure information. Conversely, low-energy electrons of a well-defined direct optical interband transition can provide a sensitive probe of the inner potential. We observe asymmetric two-photon photoelectron intensity distributions with respect to detection along the surface normal. These intensity distributions can be well described by a phenomenological model which employs the Fresnel equations to calculate the electric field components of the incident radiation inside the sample. Very good agreement is found using tabulated optical constants and a momentum matrix element, which is oriented along the surface normal. In contrast, the observed intensity distribution for one-photon photoemission from Ag(111) does not fit the simple Fresnel model. We interpret this as the influence of surface photoemission. By comparison to Cu(001), we show that the expected intensity distributions of the Fresnel model for one-photon photoemission and two-photon photoemission are valid for an orientation of the momentum matrix element along the surface normal if the influence of additional effects like surface photoemission can be neglected.

DOI: [10.1103/PhysRevB.76.195428](https://doi.org/10.1103/PhysRevB.76.195428)

PACS number(s): 79.60.Bm, 71.20.-b, 78.20.-e

I. INTRODUCTION

Angle-resolved photoemission spectroscopy (ARPES) is a powerful and general tool to investigate the energy-momentum dispersions of the electronic states, which define the band structure of solids. A wealth of knowledge about the initial and final states involved in the photoexcitation process has been obtained using this method.¹ In ARPES, by considerations based on energy and momentum conservation, peaks in the photoelectron energy spectrum can be ascribed to transitions between the occupied and unoccupied states separated by the energy of a single photon of the exciting radiation (one-photon photoemission, 1PPE). Using tunable synchrotron radiation and a fixed geometry with angle-resolved electron detection along the surface normal, a sampling of the band structure along a high symmetry direction in reciprocal space is conceptually simplified. It is also possible to obtain band-structure information by taking angle-dependent photoemission spectra at fixed photon energy in symmetry planes² or even the whole hemisphere above the sample.³ The interpretation of such experiments, however, is more involved because of the more complicated form of the sampled regions in reciprocal space due to the nonconservation of the perpendicular component of the wave vectors. In all these types of measurements, information about the electronic band structure can be gained, first of all, by the analysis of the observed dispersion of peak *positions* in the photoelectron spectrum. To access the information contained in the photoemitted *intensities* is more complicated, because, in the general case, this has to involve comparison with calculated photoelectron spectra.⁴

With the application of high-power ultrafast laser systems, it also became possible to observe two-photon photoemission

(2PPE), where the initial state electrons are excited by the energy of two photons instead of only single photons as is the case in ARPES.^{5,6} In the two-photon photoemission process, intermediate unoccupied states above the Fermi energy are involved. One of the main successes of 2PPE is to observe the energy- and momentum-dependent dynamics of excited electrons in these intermediate states directly in the time domain by using a pump-probe configuration.⁷ Experimentally, the application of 2PPE is usually limited to photon energies where no one-photon photoemission can occur because this would overwhelm the 2PPE signal. However, apart from this limitation, the basic mechanisms governing both angle-resolved coherent 2PPE and ARPES are expected to be closely related.

As a model system for the quantitative analysis of photoemission spectra, the bulk band structure of silver has been extensively studied by 1PPE ARPES.⁸⁻¹⁰ The importance of the polarization of the incident light on the distribution of the photoemitted electrons was studied experimentally and theoretically,¹¹⁻¹³ and the importance of the momentum matrix elements for the observed intensities of energy-dependent transitions was shown.¹⁴ Spin-resolved measurements in combination with relativistic one-step photoemission calculations for Ag(111) have been used to compare different approximations for the exchange-correlation potential.¹⁵ The Shockley surface state on Ag(111) was also investigated by ARPES.¹⁶⁻²⁰ The ARPES results have been analyzed using several theoretical bulk band-structure calculations.²¹⁻²³ Recently, the bulk valence band structure of silver has been investigated by hard x-ray photoemission spectroscopy.²⁴ In a photon energy range relevant to our investigation, significant interference between surface and bulk

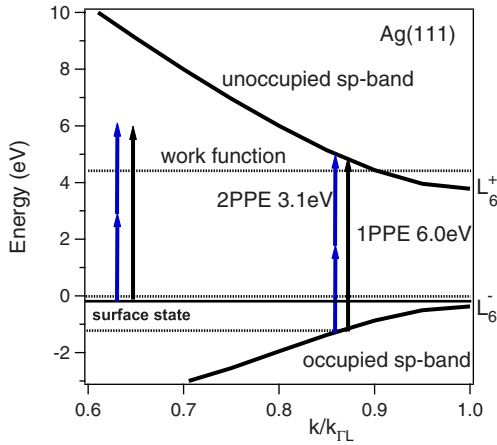
WINKELMANN *et al.*PHYSICAL REVIEW B **76**, 195428 (2007)

FIG. 1. (Color online) Bulk band structure along the ΓL line relevant for normal emission Ag(111), with indicated direct optical transitions between occupied and unoccupied sp bands by 2PPE and 1PPE. Also shown is the position of the occupied Shockley surface state at -65 meV, which is excited to a free-electron final state.

photoemission has been observed for Ag(111),^{25,26} and the influence of collective surface plasmon excitations on the angle- and energy-resolved photoyield was studied.²⁷

The 2PPE studies involving Ag(111) have mainly focused on the observation of image-potential states and their relaxation dynamics.^{28–30} Concerning direct optical bulk transitions, it was shown that a systematic comparison of 1PPE and 2PPE measurements can be used to differentiate between surface states and bulk contributions.³¹ An analysis of near-threshold two-photon electron emission from smooth and rough polycrystalline silver films has been given on the basis of a two-orthogonalized-plane-wave model for the involved sp bands.³²

In a previous study, it was shown how the 2PPE spectrum of Ag(111) at $\hbar\omega=3.1$ eV can be simulated using optical Bloch equations and a nearly-free-electron model for the band structure.³³ In this contribution, we will present results of angle-dependent 2PPE and 1PPE measurements from the Ag(111) surface. Specifically, we will look at the effects observed when a transition between occupied and unoccupied sp bands is excited either by single photons (1PPE) or by simultaneous excitation by two photons (2PPE) of nearly half the energy used for 1PPE. For electrons emitted in the direction of the surface normal, the corresponding band structure is shown in Fig. 1. It will be shown that based on the observed dispersion, the direct optical transition from occupied to unoccupied sp -bulk bands agrees with the theoretically expected dispersion obtained from a nearly-free-electron band-structure model. The observed dispersion of this transition is very similar for 1PPE and 2PPE measurements on the Ag(111) surface. The intensity variation observed in the angle-dependent 2PPE spectra can be well explained by the application of the Fresnel equations of classical optics. From this model, we expect characteristic differences between the angular intensity variations in 1PPE and 2PPE, which should be almost independent of the spe-

cific substrate and photon energy used if additional influences like surface photoemission are negligible. This is shown by comparison with measurements on Cu(001). In contrast, the 1PPE intensity from Ag(111) does not fit a simple Fresnel model and seems to be strongly influenced by interference from surface photoemission.

Additionally, we suggest that the strong refraction effect of the very low kinetic energy photoelectrons at off-normal detection is a sensitive probe to gain insight into the behavior of the inner potential, which is not exactly known at these energies and which is expected to be strongly influenced by exchange and correlation effects.³⁴ At the same time, knowledge of the potential at the surface is crucial for the interpretation of imaging techniques using low-energy electrons and for the understanding of the chemical reactivity of surfaces.

The structure of the paper is as follows: after specifying the experimental details, we will extract from the general features of photoemission theory a phenomenological model which takes into account the most relevant angular dependencies. Then we will apply this model for the analysis of the experimental data. We will also discuss the implications of our findings for the mapping of electronic structure by angle-resolved 2PPE.

II. EXPERIMENTAL DETAILS AND RESULTS

For the photoemission measurements, a commercial Ag(111) crystal was prepared by standard techniques of multiple, sequential cycles of Ar⁺-ion sputtering and annealing under UHV conditions. The sample surface quality was checked by the quality of the photoemission spectra converging to minimum inelastic background and maximum work function.

The photoemission light source is a self-made Ti:sapphire oscillator with chirped mirrors for dispersion compensation operating at 90 MHz repetition rate. For the two-photon photoemission measurements, second harmonic pulses are generated from the fundamental in an 80 μm $\beta\text{-BaB}_2\text{O}_4$ (BBO) crystal (3.1 eV photon energy, 200 meV bandwidth, and 10 fs pulse length). Additionally, one-photon photoemission spectra were measured with the fourth harmonic of the Ti:sapphire laser, which is generated by subsequent frequency doubling of the second harmonic.

The angle-resolved photoemission spectra are recorded under UHV conditions (10^{-10} mbar) at 100 K sample temperature by a commercial hemispherical electron analyzer (OMICRON EA125) with an angular resolution of 0.5° and an energy resolution of 40 meV. For the measurements, the sample was biased at -2 V. At the UHV chamber, the angle of the p -polarized incident light and the direction of the electron analyzer are fixed to 45° , leading to a simultaneous change in incidence and emission angles when the sample is rotated along an axis perpendicular to the optical plane for angle-dependent measurements (see Fig. 2).

In Fig. 3, we show an angle-dependent measurement of 2PPE and 1PPE spectra from Ag(111) for p -polarized incident light. The spectral features due to the sp -band transition and the surface state are clearly discernable. The surface state has dispersed above the Fermi level for detection angles

ANGLE-DEPENDENT STUDY OF A DIRECT OPTICAL...

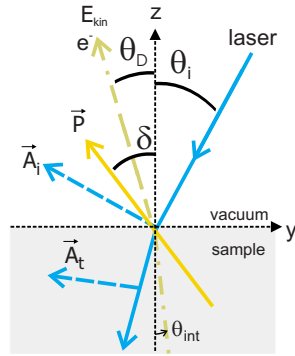


FIG. 2. (Color online) Geometry used for angle-dependent measurements. The direction between incident light and detected electrons is fixed to $\theta_i = 45^\circ + \theta_D$. The direction of the photoemitted electron inside the sample is θ_{int} . Incident and refracted vector potentials \vec{A}_i and \vec{A}_r . Momentum matrix element \vec{P} , characterized by the angle δ .

larger than 10° , while the sp -band transition can be seen in the whole observed energy range. The 2PPE intensity is clearly asymmetric with respect to the surface normal, while the 1PPE intensity looks more symmetric. The increased intensity of the surface state relative to the sp -band transition in 1PPE with respect to 2PPE is caused by a stronger surface photoemission component and, to a lesser extent, the decreased spectral width of the 6.0 eV pulses, which is due to the phase matching limits of the BBO crystal.

From the width of the observed spectra at normal emission, the work function can be deduced as 4.5 eV in accordance with previous studies.^{26,28}

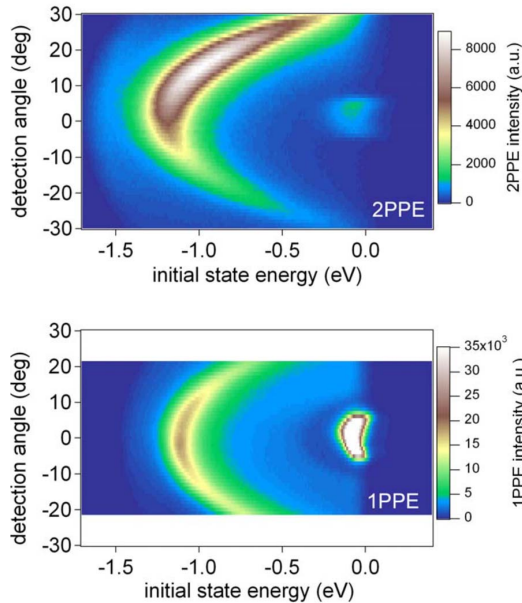


FIG. 3. (Color online) Experimentally measured intensities from Ag(111) by 2PPE ($\hbar\omega = 3.1$ eV) and 1PPE ($\hbar\omega = 6.0$ eV). Intensity scales are indicated.

PHYSICAL REVIEW B 76, 195428 (2007)

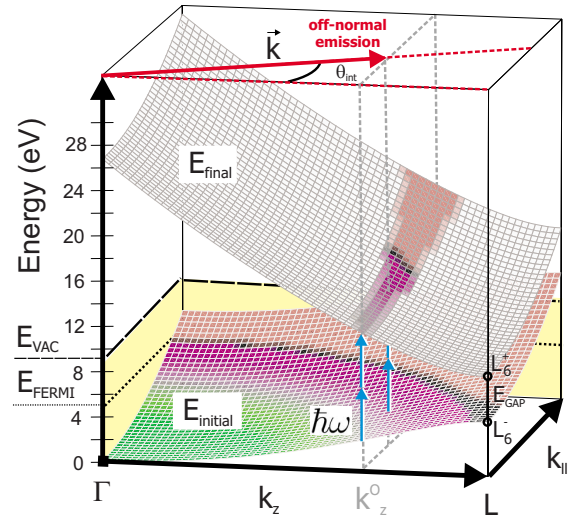


FIG. 4. (Color online) Nearly-free-electron band structure for initial and final sp states involved in the direct optical two-photon transition on Ag(111). Initial states which can be directly excited have been mapped onto the final state band. Only states up to the Fermi energy (black border) are occupied. The emitted direction is changed from θ_{int} by refraction when the photoelectron escapes the sample.

III. THEORETICAL MODELING OF PHOTOEMISSION

A. Dispersion

We first need to explain the observed change in the peak position of the sp -band transition when changing the direction of the detected outgoing electrons. To accomplish this, we model the relevant initial and final state band structures to define the curve of constant energy difference that shows where the incident radiation can induce direct optical transitions between these states.³⁵

The sp bands relevant for our observed transitions are well described by a nearly-free-electron (NFE) model taking into account two orthogonalized plane waves (OPW).³⁶ We show the initial and final sp -band states near the Γ - L line calculated using this approximation in Fig. 4. The 2-OPW NFE model implies rotational symmetry around the Γ - L line. The size of the gap between L_6^- and L_6^+ is taken to be 4.2 eV, with L_6^- located -0.3 eV below the Fermi energy.⁹ The band bottom is at 9.5 eV below the vacuum level.

The direct optical transition will take place in a region of k space where the difference between initial and final states is equal to the photon energy for 1PPE or to two times the photon energy in 2PPE. In this way, the perpendicular and parallel components of the \vec{k} vectors taking part in the transition and, thus, the internal angle θ_{int} of \vec{k} with respect to the surface normal in the $\langle 111 \rangle$ direction are determined. In the 2-OPW NFE model, these transitions take place at fixed k_z along Γ - L and varying parallel momentum $k_{||}$ (Fig. 4). This is a special feature of the free (1-OPW) and nearly free (2-OPW) electron models. For a more general band structure, the curves of constant energy difference are more complicated.

WINKELMANN *et al.*PHYSICAL REVIEW B **76**, 195428 (2007)

To describe the refraction of the photoelectrons, we assume that a potential step $V_R > 0$ has to be overcome when crossing the sample-vacuum barrier. In the NFE model, this energy corresponds to the height E_{vac} of the vacuum level above the band bottom. As the kinetic energies are measured with respect to the vacuum level, the electrons inside the sample will have an energy of $E_{kin} + V_R$. This will have the effect that electrons emitted at the angle θ_{int} inside the sample will be detected at the angle θ_D in vacuum:

$$\frac{\sin \theta_D}{\sin \theta_{int}} = \sqrt{\frac{E_{kin} + V_R}{E_{kin}}}. \quad (1)$$

By using this simplified model, the dispersion of the direct sp transition is determined by a small number of parameters: the gap size $E_{gap} = 2V_{111}$, with V_{111} the pseudopotential Fourier component of the reciprocal lattice vector $\vec{G} = (\bar{1}, \bar{1}, \bar{1})$, the position of vacuum E_{vac} , and the Fermi energy E_{Fermi} (Fig. 4), with the work function $\Phi = E_{vac} - E_{Fermi}$. Furthermore, in the NFE model, the momentum matrix element has the simple form³⁷ of $\vec{P}_{if} \propto \vec{G}$, which will be relevant for the analysis of the observed intensities. Of course, we can expect this model to be valid only for a limited range of parallel momenta k_{\parallel} beyond which the band structure will start to deviate from the simple NFE model assumed here.

B. Photoemitted intensity

By using first order perturbation theory to describe the interaction of the electromagnetic field with the sample atoms,^{1,38} a Fermi golden rule expression for the photocurrent $I(f)$ from an initial wave function ψ_i emitted into the final state gives

$$\begin{aligned} I(f)^{1PPE} &\propto |\langle \psi_f | V_I | \psi_i \rangle|^2 \delta(E_f - E_i - \hbar\omega) \\ &= |M_{if}|^2 \delta(E_f - E_i - \hbar\omega), \end{aligned} \quad (2)$$

where ψ_f is the final state wave function in the form of a time-reversed low-energy electron diffraction (LEED) state, and V_I is the interaction potential due to the incident radiation:

$$V_I = \frac{-e}{2mc} [\vec{A} \cdot \vec{p} + \vec{p} \cdot \vec{A}]. \quad (3)$$

Only terms linear in \vec{A} are considered. The matrix element between initial and final states can be written as

$$M_{if} = \frac{ie\hbar}{2mc} \langle \psi_f | \vec{A}(\vec{r}) \cdot \nabla | \psi_i \rangle = \vec{A} \cdot \vec{P}_{if}, \quad (4)$$

where \vec{P}_{if} is called the momentum matrix element. The Coulomb gauge $\nabla \cdot \vec{A} = 0$ has been applied, which, however, is valid only in the bulk. At the surface, the nonvanishing $\nabla \cdot \vec{A}$ term will cause an additional coherent contribution which is usually termed surface photoemission and which we think is relevant for the 1PPE measurements from Ag(111) (see below).

The two-photon photoemission intensity is obtained from second order time-dependent perturbation theory as a sum

involving all possible intermediate states^{39,40} m :

$$I(f)^{2PPE} \propto \left| \sum_m \frac{\langle \psi_f | V_I | \psi_m \rangle \langle \psi_m | V_I | \psi_i \rangle}{E_m - E_i - \hbar\omega} \right|^2 \delta(E_f - E_i - 2\hbar\omega). \quad (5)$$

For the observed transition in Ag(111), there are no resonant intermediate states. For this case of nonresonant excitation in a nearly-free-electron two-band model, the square of the product of the matrix elements in Eq. (5) can be shown³² to depend as $|M_{fm} M_{mi}^*|^2 \propto \cos^4 \Theta$ on the angle Θ between \vec{A} and \vec{p} , so that we write the photoemitted intensity with an effective momentum matrix element \vec{P}_{eff} :

$$I(f)^{2PPE} \propto |\vec{A} \cdot \vec{P}_{eff}|^4. \quad (6)$$

The observed angle-dependent intensities can now be thought of as originating from two main types of contributions. Firstly, there are angle-dependent changes of the electric field vector in the surface region due to the change in the angle of incidence of the laser radiation. In traditional optics, this is described by the Fresnel equations, which quantify how the magnitude and the direction of the incident vector potential as well as the relative phase between the s and p polarization components will change when entering the metal. This is described by complex amplitude reflection and transmission coefficients.⁴¹ Secondly, the coupling of this incident polarization to the electron system will lead to an angle-dependent probability of detecting the excited electrons in the direction specified by the analyzer.

If one is only interested in the total yield of photoelectrons, irrespective of their emission direction, the total energy deposited in the sample should be relevant. This will be proportional to $(1 - R_{p(s)})^n$, where $R_{p(s)}$ is the reflectivity of the sample for $p(s)$ -polarized incident light and n is the order of the photoemission process. For p -polarized light, increased photoemission should occur near the pseudo-Brewster angle, where the reflectivity is minimized and more intensity is transmitted into the sample. Good agreement with these expectations has been shown in multiphoton photoemission experiments from tungsten and copper.⁴²

For angle-resolved photoemission, the transition matrix element is governed to a large extent by the relative orientation of the vector potential \vec{A}_i and the photoelectron momentum \vec{p} , as can be seen from Eq. (3). These effects are separated in Eq. (4) into the vector potential \vec{A}_i and the momentum matrix element \vec{P}_{if} , which depends on the angle of the emitted final state electron. In our experiment, this angle is in a fixed relation to the incidence angle of the laser. We will show below that the variation in the z component of \vec{A}_i (Fig. 2) is the most relevant contribution for p -polarized incident light.

A nonvanishing $\nabla \cdot \vec{A}$ term due to the symmetry breaking by the surface will provide an additional coherent channel by which initial and final states can be coupled. Because the $\nabla \cdot \vec{A}$ term is only relevant in a very narrow spatial region near the surface, this part of the interaction potential provides Fourier components of a broad spectrum of crystal mo-

mentum. This means that initial and final states of different crystal momenta will be coupled, and the condition of vertical optical transitions in the reduced zone scheme is relaxed. The simplest model to account for the $\nabla \cdot \vec{A}$ term at the surface is a step dielectric function which leads to a contribution $dA_{\perp}(z)/dz$ proportional to $[\epsilon(\omega)-1]\delta(z)$, where in the real situation the delta function is broadened. The contribution of surface photoemission to the matrix element was estimated as^{26,43}

$$M_{if} \propto \vec{A}_i \cdot \vec{P}_{if} + \Delta A_z \frac{C}{2d} \equiv \vec{A}_i \cdot \vec{P}_{if} + M_S(\vec{A}_i, \epsilon(\omega), C_S), \quad (7)$$

with the change of the z component of \vec{A} when going from vacuum into the sample over an effective thickness d :

$$\Delta A_z = |\vec{A}_i| \left(\frac{2 \cos \theta_i \sin \theta_i}{\epsilon \cos \theta_i + \sqrt{\epsilon - \sin^2 \theta_i}} - \sin \theta_i \right) \quad (8)$$

for the incident vector potential \vec{A}_i . If this model is assumed, an additional complex fit parameter $C_S = C/2d$ enters into the description of the angle-dependent intensities.

Several other processes are present which might influence the angular dependence of the photoemitted intensity. For instance, more of the excited photoelectrons from a certain depth will be scattered inelastically when they have to travel longer inside the material at larger exit angles. The electrons which are left and approach the solid-vacuum barrier from inside the sample within a certain solid angle are refracted into a larger solid angle in vacuum. This again reduces the intensity at larger exit angle in a symmetric way like the inelastic losses. Also, the observed peak shapes will be changed due to the varying \vec{k} -space resolution with exit angle. All these effects will be most pronounced at exit angles typically larger than 30° , and will be symmetric as a function of the emission angle with respect to the surface normal. Thus, if they are relevant, they are expected to reduce any asymmetry that is present rather than be a cause of it.

1. Electromagnetic field at the surface

At the solid-vacuum interface, the incident light is subject to refraction. This causes the vector potential inside the sample to be different than in vacuum. We will assume in our model that the Fresnel equations^{44,45} can be used to give the components of the transmitted vector potential \vec{A}_t as a function of the incident vector potential \vec{A}_i and the dielectric function of the substrate $\epsilon(\omega)$:

$$\vec{A}_t = \vec{A}_i(\vec{A}_i(\theta_i), \epsilon(\omega)). \quad (9)$$

If the dipole matrix element for the observed transition is directed along the surface normal, the photoemitted intensity is governed by the A_z component of the vector potential. This is given by^{44,45}

$$\frac{A_z}{A_0} = \frac{2 \cos \theta_i \sin \theta_i}{\epsilon \cos \theta_i + \sqrt{\epsilon - \sin^2 \theta_i}}. \quad (10)$$

In Fig. 5, it can be seen that the angular variation of the A_z

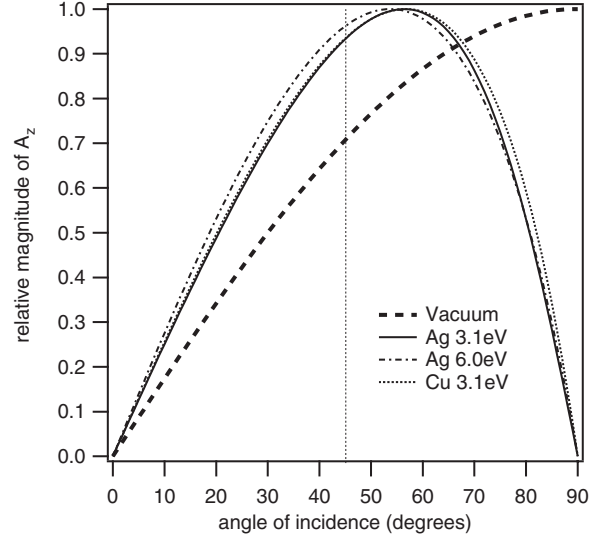


FIG. 5. Relative variation of the magnitude of the A_z component of the field inside the substrate for different photon energies and materials.

component is almost independent of the photon energy and whether we look at silver or copper. This behavior applies to a large selection of materials and photon energies used in angle-resolved photoemission, as can be seen, for instance, in Ref. 45. This means that our results will be of general significance for the comparison of angle-dependent linear and nonlinear photoemission experiments in our type of setup because, obviously, the optical properties at the surface do not have to be known very exactly.

We have to stress here that our treatment will be valid only if the observed transition can be assumed to take place inside the bulk, where the refracted electromagnetic field is relevant. The situation will become more difficult to treat if one is interested in transitions involving surface states, where there is interference of reflected and refracted radiations and where the influence of boundary effects of the electromagnetic field and of collective excitations like surface plasmons is most pronounced. In the general case, for arbitrary direction of the momentum matrix element, one has to include, of course, all components of the electromagnetic field in the analysis. Also, for the analysis of photoemission from *adsorbed* species, the field just *outside* the surface is relevant. Approaches to describe the corresponding electric fields are known from surface infrared spectroscopy.⁴⁶ For the case of 2PPE, angle-dependent measurements then allow conclusions about the direction of the dipole matrix elements for the photoemission process from the adsorbate.⁴⁷

2. Momentum matrix element

The momentum matrix element \vec{P}_{if} which appears in Eq. (4) is a complex vector which, in general, will depend on the initial and final states under investigation; especially, it will be, in general, a function of the magnitude and direction of the wave vector of the emitted photoelectron.

WINKELMANN *et al.*

PHYSICAL REVIEW B 76, 195428 (2007)

The study of the momentum matrix element by angle-dependent photoemission is potentially powerful because it gives information on the wave functions of the states involved and their symmetry character.⁴⁸ Because in our setup the photoelectron emission angle changes, the corresponding change in \vec{P}_{if} has to be considered. Basic insight into the functional behavior of \vec{P}_{if} can be gained from considerations of localized core level states of oriented atoms. Here, \vec{P}_{if} can be explicitly written down as a function of the initial state quantum numbers (l, m), radial matrix elements for the ($l+1$) and ($l-1$) excitation channels, the corresponding partial wave scattering phase shifts due to the emission process, and the detection direction θ_D .⁴⁹ Already for this very simple case, rather complicated analytical expressions result.

In contrast to photoemission from single, localized core level states, a continuum of states defined by their band index and three-dimensional wave vector \vec{k} has to be considered in the case of photoemission from valence bands. By using the picture of a linear combination of atomic orbitals (LCAOs), it is possible to express the valence band states as coherent combinations of basis states localized at the atoms of the crystal unit cell.³⁸ Writing the final state in the same basis set allows us, in principle, to calculate \vec{P}_{if} [see Eq. (4)] and to gain insight into the angular distributions contributed by certain types of atomic orbitals. For the simplified case of emission from a single type of atomic orbital, the result is basically a product of the angular distribution caused by the single atomic orbital, which is then modified by a photoemission structure factor describing interference caused by the periodic arrangement of this atomic orbital.⁵⁰

These interference effects due to the plane wave part in the initial and final state wave functions will be dominating if we switch from the LCAO view to the 2-OPW nearly-free-electron model. As shown in Ref. 37, \vec{P}_{if} will be a constant vector pointing into the direction of the reciprocal lattice vector \vec{G} involved in the generation of the NFE bands:

$$\vec{P}_{if} \propto \vec{G}(V_G/\hbar\omega). \quad (11)$$

For our case, we can, thus, assume that the momentum matrix element will be directed in the direction of the surface normal, and the angular dependence of the A_z component of the electric field in the sample will be a determining factor of the overall angular dependence of the photoemitted intensity under p -polarized excitation.

The 2-OPW model expression, however, clearly is valid only in a limited region of \vec{k} space. An increasing number of plane wave components will be necessary to describe an extended region of the band structure. The direction and magnitude of \vec{P}_{if} will then be determined by the respective wave vectors and pseudopotential components of the initial and final states in a more complicated but straightforward way.¹¹

To summarize, from the various angle-dependent factors discussed above, the following simple model for the photoemitted angle-dependent intensities in our experimental setup emerges:

$$I_{if}^{nPPE} \propto |A_z(\theta_i, \epsilon) \cdot P_z|^{2n}. \quad (12)$$

In Fig. 6, we show how the angular dependence of the A_z

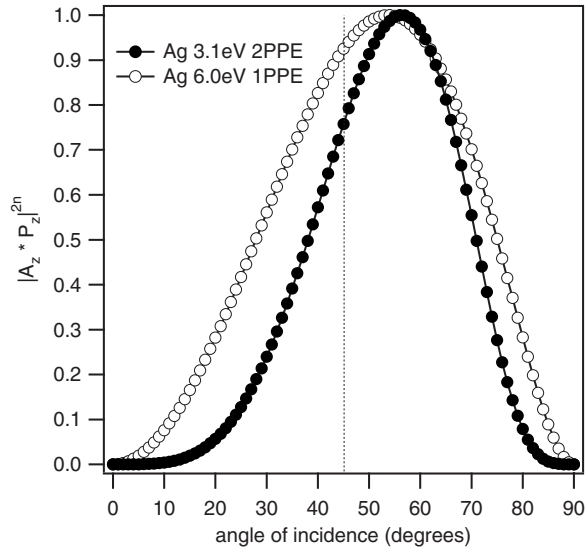


FIG. 6. Relative variation of the intensity factor $|A_z P_z|^{2n}$ for n PPE from silver assuming constant P_z and considering only effects due to the changing angle of incidence.

components shown in Fig. 5 translates to the photoemitted intensity by looking at the square (1PPE) or the fourth power (2PPE) of A_z . Due to the higher nonlinearity, a sharper and more asymmetric distribution with respect to detection relative to the surface normal at 45° is expected for 2PPE.

IV. RESULTS AND DISCUSSION

We will first discuss the results relevant to the observed dispersion of the sp -band transition peak and then go on to analyze the observed intensity variation.

A. Dispersion of the observed transitions

We have calculated the theoretically expected dispersion for a 2-OPW nearly-free-electron band structure of the sp bands near the Γ - L direction using a value of $E_{gap} = 2V_{111} = 4.2$ eV,^{9,10} the perpendicular component of the reciprocal lattice vector $\vec{G}(\bar{1}, \bar{1}, \bar{1}) = g_z = -2\pi/2.36$ Å, and a variable inner potential of V_0 . The optical transitions and the observed angles outside the sample have been determined for the transition energies of 6.0 and 6.2 eV, corresponding to 1PPE and 2PPE, respectively.

To estimate the influence of the bias voltage on the observed parallel component of k , we have also measured the dispersion of the surface state and found effective masses of $m_{eff} = 0.3$. This is slightly less than the published values of $m_{eff} = 0.40$ (Ref. 20) or $m_{eff} = 0.45$,¹⁹ and means that we will observe an apparently increased dispersion of the sp -band transition with angle, which, in turn, leads to an inner potential which is systematically too low. A large inner potential has the effect to limit the k space which is accessible and, thus, would reduce the observed dispersion.

The obtained theoretical angular dispersions of the sp -band transition are compared to the experimental ones in

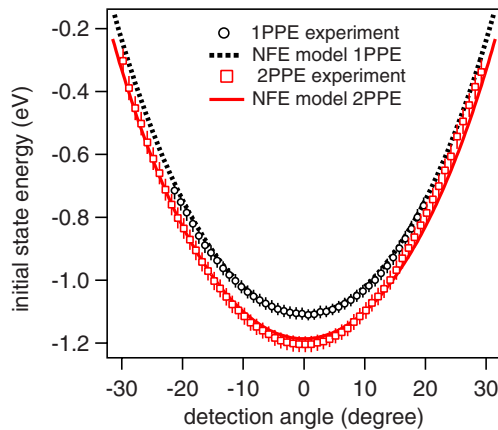


FIG. 7. (Color online) Comparison of the experimentally measured and calculated dispersions from a 2-OPW nearly-free-electron model for the sp -band transition on Ag(111) by 1PPE ($\hbar\omega = 6.0$ eV) and 2PPE ($\hbar\omega = 6.2$ eV).

Fig. 7. Our model only slightly underestimates the change in apparent binding energy at normal emission when going from 6.0 to 6.2 eV photon energy. This should be considered as a reliable measure of the degree of agreement with the assumed band-structure model because the dispersion with energy at normal emission is not influenced by electron refraction. The binding energy changes by approximately 0.1 eV, which is half the effective photon energy change of 0.2 eV. This behavior is caused by the dispersion of both the initial and final sp -band states, and the observed value agrees with previous studies.^{28,31}

Good agreement is also obtained for the angular dispersion, considering the simplicity of the model we applied. However, in addition to the dispersion caused by the change in the observed direct transition in \vec{k} space, the change of the peak position observed in the spectrum will be governed to a large extent by refraction. Refraction is strong because the potential step V_R [Eq. (1)] that has to be overcome at the surface is of nearly the same size as the energy of the photoelectron inside the material. This means that the influence of the potential step has to be known sufficiently well to still allow insight into the band structure of the sample by using very low energy photoelectrons. We find the best agreement with values of the inner potential $V_0 = V_R - \Phi = 2$ eV when neglecting the effect of the bias voltage and of $V_0 = 5$ eV when assuming that the relative change in the parallel component of k is roughly similar to the value observed for the surface state relative to the published values. In previous ARPES studies, inner potentials V_0 of 4 eV,¹⁴ 5 eV,¹³ and 6.7 eV (Ref. 51) (defined with respect to the Fermi level) have been used. This compares quite well with our value. It has to be noted, however, that in most ARPES studies, the inner potential is mainly used to fix the position of the free electron final state, and then to infer from this the initial state dispersion in synchrotron experiments with varying photon energy and electron detection along the surface normal, which avoids refraction effects. Also, because of the higher photon energies in ARPES experiments, the refraction effects

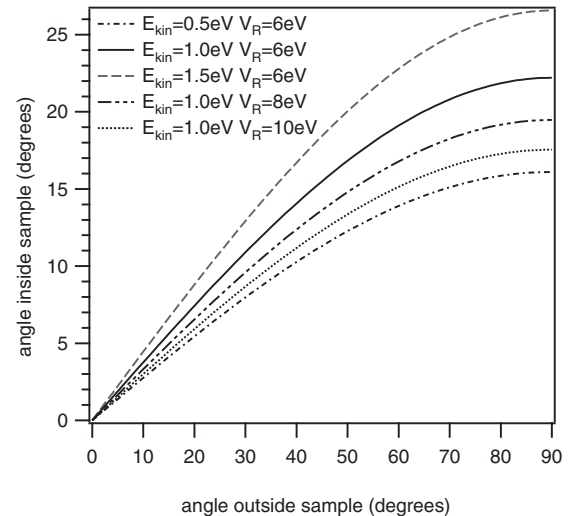


FIG. 8. Refraction of photoelectrons limits the range of angles inside the sample which can be sampled outside. Calculations according to Eq. (1). Electrons which are detected at angles up to $\pm 30^\circ$ originate from a cone of typically 10° or less in our experimental setup.

are still comparatively less significant even at off-normal detection.

In a realistic band structure, one and the same parameter does not describe the final state band structure and the refraction effect at the same time. Also, the inner potential is known to be energy dependent from LEED studies.⁵² Taking all this into account, there is considerable uncertainty about the exact value of the potential step that causes refraction, especially at the very low energies involved in 2PPE experiment. In the ARPES experiments, a spread of nearly 3 eV in V_0 is seen in the different studies. While this variation might be insignificant for band mapping in ARPES experiments at high photon energies, the error in the outside angles introduced at low electron energies will overwhelm the effects caused by the band structure, because much of the observed dispersion can be adjusted by simply assuming a different inner potential V_0 . If we reverse the assumptions realizing that the sp -band structure is sufficiently well known from ARPES studies with high energy photons, we have a sensitive probe of the inner potential in the form of the very low energy photoelectrons with a known initial k -space distribution before the refraction. In this sense, the well-defined sp -band transition could serve as a calibration against which to measure the inner potential effects.

The knowledge of the inner potential is crucial for the interpretation of spectroscopic and imaging techniques which involve low-energy electrons,³⁴ for instance, low-energy electron microscopy and photoemission electron microscopy. Furthermore, the effective potential at very low energies is influenced to a large extent by exchange and correlation effects,³⁴ and as only a few methods exist for the measurement of the surface potential step,⁵³ the analysis of low-energy photoelectrons could provide additional insight about the importance of these interactions.

WINKELMANN *et al.*PHYSICAL REVIEW B **76**, 195428 (2007)

As we show in Fig. 8, all electrons detected in vacuum will originate from a cone with half opening angle near 10° inside the sample for the kinetic energies employed in our experiment. This will effectively mean that the sensed region of reciprocal space is reduced considerably, and along with this, the sensitivity to any change in the momentum matrix element \vec{P}_{if} . This does not mean, however, that bulk band mapping by angle-dependent 2PPE is generally impossible. Let us assume that typically the largest kinetic energies in 2PPE experiments can be of the order of the work function, e.g., $E_{kin}=4$ eV, then taking $V_R \approx 8$ eV and a maximum outside detection angle of $\theta_D=70^\circ$, one arrives at internal angles θ_{int} of approximately 30° , which translate to a parallel k component $k_{\parallel}^{max} = \sqrt{(2m/\hbar^2)(E_{kin} + V_R)(1 - \cos^2 \theta_{int})} = 0.88 \text{ \AA}^{-1}$, which is of the order of the Brillouin zone dimension. Thus, significant information about the dispersion of the parallel wave vector components can be obtained in principle.

To summarize, on one hand, the low energy of the observed electrons is clearly a severe practical limitation for their application to map electronic band structure if the refraction cannot be taken into account quantitatively. On the other hand, if we assume that the sp -band structure is known sufficiently well, we have a sensitive probe of the inner potential.

B. Intensities

Because of the inherent asymmetry in the experimental setup, for both 1PPE and 2PPE, an asymmetric angular intensity distribution is expected. Because the incident angle θ_i is changed asymmetrically with respect to the surface normal, all other factors depending on the incidence angle are expected more or less to also show this asymmetry. This can be seen in Fig. 6. Both the 1PPE and 2PPE distributions should be clearly asymmetric with respect to the surface normal, and the 2PPE intensity should be narrower. The 1PPE intensity that we observe (Fig. 3), however, does not fit the simple Fresnel model. Instead, we suggest that, in this case, we see the influence of surface photoemission. This is supported by 1PPE measurements on Cu(001), where we observe excellent agreement with the Fresnel model.

We have simulated the photoemitted intensities as a function of the detection angle for the case of 1PPE and 2PPE according to the model of Eq. (12). For the dielectric function of silver, we used the values of $\epsilon = (n+ik)^2$, with $(n+ik)=0.05+2.275i$ ($\hbar\omega=3.1$ eV) and $(n+ik)=1.18+1.312i$ ($\hbar\omega=6.0$ eV).⁵⁴ For the dielectric function of copper, we used the values of $(n+ik)=1.32+2.12i$ ($\hbar\omega=3.1$ eV) and $(n+ik)=1.01+1.60i$ ($\hbar\omega=6.0$ eV),⁵⁴ with the final result not very sensitively depending on the exact value of all of these parameters.

The peaks of the sp -band transitions in the experimental photoemission spectra were fitted to Gaussians on a linear background, and from this fit, the intensity in the peak was obtained. The results are shown in Fig. 9. Very good agreement is found assuming an effective momentum matrix element pointing along the surface normal and having a constant magnitude. This is in agreement with the expectation from the 2-OPW NFE model, where \vec{P}_{if} will be constant and

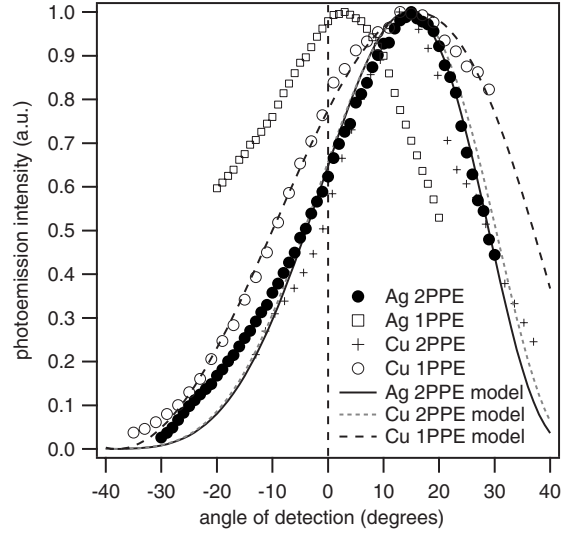


FIG. 9. Comparison of experimentally measured and simulated intensities in the sp -band transition on Ag(111) by 2PPE and 1PPE, and measured and simulated intensities for 2PPE and 1PPE from electrons with initial states at the Fermi energy of Cu(001). The expected distribution for 1PPE from Ag(111) according to the Fresnel model corresponds closely to the model curve shown for 1PPE from Cu(001). For both experiments, $\hbar\omega=3.1$ eV for 2PPE and $\hbar\omega=6.0$ eV for 1PPE.

point in the direction of $\vec{G}=(1,1,1)$. The agreement of the experimental data of Ag(111) is not as good at negative exit angles, which we attribute mainly to the uncertainty in extracting low peak intensities on an unknown background (note the very low intensity at negative angles in Fig. 3).

As can be seen in Fig. 9, the experimental intensities in 1PPE from Ag(111) do not fit the expected behavior of Fig. 6. To motivate why we think that this behavior is anomalous, we apply our model to a different substrate, Cu(001). So far, the only assumptions we have made for the analysis of the angle-dependent intensity on Ag(111) is that P_{if} is constant and points along the z axis. We also showed that the A_z component of the electric field at the surface shows a universal angle-dependent change with incidence angle. Thus, the intensity variation that we have observed in 2PPE on Ag(111) should be quite generally valid for transitions which are governed by this field component, also on different substrates. This is why we choose to compare in Fig. 9 the data measured on Cu(001). The intensity data were obtained for initial state electrons near the Fermi energy. For these electrons originating from the Cu sp band (Δ_1 symmetry), the optical selection rules for fcc surfaces (Δ_1 final state) dictate that again the A_z component is the most relevant near normal emission. So we should have a comparable intensity variation as on Ag(111). Figure 9 shows that this is indeed the case for the 2PPE measurements on Cu(001) and, moreover, that the 1PPE data from Cu(001) shows the expected broader intensity distribution with a pronounced asymmetry, in contrast to what is observed for 1PPE on Ag(111).

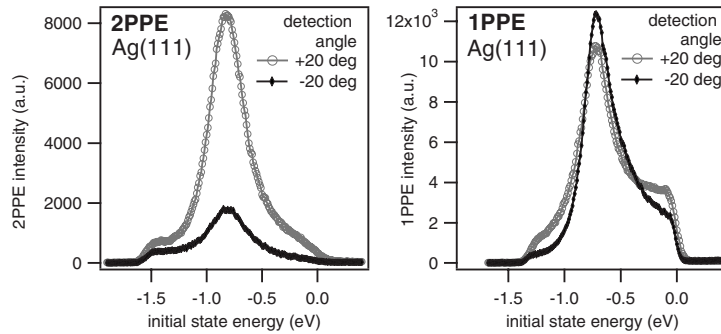


FIG. 10. Comparison of 1PPE and 2PPE spectra for detection angles symmetrically $\pm 20^\circ$ to the surface normal. The 1PPE spectra show the influence of surface photoemission, indicated by a very asymmetric peak shape and large background.

To analyze the 1PPE data further, we show in Fig. 10 1PPE and 2PPE spectra taken from Ag(111) (data from Fig. 3) at detection angles of $\pm 20^\circ$ to the surface normal. Firstly, one immediately notes the much more asymmetric peak shape of the 1PPE spectra as compared to a rather symmetric 2PPE peak. Secondly, the peak intensity relative to the background clearly shows an anomalous behavior for 1PPE. Whereas for 2PPE both peak height and background are increased at positive angles (larger A_z component), the 1PPE spectra show a larger background at positive angles, but with a reduced peak height. Both these observations point to the influence of surface photoemission. It has been shown previously that surface photoemission causes a very asymmetric peak shape for the sp -band transition on Ag(111).^{25,26} This asymmetry is created by additional photoemission due to transitions that do not need to conserve crystal momentum and which show up as a broad background in the spectrum. These transitions involve an increased range of k vectors different from the ones determined by crystal momentum conservation in the bulk sp -band transition. Our observations are also consistent with the fact that we observe an increased influence of surface photoemission at angles where the A_z component and also its change at the surface become larger according to Eq. (8). Because the surface photoemission is an alternative coherent pathway for photoemission, the surface and bulk photoemission channels interfere, modifying the intensity and asymmetry of the bulk transition peak. This is observed as the reduced peak height of the 1PPE transition as compared to an increased background. As is shown in Eq. (7), one can try to model the influence of surface photoemission by an additional complex fit parameter C_S in the transition matrix element, by which the interference between surface and bulk photoemissions is phenomenologically simulated. While we can obtain very good agreement with the measured data for a specific choice of C_S (not shown), the measured angular range of 1PPE spectra does not allow a final conclusion about the physical significance of this approach. Additionally, one should expect that the interference effects will be a function of the position of the sp -band peak in the spectrum, and thus, an energy-independent C_S might not be sufficient. This is why we limited ourselves to demonstrate that in agreement with previous studies, surface photoemission seems to have an appreciable angle-dependent effect also in our 1PPE measurements. In contrast, it has been shown previously that the 2PPE spectra can be simulated without taking into account surface photoemission.³³

This is consistent with our measurements.

Our observations are relevant in a further context. The Fresnel equations neglect the nonlocal influences on the electromagnetic field at the surface that would have to be described via a dielectric function $\epsilon(\vec{q}, \omega)$ that not only depends on the frequency ω but also on the wave vector \vec{q} .^{55,56} These effects are most pronounced near the plasmon energy, and lead to characteristic changes in the A_z component of the field in the first few angstroms of the surface. Because we were observing a bulk transition, the sensitivity to such optical effects intrinsic to the presence of a surface should be diminished. It is interesting to note, however, that such effects might be within reach of comparative 2PPE and 1PPE experiments. For instance, the plasmon resonance of silver is at 3.8 eV,⁵⁷ an energy which can be bracketed by common double- and single-photon energies to possibly acquire photoemission data which are more or less strongly influenced by nonlocal effects.⁵⁸ In this context, the observation that surface photoemission is unimportant in 2PPE with single-photon energies below the plasmon energy, but visible in 1PPE with a photon energy above the plasmon threshold, could be important.

V. SUMMARY

We have shown that the observed dispersion of the sp -band transition on Ag(111) in 1PPE and 2PPE can be analyzed using a nearly-free-electron model for the initial and final states involved. The observed dispersion agrees with the known band structure. To gain exact band-structure information, the strong refraction of the low-energy electrons needs to be taken into account quantitatively. This is limited by the degree to which the inner potential is known. We suggest using the low-energy photoelectrons from the sp -band transition as a probe for the potential step at the surface. The observed intensity distributions in 2PPE from Ag(111) can be well described by a phenomenological model which employs the Fresnel equations to calculate the electric field components inside the sample. Very good agreement is found using known optical constants and a momentum matrix element which is directed into the direction of the surface normal. By comparison to Cu(001), we have shown that the observed intensity distributions for 1PPE and 2PPE are

WINKELMANN *et al.*PHYSICAL REVIEW B **76**, 195428 (2007)

valid for this orientation of the momentum matrix element, and surface photoemission can be neglected. In contrast, the observed intensity distribution for one-photon photoemission from Ag(111) does not fit the simple Fresnel model. We interpret this as the influence of surface photoemission. With the mentioned limitations in mind, our study shows that relevant information about the electronic structure at surfaces can be obtained with angle-dependent 2PPE measurements.

ACKNOWLEDGMENTS

This research was supported by U.S. DOE DE-FG02-03ER15434 and PRF 44158-ACS grants. Some calculations were performed in the Environmental Molecular Sciences Laboratory, a user facility sponsored by the U.S. Department of Energy, Office of Biological and Environmental Research. A.K. thanks PRESTO JST for financial support.

*petek@pitt.edu

- ¹S. Hüfner, *Photoelectron Spectroscopy* (Springer Verlag, Berlin, 1995).
- ²J. K. Grepstad and B. J. Slagsvold, *Solid State Commun.* **34**, 821 (1980).
- ³P. Aebi, J. Osterwalder, R. Fasel, D. Naumovic, and L. Schlapbach, *Surf. Sci.* **307-309**, 917 (1994).
- ⁴J. Braun, *Rep. Prog. Phys.* **59**, 1267 (1996).
- ⁵R. Haight, *Surf. Sci. Rep.* **21**, 275 (1995).
- ⁶H. Petek and S. Ogawa, *Prog. Surf. Sci.* **56**, 239 (1997).
- ⁷S. Ogawa, H. Nagano, and H. Petek, *Phys. Rev. B* **55**, 10869 (1997).
- ⁸P. S. Wehner, R. S. Williams, S. D. Kevan, D. Denley, and D. A. Shirley, *Phys. Rev. B* **19**, 6164 (1979).
- ⁹J. G. Nelson, S. Kim, W. J. Gignac, R. S. Williams, J. G. Tobin, S. W. Robey, and D. A. Shirley, *Phys. Rev. B* **32**, 3465 (1985).
- ¹⁰M. A. Mueller, A. Samsavar, T. Miller, and T.-C. Chiang, *Phys. Rev. B* **40**, 5845 (1989).
- ¹¹H. Becker, E. Dietz, U. Gerhardt, and H. Angermüller, *Phys. Rev. B* **12**, 2084 (1975).
- ¹²D. J. Spanjaard, D. W. Jepsen, and P. M. Marcus, *Phys. Rev. B* **15**, 1728 (1977).
- ¹³S. C. Wu, H. Li, J. Sokolov, J. Quinn, Y. S. Li, and F. Jona, *J. Phys.: Condens. Matter* **1**, 7471 (1989).
- ¹⁴H. Wern, R. Courths, G. Leschik, and S. Hüfner, *Z. Phys. B: Condens. Matter* **60**, 293 (1985).
- ¹⁵E. Tamura, R. Feder, B. Vogt, B. Schmiedeskamp, and U. Heinzmann, *Z. Phys. B: Condens. Matter* **77**, 129 (1989).
- ¹⁶P. Heimann, H. Neddermeyer, and H. F. Roloff, *J. Phys. C* **10**, L17 (1977).
- ¹⁷H. F. Roloff and H. Neddermeyer, *Solid State Commun.* **21**, 561 (1977).
- ¹⁸T. C. Hsieh, P. John, T. Miller, and T.-C. Chiang, *Phys. Rev. B* **35**, 3728 (1987).
- ¹⁹R. Paniago, R. Matzdorf, G. Meister, and A. Goldmann, *Surf. Sci.* **336**, 113 (1995).
- ²⁰G. Nicolay, F. Reinert, S. Schmidt, D. Ehm, P. Steiner, and S. Hüfner, *Phys. Rev. B* **62**, 1631 (2000).
- ²¹N. E. Christensen, *Phys. Status Solidi B* **54**, 551 (1972).
- ²²O. Jepsen, D. Glötzel, and A. R. Mackintosh, *Phys. Rev. B* **23**, 2684 (1981).
- ²³H. Eckardt, L. Fritsche, and J. Noffke, *J. Phys. F: Met. Phys.* **14**, 97 (1984).
- ²⁴G. Panaccione, G. Cautero, M. Cautero, A. Fondacaro, M. Grioni, P. Lacovig, G. Monaco, F. Offi, G. Paolicelli, M. Sacchi, N. Stojic, G. Stefani, R. Tommasini, and P. Torelli, *J. Phys.: Condens. Matter* **17**, 2671 (2005).
- ²⁵T. Miller, W. E. McMahon, and T.-C. Chiang, *Phys. Rev. Lett.* **77**, 1167 (1996).
- ²⁶T. Miller, E. D. Hansen, W. E. McMahon, and T. C. Chiang, *Surf. Sci.* **376**, 32 (1997).
- ²⁷S. R. Barman, C. Biswas, and K. Horn, *Phys. Rev. B* **69**, 045413 (2004).
- ²⁸K. Giesen, F. Hage, F. J. Himpsel, H. J. Riess, and W. Steinmann, *Phys. Rev. Lett.* **55**, 300 (1985).
- ²⁹R. W. Schoenlein, J. G. Fujimoto, G. L. Eesley, and T. W. Capehart, *Phys. Rev. B* **43**, 4688 (1991).
- ³⁰R. L. Lingle, N. H. Ge, R. E. Jordan, J. D. McNeill, and C. B. Harris, *Chem. Phys.* **205**, 191 (1996).
- ³¹S. Pawlik, R. Burgermeister, M. Bauer, and M. Aeschlimann, *Surf. Sci.* **402-404**, 556 (1998).
- ³²V. M. Shalaev, C. Douketis, T. Haslett, T. Stuckless, and M. Moskovits, *Phys. Rev. B* **53**, 11193 (1996).
- ³³N. Pontius, V. Sametoglu, and H. Petek, *Phys. Rev. B* **72**, 115105 (2005).
- ³⁴D. K. Saldin and J. C. H. Spence, *Ultramicroscopy* **55**, 397 (1994).
- ³⁵R. Courths and S. Hüfner, *Phys. Rep.* **112**, 53 (1984).
- ³⁶R. Y. Koyama and N. V. Smith, *Phys. Rev. B* **2**, 3049 (1970).
- ³⁷A. I. Golovashkin, A. I. Kopeliovich, and G. P. Motulevich, *Sov. Phys. JETP* **26**, 1161 (1968).
- ³⁸W. Schattke, M. A. Van Hove, F. J. Garcia de Abajo, R. Diez Muino, and N. Mannella, *Solid-State Photoemission and Related Methods: Theory and Experiment* (Wiley-VCH, 2003), pp. 50–115.
- ³⁹R. Loudon, *The Quantum Theory of Light* (Oxford University Press, New York, 2000).
- ⁴⁰H. Ueba and B. Gumhalter, *Prog. Surf. Sci.* **82**, 193 (2007).
- ⁴¹M. V. Klein and T. E. Furtak, *Optics* (Wiley, New York, 1986).
- ⁴²A. Damascelli, G. Gabetta, A. Lumachi, L. Fini, and F. Parmigiani, *Phys. Rev. B* **54**, 6031 (1996).
- ⁴³F. Pforte, T. Michalke, A. Gerlach, A. Goldmann, and R. Matzdorf, *Phys. Rev. B* **63**, 115405 (2001).
- ⁴⁴P. J. Feibelman, *Surf. Sci.* **46**, 558 (1974).
- ⁴⁵M. A. B. Whitaker, *J. Phys. C* **11**, L151 (1978).
- ⁴⁶Y. J. Chabal, *Surf. Sci. Rep.* **8**, 211 (1988).
- ⁴⁷L. Gundlach, J. Szarko, L. D. Socaciu-Siebert, A. Neubauer, R. Ernstorfer, and F. Willig, *Phys. Rev. B* **75**, 125320 (2007).
- ⁴⁸F. Pforte, A. Gerlach, A. Goldmann, R. Matzdorf, J. Braun, and A. Postnikov, *Phys. Rev. B* **63**, 165405 (2001).
- ⁴⁹S. M. Goldberg, C. S. Fadley, and S. Kono, *J. Electron Spectrosc. Relat. Phenom.* **21**, 285 (1981).
- ⁵⁰H. Daimon and F. Matsui, *Prog. Surf. Sci.* **81**, 367 (2006).
- ⁵¹A. Samsavar, T. Miller, and T. C. Chiang, *J. Phys.: Condens. Matter* **17**, 2671 (2005).

ANGLE-DEPENDENT STUDY OF A DIRECT OPTICAL...

PHYSICAL REVIEW B **76**, 195428 (2007)

- Matter **2**, 1141 (1990).
- ⁵²S. Walter, V. Blum, L. Hammer, S. Müller, K. Heinz, and M. Giesen, Surf. Sci. **458**, 155 (2000).
- ⁵³J. C. H. Spence, H. C. Poon, and D. K. Saldin, Microsc. Microanal. **10**, 128 (2004).
- ⁵⁴P. B. Johnson and R. W. Christy, Phys. Rev. B **6**, 4370 (1972).
- ⁵⁵K. L. Kliewer, Surf. Sci. **101**, 57 (1980).
- ⁵⁶P. J. Feibelman, Prog. Surf. Sci. **12**, 287 (1982).
- ⁵⁷S. Suto, K.-D. Tsuei, E. W. Plummer, and E. Burstein, Phys. Rev. Lett. **63**, 2590 (1989).
- ⁵⁸A. Liebsch and W. L. Schaich, Phys. Rev. B **52**, 14219 (1995).

2

Higher Order Photoemission from Metal Surfaces

*Aimo Winkelmann, Cheng-Tien Chiang, Francesco Bisio, Wen-Chin Lin,
Jürgen Kirschner, and Hrvoje Petek*

2.1

Introduction

Photoemission spectroscopy (PES) is a widely employed method for mapping the electronic structure of solids [1, 2]. In the simplest picture, the incident radiation induces transitions of electrons from occupied to unoccupied single-particle states separated by the photon energy. By invoking the laws of energy and momentum conservation, the photoemission process can be applied to map the occupied band structure of solids by detecting the photoelectrons in final states above the vacuum barrier.

A generalization of the linear one-photon photoelectric effect can be realized by nonlinear multiphoton processes induced by ultrashort laser pulses of high intensity, where the occupied initial states, the unoccupied intermediate states, and the coupling between them play a central role. The unique power of these effects stems from the fact that the dynamical processes in the intermediate excited states become directly accessible in the time domain when using delayed excitation pulses. Especially the technique of time-resolved two-photon photoemission (2PPE) has been used to gain information on the decay rates of electronic populations and their dephasing times [3–5].

Compared to 2PPE, higher order multiphoton photoemission processes (mPPE) in solids, which can extend the energy range of the studied unoccupied states and provide further information on photoexcitation processes, have received only little attention. This is mainly because their observation requires very intense optical fields and their considerably reduced photoelectron yields can be overwhelmed by space charge effects from the lower order processes [6–15]. Moreover, nonphotoelectric effect emission through the surface plasmon excitation and possibly tunneling, leading to ponderomotive acceleration of photoelectrons up to 0.4 keV energy [9, 16], has been reported with comparatively low external fields. Therefore, the mechanisms for high-order photoelectric excitations at solid surfaces, in particular to what extent they are governed by the band structure of metals, are largely unexplored.

34 | 2 Higher Order Photoemission from Metal Surfaces

As multiphoton photoemission experiments depend sensitively on the wave functions and energy levels of the states that are involved in the excitation, they are expected to provide band structure information about occupied and unoccupied states in solids with high precision [17]. Using procedures very similar to conventional angle-resolved PES, multiphoton resonances can be exploited to determine the separation of electronic bands at specific \vec{k} -points by looking for resonances between the multiple states coupled by the incident radiation.

In this chapter, we summarize our observations of higher order photoemission at copper surfaces. The electronic structure of Cu(001) supports resonant three-photon photoemission with photon energies of ~ 3 eV. We will show how coherent multiphoton photoemission carries information about the bulk band structure of copper via the resonant excitation of electronic bulk states through unoccupied intermediate surface states. In the 3PPE and 4PPE experiments, we can also observe electrons that have absorbed more energy than is necessary to overcome the work function of the material, and therefore undergo above-threshold photoemission (ATP). We will analyze an example of how momentum conservation restrictions can keep these electrons in quasibound states above the thermodynamic vacuum level. Finally, we will briefly discuss how the spin-orbit coupling (SOC) in the Cu d-bands can be exploited to excite and control the spin-polarized higher order photoemission using circularly polarized light for excitation and spin-dependent scattering for the spin-resolved detection of photoelectrons.

2.2

Observation of Higher Order Photoemission at Cu Surfaces

We investigated nonlinear photoemission spectra from Cu(001) and Cu(111) surfaces. The photoemission experiments were carried out in an ultrahigh vacuum system (pressure $< 5 \times 10^{-11}$ mbar) [18, 19]. The Cu surfaces were prepared with standard sputtering and annealing procedures. All the experiments, unless specified, were carried out at 300 K. The electrons photoemitted along the surface normal were analyzed by a cylindrical sector analyzer (Focus CSA300) with parallel momentum (k_{\parallel}) resolution below $\pm 0.07 \text{ \AA}$. The ultrashort excitation pulses were provided by the frequency-doubled output of a self-built Ti:sapphire oscillator operating at 81 MHz. The pulse central energy could be continuously varied in the range of $h\nu = 2.99 - 3.15$ eV by tuning the phase-matching angle of the frequency-doubling β -BaB₂O₄ (BBO) crystal. At the energy of $h\nu = 3.07$ eV, the pulse length at the surface was ≤ 20 fs and the pulse energy ~ 1 nJ. The peak power densities that were reached at the sample surface were in the order of 10 GW/cm^2 , the measured sample current was in the order of 1 nA, corresponding to a total of less than 100 emitted electrons per pulse. Significant space charge effects beyond the experimental resolution could not be detected in the experiments reported below.

In Figure 2.1, we show multiphoton photoemission spectra recorded simultaneously for two-, three-, and four-photon excitation for Cu(001) and Cu(111) surfaces as a function of the final-state energy above the Fermi level E_F . The

2.2 Observation of Higher Order Photoemission at Cu Surfaces | 35

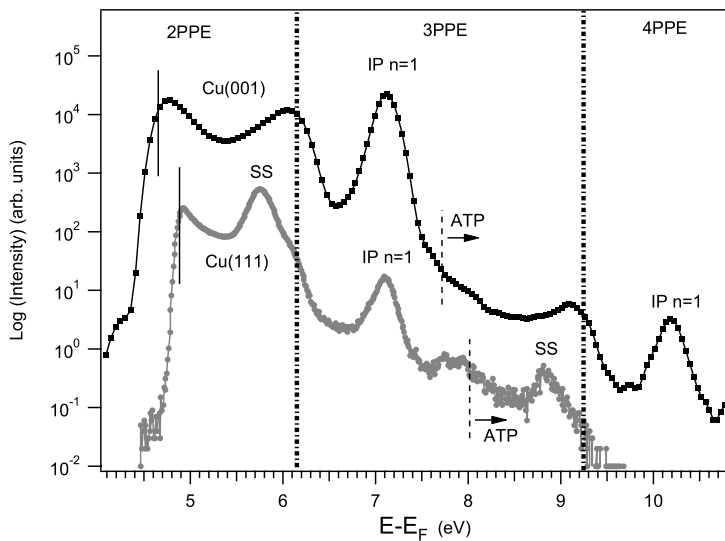


Figure 2.1 Nonlinear photoemission spectra from Cu(001) (black squares) and Cu(111) (gray circles), for emission perpendicular to the surface, single-photon energy of $h\nu = 3.07$ eV, and p-polarized light. Indicated are the energy regions that are reached from the occupied initial states by 2, 3, and 4 photons, respectively.

Multiphoton replicas of the $n = 1$ image potential (IP) state peak and the Cu(111) Shockley surface state (SS) peak can be distinguished. Above-threshold processes are indicated by ATP. The energy resolution was ≈ 100 meV. The spectra are not normalized with respect to each other.

low-energy onsets of the spectra represent the work function thresholds of 4.6 eV for Cu(001) and 4.9 eV for Cu(111) [5]. The highest energies that can be reached by photoelectrons from the Fermi level by absorption of two and three photons are indicated by dashed–dotted vertical lines. These delimit the regions of 2PPE, 3PPE, and 4PPE.

In the 2PPE spectral region of Cu(111), we identify the well-known occupied Shockley surface state (SS) ($E_F - 0.4$ eV), while there are no distinctive features in the Cu(001) spectrum. In the 3PPE part of both surfaces, we can clearly see the $n = 1$ image potential (IP) state peak at a final-state energy of 7.1 eV. The binding energies of the $n = 1$ IP states measured with respect to the vacuum level are 0.59 eV for Cu(001) and 0.84 eV for Cu(111) [5]. Due to the difference of 0.3 eV between the work functions of the two surfaces, their IP states appear at approximately the same energy with respect to the Fermi level.

Above the IP states, we indicate by dashed lines the position of the vacuum levels plus one photon energy. Photoelectrons with energies above the indicated limits emerge with kinetic energies larger than the single-photon energy. The contribution of this above-threshold photoemission effect is seen especially clearly for the three-photon copy of the Cu(111) surface state near 8.8 eV: These electrons can however escape after absorbing only two photons (the 2PPE peak at 5.7 eV). A very similar process is apparent in the 4PPE IP state feature, which corresponds to absorption of two photons to reach the vacuum instead of only one.

36 | 2 Higher Order Photoemission from Metal Surfaces

The most striking effect is seen in the intensity of the 3PPE through the IP state at Cu(001) compared with Cu(111): The 3PPE signal from Cu(001) at the IP state can reach higher intensity than the 2PPE signal and is orders of magnitude stronger than the 3PPE signal through the IP state of Cu(111). In the next section, we will analyze how the Cu(001) electronic structure can support such an efficient 3PPE process.

2.2.1

Resonant 3PPE in the Cu(001) Electronic Band Structure

In order to interpret our experimental results on 3PPE from Cu(001), we show in Figure 2.2 the relativistic band structure of copper for the k -space line relevant to emission normal to the Cu(001) surface (Δ -line from Γ to X) according to the calculated band structure of Ref. [20]. We indicate a three-photon process for photon energies near 3 eV starting from the Cu d-bands via the unoccupied sp-band and the $n=1$ image potential state, which has been demonstrated previously [18]. At sufficiently high laser fluence, this process leads to a 3PPE signal higher in intensity than the simultaneously observed nonresonant 2PPE signal.

As is well known, a theoretical band structure such as shown in Figure 2.2 usually does not describe experimental photoemission data quantitatively [22, 23]. Because of this, we assume in the following that the calculation still describes the *dispersion*

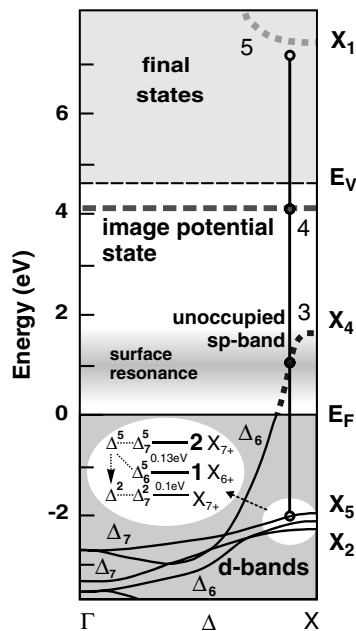


Figure 2.2 Relativistic bulk band structure [20] of Cu(001) with the proposed three-photon resonance for a photon energy near 3 eV. In addition, the $n=1$ image potential state is shown at an energy of 4.04 eV [5]. A broadened unoccupied surface resonance is expected near 1 eV [21].

of the bands correctly, but we make the absolute values for the critical points adjustable to known experimental data. Then we try to find k -conserving resonances in the band structure as a function of photon energy. In a first approximation, this is realized by shifting the involved bands according to the number of photons needed to reach the final-state energy. A resonance is given when the energy levels cross (see also Ref. [17]). This imposes stringent conditions on the relative energy separation between the energy levels involved.

The image potential state is a surface state, which by definition does not disperse with momentum in the direction perpendicular to the surface and thus is drawn horizontally for the Γ -X direction of Figure 2.2, at an energy of 4.04 eV [5]. The observed spectral structure can be expected to be produced mainly by the IP state in combination with the initial d-bands that show a reduced k_{\perp} -dispersion near the X point. This is why we look for a two-photon resonance between the $n = 1$ image potential state and the initial d-bands. In addition, the dispersing unoccupied sp-band can supply states near simultaneous one-photon resonance to the d-bands and the image potential, respectively. Adjusting the critical points of the bulk band structure, the d-bands are assumed to have X_5 at -1.99 eV and X_2 at -2.18 eV [22]. Due to spin-orbit coupling, the band with Δ^5 spatial symmetry is split into Δ_7^5 and Δ_6^5 bands with reported experimental splittings between 100 [24] and 170 meV [25] in the region of interest near the X point. For comparison, the theoretical value is 160 meV [22] at the X point. The upper sp-band is assumed with X_1 at 7.67 eV [22] and thus cannot be reached resonantly with the photon energies in our experiment. In Figure 2.3, we show the bands after shifting up the IP state by one photon energy, the sp-band by two photon energies, and the d-bands by three photon energies to the final-state energy.

The results in Figure 2.3 strongly support a resonance mechanism in 3PPE from Cu(001). In the two panels of Figure 2.3, we can expect the near-crossing of three bands for a pair of photon energies approximately 110 meV apart, at 2.97 and 3.08 eV, which can be excited simultaneously with our 170 meV bandwidth laser pulse. The crossing of the three bands in Figure 2.3 means that not only we have a two-photon resonance between the d-bands and the IP state (which could be fulfilled for a range of photon energies due to the dispersion of the d-bands) but also the unoccupied sp-band is near one-photon resonance to the d-bands and the IP state. In this situation, the transitions involved are emphasized because energy conservation is fulfilled for the one-photon and two-photon transitions at the same time. The two separate resonances are labeled A and B in the higher resolution experimental data shown in Figure 2.3. In view of the very simple model, both the photon energies and the separation of the resonances are in good agreement with the measured values.

The 3PPE resonances discussed involve two initial states belonging to spin-orbit split Δ^5 d-bands. They both proceed at different k -values via the dispersing unoccupied portion of the sp-band states [26–28] to the image potential state. A possible contribution from an unoccupied surface resonance [21], which is expected near or higher than 1 eV above the Fermi level (Figure 2.2), cannot be excluded, but in our model it can hardly be responsible for the two simultaneous resonances

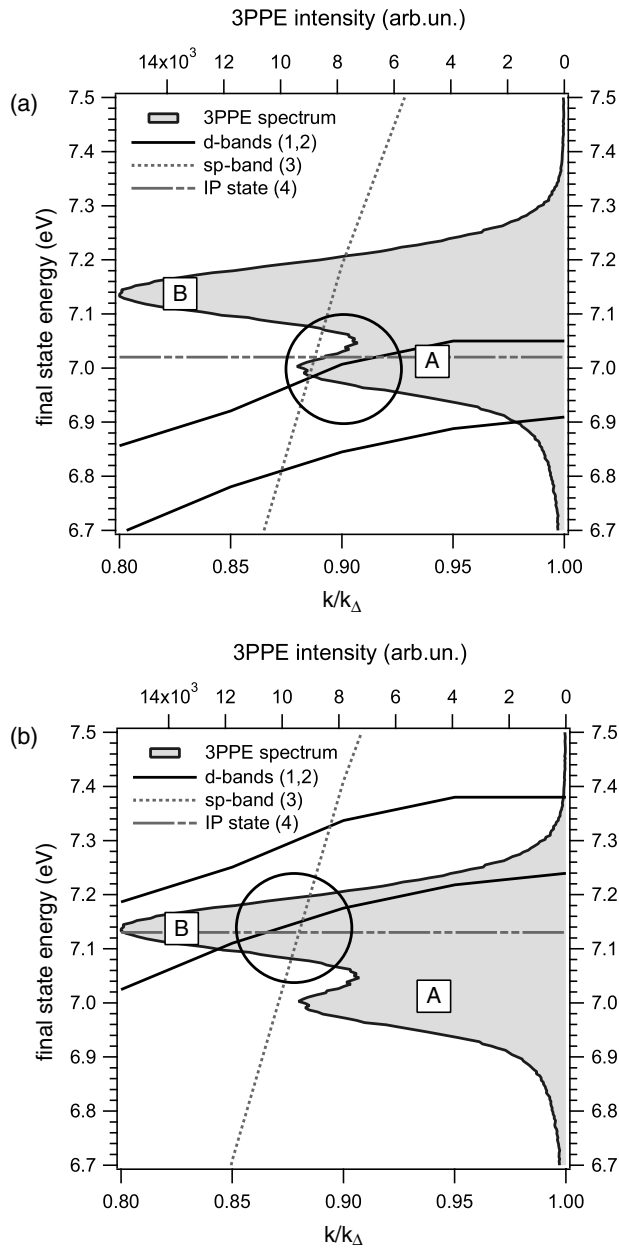


Figure 2.3 Analysis of the possible resonance conditions between the initial d-bands (solid black), the intermediate sp-band (dotted), and the image potential state (dash-dot-dotted). The bands are numbered according to Figure 2.2. The initial d-bands are shifted upward by the energy of three photons, the sp-band by two-photon energies, and the intermediate $n = 1$ image potential state is shifted by the energy of one photon to the final-state energy. The near

crossing of three bands indicates simultaneous two-photon and one-photon resonances. Due to the broad pulse spectrum (≈ 170 meV), the separate resonances for $h\nu = 2.97$ eV (a) and $h\nu = 3.08$ eV (b) connected to the two d-bands are simultaneously observed as features A and B in the experimental spectrum (solid gray, experimental data for 3.04 eV central photon energy of the laser pulse, energy resolution ≈ 50 meV).

observed. This is because of the missing k_{\perp} dispersion of the surface resonance and the IP state that fixes their one-photon resonance at *one* specific photon energy for all k_{\perp} . The unoccupied surface resonance would not allow *two* photon energies to be in simultaneous two-photon and one-photon resonances with the IP state and the d-bands, that is, the crossing of three bands as shown in Figure 2.3 for two different photon energies would not be possible. In this respect, a dispersing intermediate-state band seems to be necessary to explain our observations (compare also Figure 2.6).

An interesting feature of the multiphoton resonances is that they proceed via the *same* image potential state, but still show a two-peak structure corresponding to the different initial states. This points to the influence of multiphoton excitation processes that cannot be pictured as sequential stepwise processes from one level to the next, in which the information (coherence) on the excitation pathway would be lost. The application of these coherent excitation processes for electronic structure mapping is discussed in the next section.

2.3

Electronic Structure Mapping Using Coherent Multiphoton Resonances

An analysis of the double-peak 3PPE structure A and B in Figure 2.3 shows that this part of the spectrum can be fitted by the sum of two Gaussian peaks with widths (FWHM) of 110 meV for (A) and 130 meV for (B) and a separation of 150 meV. Peak A is located at a final-state energy of 6.95 eV, while peak B is at 7.15 eV. Considering that the optical spectrum of the excitation pulses has a width of 170 meV, and the light field acts on the sample three times, it is striking that the resolution of the 3PPE spectrum is well below the excitation linewidth [29].

The mechanism behind the formation of the double-peak structure in Figure 2.3 can be analyzed by using the density matrix formalism, where the populations of the states involved are described by the diagonal elements ρ_{aa} and the coherences between states by the off-diagonal elements ρ_{ab} of the density matrix ρ [5, 30–34].

We assume that the part of the Cu band structure that is relevant for the observed 3PPE process can be effectively simplified to a four-level system. The unperturbed Hamiltonian \hat{H}_S of the system is written on the basis of four orthonormalized states ($\langle a|b\rangle = \delta_{ab}$) representing either one of the initially occupied d-band states $|i_{1,2}\rangle$, the intermediate unoccupied sp-band $|s\rangle$, the image potential state $|m\rangle$, and the final photoemitted state $|f\rangle$ at the respective energy levels $\varepsilon_{i,s,m,f}$. This simplification disregards the dispersion of the electronic states with crystal momentum \mathbf{k} that is a major inhomogeneous contribution to nonresonant 2PPE spectra [34] and the various inter- and intraband relaxation mechanisms that would need to be part of a quantitative theory for a crystalline solid state system. This could be handled, for example, by introducing sets of k -dependent multilevel systems with appropriate couplings that represent the above effects [34, 35]. We also assume that the perturbation of the system by the laser pulse is weak. The 3PPE processes are

40 | 2 Higher Order Photoemission from Metal Surfaces

assumed to proceed independently from either of the two different sets of initial d-band states $|i_{1,2}\rangle$.

The density operator $\hat{\rho}$ of this simplified four-level system explicitly expands as.

$$\hat{\rho} = \begin{pmatrix} \rho_{ii} & |i\rangle\langle i| & \rho_{is} & |i\rangle\langle s| & \rho_{im} & |i\rangle\langle m| & \rho_{if} & |i\rangle\langle f| \\ \rho_{si} & |s\rangle\langle i| & \rho_{ss} & |s\rangle\langle s| & \rho_{sm} & |s\rangle\langle m| & \rho_{sf} & |s\rangle\langle f| \\ \rho_{mi} & |m\rangle\langle i| & \rho_{ms} & |m\rangle\langle s| & \rho_{mm} & |m\rangle\langle m| & \rho_{mf} & |m\rangle\langle f| \\ \rho_{fi} & |f\rangle\langle i| & \rho_{fs} & |f\rangle\langle s| & \rho_{fm} & |f\rangle\langle m| & \rho_{ff} & |f\rangle\langle f| \end{pmatrix} \quad (2.1)$$

$\rho_{ii}(t = -\infty) = 1.$

We have emphasized with a dark gray box the matrix element ρ_{ii} , which is the only nonzero element in the ground state at time $t = -\infty$, representing the initial population of the relevant d-band state.

The other emphasized matrix element ρ_{ff} (light gray box) determines the quantity we measure in the experiment: the very small population that is transferred to the final state by the ultrashort optical pulse. Initially, $\rho_{ff} = 0$, and it can only become nonzero due to the coupling to the initial state via the intermediate states. This coupling is provided by the electric field $E(t)$ of the excitation pulse.

For simplicity, we assume here that the most relevant couplings are between those states that are nearly a photon energy $\hbar\omega_p$ apart in the level scheme:

$$|i\rangle \xleftrightarrow{\hbar\omega_p} |s\rangle \xleftrightarrow{\hbar\omega_p} |m\rangle \xleftrightarrow{\hbar\omega_p} |f\rangle. \quad (2.2)$$

Starting at $t = -\infty$ from only $\rho_{ii} \neq 0$, the interaction Hamiltonian \hat{H}_{int} allows finite values to develop in the matrix elements during the time evolution of the density operator $\hat{\rho}$. This time evolution is described by the equation of motion for the density matrix (Liouville – von Neumann equation) [5, 30, 32, 33, 36]:

$$\frac{d\rho_{ab}}{dt} = -\frac{i}{\hbar} \langle a | [\hat{H}_S + \hat{H}_{\text{int}}, \hat{\rho}] | b \rangle - \Gamma_{ab} \rho_{ab}, \quad a, b = i, s, m, f. \quad (2.3)$$

The numerical treatment of Eq. (2.3) is in principle straightforward. With respect to the physical interpretation, however, a perturbative expansion of $\hat{\rho}$ with respect to interactions with the electrical field is useful. A perturbative expansion allows to visualize the induction of nonzero matrix elements ρ_{ab} as a sequence of steps in which the commutators $[\hat{H}_{\text{int}}, \rho_{ab}]$ in Eq. (2.3) are recursively expanded up to a specified order. This expansion can be symbolized by double-sided Feynman diagrams that keep track of both the time development of the population in the states involved as well as the coherences induced between these states that are described by the diagonal and off-diagonal elements of the density matrix, respectively [36]. Another related visualization allows to show the possible coupling of two generic elements ρ_{ab} and ρ_{cd} of the density matrix as Liouville space pathways [36].

These Liouville space pathways show that besides the sequential one-photon pumping of population from one state to the next (compare Eq. (2.2)):

$$\mathcal{Q}_{ii} \rightarrow \mathcal{Q}_{ss} \rightarrow \mathcal{Q}_{mm} \rightarrow \mathcal{Q}_{ff}, \quad (2.4)$$

there are contributions to \mathcal{Q}_{ff} containing only coherences, schematically written as

$$\mathcal{Q}_{ii} \rightarrow \mathcal{Q}_{is} \rightarrow \mathcal{Q}_{im} \rightarrow \mathcal{Q}_{if} \rightarrow \mathcal{Q}_{ff}, \quad (2.5)$$

which implies that these contributions produce no population in the intermediate states $|m\rangle$ (corresponding to the observable $N_m = \text{Tr}[|m\rangle\langle m|\hat{\rho}]$), due to the fact that the density matrix components \mathcal{Q}_{mm} (as well as \mathcal{Q}_{ss}) are not affected by these processes. It is emphasized that despite the fact that no population in the intermediate state is involved, these states nevertheless have a decisive role. They contribute via their coherent superposition with the other states. From our experimental data, we see that the coherent coupling of the d-band states to the image potential state via the sp-bands contributes to the initial-state peaks in the photoelectron spectrum ($\mathcal{Q}_{ff}(E)$). We keep in mind that the pathways (2.4) and (2.5) are two particular pathways in a general coherent 3PPE process and occur together with all other pathways and should be added coherently in calculating $\mathcal{Q}_{ff}(E)$.

Features A and B in Figure 2.3 are not a consequence of the presence of the IP state alone, but are inherently caused by a nonlinear resonance effect between initial, first intermediate states, and second intermediate (IP) states. Very qualitatively, a memory of its excitation pathway must be imparted on an electron because it starts at a specific energy level (one of the two d-bands), then goes through the *same* energy level of the IP state as the other electrons, and finally ends up at a specific energy again. In this sequential picture where only the actual population of the IP state is measured by the third ionizing photon, no initial-state peaks could show up in the photoelectron spectrum if the electrons from different initial states lose memory of their excitation pathway in the IP state before their final ionization. In this respect, the simple observation of two IP state related peaks (which do not move when the central pulse energy is tuned [29]) is a sign of specific nonlinear-optical pathways that cannot be pictured as sequential one-photon transitions, but that allow the electron to keep its initial-state information as it is emitted into the vacuum.

The resonance effect also provides an effective energy filter, which would explain why the widths of the observed peaks A and B are smaller than the optical spectrum of the excitation pulses. Strictly, energy conservation is imposed only on the overall coherent 3PPE process from an initial to a final state that are separated by an energy $\hbar\omega_{03}$. In principle, all three-photon processes that fulfill $\hbar\omega_{03} = \hbar\omega_{01} + \hbar\omega_{12} + \hbar\omega_{23}$ are allowed (with different single-photon energies $\hbar\omega_{01,12,23}$). However, if the excitation energy is additionally near one-photon resonances $\hbar\omega_R \approx \hbar\omega_{01} \approx \hbar\omega_{12} \approx \hbar\omega_{23}$ between dispersing levels (compare also Figure 2.3), energy conservation is also approximately fulfilled for the intermediate levels. This favors the photon energies near the simultaneous one-photon, two-photon, and three-photon resonances $\hbar\omega_{03} = \hbar(\approx \omega_R) + \hbar(\approx \omega_R) + \hbar(\approx \omega_R)$ and thus provides an energy filtering mechanism.

The main physics of the coherent multiphoton photoemission effect is expected to be already present in three-level systems of initial, intermediate, and final states. For these systems, analytical solutions exist for single-frequency interactions in

two-photon photoemission [37]. Assuming that the two initial d-band levels and the intermediate IP state play a dominant role in the mechanism we focus on here, we can simplify our four-level system (3PPE) to a three-level system (2PPE) by artificially moving the two initial d-band states to the original energy level of the first intermediate sp-bands, which are neglected in the following. We then apply the model of Wolf *et al.* [37] to our special simplified system that models 2PPE from two closely spaced, independent initial states via the same intermediate state.

For the intermediate state, we assumed a constant lifetime of 35 fs and a dephasing of 1 meV [5]. For the final state, we assumed infinite population lifetime and 1 meV dephasing rate [5]. The initial states are separated by 150 meV at energy levels that reproduce the experimentally observed final-state positions via the intermediate state at 4.04 eV, corresponding to the $n = 1$ IP state on Cu(001). We then calculated the resulting 2PPE spectra for a range of initial-state dephasing rates (assuming no population decay in the initial state). While for faster dephasing only a single peak is present, it turns out that – in order for the two-peak structure to appear – the dephasing time of the initial states must be in the order of 10–20 fs [29]. Although this value cannot be taken as a quantitative determination, nevertheless it compares well with direct time domain observations of Cu d-band hole dephasing times of >20 fs in the observed d-band region near the X point [38].

The result for a model 2PPE process shows how the dephasing rate between the initial and intermediate states contributes to the peak width of the transition. If the dephasing rate is high, the two independent transitions from the closely spaced initial states are broadened to an extent that they are not separable anymore and appear as a single peak. With decreasing dephasing, the peak widths of the two resonances become sharp enough to give two peaks in the final-state spectrum. This process can be expected to be of very general character, and a similar influence of dephasing is expected to be relevant in the actual 3PPE experiment. This means that a sufficiently low dephasing rate of the initial states with respect to the intermediate states will be required in any case to distinguish two initial-state peaks in a transition that proceeds via a common intermediate-state level, like the IP state considered here.

Our observations of the direct influence of coherent excitation pathways in 3PPE from Cu(001) are relevant for applications of nonlinear photoemission in electronic structure investigations, which can be carried out using high-intensity laboratory laser sources and accelerator-based free electron lasers. It has been predicted theoretically [17] that resonant two-photon photoemission could give the separation between occupied initial states and unoccupied intermediate *bulk* states within the fundamental limit imposed by the intrinsic energy and momentum widths of the coupled states. The important advantage in such two-photon measurements is that the optical transition from the initial state to the intermediate state would couple bulk states that are not influenced by the symmetry breaking due to the surface [39] and the perpendicular crystal momentum k_{\perp} in such a transition would need to be conserved (at negligible photon momentum).

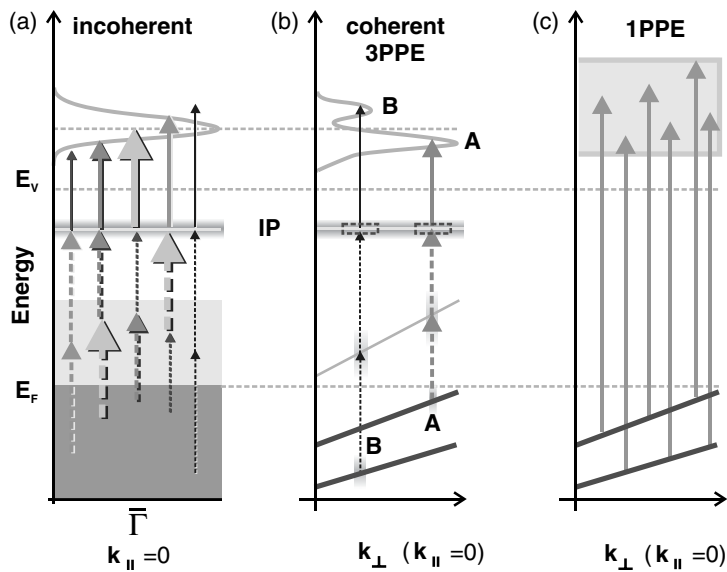


Figure 2.4 Principle of detecting coherent bulk band structure resonances in 3PPE via an image potential state on Cu(001). (a) Nonresonant incoherent excitation of the IP state from unspecific bulk bands at normal emission ($k_{\parallel} = 0$). The initial states are averaged over k_{\perp} illustrating the loss of k_{\perp} information in the sequential one-photon pathways due to the lack of a k_{\perp} selection rule in the IP to final-state one-photon transition (k_{\perp} is undefined for surface states). The colors of the arrows correspond to photon frequencies provided by the excitation pulse, their thickness corresponds to the respective spectral weight. The photons can act in any combination for sequential incoherent excitations. The peak position of the IP state is

determined by the central photon energy of the pulse (thickest arrow) and the measured width of the IP state is determined by the width of the pulse spectrum. (b) Coherent 3PPE resonances in the bulk band structure coupled to the image potential state produce specific peaks A and B in the spectrum, providing k_{\perp} information. A fixed photon energy defines each resonant pathway. The width of features A and B is not limited by the spectral pulse width. (c) The corresponding 1PPE process for the same level scheme using a single-photon energy three times as large as that in the corresponding 3PPE process is not k -selective if no resonance to a dispersing final-state band is present. (Please find a color version of this figure on the color plates.)

The extension of this idea to 3PPE is straightforward, and we illustrate in Figure 2.4 the qualitative difference between unspecific bulk excitations and coherent resonances that sensitively depend on the band dispersion. It can also be easily imagined that this approach can be generalized to multiple excitation frequencies that can be tuned to search for the simultaneously possible single-photon resonances in a multiphoton process. When surface states are involved in the multiphoton resonances, it has to be taken into account that the periodicity of the surface-state wave function may emphasize transitions near the bulk Brillouin zone boundaries [40, 41]. The use of multiphoton resonances corresponding to very well-defined k -space positions should also allow improved time domain investigations [3] of band-resolved electron dynamics. The demonstrated coherent coupling of bulk states to surface states through a two-photon resonance could also lead to

44 | 2 Higher Order Photoemission from Metal Surfaces

improved possibilities of controlling electron motion at surfaces by interferometric techniques [42, 43].

2.4

Dynamical Trapping of Electrons in Quasibound States

In the previously discussed experiments shown in Figure 2.1, the IP states populated via two-photon excitation have been measured in normal emission, corresponding to $k_{\parallel} = 0$. For $k_{\parallel} > 0$, the energy of an electron in the IP states disperses with an effective mass m^* near the free electron mass m_e as $E_{\text{IP}}(k_{\parallel}) = E_0 + \hbar^2 k_{\parallel}^2 / 2m^*$. This dispersion can be seen in the measurements shown for Cu(001) in Figure 2.5. We detected electrons with $k_{\parallel} > 0$ in off-normal emission by rotating the sample. Starting from the value at $k_{\parallel} = 0$, the IP state disperses toward higher energies with increasing k_{\parallel} . Interestingly, at one point, the kinetic energy of the IP electrons is more than one-photon energy larger than the energy of an electron that has overcome the vacuum barrier E_v . This means that electrons can stay long enough in the IP state to absorb an additional third photon although their total kinetic energy would be already sufficient to leave the sample after two-photon excitation. As we will discuss below, quasibound states can exist above the thermodynamic vacuum level on account of the vectorial nature of momentum conservation, in addition to quantitative energy conservation.

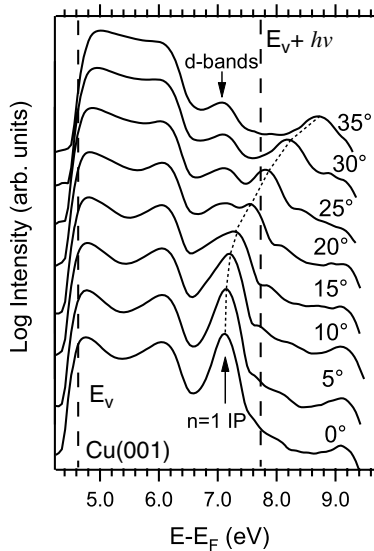


Figure 2.5 Dispersion of the $n = 1$ IP state on Cu(001) with $k_{\parallel} \geq 0$. Above $E_v + h\nu$, the two-photon excited electron in the IP state already has higher energy than the work function $E_v - E_F$, but cannot leave the sample because its

perpendicular momentum is too low to overcome the surface barrier. Only after absorbing a third photon, the electron is photoemitted.

If electrons are to be emitted from a sample, they have to overcome the potential barrier of the surface. In a classical picture, the perpendicular component of the electron momentum vector is reduced outside the sample due to the force acting along the surface normal direction when the electron overcomes the potential step at the surface. If the perpendicular momentum component p_{\perp} of an electron, which travels along an inclined trajectory toward the surface barrier, is below the critical value p_{\perp}^0 , then it is deflected back into the direction away from the surface, although its total kinetic energy might actually be sufficiently high to leave the sample. Quantum mechanically, the self-consistent reflection and transmission of the electron waves at the surface and at the bulk potential determine the formation of standing waves for the energies of surface states and resonances, which correspond to electrons trapped in a surface quantum well [44]. Under the simplest approximation, in this multiple scattering picture, only the projection of the electron wave vectors on the surface normal direction is relevant for scattering in a surface barrier potential that varies only in the dimension perpendicular to the surface.

This perpendicular momentum of the scattered electron waves at the surface is affected, for instance, by the exchange of reciprocal lattice vectors in low-energy electron diffraction (LEED). In LEED experiments, external electrons with total energies *above* the vacuum level can be trapped in the surface potential well by momentum restrictions. When entering the surface, the external electron beam is accelerated due to the lower inner potential of the sample and it can be diffracted into various beams, some of which can move nearly parallel to the surface. In this way, the momentum and energy in the surface parallel motion are increased for the diffracted beams and the respective electrons effectively lose “perpendicular energy.” The effective perpendicular energy can drop below the vacuum level, and the electron waves are then scattered in a similar way as electrons in the bound states, that is, the IP states, of the one-dimensional perpendicular potential. This is seen near the emergence threshold of diffracted beams moving nearly parallel to the surface, where fine structure effects appear in the reflected electron intensity via the interference of waves reflected only at the bulk and diffracted waves that have been reflected at the bulk and surface barriers (possibly multiple times) [45]. Similar trapping effects can be seen in the scattering of He atoms at surfaces [46].

As we see in the measurements of Figure 2.5, multiphoton excitation can provide an alternative way to study electrons under restricted surface perpendicular momentum that are trapped in the IP states. According to the discussed model, the electrons in the IP state could, in principle, acquire any amount of energy if their motion is free electron-like in the direction parallel to the surface and as long as their perpendicular momentum stays low enough. If the surface-parallel velocity of the electrons in the IP state could be sufficiently increased by multiphoton excitation, this could give access to the dynamical screening properties of the electrons in the occupied states, which lead to a finite response time for the buildup of the image potential state and a velocity-dependent binding energy [47]. As the electron motion at the surface is not completely free, however, reflection by the periodic part of the lateral surface potential will influence the electron motion in the IP states and thereby impose limits on their velocity.

2.5

Above-Threshold Photoemission

The effect of above-threshold photoemission is well known in atomic physics [48]. It provides the possibility that an electron absorbs one or more photons than are actually necessary to ionize an atom or, in our case, to be photoemitted from a surface. We have seen in the previous section that momentum restrictions can lead to a situation in which an electron with sufficient energy to overcome the work function is trapped at a surface. However, the intrinsic ATP effect is seen even in the absence of similar restrictions.

This can be realized when looking at our experimental spectra in Figure 2.1. For Cu(111), we have two peaks that originate from the Shockley surface state ($E_B = -0.4$ eV): one at 5.7 eV, due to excitation by two photons. But clearly, there is a process in which the surface-state electron absorbs one additional photon, as we see by the three-photon copy of the SS peak near 8.8 eV. A very similar process gives rise to the $n = 1$ IP state feature in the 4PPE spectrum of Cu(001). This corresponds to photoemission of electrons from the IP state by two photons instead of only one, which would be sufficient enough to reach the vacuum. While multiphoton ATP effects from solids under high-intensity excitation can produce unwanted background effects that are largely unspecific with respect to the sample electronic structure, our experimental spectra of Figure 2.1 clearly display very specific signals from surface states and the Fermi edge from Cu(001) and Cu(111) in different nonlinear orders. Such information should be very useful for comparison with quantitative theories that predict the relative yields of the different orders of multiphoton excitation.

Compared to atomic physics, the nonlinear effects at solid surfaces show important differences. In this respect, one of the most obvious questions is how the complex electronic structure of a crystalline system influences multiphoton photoemission, and how the electronic structure of a solid is modified by the nonlinear interaction with the laser field [49]. Furthermore, the symmetry breaking at the surface introduces additional influences such as refraction and reflection of electrons and light at the solid–vacuum interface [50]. Correspondingly, the measurement of ATP effects from solids by ultrashort pulses can provide important information about the occupied and unoccupied electronic states and the relevant timescales of the elementary processes involved. It has been shown, for example, that multiphoton excitations can give access to final-state effects in photoemission from solids, like the process of photoexcited electrons leaving a sample [51]. The involved timescales can be sensed by comparing the signals of specific excited electronic states and the corresponding signals of higher order excitations induced by an additional laser pulse. The experimental scheme involves electrons that are photoemitted, for example, by attosecond XUV pulses. Access to the dynamics of the excited electrons is given by the time-resolved sideband structure in the photoelectron spectra, which is due to low-energy photon absorption and stimulated emission induced by the dressing field [13, 52] (see also chapters 21 and 22 in this book).

2.6

Spin-Polarized Multiphoton Photoemission

It is well known that photoexcited spin-polarized electrons can be produced at unpolarized targets, provided that the incident light has circular polarization. Spin-orbit coupling in combination with optical selection rules provides the mechanism by which electrons can be spin selectively excited. This forms the basis of various effects related to optical spin orientation [53]. For one-photon photoemission from metals, it has been demonstrated that significant spin-orbit coupling leads to strong spin-polarization effects of the photoelectrons even in a relatively low- Z material like copper [24]. The extension of the optical spin orientation effect to multiphoton transitions in solids would allow to transiently spin polarize excited intermediate states below the photoemission threshold that in principle cannot be sensed by one-photon photoemission. Such a multiphoton excitation scheme can then be directly exploited to study spin-dependent scattering of excited electrons in solids. In this respect, the Cu(001) surface provides an especially interesting system, since we have seen how the spin-orbit-coupled Cu d-bands can be coupled to the IP states. This is why we studied spin-resolved 3PPE under excitation of circularly polarized laser pulses.

The principle of the spin-polarized 3PPE from Cu(001) is shown in Figure 2.6a. The relativistic selection rules for normal emission from an fcc(001) surface dictate the final-state symmetry to be Δ_6^1 . Furthermore, right circularly polarized (RCP) light couples spin-down (spin-up) electrons from a Δ_6^5 (Δ_7^5) symmetry initial state to a Δ_6^1 symmetry final state (and vice versa for left circular excitation) [54]. This provides

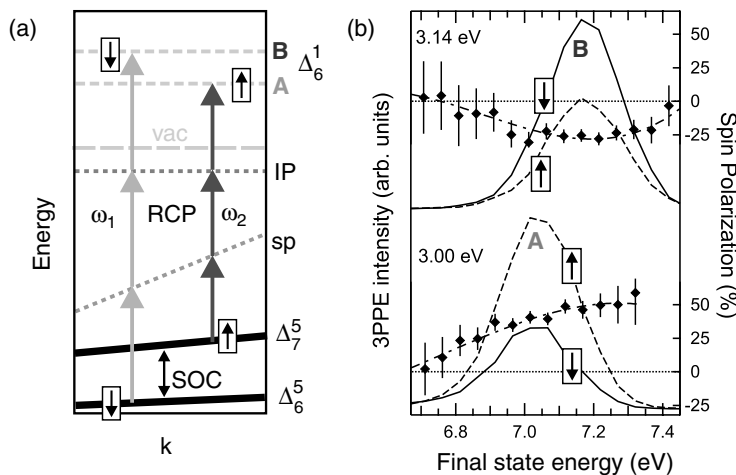


Figure 2.6 (a) Principle of spin-polarized three-photon photoemission from Cu(001). Spin-polarized electrons are selectively excited by the right circularly polarized (RCP) light due to the spin-orbit coupling in the Cu d-bands. By the two-photon resonance to the image potential state, spin-polarized electrons transiently occupy a surface state of nonmagnetic Cu. (b) Experimental data

showing that oppositely spin-polarized electrons are excited by photons of 3.00 and 3.14 eV, respectively [19]. A and B symbolize the two possible resonances (Figure 2.3), which are not separately resolved due to the limited experimental resolution (100 meV) imposed by spin-resolved detection. Reprinted with permission from [17]. Copyright 2007 by the American Physical Society.

48 | 2 Higher Order Photoemission from Metal Surfaces

the basic mechanism by which oppositely spin-polarized photoelectrons are excited selectively from the two spin-orbit split bands of different symmetry to the unoccupied IP state.

The electrons photoemitted along the surface normal were analyzed by a cylindrical sector analyzer coupled with a newly developed spin detector. This detector performs spin analysis through very low-energy electron scattering on a magnetized ultrathin Fe/W(001) film [55].

In the experimental data shown in Figure 2.6b, we have demonstrated the creation of a large (40%) spin polarization of the electrons in the $n = 1$ IP state on the Cu(001) surface [19]. The spin polarization is achieved by resonantly coupling the spin-orbit split Cu d-bands with the IP state via a multiphoton transition excited by circularly polarized light. We see that both the sign and the magnitude of the IP state spin polarization can be tuned by balancing the resonant coupling to different spin-orbit split d-bands, which are selected by the photon energy in Figure 2.6. The spin polarization can also be interferometrically controlled by the delay between two ultrashort laser pulses, via selective interference of high- and low-frequency components of the excitation [56]. Using the additional degree of information provided by the spin, our excitation scheme can also provide a way to selectively study dynamics of electrons excited from d-bands of different double-group symmetry. These spin-resolved investigations may provide a basis for the coherent manipulation and probing of the spin dynamics of excited electrons at nonmagnetic surfaces via multiphoton photoemission. Such investigations can complement studies of spin-dependent electron dynamics at magnetic surfaces [57].

2.7

Summary and Outlook

In this chapter, we have shown how higher order photoemission can provide valuable information about the electronic structure of surfaces for the model system of Cu(001) excited by 3 eV laser pulses. Our findings suggest extensions to future studies of bulk band structure with tunable laboratory and free electron laser sources, exploiting multiphoton resonances for band mapping. If we note that when – in addition to the energy of the exciting radiation – the quantum mechanical phase relationships between the coupled states and the radiation also become a defining factor in the nonlinear excitation process [58], qualitatively different applications as compared to conventional band mapping with one-photon angle-resolved photoemission spectroscopy are expected by exploiting the unique properties of multiphoton transitions between occupied and unoccupied bulk states.

Acknowledgments

We thank Frank Helbig for invaluable technical support. H.P. is grateful for support by NSF grant CHE-0650756.

References

- 1 Hüfner, S. (1995) *Photoelectron Spectroscopy*, Springer-Verlag, New York.
- 2 Schattke, W. and Van Hove, M.A. (eds) (2003) *Solid-State Photoemission and Related Methods: Theory and Experiment*, Wiley-VCH Verlag GmbH.
- 3 Petek, H. and Ogawa, S. (1997) Femtosecond time-resolved two-photon photoemission studies of electron dynamics in metals. *Prog. Surf. Sci.*, **56**, 239.
- 4 Fauster, Th. (2003) Time resolved two-photon photoemission, in *Solid-State Photoemission and Related Methods: Theory and Experiment* (eds W. Schattke and M. van Hove), Wiley-VCH Verlag GmbH, Chapter 2, pp. 247–268.
- 5 Weinelt, M. (2002) Time-resolved two-photon photoemission from metal surfaces. *J. Phys. Condens. Matter*, **14**, R1099–R1141.
- 6 Banfi, F., Giannetti, C., Ferrini, G., Galimberti, G., Pagliara, S., Fausti, D., and Parmigiani, F. (2005) Experimental evidence of above-threshold photoemission in solids. *Phys. Rev. Lett.*, **94**, 037601.
- 7 Bisio, F., Winkelmann, A., Lin, W.-C., Chiang, C.-T., Nývlt, M., Petek, H., and Kirschner, J. (2009) Band structure effects in surface second harmonic generation: the case of Cu(001). *Phys. Rev. B*, **80**, 125432.
- 8 Fann, W.S., Storz, R., and Bokor, J. (1991) Observation of above-threshold multiphoton photoelectric emission from image-potential surface states. *Phys. Rev. B*, **44**, 10980–10982.
- 9 Irvine, S.E., Dechant, A., and Elezzabi, A.Y. (2004) Generation of 0.4-keV femtosecond electron pulses using impulsively excited surface plasmons. *Phys. Rev. Lett.*, **93**, 184801.
- 10 Kinoshita, I., Anazawa, T., and Matsumoto, Y. (1996) Surface and image-potential states on Pt(111) probed by two- and three-photon photoemission. *Chem. Phys. Lett.*, **259**, 445–450.
- 11 Lehmann, J., Merschorf, M., Thon, A., Voll, S., and Pfeiffer, W. (1999) Properties and dynamics of the image potential states on graphite investigated by multiphoton photoemission spectroscopy. *Phys. Rev. B*, **60**, 17037–17045.
- 12 Luan, S., Hippler, R., Schwier, H., and Lutz, H.O. (1989) Electron emission from polycrystalline copper surfaces by multiphoton absorption. *Europhys. Lett.*, **9**, 489–494.
- 13 Miaja-Avila, L., Yin, J., Backus, S., Saathoff, G., Aeschlimann, M., Murnane, M.M., and Kapteyn, H.C. (2009) Ultrafast studies of electronic processes at surfaces using the laser-assisted photoelectric effect with long-wavelength dressing light. *Phys. Rev. A*, **79**, 030901.
- 14 Ogawa, S. and Petek, H. (1996) Two-photon photoemission spectroscopy at clean and oxidized Cu(110) and Cu(100) surfaces. *Surf. Sci.*, **363**, 313–320.
- 15 Schoenlein, R.W., Fujimoto, J.G., Eesley, G.L., and Capehart, T.W. (1988) Femtosecond studies of image-potential dynamics in metals. *Phys. Rev. Lett.*, **61**, 2596–2599.
- 16 Kupersztynch, J., Monchicourt, P., and Raynaud, M. (2001) Ponderomotive acceleration of photoelectrons in surface-plasmon-assisted multiphoton photoelectric emission. *Phys. Rev. Lett.*, **86**, 5180–5183.
- 17 Schattke, W., Krasovskii, E.E., Díez Muiño, R., and Echenique, P.M. (2008) Direct resolution of unoccupied states in solids via two-photon photoemission. *Phys. Rev. B*, **78**, 155314.
- 18 Bisio, F., Nývlt, M., Franta, J., Petek, H., and Kirschner, J. (2006) Mechanisms of high-order perturbative photoemission from Cu(001). *Phys. Rev. Lett.*, **96**, 087601.
- 19 Winkelmann, A., Bisio, F., Ocana, R., Lin, W.-C., Nývlt, M., Petek, H., and Kirschner, J. (2007) Ultrafast optical spin injection into image-potential states of Cu(001). *Phys. Rev. Lett.*, **98**, 226601.
- 20 Eckardt, H., Fritsche, L., and Noffke, J. (1984) Self-consistent relativistic band structure of the noble metals. *J. Phys. F Met. Phys.*, **14**, 97–112.
- 21 Thörner, G., Borstel, G., Dose, V., and Rogozik, J. (1985) Unoccupied electronic

50 | 2 Higher Order Photoemission from Metal Surfaces

- surface resonance at Cu(001). *Surf. Sci.*, **157**, L379–L383.
- 22 Strocov, V.N., Claessen, R., Aryasetiawan, F., Blaha, P., and Nilsson, P.O. (2002) Band- and k -dependent self-energy effects in the unoccupied and occupied quasiparticle band structure of Cu. *Phys. Rev. B*, **66**, 195104.
- 23 Strocov, V.N., Claessen, R., Nicolay, G., Hüfner, S., Kimura, A., Harasawa, A., Shin, S., Kakizaki, A., Starnberg, H.I., Nilsson, P.O., and Blaha, P. (2001) Three-dimensional band mapping by angle-dependent very-low-energy electron diffraction and photoemission: methodology and application to Cu. *Phys. Rev. B*, **63**, 205108.
- 24 Schneider, C.M., Demiguel, J.J., Bressler, P., Schuster, P., Miranda, R., and Kirschner, J. (1990) Spin-resolved and angle-resolved photoemission from single-crystals and epitaxial films using circularly polarized synchrotron radiation. *J. Electron Spectros. Relat. Phenomena*, **51**, 263–274.
- 25 Courths, R. and Hüfner, S. (1984) Photoemission experiments on copper. *Phys. Rep.*, **112**, 53–171.
- 26 Mugarza, A., Marini, A., Strasser, T., Schattke, W., Rubio, A., García de Abajo, F.J., Lobo, J., Michel, E.G., Kuntze, J., and Ortega, J.E. (2004) Accurate band mapping via photoemission from thin films. *Phys. Rev. B*, **69**, 115422.
- 27 Ortega, J.E., Himpsel, F.J., Mankey, G.J., and Willis, R.F. (1993) Quantum-well states and magnetic coupling between ferromagnets through a noble-metal layer. *Phys. Rev. B*, **47**, 1540–1552.
- 28 Wegehaupt, T., Rieger, D., and Steinmann, W. (1988) Observation of empty bulk states on Cu(100) by two-photon photoemission. *Phys. Rev. B*, **37**, 10086–10089.
- 29 Winkelmann, A., Lin, W.-C., Chiang, C.-T., Bisio, F., Petek, H., and Kirschner, J. (2009) Resonant coherent three-photon photoemission from Cu(001). *Phys. Rev. B*, **80**, 155128.
- 30 Knoesel, E., Hotzel, A., and Wolf, M. (1998) Temperature dependence of surface state lifetimes, dephasing rates and binding energies on Cu(111) studied with time-resolved photoemission. *J. Electron Spectros. Relat. Phenomena*, **88–91**, 577–584.
- 31 Pontius, N., Sametoglu, V., and Petek, H. (2005) Simulation of two-photon photoemission from the bulk sp-bands of Ag(111). *Phys. Rev. B*, **72**, 115105.
- 32 Ramakrishna, S. and Seideman, T. (2005) Coherence spectroscopy in dissipative media: a Liouville space pathway approach. *J. Chem. Phys.*, **122**, 084502.
- 33 Ueba, H. and Mii, T. (2000) Theory of energy- and time-resolved two-photon photoemission from metal surfaces influence of pulse duration and excitation condition. *Appl. Phys. A*, **71**, 537–545.
- 34 Weida, M.J., Ogawa, S., Nagano, H., and Petek, H. (2000) Ultrafast interferometric pump–probe correlation measurements in systems with broadened bands or continua. *J. Opt. Soc. Am. B*, **17**, 1443–1451.
- 35 Meier, T., Thomas, P., and Koch, S.W. (2007) *Coherent Semiconductor Optics*, Springer.
- 36 Mukamel, S. (1995) *Principles of Nonlinear Optical Spectroscopy*, Oxford University Press, New York.
- 37 Wolf, M., Hotzel, A., Knoesel, E., and Velic, D. (1999) Direct and indirect excitation mechanisms in two-photon photoemission spectroscopy of Cu(111) and CO/Cu(111). *Phys. Rev. B*, **59**, 5926–5935.
- 38 Petek, H., Nagano, H., and Ogawa, S. (1999) Hole decoherence of d bands in copper. *Phys. Rev. Lett.*, **83**, 832.
- 39 Strocov, V.N. (2003) Intrinsic accuracy in 3-dimensional photoemission band mapping. *J. Electron Spectros. Relat. Phenomena*, **130**, 65–78.
- 40 Goodwin, E.T. (1939) Electronic states at the surfaces of crystals I. The approximation of nearly free electrons. *Proc. Camb. Philol. Soc.*, **35**, 205–220.
- 41 Wallauer, W. and Fauster, Th. (1996) Exchange splitting of image states on Fe/Cu(100) and Co/Cu(100). *Phys. Rev. B*, **54**, 5086–5091.
- 42 Gauyacq, J.P. and Kazansky, A.K. (2007) Modelling of interferometric multiphoton photoemission. *Appl. Phys. A*, **89**, 517–523.

- 43 Güdde, J., Rohleder, M., Meier, T., Koch, S.W., and Höfer, U. (2007) Time-resolved investigation of coherently controlled electric currents at a metal surface. *Science*, **318**, 1287–1291.
- 44 Fauster, Th. (1994) Calculation of surface states using a one-dimensional scattering model. *Appl. Phys. A*, **59**, 639–643.
- 45 Jones, R.O. and Jennings, P.J. (1988) LEED fine structure: origins and applications. *Surf. Sci. Rep.*, **9**, 165–196.
- 46 Farías, D. and Rieder, K.-H. (1998) Atomic beam diffraction from solid surfaces. *Rep. Prog. Phys.*, **61**, 1575–1664.
- 47 Bausells, J. and Echenique, P.M. (1986) Velocity dependence of binding energies and lifetimes of image states at surfaces. *Phys. Rev. B*, **33**, 1471–1473.
- 48 Delone, N.B. and Krainov, V.P. (1999) *Multiphoton Processes in Atoms*, 2nd edn, Springer, Berlin.
- 49 Faisal, F.H.M. and Kamiński, J.Z. (1998) Floquet–Bloch theory of photoeffect in intense laser fields. *Phys. Rev. A*, **58**, R19–R22.
- 50 Faisal, F.H.M., Kamiński, J.Z., and Saczuk, E. (2005) Photoemission and high-order harmonic generation from solid surfaces in intense laser fields. *Phys. Rev. A*, **72**, 023412.
- 51 Cavaliere, A.L., Müller, N., Uphues, Th., Yakovlev, V.S., Baltuska, A., Horvath, B., Schmidt, B., Blümel, L., Holzwarth, R., Hendel, S., Drescher, M., Kleineberg, U., Echenique, P.M., Kienberger, R., Krausz, F., and Heinzmann, U. (2007) Attosecond spectroscopy in condensed matter. *Nature*, **449** (7165), 1029–1032.
- 52 Drescher, M., Hentschel, M., Kienberger, R., Uiberacker, M., Yakovlev, V., Scrinzi, A., Westerwalbesloh, Th., Kleineberg, U., Heinzmann, U., and Krausz, F. (2002) Time-resolved atomic inner-shell spectroscopy. *Nature*, **419** (6909), 803–807.
- 53 Meier, F. and Zakharchenya, B.P. (eds) (1984) *Optical Orientation*, North-Holland, Amsterdam.
- 54 Kuch, W. and Schneider, C.M. (2001) Magnetic dichroism in valence band photoemission. *Rep. Prog. Phys.*, **64**, 147–204.
- 55 Winkelmann, A., Hartung, D., Engelhard, H., Chiang, C.-T., and Kirschner, J. (2008) High efficiency electron spin polarization analyzer based on exchange scattering at Fe/W(001). *Rev. Sci. Instrum.*, **79**, 083303.
- 56 Winkelmann, A., Lin, W.-C., Bisio, F., Petek, H., and Kirschner, J. (2008) Interferometric control of spin-polarized electron populations at a metal surface observed by multiphoton photoemission. *Phys. Rev. Lett.*, **100**, 206601.
- 57 Schmidt, A.B., Pickel, M., Wiemhofer, M., Donath, M., and Weinelt, M. (2005) Spin-dependent electron dynamics in front of a ferromagnetic surface. *Phys. Rev. Lett.*, **95**, 107402.
- 58 Petek, H., Heberle, A.P., Nessler, W., Nagano, H., Kubota, S., Matsunami, S., Moriya, N., and Ogawa, S. (1997) Optical phase control of coherent electron dynamics in metals. *Phys. Rev. Lett.*, **79**, 4649–4652.

High efficiency electron spin polarization analyzer based on exchange scattering at Fe/W(001)

A. Winkelmann, D. Hartung, H. Engelhard, C.-T. Chiang, and J. Kirschner
Max-Planck-Institut für Mikrostrukturphysik, Weinberg 2, D-06120 Halle(Saale), Germany

(Received 2 April 2008; accepted 2 June 2008; published online 22 August 2008)

We report on a compact electron spin analyzer based on exchange scattering from a magnetic surface. The heart of the detector is an Fe(001) thin film grown on W(001) with chemisorbed oxygen in the $p(1 \times 1)$ structure. The device is mounted at the exit of an energy dispersive analyzer and works at a scattering energy of about 13.5 eV. Its figure of merit is 2×10^{-3} , combined with an excellent stability of more than 2 weeks in UHV. © 2008 American Institute of Physics.

[DOI: [10.1063/1.2949877](https://doi.org/10.1063/1.2949877)]

I. INTRODUCTION

Electron spectroscopies aim at the reliable characterization of electrons in all their degrees of freedom. Apart from the energy and momentum, the spin is a fundamental property determining the behavior of electrons in solid state systems leading directly to such effects as magnetism and other electron correlation phenomena. This illustrates that it is of utmost importance to be able to efficiently detect and to analyze the spin in electron spectroscopic experiments.¹⁻³

All spin detectors rely in some way or another on a differing scattering cross section for electrons having opposite projections ($+\hbar/2$ or $-\hbar/2$) of their spin on a quantization axis which is defined by the geometry of the scattering experiment. Systematic comparisons of the defining properties of various types of spin detectors can be found in Refs. 4 and 5 (in addition, a recent detailed characterization of the spin polarized low energy electron diffraction (SPLEED) detector can be found in Ref. 6). The prominent example for a mechanism that provides a spin sensitivity in scattering experiments is the spin-orbit interaction, on which a large group of spin polarimeters is based. However, the size of the spin-orbit interaction energy is usually small in comparison to the Coulomb interaction, which dominates the scattering cross section in most circumstances. Experimentally, this means that one has to select special scattering conditions where the absolute effect of the Coulomb scattering is small in order to increase the sensitivity to the spin-orbit interaction. This necessity introduces an overall reduction in count rate by two to three orders of magnitude.¹

Another, different, type of spin-dependent interaction is supplied by the exchange mechanism in magnetic systems. The corresponding interaction energy is of the order of 2 eV in ferromagnetic iron. The size of this energy is significant in comparison to the energies involved in the scattering of very low energy electrons (≈ 20 eV) at surfaces and thus it can be expected that the scattering cross section for these electrons can become noticeably influenced by the spin-dependent exchange energy in specific circumstances.

For instance, a magnetic surface can show spin-dependent band gaps caused by the exchange interaction.

The presence of a band gap means that electrons of specific energies and momenta are reflected with high intensity from such a sample because in the solid there are no states which they can occupy. If at the same time this energy is low enough so that no diffracted beams are created by the periodic surface potential, practically all the reflected intensity is concentrated in the specular beam. A high spin sensitivity results if the band gap is spin dependent, so that the reflectivity is high for one spin direction, while it is low for the other. In this context, it has been predicted theoretically⁷ and observed in various investigations that the scattering of very low energy electrons at ferromagnetic Fe surfaces shows a large spin asymmetry and at the same time a large scattering efficiency due to an exchange-split band structure.^{8,9} This effect was suggested to be used in a spin detector and, subsequently, spin polarimeters have been introduced which were based on spin-dependent reflection of very low energy electrons from surfaces of Fe(001) films (thickness > 3000 Å) grown on MgO(001) (Refs. 10 and 11) or ultra-thin Fe(001) films grown on Ag(001).^{12,13}

Because of the very high intrinsic efficiency of the discussed scattering effect on Fe surfaces, we also decided to design a spin detector based on this promising principle. We chose to base the detector on Fe films grown on W(001) substrates, because of the relatively simple and fast preparation of this substrate. We have tried to optimally address the practical requirements for an efficient spin detection in the design of our spin detector which is described in this article.

II. DETECTOR DESIGN

The detector was designed to fit onto a commercially available cylindrical sector analyzer with 90° deflection angle (*Focus CSA300*). With outside dimensions fitting a space of $20 \times 20 \times 60$ cm³, the detector is very compact and easy to integrate in standard UHV systems. Except for the electron bombardment heating, the spin detector itself requires no high voltages during operation.

The most important parts and their relative arrangement are shown in the drawing in Fig. 1. The electrostatic lenses L1, L2, and L3 transfer the electrons from the exit slit of the

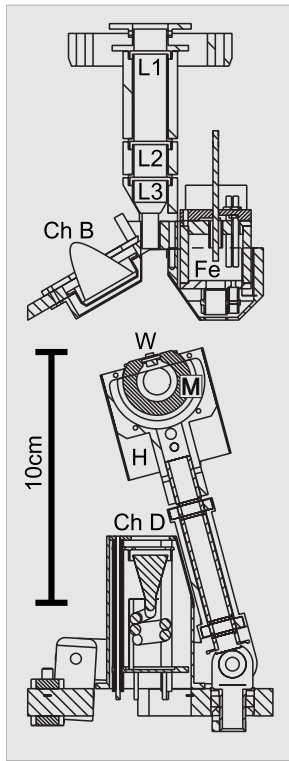


FIG. 1. Drawing of the main parts of the detector. (L1, L2, L3) electrostatic transfer and focusing lenses, (W) W(001) crystal, (M) electromagnet, (H) holder for W, M, and heating filament (can be tilted and rotated), (Ch B) the channeltron collecting the electrons reflected from W, and (Ch D) the channeltron which is used for spin-integrated measurements when H is moved into the position under the Fe evaporation source (Fe).

analyzer to the scattering target W, the Fe film on the W(001) crystal. The crystal is surrounded by the electromagnet M which consists of a ferrite ring around which a coil has been wound. The crystal and ferrite ring are mounted on a holder H which can be flipped into the path of the electrons coming from the analyzer. The electrons leaving the sample are partially collected by the “back” channeltron Ch B. The incidence angle of the analyzed electrons is 15° degrees with respect to the surface normal of the W(001) crystal.

The channeltron B is preceded by a high pass energy filter consisting of two parallel grids. The first grid seen by the electrons is at the scattering potential (i.e., the potential of the target and all the surrounding electrodes) while the second grid is 3–4 V more positive than the scattering potential. This design is based on the observation¹⁴ that electrons scattered inelastically due to the generation of Stoner excitations show a spin asymmetry of about 25% at ≈ 10 eV. The inclusion of these electrons in addition to the elastically scattered ones enhances the count rate without major sacrifice of spin sensitivity, while secondary electrons from the inner part of the detector region (presumably with no spin asymmetry) are suppressed. The very moderate energy filtering reduces the part of the apparatus asymmetry which is due to slight changes in the elastic scattering conditions. It was reported in Ref. 14 for Fe(110) and in Ref. 15 for Fe(001) that the variation of the spin sensitivity with respect to the

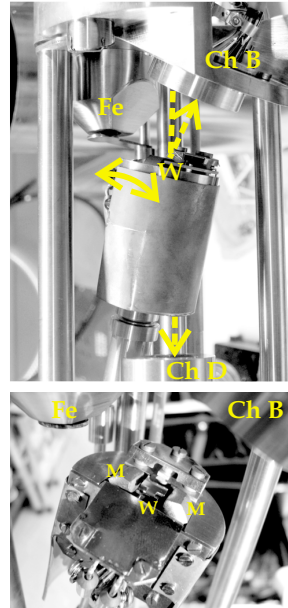


FIG. 2. (Color online) Photographs showing the crucial parts of the spin detector. The following parts are marked: (W) the W(001) crystal, (Ch B) the channeltron collecting the electrons reflected from W(001), and (Ch D) the channeltron which is used for spin-integrated measurements when W is moved into the position under the Fe evaporation source (Fe). In the lower photograph, (M) are the ends of the ferrite ring used to magnetize the ultrathin Fe film on the W(001) crystal.

angle of incidence is small from 0° of incidence up to about 15°. This also ensures that the spin sensitivity of the detector is practically independent of the azimuthal rotation of the detector crystal. This means that any orientation of the transversal spin polarization vector of the beam leaving the energy analyzer can be measured with the same spin sensitivity.

The spin asymmetry is measured under reversal of the Fe film magnetization by application of current pulses through the electromagnet M. The projection of the spin quantization axis onto the magnetization direction can be selected by rotating the holder H about the surface normal of the crystal W. This is accomplished by a rotation feedthrough. An additional linear feedthrough connected to a lever at the bottom of the holder H allows to flip the holder into the preparation position with the crystal W exactly below the electron beam evaporator Fe used to grow the iron film. This position also allows spin-integrated measurements because the electrons coming from the analyzer are going to the “direct” channeltron Ch D, as illustrated in the drawing of Fig. 1 and in the photographs of Fig. 2. We show the assembled device in Fig. 3.

For preparation of the W(001) crystal, electron beam heating is used. This is realized by a heated filament below the W crystal and by putting the W crystal on a positive voltage of about 1 kV with respect to the filament. In this way, crystal temperatures of 2500 K can be reached. This can be checked by observing the W(001) crystal with a pyrometer through a small viewport. Oxygen can be dosed by a leak valve. The whole spin detector is pumped by a separate ion getter pump and a titanium sublimation pump nearby.

083303-3 Electron spin polarization analyzer

Rev. Sci. Instrum. 79, 083303 (2008)

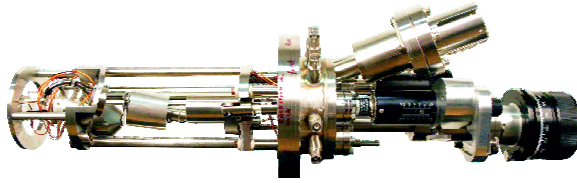


FIG. 3. (Color online) Photograph of the assembled device with the inner shielding taken off. The mounting flange (seen near the center) is a 100 mm inner diameter conflat flange.

To prepare the spin detector for operation, the W(001) crystal is treated in a similar way as in the SPLEED detector where the same type of crystal is used. One removes carbon contaminants, tungsten oxides, and carbon monoxide by treatments of the sample with oxygen and by flashing the crystal to different temperatures.⁶ In our case, the oxygen cleaning treatments are necessary only after bakeout. During regular operation, removing a used iron film and preparing a surface for growth of a new film is accomplished by flashing the crystal to 2000 K. After this, the Fe film is grown using the electron beam evaporator. The pressure in the device during growth is in the lower 10^{-10} mbar range. Immediately after the growth of the Fe film, it is dosed with 3 to 5 L O_2 , in our case this is done for 60–100 s at 3×10^{-8} mbar. At this oxygen coverage, the Fe(001)- $p(1 \times 1)O$ surface structure is expected to form.¹⁶ Finally, the sample is heated to about 600 K to anneal the film and desorb excess oxygen. A complete preparation cycle takes less than 15 min.

III. CHARACTERIZATION

In the spin detector, we measure the normalized intensity asymmetry A by counting the electrons that reach the back channeltron when the Fe film magnetized either parallel (\Rightarrow) or antiparallel (\Leftarrow) along the spin quantization axis.

$$A = \frac{I_{\Rightarrow} - I_{\Leftarrow}}{I_{\Rightarrow} + I_{\Leftarrow}}. \quad (1)$$

These two measurements necessarily have to be carried out at successive times and the time difference has to be kept short enough as to minimize the influence of intensity variations. From the measured asymmetry A , one determines the spin polarization component P along the magnetization axis as

$$P = A/S, \quad (2)$$

where S is the spin sensitivity (also called Sherman function with Mott detectors), which describes which asymmetry A the spin detector would measure for a completely polarized beam with $P=1.0$.

If one assumes that the intensity variations of the electron beam to be analyzed are approximately linear in time, this can be taken into account by adopting a special measurement sequence. The counts in the back channeltron are measured for a magnetization pulse sequence of

$$I_{\Rightarrow}(t_1), I_{\Leftarrow}(t_2), I_{\Rightarrow}(t_3), I_{\Leftarrow}(t_4), \dots, I_{\Rightarrow}(t_{2m-3}), \\ I_{\Leftarrow}(t_{2m-2}), I_{\Rightarrow}(t_{2m-1}), I_{\Leftarrow}(t_{2m}) \quad (3)$$

and then forming the sums for calculation of the asymmetry:

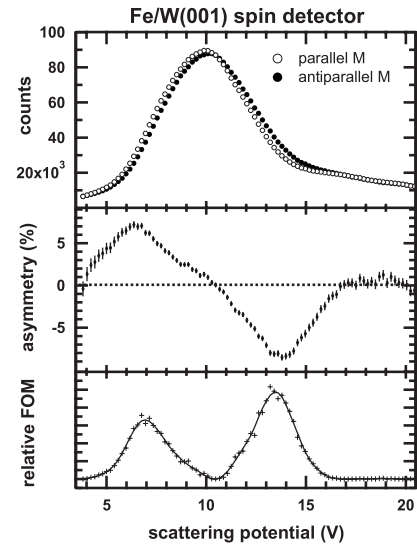


FIG. 4. Measured intensity (top) and asymmetry (middle) as a function of scattering potential (this is the potential difference between the stainless steel inner cylinder of the CSA and the Fe- $p(1 \times 1)O$ target. Up to a small work function difference between stainless steel and the target of a few tenths of an eV this corresponds to the kinetic energy of the electrons in eV). In the bottom part, the corresponding relative figure of merit (FOM) is shown, indicating optimum operation at 13.5 eV scattering energy.

$$I_{\Rightarrow} = \sum_t I_{\Rightarrow}(t), \quad (4)$$

$$I_{\Leftarrow} = \sum_t I_{\Leftarrow}(t). \quad (5)$$

Because the spin detection principle in our device does not involve different geometrical pathways to measure the two conjugated scattering intensities (e.g., a “left” and a “right” counter as in Mott or SPLEED detectors), the corresponding instrumental asymmetry due to unsymmetrical alignments is largely suppressed. In addition, the asymmetry due to a magnetic field is suppressed as much as possible by carefully designing the electromagnet and its surroundings to show a negligible remanent magnetic field. The use of a thin magnetic Fe film instead of a bulk Fe sample reduces the magnetic stray fields. In sum, this leads to a spurious instrumental asymmetry of about $\pm 0.3\%$, as is measured for unpolarized electrons.

To determine the optimum scattering energy in the detector, we measured the reflected number of electrons N and the corresponding asymmetry A under reversal of the magnetization of the Fe film in the detector. The maximum of the relative figure of merit defined by $F_R = A^2 \times N$ as a function of the potential of the scattering film then indicates the optimum working condition for the detector. This is shown in Fig. 4. The spin polarization of the measured electrons was about 30%.

To calculate the polarization from a measured asymmetry like in Fig. 4, we need to determine the Sherman function. For this purpose, we measured the low energy secondary electrons (kinetic energy of 2 eV) from a Co film grown on Cu(001) using a primary electron beam of 2 keV energy

from an electron gun. The secondary electrons are estimated to have a spin polarization P of $0.35(\pm 0.03)$. This value was determined in Ref. 17 for secondary electrons excited from Co(0001) by photons of 58 eV energy. From the measured asymmetry A of $0.085(\pm 0.005)$ with our detector, we can calculate the Sherman function $S=A/P$ to be $0.24(\pm 0.03)$ at the optimum scattering energy of 13.5 eV. A comparison with an in-plane magnetized 12 ML thick Fe film on Cu(001) resulted in an asymmetry of 0.075 for the low energy secondary electrons measured at 120 K. With our calibration of the spin sensitivity ($S=0.24$) we arrive at 31% for the spin polarization of the Fe film, in good agreement with the values of 25%–35% reported in the literature for this system.^{18,19}

We additionally cross-checked our spin sensitivity with two-photon photoemission measurements from Co films on Cu(001), which are expected to show a spin polarization of about 45%–60% when excited with p -polarized optical pulses of 3 eV photon energy.^{20,21} Using our spin detector, we observe an asymmetry of 0.15 at a binding energy -0.5 eV below the Fermi level, which would translate into a Sherman function between 0.23 and 0.30 for the mentioned values of the spin polarization, which is in good agreement with the value obtained from the secondary electron spin polarization measurements.

We have found that our detector shows a reproducible asymmetry over at least 2 weeks without any reparation. This is due to the chemical inertness of the Fe surface with chemisorbed oxygen and has been also observed in other applications of this system.¹¹ This is a major advantage for long-term experiments with intrinsically low count rates.

To compare our spin detector quantitatively to other devices, we estimate the figure of merit F which determines the counting time needed to reach a given statistical error in the spin polarization.¹ The statistical figure of merit is determined by the Sherman function S and the relative intensity response I/I_0 (which describes how many incident electrons are needed for one detection event):

$$F = S^2 I/I_0. \quad (6)$$

From this formula it can be seen that a spin detector is desired to show a large Sherman function as well as a high intensity response, while a relative improvement of the Sherman function is potentially more efficient in decreasing the required counting time.

An upper bound for the intensity response I/I_0 can be gained from the relative counting rates in the direct channeltron ($\approx I_0$) without the scattering crystal, and the counts in the back channeltron (I) with the scattering crystal in the path. We observe that I_0 is a factor of 13 higher than I at maximum, corresponding to $I/I_0 \approx 0.076$ at the scattering potential of 13.5 V. Since we do not measure the incident current at the position of the detector crystal but several centimeters downstream, there might be fewer electrons arriving at channeltron D than at the crystal.

In the literature, a value of $I/I_0 \gtrsim 0.10$ is reported for clean Fe(001)/Ag(001) (Ref. 13) and a value of 0.06 for Fe(001)- $p(1 \times 1)O$.¹⁰ Assuming $S=0.24$ and $I/I_0=0.076$ and taking into account that it is necessary to perform two

sequential measurements with reversed Fe film magnetization, we arrive at $F \approx 2.2 \times 10^{-3}$ for the figure of merit of our detector. This value is consistent with Hillebrecht *et al.*,¹³ where a lower limit of about 1×10^{-3} has been estimated (with a maximum of up to 10×10^{-3}) and with Bertacco *et al.*¹¹ who report 0.7×10^{-3} for their combination of energy analyzer and detector. These lower limit values show that the detection principle based on exchange scattering at an Fe surface is about one order of magnitude more efficient than the Mott and the SPLEED detectors.^{5,6} It has to be kept in mind, however, that the high efficiency in spin analyzers of the presented design is available only in a limited energy range. This means that this type of spin analyzer is best suited for electron spectroscopic experiments which anyway detect a limited bandwidth of electron energies, e.g., using electrostatic energy analyzers. In cases where a broader range of electron energies is to be analyzed by the spin detector (e.g., secondary electrons without energy analysis), other types of detectors might be more favorable.

IV. DISCUSSION

Among the class of spin polarization detectors with energy analysis and single-electron detection, two devices have been described based on exchange scattering: one by Bertacco *et al.*¹¹ and the other by Hillebrecht *et al.*¹³ Among these, the detector of Bertacco is closest to ours and we therefore discuss similarities and dissimilarities compared to our detector. Both use Fe(001)- $p(1 \times 1)O$ which shows extraordinary time stability, as is confirmed by our results. Bertacco *et al.* use thick epitaxial Fe films on MgO, with the property that the detector can be “rejuvenated” many times by simple heating in oxygen atmosphere. A new crystal, however, is prepared in a separate vacuum system, requiring a new MgO crystal preparation. In our case, rejuvenation is not possible. We deposit Fe on W(001) at a thickness beyond the spin reorientation transition (≈ 40 ML). This is a metastable system with respect to high temperatures because the Fe film disintegrates into μm -sized crystallites with a 1 ML Fe carpet underneath (Stranski-Krastanov growth). Therefore, a used film must be replaced by a new one (after about 2 weeks). This is done *in situ*, within less than 15 min.

The electron reflectivity shows consistently a broad peak around 10 eV kinetic energy, with sizable polarization effects on the lower as well as the higher kinetic energy sides (Fig. 4). We work on the high energy side, while Bertacco *et al.* prefer the low energy side. In their test measurements with an elastic reflection of a well defined beam⁹ they found a high exchange asymmetry of up to 44%, which decreased by more than a factor of 2 in their actual device.¹¹ We do not find this large asymmetry either in our device. This feature seems to be extremely sensitive to unknown factors. However, the performance of our instrument in terms of figure of merit is clearly better than their instrument.¹¹

Another important design consideration concerns the geometrical constraints: our combined device uses an electron spectrometer with a deflection angle of 90° . If we define the deflection plane of the analyzer by the incoming beam axis and the outgoing beam axis, an ingoing longitudinally

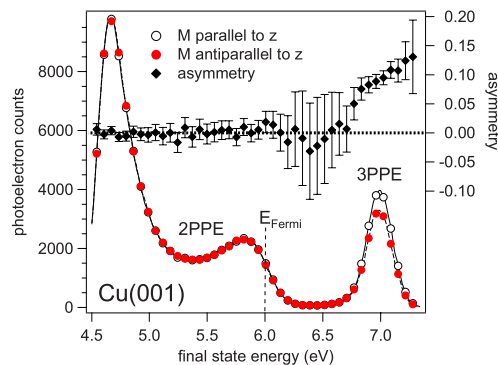


FIG. 5. (Color online) Photoelectron spectra and measured spin asymmetry for excitation of Cu(001) with circularly polarized laser pulses of $h\nu=3.0$ eV. The spin quantization axis is oriented along the surface normal z of Cu(001). Two-photon excitation is possible up to 6.0 eV final state energy, above that we see a three-photon photoemission peak at 7 eV. Electrons in this peak are spin polarized by as much as about 45%, as calculated from the measured asymmetry.

polarized beam is transformed into a transversely polarized beam while the transverse component perpendicular to the deflection plane of the analyzer stays perpendicular. By virtue of our rotatable detector crystal, both these components can be measured. A transverse component in the deflection plane cannot be measured. However, if the whole device (energy analyzer plus detector) is rotated by 90° about the axis of the incoming beam, the remaining component can be measured. The longitudinal component is then measured redundantly. The device is sufficiently lightweight and compact to be mounted on a differentially pumped rotary platform (100 mm inner diameter). In this way, the full polarization vector of the beam (arbitrarily oriented in space) can be measured. This is not possible with a 180° degree deflector, such as used in Refs. 11 and 13 because the longitudinal component stays orthogonal to the in-plane magnetization of the detector crystal, but, alternatively, the other detectors could, in principle, be also used with a 90° degree deflecting analyzer.

As an application of our spin detector, we show in Fig. 5 a photoelectron spectrum from a Cu(001) surface which was excited by ultrashort circularly polarized laser pulses with a photon energy of 3 eV. The energy resolution of the energy-analyzer/spin-detector combination was set to 150 meV. Because the work function of Cu(001) is about 4.6 eV, these electrons must have absorbed the energy of at least two photons to leave the sample. With two photons, electrons initially at the Cu(001) Fermi level can be excited up to 6 eV above the Fermi level, which is where the Fermi edge is visible in the final state energy scale of Fig. 5. Beyond the two-photon Fermi edge, we see a peak at 7 eV which is due to a resonant three-photon transition of electrons from the Cu d bands via unoccupied sp bands and the $n=1$ image-potential state.²² Using our spin detector, we have been able to show that the d band electrons excited by three circularly polarized photons are spin polarized.²³ This can be seen in Fig. 5 where the measured asymmetry for the spin quantization axis along the surface normal z of the Cu(001) sample is shown as black diamonds. The origin of the effect is the

spin-orbit interaction in the Cu d bands which in connection with the optical selection rules for circularly polarized light leads to the excitation of spin-polarized electrons even from nonmagnetic materials such as Cu.²⁴ In contrast, the photoelectrons excited from clean Cu(001) by only two photons (energies up to 6 eV in Fig. 5) originate from initial states in the sp band near the Fermi level. These initial states are not influenced by the spin-orbit interaction and thus the measured two-photon part of the spectrum in Fig. 5 does not show a spin polarization.

By our observation we have demonstrated a way to excite spin polarized electrons into unoccupied image-potential states of a nonmagnetic surface. Moreover, the excitation of spin-polarized electrons by circularly polarized ultrashort laser pulses at an extremely well-defined system such as clean Cu(001) might provide a reliable standard for calibration purposes.

Summarizing, we have designed and characterized a compact and reliable spin detector with excellent long-term stability based on the scattering of very low energy electrons on ultrathin Fe films on W(001). This instrument has been built in 1999 and has operated satisfactorily ever since.

ACKNOWLEDGMENTS

We acknowledge valuable experimental and technical support from W.-C. Lin, R. Ocaña, and F. Helbig.

- ¹J. Kessler, *Polarized Electrons* (Springer, Berlin, 1985).
- ²J. Kirschner, *Polarized Electrons at Surfaces* (Springer, Berlin, 1985).
- ³*Polarized Electrons in Surface Physics*, edited by R. Feder (World Scientific, Singapore, 1985).
- ⁴D. T. Pierce, R. J. Celotta, M. H. Kelley, and J. Unguris, *Nucl. Instrum. Methods Phys. Res. A* **266**, 550 (1988).
- ⁵M. Getzlaff, B. Heidemann, J. Bansmann, C. Westphal, and G. Schönhense, *Rev. Sci. Instrum.* **69**, 3913 (1998).
- ⁶D. Yu, C. Math, M. Meier, M. Escher, G. Rangelov, and M. Donath, *Surf. Sci.* **601**, 5803 (2007).
- ⁷E. Tamura and R. Feder, *Phys. Rev. Lett.* **57**, 759 (1986).
- ⁸D. Tillmann, R. Thiel, and E. Kisker, *Z. Phys. B: Condens. Matter* **77**, 1 (1989).
- ⁹R. Bertacco and F. Ciccacci, *Phys. Rev. B* **59**, 4207 (1999).
- ¹⁰R. Bertacco, D. Onofrio, and F. Ciccacci, *Rev. Sci. Instrum.* **70**, 3572 (1999).
- ¹¹R. Bertacco, M. Marcon, G. Trezzi, L. Duò, and F. Ciccacci, *Rev. Sci. Instrum.* **73**, 3867 (2002).
- ¹²R. Jungblut, C. Roth, F. U. Hillebrecht, and E. Kisker, *Surf. Sci.* **269**, 615 (1992).
- ¹³F. U. Hillebrecht, R. M. Jungblut, L. Wiebusch, C. Roth, H. B. Rose, D. Knabben, C. Bethke, N. B. Weber, S. Manderla, U. Rosowski, and E. Kisker, *Rev. Sci. Instrum.* **73**, 1229 (2002).
- ¹⁴M. S. Hammond, G. Fahsold, and J. Kirschner, *Phys. Rev. B* **45**, 6131 (1992).
- ¹⁵R. Bertacco, M. Merano, and F. Ciccacci, *Appl. Phys. Lett.* **72**, 2050 (1998).
- ¹⁶K. O. Legg, F. Jona, D. W. Jepsen, and P. M. Marcus, *Phys. Rev. B* **16**, 5271 (1977).
- ¹⁷E. Kisker, W. Gudat, and K. Schröder, *Solid State Commun.* **44**, 591 (1982).
- ¹⁸D. P. Pappas, C. R. Brundle, and E. Hopster, *Phys. Rev. B* **45**, 8169 (1992).
- ¹⁹R. Allenspach and A. Bischof, *Phys. Rev. Lett.* **69**, 3385 (1992).
- ²⁰O. Andreyev, Y. M. Koroteev, M. S. Albaneda, M. Cinchetti, G. Bihlmayer, E. V. Chulkov, J. Lange, F. Steeb, M. Bauer, P. M. Echenique S. Blügel, and M. Aeschlimann, *Phys. Rev. B* **74**, 195416 (2006).

083303-6 Winkelmann *et al.*

Rev. Sci. Instrum. **79**, 083303 (2008)

²¹M. Aeschlimann, M. Bauer, S. Pawlik, W. Weber, R. Burgermeister, D. Oberli, and H. C. Siegmann, *Phys. Rev. Lett.* **79**, 5158 (1997).

²²F. Bisio, M. Nyvlt, J. Franta, H. Petek, and J. Kirschner, *Phys. Rev. Lett.* **96**, 087601 (2006).

²³A. Winkelmann, F. Bisio, R. Ocana, W.-C. Lin, M. Nyvlt, H. Petek, and J. Kirschner, *Phys. Rev. Lett.* **98**, 226601 (2007).

²⁴C. M. Schneider, J. J. Demiguel, P. Bressler, P. Schuster, R. Miranda, and J. Kirschner, *J. Electron Spectrosc. Relat. Phenom.* **51**, 263 (1990).

Ultrafast Optical Spin Injection into Image-Potential States of Cu(001)

A. Winkelmann,^{1,*} F. Bisio,² R. Ocaña,¹ W.-C. Lin,¹ M. Nývlt,³ H. Petek,⁴ and J. Kirschner¹

¹Max-Planck-Institut für Mikrostrukturphysik, Weinberg 2, D-06120 Halle (Saale), Germany

²CNISM, Sede consorzata di Genova, via Dodecaneso 33, I-16146 Genova, Italy

³Charles University, Faculty of Mathematics and Physics, Institute of Physics, Ke Karlovu 5, CZ-12116 Praha 2, Czech Republic

⁴Department of Physics and Astronomy, University of Pittsburgh, Pennsylvania 15260, USA

(Received 22 February 2007; published 31 May 2007)

We report the observation of a net spin polarization in the $n = 1$ image-potential state at the Cu(001) surface. The spin polarization is achieved by spin-selective multiphoton excitation of electrons from the spin-orbit split Cu d bands to the image-potential state using circularly polarized ultrafast light pulses. We show that by tuning the exciting photon energy, we can adjust the resonant coupling of the image-potential state to d bands of different double-group symmetry. This allows us to tune the spin polarization injected into the image-potential state.

DOI: [10.1103/PhysRevLett.98.226601](https://doi.org/10.1103/PhysRevLett.98.226601)

PACS numbers: 72.25.Fe, 73.20.-r, 79.60.-i, 82.50.Pt

Optical manipulation of spins in magnetic [1–3] and nonmagnetic solids [4,5] and their surfaces is of great interest for ultrafast magnetism, spintronics, and quantum information processing. The observation that magnetization dynamics can be traced to single-electron spin-flip processes [6] underscores the importance of addressing elementary spin scattering processes to understand macroscopic phenomena like laser-induced demagnetization [7]. To this end, spin and time-resolved multiphoton photoemission [1,6,8,9] provides one of the most specific and sensitive probes of electron-spin phenomena on the femtosecond time scale.

The strong coupling of spins in ferromagnetic materials, however, can make the measurement and analysis of the spin dynamics of excited electrons intrinsically difficult. Spin dynamics can in fact occur through a superposition of both magnetism-induced as well as magnetism-independent processes, whose separate contributions are sometimes difficult to address selectively. In this respect, the investigation of spin dynamics by nonlinear photoemission would surely benefit from the availability of a source of spin-polarized excited electrons at nonmagnetic surfaces. Spin-dependent transport and scattering at interfaces, relevant to the operation of spintronic devices, could also be studied in more detail.

It is well known that photoexcited spin-polarized electrons can be produced at unpolarized targets, provided that the incident light has circular polarization. Spin-orbit coupling (SOC) in combination with optical selection rules provides the mechanism by which electrons can be spin-selectively excited. This forms the basis of various effects related to optical spin orientation [10,11]. For one-photon photoemission from metals, it has been demonstrated that significant spin-orbit coupling leads to strong spin-polarization effects of the photoelectrons even in a relatively low- Z material like copper [12]. The extension of the optical spin orientation effect to multiphoton transitions in solids would allow one to transiently spin polarize excited

intermediate states below the photoemission threshold which in principle cannot be sensed by one-photon photoemission. Such a multiphoton excitation scheme can then be directly exploited to study spin-dependent scattering of excited electrons in solids.

In this Letter, we report the observation of large (40%) spin polarization of the $n = 1$ image-potential (IP) state on the Cu(001) surface by means of spin-resolved multiphoton photoemission. The spin polarization is achieved by resonantly coupling the spin-orbit split Cu d bands with the IP state via a multiphoton transition excited by circularly polarized light. We observe that both the sign and the magnitude of the IP-state spin polarization can be selected by balancing the resonant coupling to different spin-orbit split d bands. Our observation provides the basis for the coherent manipulation and probing of the spin dynamics of excited electrons at nonmagnetic surfaces.

The photoemission experiments were carried out in an ultrahigh vacuum system (pressure $< 5 \times 10^{-11}$ mbar). The ultrashort excitation pulses were provided by the frequency-doubled output of a self-built Ti:sapphire oscillator. The pulse central energy could be continuously varied in the range of $h\nu = 3.00$ – 3.14 eV by tuning the phase-matching angle of the frequency-doubling $80 \mu\text{m}$ -thick $\beta\text{-BaB}_2\text{O}_4$ (BBO) crystal. At the energy of $h\nu = 3.07$ eV, the pulse length at the surface was ≤ 20 fs, and the pulse energy ~ 1 nJ. Right- and left-circular (RCP, LCP) and linear polarization were set by a combination of achromatic $\lambda/4$ and $\lambda/2$ wave plates. The laser beam was focused to a spot of $\approx 40 \mu\text{m}$ in diameter on the surface. The angle between the incident beam and the axis of the analyzer was fixed at 42° (Fig. 1). A clean and ordered Cu(001) surface was prepared by standard sputtering and annealing procedures. The optical plane was aligned parallel to the [100] direction. All the experiments were carried out at 300 K.

The electrons photoemitted along the surface normal were analyzed by a cylindrical sector analyzer (set to

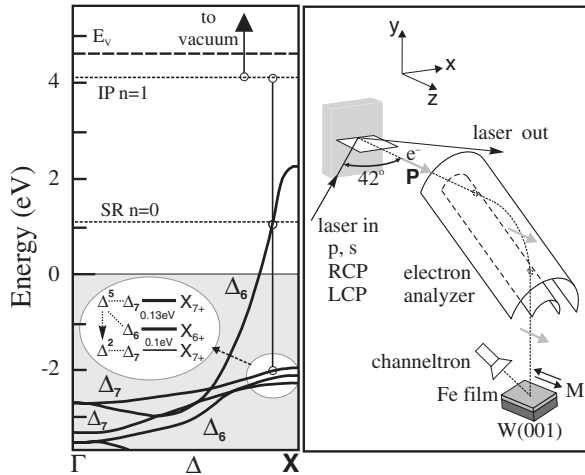


FIG. 1. Left: Relativistic band structure of Cu(001) along the Δ line (after Ref. [15]). The energy position of the $n = 0$ SR and $n = 1$ IP state at $\bar{\Gamma}$ is shown. Vertical lines represent photo-induced electronic transitions at typical energies employed in our experiment. The open circles at line termini represent the spectral width of the excitation pulses. The inset shows a magnified view of the spin-orbit split d -band region near the X point. Right: Experimental setup in the normal-emission geometry.

150 meV energy resolution) coupled with a newly developed spin detector, based on very low energy electron scattering on a magnetized ultrathin Fe/W(001) film [13,14] (Fig. 1). The spin detector included facilities for W(001) crystal flashing, Fe film growth, magnetization reversal of the Fe film, additionally allowing a non-spin-resolved mode. The detector Sherman function was $S = (0.23 \pm 0.02)$, with excellent long-term stability as characterized by constant reference measurements over typically two weeks without reparation of the Fe film.

The basic principle underlying the multiphoton optical orientation process for the Cu(001) IP state is shown in Fig. 1. There we show the calculated relativistic band structure of Cu(001) along the Δ line (after Ref. [15]), pertinent to the normal-emission geometry, along with the $\bar{\Gamma}$ energy positions of the $n = 0$ surface resonance (SR) and the $n = 1$ IP state [16]. One-photon transitions at energies representative of the ones employed in our experiment are depicted as the vertical lines. The spatial single-group and the double-group symmetry character of the states involved is denoted by superscripts and subscripts, respectively. It can be clearly seen that the IP state can be populated from initial states located in the d bands in the proximity of the X point by a resonant excitation pathway proceeding via the unoccupied sp band or the $n = 0$ SR [17]. The magnification of the band structure in the region near the X point (inset of Fig. 1) shows that the Δ^5 band is spin-orbit split in two bands with strong Δ^5 spatial symmetry and Δ_7 and Δ_6 double-group symmetry, with reported binding energy differences between 100 meV [12] and 130 meV [18], while a

Δ_7 band with strong hybridization of Δ^5 and Δ^2 spatial symmetry is present at about 100 meV larger binding energy.

The relativistic selection rules for normal emission from an fcc(001) surface dictate the final state symmetry to be Δ_6^1 . Furthermore, RCP light couples spin-down (spin-up) electrons from a Δ_6^5 (Δ_7^5) symmetry initial state to a Δ_6^1 symmetry final state (and vice versa for LCP excitation) [19]. This provides the basic mechanism by which oppositely spin-polarized photoelectrons are excited selectively from the two spin-orbit split bands of different symmetry to the unoccupied IP state. In our experimental geometry, no asymmetry in photoelectron intensity (dichroism) is expected for excitation with reversed helicity [20], and the spin-polarization vector points in a direction very close to the surface normal [21]. We will henceforth discuss the z component of the spin polarization only.

The experimental observation of spin injection from spin-orbit split d bands into the IP state is demonstrated in Fig. 2. There, in the upper panel, we show two typical spin-up and spin-down photoelectron spectra I_\uparrow and I_\downarrow , measured with RCP incident light at $h\nu = 3.02$ eV photon energy (dashed lines and solid lines, respectively). The spin-resolved spectra are calculated from the measured intensity asymmetry under reversal of the magnetization direction of the Fe/W(001) spin detector. The spin polarization along the z direction for RCP (LCP) incident ra-

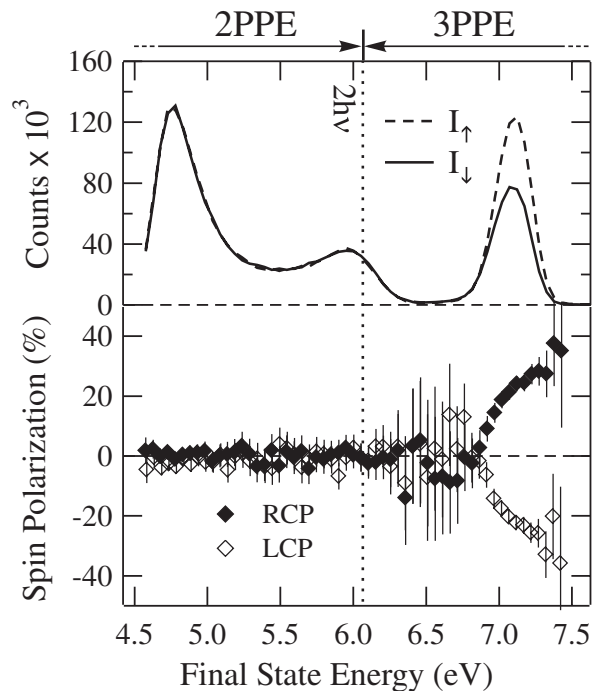


FIG. 2. Top panel: Spin-up (dashed line) and spin-down spectra (solid line) for RCP incident radiation at $h\nu = 3.02$ eV. Bottom panel: Spin polarization for RCP (solid diamonds) and LCP (open diamonds) incident radiation.

diation is reported in the lower panel as solid (open) diamonds. No detectable spin polarization was observed for excitation with p -polarized light (not reported). In the spectra, the two-photon photoemission (2PPE) Fermi edge is clearly observable at $2h\nu = 6.04$ eV, whereas the prominent peak near 7.0 eV corresponds to three-photon photoemission (3PPE) via the IP state [17]. A significant spin polarization of up to 30% appears in the 3PPE region at final state energies roughly between 6.5 and 7.5 eV, including the IP-state photoemission peak. This demonstrates the successful injection of a spin-polarized electron population into the IP state. The observation that the helicity reversal of the exciting light causes a sign change of the spin polarization further confirms that the spin polarization appears due to the multiphoton optical spin orientation effect described above. We also notice that the photoelectrons in the 2PPE part of the measured spectra originate from the sp band just below the Fermi energy. As can be seen from the relativistic band structure, these states are not split by SOC, and accordingly, spin-selective excitation is not observed.

We can strongly influence the multiphoton optical orientation process by changing the excitation photon energy and tuning the two-photon resonance between the d bands

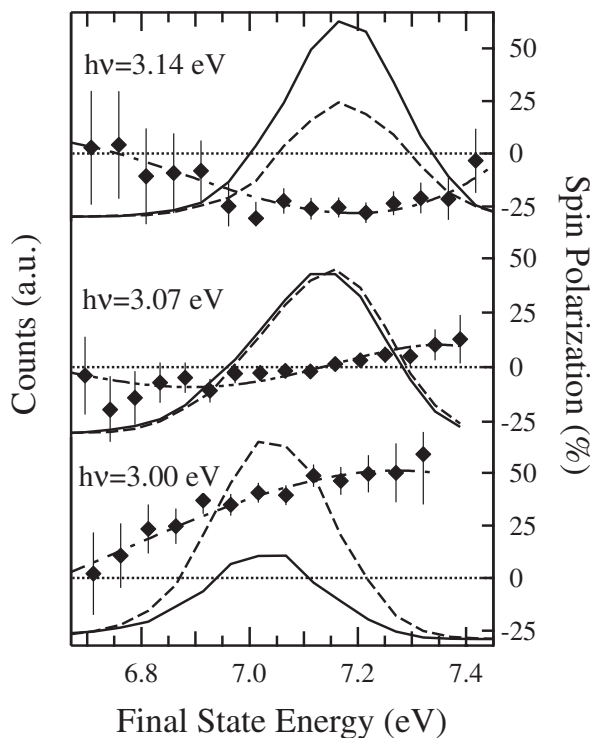


FIG. 3. Spin-up (dashed line) and spin-down (solid line) spectra, respectively, measured with RCP light for three different exciting photon energies (top to bottom: 3.14, 3.07, and 3.00 eV). Symbols: Corresponding spin polarizations obtained from the experimental spectra. Dash-dotted lines are guides to the eye.

and the IP state. In Fig. 3 we show the IP state spectral region of spin-up and spin-down spectra (dashed lines and solid lines, respectively) and corresponding spin polarizations (solid symbols) measured at three different incident photon energies with RCP light. The spectra are plotted normalized to the IP-state intensity, whereas the spin-polarization data are plotted with equal vertical scales. When decreasing the photon energy from $h\nu = 3.14$ eV (top curves) to $h\nu = 3.00$ eV (bottom curves), we observe a systematic change of the IP-state spin polarization, whose value swings from approximately -25% at $h\nu = 3.14$ eV to $+40\%$ at $h\nu = 3.00$ eV, passing through zero at the intermediate energy of $h\nu = 3.07$ eV.

For a better understanding of the strong photon-energy dependence of the IP-state polarization, we summarize in Fig. 4 the results of a larger set of measurements, performed at different photon energies with RCP incident light. Defining the final state energy of the IP-state peak as E_{IP} , the initial state energy E_d of the d band electrons populating the IP state is given by $E_d = E_{IP} - 3h\nu$. In Fig. 4 we report the photon-energy dependence of E_{IP} (top panel, open circles), E_d (middle panel, open squares), and the corresponding spin polarization at the IP-state peak (bottom panel, solid diamonds). The solid black lines are linear fits to the photon-energy dependence of E_{IP} and E_d . The energies E_{IP} and E_d exhibit a linear dependence on the photon energy, with respective slopes of 1.1 ± 0.1 and

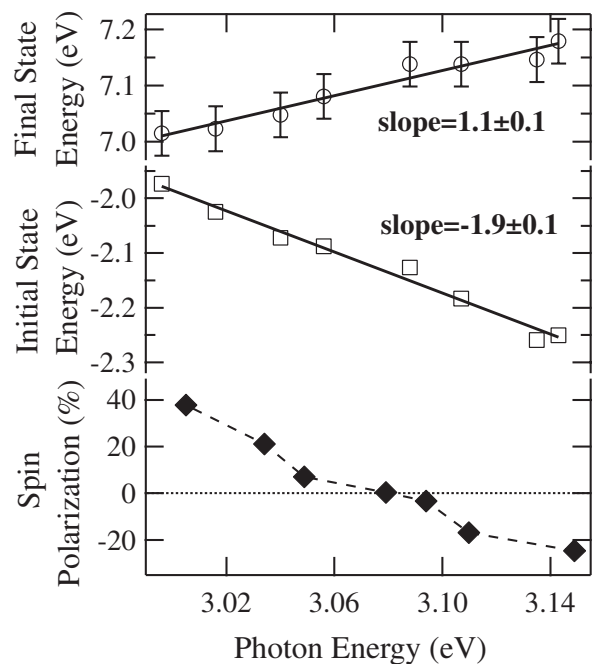


FIG. 4. Photon-energy dependence of the photoemission peak corresponding to IP-state electrons (open circles), of the d -electron initial energy E_d (open squares), and of the IP-state peak polarization (RCP excitation, solid diamonds). Solid lines are linear fits to the $h\nu$ dependence of E_{IP} and E_d .

-1.9 ± 0.1 . This is expected, since the IP state acts as the penultimate state in a three-photon process (see Fig. 1). The energy of the IP state, which defines the resonance condition for a particular photon energy, is fixed relative to the vacuum level and does not disperse with perpendicular momentum. Therefore, increasing the photon energy by $\Delta h\nu$ near resonance also increases the final state energy E_{IP} by $\Delta h\nu$, whereas the initial state energy E_d has to decrease by $-2\Delta h\nu$. Accordingly, increasing the photon energy from $h\nu \approx 3.00$ eV to $h\nu \approx 3.14$ eV tunes the initial state binding energy from approximately 1.95 to 2.25 eV. This tuning range covers the region of spin-orbit split d bands shown in the inset of Fig. 1.

The evolution of the IP-state peak spin polarization in Fig. 4 from +40% to -25% with increasing photon energy can therefore be ascribed to the tuning of the resonance conditions between each of the individual spin-orbit split d bands and the IP state. At lower photon energies, the Δ_7^5 band lies closer to resonance with the IP state than the Δ_6^5 band, and a positive spin polarization of +40% is accordingly observed. With larger photon energy, the Δ_6^5 band increasingly contributes in the two-photon resonance with an opposite spin polarization. This lowers the net spin polarization at the IP-state peak, which reaches zero for $h\nu \approx 3.07$ eV. Increasing the photon energy further to $h\nu \approx 3.14$ eV, the Δ_6^5 band resonance finally dominates and the sign of the IP-state spin polarization is accordingly reversed. The lower observed value of spin polarization for excitation from the Δ_6^5 band can be ascribed to the contribution arising from the Δ_7 band at higher binding energy, which shows partial Δ^5 character due to hybridization [12].

The values of spin polarization that we observe in our multiphoton experiment are in close agreement with the ones observed in one-photon experiments from Cu(001), where a +45% and -25% spin-polarized signal originating from d bands, respectively, at 1.9 and at 2.3 eV binding energy was measured with $h\nu = 11$ eV photons [12]. Such close agreement suggests that in our experiment the spin polarization is generated within the $\Delta_{6(7)}^5 \rightarrow \Delta_6^1$ one-photon transition that couples the initial spin-orbit split d bands to either the unoccupied sp bands or the $n = 0$ SR, whereas the subsequent transitions, coupling states all of Δ_6^1 symmetry, transfer spin polarization into the image-potential state and, finally, to the photoemitted states. Although very similar spin polarizations are observed in the two experiments, we have to point to characteristic differences. Off-normal light incidence will cause a deterioration of the pure circular polarization inside the metal, and it also will allow unpolarized contributions from Δ_6^1 initial states [21]. The close agreement of our spin-polarization values with respect to Ref. [12] suggests that these influences are effectively small. A quantitative description of the observed spin polarizations requires the calculation of transition matrix elements using realistic wave functions and taking into account the dynamics of

the spin-dependent multiphoton photoemission process, which is clearly beyond the scope of this Letter.

In conclusion, our experiment demonstrates the possibility of injecting spin-polarized electrons into excited states at nonmagnetic surfaces, and it proves that the spin polarization can be adjusted by selecting the appropriate excitation energy. With its straightforward application to pump-probe experiments, this multiphoton optical orientation process opens the way to address directly in the time domain the ultrafast spin dynamics and spin transport in the absence of relaxation processes influenced by magnetism. For the specific case of Cu(001), the relatively long coherence time of the $n = 1$ IP state [22] and d -band holes [18] (>30 fs) could even allow a coherent manipulation of electron spins at metal surfaces by suitable ultrashort laser pulses [23]. Finally, the complete generality of the spin-injection principle here reported suggests that the outlined method could be applied to a large variety of materials other than copper, thereby significantly broadening the field of possible investigations and applications.

F.B. acknowledges support from the Max-Planck-Gesellschaft. M.N. thanks MSM No. 0021620834 for partial support. Technical assistance of F. Helbig is gratefully acknowledged.

*Electronic address: winkelm@mpi-halle.mpg.de

- [1] O. Andreyev *et al.*, Phys. Rev. B **74**, 195416 (2006).
- [2] A. V. Kimel *et al.*, Nature (London) **429**, 850 (2004).
- [3] V. V. Pavlov *et al.*, Phys. Rev. Lett. **98**, 047403 (2007).
- [4] M. J. Stevens *et al.*, Phys. Rev. Lett. **90**, 136603 (2003).
- [5] J. Hübner *et al.*, Phys. Rev. Lett. **90**, 216601 (2003).
- [6] M. Cinchetti *et al.*, Phys. Rev. Lett. **97**, 177201 (2006).
- [7] E. Beaupaire *et al.*, Phys. Rev. Lett. **76**, 4250 (1996).
- [8] M. Aeschlimann *et al.*, Phys. Rev. Lett. **79**, 5158 (1997).
- [9] A. B. Schmidt *et al.*, Phys. Rev. Lett. **95**, 107402 (2005).
- [10] *Optical Orientation*, edited by F. Meier and B. P. Zakharchenya (North-Holland, Amsterdam, 1984).
- [11] P. Lambropoulos, Phys. Rev. Lett. **30**, 413 (1973).
- [12] C. M. Schneider *et al.*, J. Electron Spectrosc. Relat. Phenom. **51**, 263 (1990).
- [13] D. Tillmann, R. Thiel, and E. Kisker, Z. Phys. B **77**, 1 (1989).
- [14] R. Bertacco and F. Ciccacci, Phys. Rev. B **59**, 4207 (1999).
- [15] H. Eckardt, L. Fritsche, and J. Noffke, J. Phys. F **14**, 97 (1984).
- [16] S. L. Hulbert *et al.*, Phys. Rev. B **33**, 760 (1986).
- [17] F. Bisio *et al.*, Phys. Rev. Lett. **96**, 087601 (2006).
- [18] H. Petek, H. Nagano, and S. Ogawa, Phys. Rev. Lett. **83**, 832 (1999).
- [19] W. Kuch and C. M. Schneider, Rep. Prog. Phys. **64**, 147 (2001).
- [20] J. Henk and B. Johansson, J. Electron Spectrosc. Relat. Phenom. **94**, 259 (1998).
- [21] C. M. Schneider *et al.*, Phys. Rev. B **39**, 1031 (1989).
- [22] M. Weinelt, J. Phys. Condens. Matter **14**, R1099 (2002).
- [23] A. P. Heberle *et al.*, IEEE J. Sel. Top. Quantum Electron. **2**, 769 (1996).

Interferometric Control of Spin-Polarized Electron Populations at a Metal Surface Observed by Multiphoton Photoemission

Aimo Winkelmann,^{1,*} Wen-Chin Lin,¹ Francesco Bisio,² Hrvoje Petek,^{3,4} and Jürgen Kirschner¹

¹Max-Planck Institut für Mikrostrukturphysik, Weinberg 2, D-06120 Halle (Saale), Germany

²CNISM, Sede consorziata di Genova, Dipartimento di Fisica, via Dodecaneso 33, I-16146 Genova, Italy

³Department of Physics and Astronomy, University of Pittsburgh, Pittsburgh, Pennsylvania 15260, USA

⁴Donostia International Physics Center DIPC, P. Manuel de Lardizabal 4, 20080 San Sebastian, Spain

(Received 17 January 2008; published 22 May 2008)

In an interferometric pump-probe experiment, we demonstrate the phase tuning of the spin polarization of photoelectrons emitted in a three-photon process from Cu(001). A phase shift of π between delayed ultrafast circularly polarized light pulses can switch the spin polarization from $\pm 20\%$ to $\mp 40\%$. In the delay regime of overlapping pulses, we show the dominating role of optical interference effects in determining the spin polarization. For longer delays, we detect the influence of the coherent material response, manifested in both the final state electron population as well as the final state spin polarization.

DOI: 10.1103/PhysRevLett.100.206601

PACS numbers: 72.25.Fe, 73.20.-r, 78.47.J-, 79.60.-i

The interaction of circularly polarized light with electronic states that are influenced by spin-orbit coupling provides a mechanism for selective excitation of spin-polarized electrons in nonmagnetic and magnetic solids. This type of interaction bears close analogy to the effect of a magnetic field, and it enables the control of magnetic and other spin-dependent phenomena by optical means on time scales of the order of the applied laser pulse lengths and electron-hole pair dephasing times in solids and at solid surfaces. For example, a method of all-optical magnetic recording using circularly polarized 40 fs laser pulses has recently been demonstrated [1]. The successful application of the spin degree of freedom in future spintronic devices [2] equally relies on a fundamental understanding of how to create and manipulate spin-polarized electrons—potentially on ultrafast time scales.

From a fundamental point of view, a particularly direct way to study the relevant mechanisms is to optically excite unoccupied electronic states and then detect spin-polarized photoelectrons emitted from crystalline surfaces. Using nonlinear photoemission in a pump-probe configuration, one can gain access to the electron and spin dynamics in excited states [3–8]. It clearly would be of fundamental interest to elucidate mechanisms by which not only the number but also the spin of the emitted photoelectrons could be influenced by the relative optical phase of two excitation pulses. Ultimately, this could also allow the generalization of the recently demonstrated all-optical control of charge currents on surfaces [9] to spin-polarized surface currents. The steering of the electron's spin, charge and spatial degrees of freedom at surfaces could then be observed directly by spectroscopic and imaging techniques based on photoemission [10–12] to allow fundamental insights, which are relevant in the ineluctable convergence of the optical, electronic and spintronic technologies on the nanometer scale.

In this Letter, we show that the spin-polarized photoemission from the Cu(001) surface can be controlled by

interferometrically changing the delay between two circularly polarized ultrashort optical pulses. We exploit a two-photon resonant transition [13] to selectively populate the $n = 1$ image potential (IP) state with spin-polarized electrons originating from the spin-orbit split Cu d -bands [14] and then detect the IP state population and spin polarization by a third photon. Comparing the time-resolved three-photon photoemission (3PPE) signal with a simultaneous measurement of the surface second-harmonic generation (SSHG) signal, we show that the spin-polarized photoemission is influenced by the effective optical excitation spectrum and by the quantum-mechanical response of the excited system.

The experimental setup is schematically pictured in Fig. 1. We have described most of the experimental details previously [13,14]. In the present study, the ultrashort excitation pulses ($h\nu = 3.00 \dots 3.14$ eV, pulse length < 20 fs, pulse energy ~ 1 nJ) were split into equal pump and probe replicas in a stabilized scanning Mach-Zehnder interferometer. The delay could be kept stable with an accuracy of $\lambda/25$. The electrons photoemitted along the surface normal were analyzed angle-resolved by a cylindrical sector analyzer coupled with a spin detector based on very low energy electron scattering on a magnetized ultrathin Fe/W(001) film. The analyzer energy resolution was set to 100 meV. To determine the laser pulse autocorrelation, simultaneously with 3PPE, we measured the surface SHG signal from the Cu(001) sample using a prism assembly to separate the SHG signal from the fundamental light before detection with a photomultiplier tube (Fig. 1). A clean and ordered Cu(001) surface was prepared by standard procedures. The optical plane was aligned parallel to the [100] direction.

In Fig. 2(a) we show the relativistic bulk band structure of the Cu(001) surface along the surface normal (ΓX) direction, whereas a simplified level scheme accounting for the mechanism of spin-polarized 3PPE [14] is reported in Fig. 2(b). According to optical selection rules, oppo-

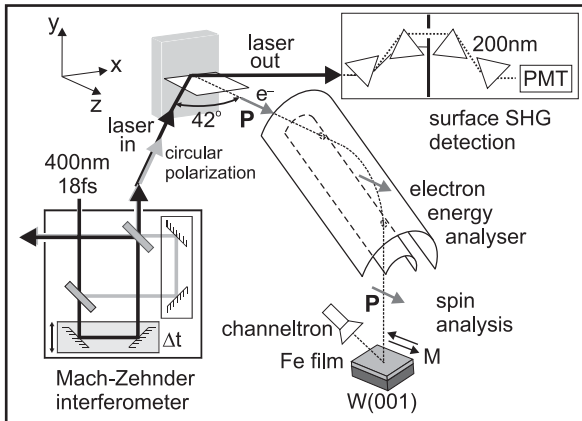


FIG. 1. Experimental setup for interferometric control of spin-polarized electron populations in multiphoton photoemission.

sitely spin-polarized electrons can be excited by circularly polarized light from the d bands of Cu with Δ_7 and Δ_6 symmetry. The two-photon resonance between these initial states, the intermediate unoccupied sp -band, and the penultimate $n = 1$ image potential state in the 3PPE process governs the distribution of spin-polarized electrons at the

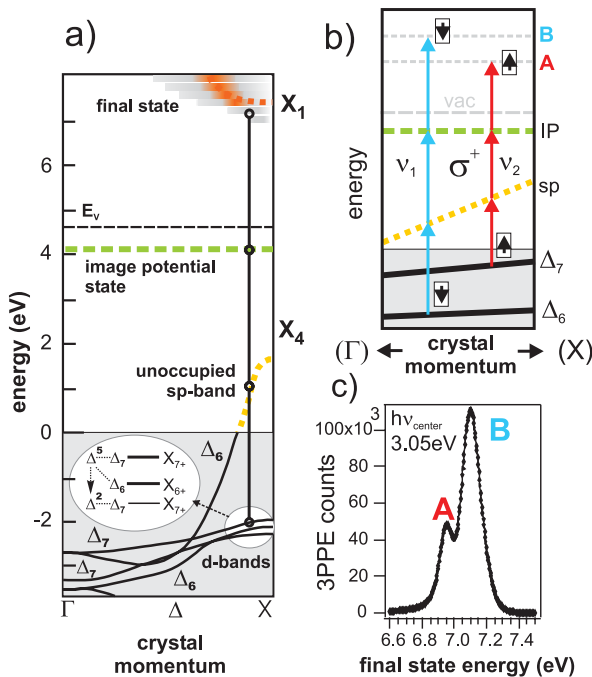


FIG. 2 (color). (a) Relativistic band structure relevant to normal emission from Cu(001), (b) Qualitative excitation scheme for spin-polarized 3PPE using pulses with a frequency spectrum covering ν_1 and ν_2 (σ^+ right circular polarized light). (c) 3PPE resonance peak measured in a non-spin-resolved experiment with higher energy resolution directly showing the spin-orbit splitting of the two resonances A and B .

final state energy. As can be seen in Fig. 2(b), two different resonances take place at photon energies $h\nu_1$ and $h\nu_2$. This leads to the features A and B in the photoelectron spectrum shown in Fig. 2(c). The separation of 150 meV between A and B is determined by spin-orbit coupling, which causes the splitting of the Δ_7 and Δ_6 bands. Because the pulses have a spectral width of 170 meV, both resonances of opposite spin polarization are excited simultaneously weighted by the spectral distribution of excitation frequencies. In principle, the spin polarization detected via the IP state as a function of pump-probe delay can change due to a combination of spin-dependent excitation effects and spin-dependent scattering in the excited state. With measured values of the spin-flip lifetime in bulk copper of about 10 ps [15] we can expect that spin-flip processes in the excited state are not significant in our measurements.

The time-resolved experiments can be carried out in two ways. Measuring the photoelectrons at a fixed energy as a function of delay between the pulses gives an interferometric two-pulse correlation (I2PC) signal, while measuring the photoelectron intensity at fixed pulse delays as a function of photoelectron kinetic energy gives the corresponding energy and spin polarization control spectra. We will begin by discussing the observed spin polarization for pulse delays up to about 15 fs (Fig. 3). At these delays, the pulses are overlapping significantly so that the optical interference of the electromagnetic fields of the two constituting pulses dominantly determines the measured signal [16]. As a function of pulse delay, this results in interference maxima spaced in time by the duration of an optical cycle.

In the top part of Fig. 3, we report the spin polarization measured at the final state energy of 6.95 eV above the Fermi energy E_F with $h\nu = 3.04$ eV, as a function of the pulse delay. Each data point for the spin polarization is shown in a gray scale corresponding to its statistical error, where black points correspond to the minimum error. Data points on the white end of the scale are effectively suppressed, as they fall in the regions of destructive interference where the count rate is too low for a statistically significant result. The spin polarization exhibits dramatic oscillations with a frequency of about 1.3 fs^{-1} which corresponds to an optical cycle. Starting from about +10% at zero delay, the amplitude of the polarization oscillations also grow larger in intensity, reaching values ranging from +40% to -20% for delays between 10 and 15 fs.

Additional insights into this oscillating behavior can be gained by measuring spin-resolved photoelectron spectra at selected fixed delays within one representative optical cycle. In the bottom part of Fig. 3, we therefore report the intensity spectra (hatched areas) and the corresponding spin polarizations (markers) obtained for delays near 11 optical cycles, along with the reference zero-delay results. Whereas the spin polarization spectrum at zero delay perfectly agrees with our previous study [14], marked changes are observed in the spin polarization spectra for the chosen

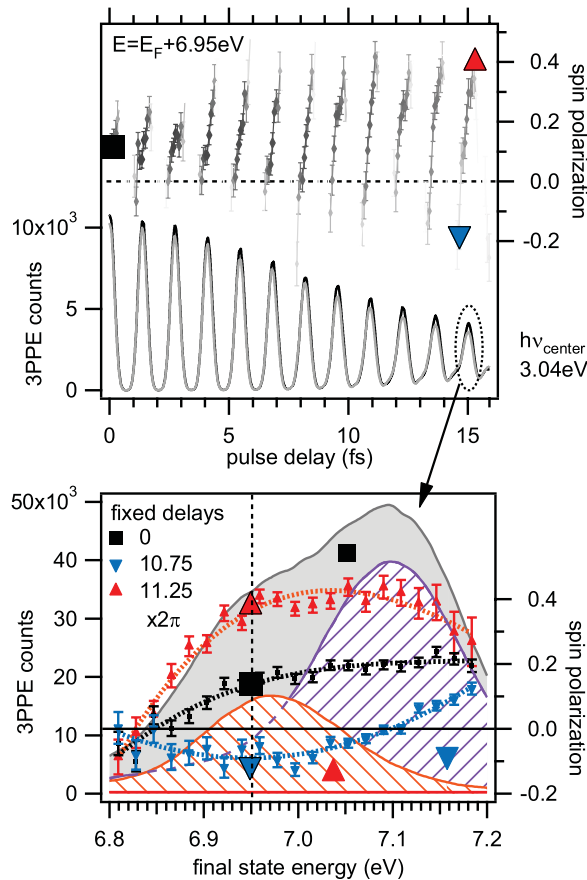


FIG. 3 (color). Top panel: spin polarization (markers with error bars) and corresponding interferometric 3PPE signals for reversed magnetizations of the spin detector (solid lines) at the final state energy $E = 6.95 \text{ eV}$ as a function of pulse delay. Data points for the spin polarization with lower error are colored darker (see text). Bottom panel: measured spin polarization as a function of final state energy for selected fixed pulse delays of 0, 10.75, and 11.25 optical cycles (markers with error bars). The lines are guides to the eye. The gray shaded and hatched areas in the background show the spin-averaged three-photon photoemission spectra at delays of 0, 10.75 and 11.25 optical cycles, respectively.

values of pulse delay. In agreement with the upper part of the figure, at 6.95 eV final state energy we observe a spin polarization near -20% for 10.75 cycles and $+40\%$ near 11.25 optical cycles delay. The connection to the upper part of the figure is made by the colored symbols in both parts of Fig. 3.

The dramatic changes in the spin polarization spectra become clear when we compare the spin-averaged intensity spectra for different delays. It can be seen in fact that at zero delay, the spin-averaged intensity spectrum (gray spectrum in bottom part of Fig. 3) is relatively broad, caused by the nearly equal excitation of the A and B resonances by our ultrashort pulses with an extended fre-

quency spectrum. When the two pulses are delayed by less than their pulse width and thus still significantly overlapping, their superposition can be effectively viewed as a single, longer pulse, whose amplitude and frequency structure is determined by the interference of the overlapped pulses. For delays of only one or two optical cycles, the pulses are still almost completely overlapping. This leads to almost total destructive and constructive interference of all frequency components, causing the high interference contrast near zero delay in the I2PC curves in the upper part of Fig. 3. The spin polarization is only mildly influenced at these very short delays with respect to the zero-delay case because the *complete* frequency spectrum of the pulse pair is alternately enhanced or suppressed, without preferential excitation of the A or B resonance. This gradually changes at longer pulse delays (> 3 optical cycles), when the decreasing overlap between the pulses causes a more complicated frequency interference that, advancing the delay by an optical cycle, leads to spectral distributions that are markedly asymmetric with respect to the original pulse spectra. Thus, under these conditions, changing the delay by less than an optical cycle, we can correspondingly change the spectrum of two combined pulses to preferentially excite resonance A or resonance B . As is apparent from the red and the blue hatched intensity spectra in the bottom part of Fig. 3, the constructive and destructive interferences between the different spectral components of the excitation light at, respectively, 10.75 and 11.25 cycles delay occur at opposite sides of the original spectrum. In effect, the spectral maximum corresponding to the constructive interference between the two pulses is shifted towards higher or lower energies depending on the selection of the relative phase. The excitation energy is known to strongly affect the spin polarization measured from the $n = 1$ IP state [14]. What we therefore accomplish in our time-resolved experiment is the control of this spin polarization via a preferential selection of one or the other of the two simultaneous resonances A or B , obtained by a change of the effective optical spectrum in the course of the coherent nonlinear excitation.

We have demonstrated that, for strongly overlapping pulses, an effective optical spectrum can be viewed as dominant in determining the observed 3PPE spin polarization oscillations. When the two pulses are delayed by intervals longer than their pulse width, however, the time development of the excited quantum-mechanical system has to be taken into account appropriately. The evolution and possible decay of the polarization phase between the action of the two pulses determines how the phase information imprinted by the pump pulse is transmitted over time to result in the interference with the probe pulse. Qualitatively, the nonlinear material response results in the appearance of additional frequencies in the interferometric correlation signal [17]. In order to probe this regime, in Fig. 4, we report time-dependent measurements of the 3PPE spin polarization recorded with a central photon energy of 3.09 eV for pulse delays between 42 and 46 fs,

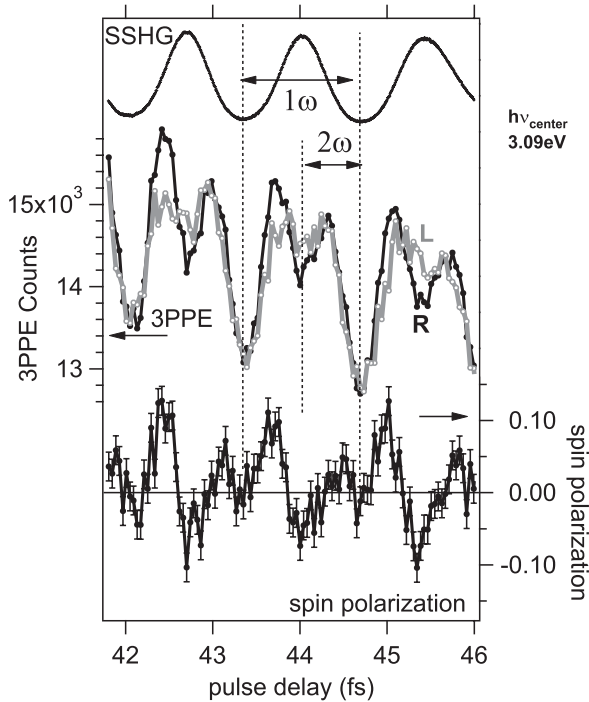


FIG. 4. Top: SSHG intensity measured as a function of the pulse delay. Middle: 3PPE signal as a function of the pulse delay (L/R are data measured for reversed magnetization of the spin detector). Bottom: spin polarization extracted from the L/R curves. The presence of oscillations in the 3PPE signal and spin polarization at the frequency 2ω is highlighted. Data were measured with $h\nu = 3.09$ eV photon energy.

times which are sufficiently longer than the pulse width. In the top part of Fig. 4, the autocorrelation signal obtained by SSHG is reported, clearly showing oscillations at the fundamental frequency ω corresponding to one optical cycle of delay. In the center of the figure, we report the 3PPE signal measured at $E = E_F + 6.95$ eV for the two orientations of the magnetization of the Fe film in the spin detector (R/L in Fig. 4), and the relative spin polarization (bottom). Under these excitation and measurements conditions, we notice that the average spin polarization is near zero and can be changed to positive as well as to negative values by the pulse delay. When we compare the 3PPE signal with the simultaneously measured SSHG, we notice that clear oscillations at twice the optical frequency appear, which originate from the coherent nonlinear response characterized by dephasing times of the d -band holes of about 30 fs [18,19] and the image potential state lifetimes of about 35 fs [5]. The same 2ω contribution is also seen clearly in the spin polarization. By this observation of the

appearing 2ω contributions, we directly demonstrate that the phase of the material polarization affects the photoelectron spin polarization in the regime of delayed pulses which are separated by delays sufficiently larger than the temporal pulse width but within the relevant dephasing time scales of the excited system. Because the observed spin polarization is a function of the relative excitation of the A and B resonances which are originating from different d bands, the additional spin information in principle gives the possibility to extract band-resolved dephasing times of d -band holes and to monitor band-resolved population dynamics.

In summary, we reported the interferometric control of the spin polarization of photoelectrons by changing the delay between two ultrashort optical pulses. Our results show that the study of coherent electron dynamics at metal surfaces can be extended to spin-polarized electron populations. Our studies can be readily generalized to cases involving the control of the time-dependent optical polarization of the excitation pulses [20].

Technical assistance from F. Helbig is gratefully acknowledged. H. Petek thanks the Department of Energy Grant No. DE-FG02-03ER15434 and Ikerbasque for financial support. F.B. acknowledges the CNR-CNISM agreement for financial support.

*winkelm@mpi-halle.mpg.de

- [1] C.D. Stanciu *et al.*, Phys. Rev. Lett. **99**, 047601 (2007).
- [2] I. Zutic, J. Fabian, and S.D. Sarma, Rev. Mod. Phys. **76**, 323 (2004).
- [3] R. Haight, Surf. Sci. Rep. **21**, 275 (1995).
- [4] H. Petek and S. Ogawa, Prog. Surf. Sci. **56**, 239 (1997).
- [5] M. Weinelt, J. Phys. Condens. Matter **14**, R1099 (2002).
- [6] M. Aeschlimann *et al.*, Phys. Rev. Lett. **79**, 5158 (1997).
- [7] A.B. Schmidt *et al.*, Phys. Rev. Lett. **95**, 107402 (2005).
- [8] M. Weinelt *et al.*, Prog. Surf. Sci. **82**, 388 (2007).
- [9] J. Güdde *et al.*, Science **318**, 1287 (2007).
- [10] M. Cinchetti *et al.*, Phys. Rev. Lett. **95**, 047601 (2005).
- [11] A. Kubo, N. Pontius, and H. Petek, Nano Lett. **7**, 470 (2007).
- [12] M. Aeschlimann *et al.*, Nature (London) **446**, 301 (2007).
- [13] F. Bisio *et al.*, Phys. Rev. Lett. **96**, 087601 (2006).
- [14] A. Winkelmann *et al.*, Phys. Rev. Lett. **98**, 226601 (2007).
- [15] F.J. Jedema, A.T. Filip, and B.J. van Wees, Nature (London) **410**, 345 (2001).
- [16] V. Blanchet *et al.*, Phys. Rev. Lett. **78**, 2716 (1997).
- [17] H. Petek *et al.*, Phys. Rev. Lett. **79**, 4649 (1997).
- [18] S. Ogawa *et al.*, Phys. Rev. Lett. **78**, 1339 (1997).
- [19] H. Petek, H. Nagano, and S. Ogawa, Phys. Rev. Lett. **83**, 832 (1999).
- [20] A.P. Heberle *et al.*, IEEE J. Sel. Top. Quantum Electron. **2**, 769 (1996).

New Journal of Physics

The open-access journal for physics

Spin-polarized multi-photon photoemission and surface electronic structure of Cu(001)

W-C Lin^{1,2}, A Winkelmann^{1,4}, C-T Chiang¹, F Bisio³
and J Kirschner¹

¹ Max-Planck-Institut für Mikrostrukturphysik, Weinberg 2, D-06120 Halle (Saale), Germany

² Department of Physics, National Taiwan Normal University, Taipei 11677, Taiwan

³ CNR-SPIN, Corso Perrone 24, I-16152 Genova, Italy

E-mail: winkelmann@mpi-halle.mpg.de

New Journal of Physics **12** (2010) 083022 (13pp)

Received 4 March 2010

Published 10 August 2010

Online at <http://www.njp.org/>

doi:10.1088/1367-2630/12/8/083022

Abstract. We have investigated the influence of controlled modifications of the surface electronic structure of Cu(001) on the spin polarization of photoelectrons emitted via multi-photon excitation. Using ultrashort, circularly polarized laser pulses with ~ 3 eV photon energy, spin-polarized electrons can be selectively excited from the spin-orbit (SO) coupled d -bands of Cu into the unoccupied $n = 1$ image potential (IP) state on the Cu(001) surface. Upon lowering the IP state energy level by submonolayer Cs deposition, we show that the IP energy can be tuned into two-photon resonance with initial state d -bands of different double group symmetry, leading to a sign reversal of the spin polarization that is observed at the IP state level. Similarly, exploiting the parallel-momentum IP state dispersion, the resonant tuning of the IP state energy level to different branches of the SO split d -bands is demonstrated. Our results highlight the role of resonant and off-resonant excitation pathways in determining the spin polarization in the excited states. The additional information contained in spin-resolved multi-photon photoemission experiments can be exploited to obtain insights into the mechanism of population of excited states.

⁴ Author to whom any correspondence should be addressed.

Contents

1. Introduction	2
2. Experiment	3
3. Results	4
3.1. Three-photon photoemission (3PPE) from Cs/Cu(001)	4
3.2. Angle-dependent 3PPE	6
4. Discussion	8
5. Summary	11
Acknowledgments	11
References	12

1. Introduction

Spin-resolved photoemission is a powerful tool for the analysis of the relativistic electronic band structure on surfaces [1, 2]. In the presence of spin-orbit coupling (SOC) in the electronic structure, circularly polarized light can be utilized to selectively excite spin-polarized electrons in nonmagnetic materials [3]–[10]. The extension of this approach to nonlinear photoemission using ultrashort laser pulses for excitation offers the possibility to optically control spin-dependent excitation processes of electrons into unoccupied states at nonmagnetic surfaces [11, 12]. Similarly, access to unoccupied states and to dynamical spin-dependent scattering processes at magnetic surfaces can be gained via two-photon photoemission in spin-resolved pump-probe experiments [13]–[15].

In previous studies, we demonstrated the control over the spin polarization of the excited photoelectrons at a Cu(001) surface by fine-tuning the excitation photon energy [11, 12], exploiting the efficient multi-photon resonant coupling between the SO-split Cu *d*-bands and the unoccupied $n = 1$ image-potential (IP) state [16]. This can be seen in figure 1(a), where we show a simplified level scheme derived from the relativistic Cu(001) band structure shown in detail in figure 3. The unique combination of efficient resonant multi-photon photoemission and the possible spin-selective photoexcitation by circularly polarized light makes the Cu(001) surface a highly interesting and well-defined model system for further investigations. As the resonant excitation pathways are highly *k*-space selective and magnetism-induced spin relaxation channels are absent, the nonmagnetic Cu(001) surface is particularly suited to investigating the specific details of the buildup and decay of spin-polarized electron populations. Spin-polarized electrons can in fact be effectively ‘labelled’ by their own spin orientation, thereby providing clues to their initial state and their decay path that would be more difficult to obtain otherwise. In this respect, extending our knowledge of different mechanisms of creating and manipulating excited spin populations at nonmagnetic surfaces represents an interesting issue.

Besides the experiments mentioned above, in which the spin polarization of the photoemitted electrons is tuned by acting on the characteristics of the incident excitation light, alternative approaches are available to influence the electron spins. They involve, for instance, the controlled manipulation of the intermediate states in a multi-photon process in order to influence their resonant light-induced coupling with the SO-split initial states.

3

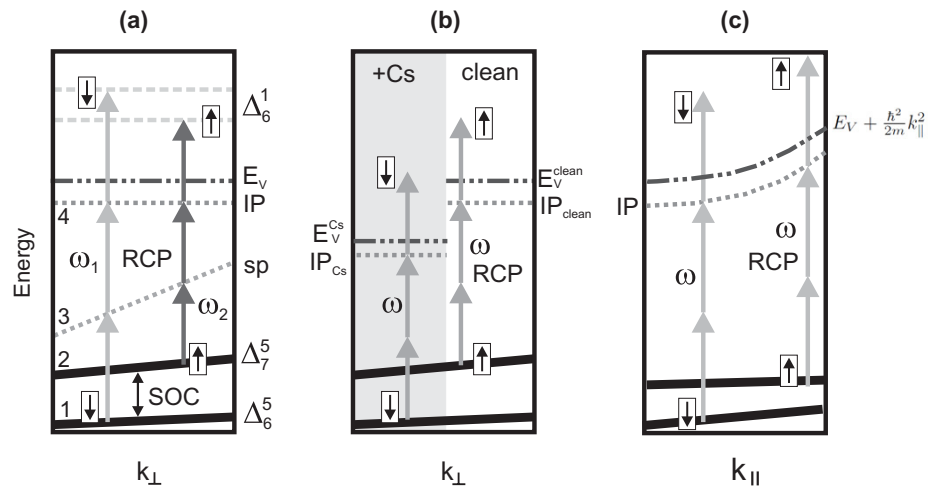
IOP Institute of Physics Φ DEUTSCHE PHYSIKALISCHE GESELLSCHAFT

Figure 1. Simplified level schemes for tuning the excited spin polarization at Cu(001) by different approaches (compare with figure 3 for the numbering of the bands). Previous work: (a) tuning of the photon energy from ω_1 to ω_2 [11, 12]. This work: (b) tuning of the IP state level by workfunction reduction (vacuum level E_V) under Cs adsorption in normal emission; (c) using the IP state level dispersion with $k_{||}$ in off-normal emission (only electrons with energies larger than $E_V + (\hbar^2/2m)k_{||}^2$ can overcome the surface barrier). The initial occupied d -band of Δ^5 spatial symmetry is split by SOC into the two relativistic Δ_6^5 and Δ_7^5 symmetries. The optical selection rules are shown for right-circular polarized (RCP) light.

In this paper, we report the results we obtained applying two such different methods for tuning the spin polarization of electrons photoemitted in a multi-photon process from Cu(001). The methods are illustrated in figures 1(b) and (c). The first approach (figure 1(b)) consists in tuning the energy level of the $n = 1$ IP state to control the resonance conditions with the SO-split initial states via the deposition of a submonolayer Cs coverage on the Cu(001) surface. The second approach (figure 1(c)) is to exploit the free-electron-like dispersion of the $n = 1$ IP state as a function of surface-parallel momentum $k_{||}$ [16] to achieve resonant coupling with the d -bands off the surface Brillouin zone (BZ) centre. The results obtained following these two approaches are compared with corresponding available data obtained by one-photon photoemission [10] or spectroscopic multi-photon photoemission [11], allowing us to assess the influence of the different excitation pathways and the characteristics of the intermediate states on the final-state spin polarization.

2. Experiment

The experiments were carried out in an ultrahigh vacuum (UHV) system described previously in [11, 16]. A sketch of the experimental setup is shown in figure 2. Ultrashort laser pulses (<20 fs) with photon energy tuneable in the range $h\nu = 3.00$ – 3.15 eV were provided by the frequency-doubled output of a self-built Ti:sapphire oscillator. Right- and left-circular

4

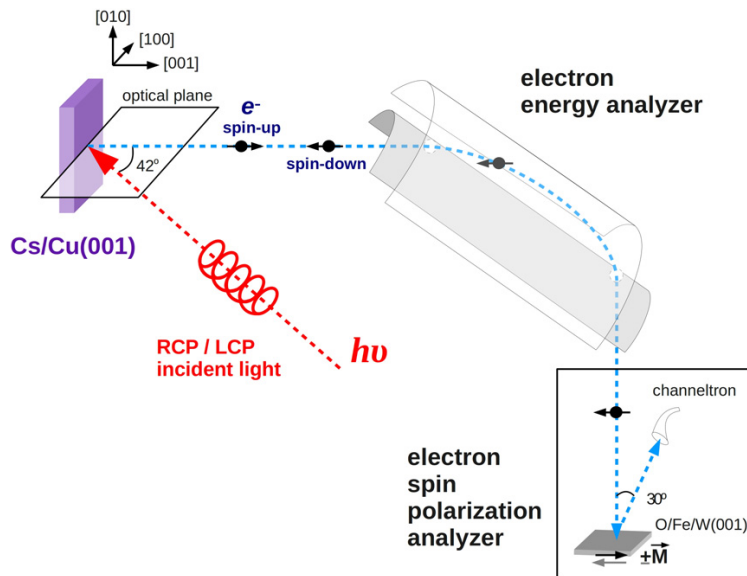
IOP Institute of Physics Φ DEUTSCHE PHYSIKALISCHE GESELLSCHAFT

Figure 2. The experimental setup.

polarization (RCP and LCP) could be set by a combination of achromatic $\lambda/4$ and $\lambda/2$ wave plates. After cycles of sputtering and annealing, a clean and well-ordered Cu(001) surface was prepared. Caesium (Cs) was deposited on Cu(001) at a background pressure lower than 5×10^{-10} mbar from a commercial getter source (SAES). The optical plane was aligned parallel to the [100] Cu direction. The photoemission spectra were measured by a cylindrical sector analyser (Focus CSA300, energy resolution 150 meV, angular resolution $\approx 3^\circ$) coupled to a spin detector based on exchange scattering at a magnetic Fe thin film [17]. For the normal-emission measurements, the spin component perpendicular to the Cu(001) surface was analysed [9]. For off-normal emission measurements, the sample was rotated about the axis normal to the optical plane while keeping the angle between the incident laser beam and the collection axis of the electron analyser constant (42°). The orientation of the magnetization vector in the spin detector was kept unchanged with respect to the normal emission case (see below).

3. Results

3.1. Three-photon photoemission (3PPE) from Cs/Cu(001)

The general mechanism for the multi-photon coupling between d -bands and IP state in normal emission [16, 18] is illustrated in figure 3, where we show the relativistic Cu bulk band structure along the [001] surface normal direction (Γ to X) [19] together with the positions of the $n = 1$ IP state [20] and a relatively broad unoccupied surface resonance observed by inverse photoemission [21]. The vertical lines indicate a possible resonant condition for 3PPE for photon energies around 3 eV, coupling the SO-split d -bands with the IP state (the separation of the d -bands is about $\Delta E_{\text{so}} \approx 150$ meV [10]). A simplified close-up view of the energy levels involved is shown in figure 1(a). According to the relativistic optical selection rules in the

5

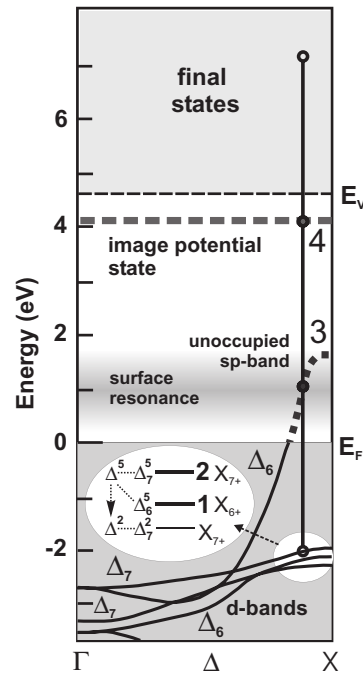
IOP Institute of Physics Φ DEUTSCHE PHYSIKALISCHE GESELLSCHAFT

Figure 3. Relativistic band structure of Cu(001) along the Δ line, with possible resonant 3PPE excitation pathways for $h\nu \sim 3$ eV indicated by the vertical lines.

presence of SOC in the Cu d -bands, spin-polarized electrons can be resonantly excited from Δ_6 or Δ_7 d -bands, through the intermediate unoccupied sp -band, and the $n = 1$ IP state [22].

If the photon energy is such as to resonantly couple the upper d -band branch with the IP state on the clean surface, then lowering the IP state energy by an amount similar to ΔE_{so} should result in resonant coupling with the lower d -band branch. Accordingly, this should result in a sign reversal of the 3PPE spin polarization excited via the IP state (compare with figure 1(b)). Since the IP state level intrinsically correlates with the position of the vacuum level E_V , it is straightforward to consider the tuning of the vacuum level by lowering the workfunction by means of Cs deposition [23, 24].

In figure 4, we show the spin-resolved measurements of the 3PPE IP peak with photon energy $h\nu = 3.05$ eV for two Cs coverages. The Cs deposition and the measurements were performed at 300 K. The energy scale refers to the Fermi level E_F . The Cs coverage is calibrated from the workfunction value extracted from the low-energy cutoff of the spectra (not shown) [25, 26], with 1 monolayer (ML) containing 4.12×10^{14} atoms cm^{-2} , corresponding to the saturation coverage of Cs/Cu(001) [26]. Upon 0.022 ML Cs deposition, the workfunction is lowered from 4.6 to 4.3 eV, whereas the 3PPE final state is shifted downwards by 0.1 eV. The different energy shift of the vacuum level and of the IP state has also been observed previously [25, 26] and was ascribed to the influence of the local positive electric field produced by the Cs ions on the Cu(001) surface [23], [27]–[29].

In the graph panels, the spin-up (spin-down) spectra measured by LCP radiation are reported as black dotted (solid) lines. The corresponding spin polarization spectra are reported

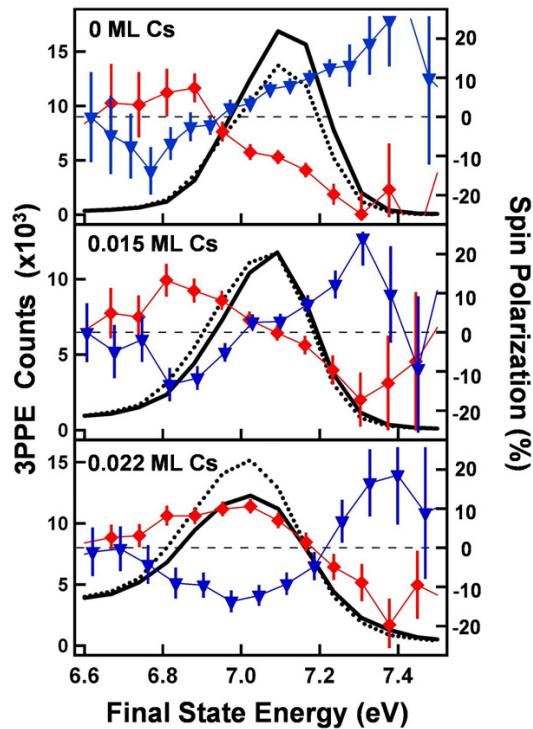


Figure 4. Spin-up (dotted lines) and spin-down (solid lines) spectra measured with LCP light for different Cs coverages on Cu(001). Photon energy $h\nu = 3.05$ eV. The symbols \blacktriangledown and \blacklozenge indicate the corresponding spin polarization obtained from the measured spectra excited by RCP and LCP light, respectively. The lines are a guide to the eye.

as red diamonds. The blue triangles refer to RCP light, for which the spin polarization reverses its sign according to selection rules. In accordance with the IP state peak maximum, the 3PPE spin polarization gradually evolves from +8% on the clean Cu(001) to 0% at 0.015 ML Cs and then changes sign to reach -11% at 0.022 ML Cs/Cu(001), in agreement with the expected switch of resonant coupling from the upper to the lower branch of the d -band initial states. Besides the sign reversal in accord with the peak IP intensity, we notice that the spin-polarization spectra do not retain a constant shape when the excitation conditions are changed (i.e. the zero crossings do not stay at a constant energy). This effect we will address in the discussion. The further increase in the Cs coverage beyond the values addressed in the measurements shown here causes a marked broadening of the IP state peak accompanied by a strong decrease in its intensity, which prevented spin-resolved 3PPE measurements with sufficient statistics.

3.2. Angle-dependent 3PPE

Moving away from the normal emission condition, the free-electron-like k_{\parallel} -dispersion of the IP $n = 1$ energy level on Cu(001) in principle provides another method to modulate the 3PPE spin polarization [16]. In this case, it is the upward IP level shift with increasing k_{\parallel} that provides

7

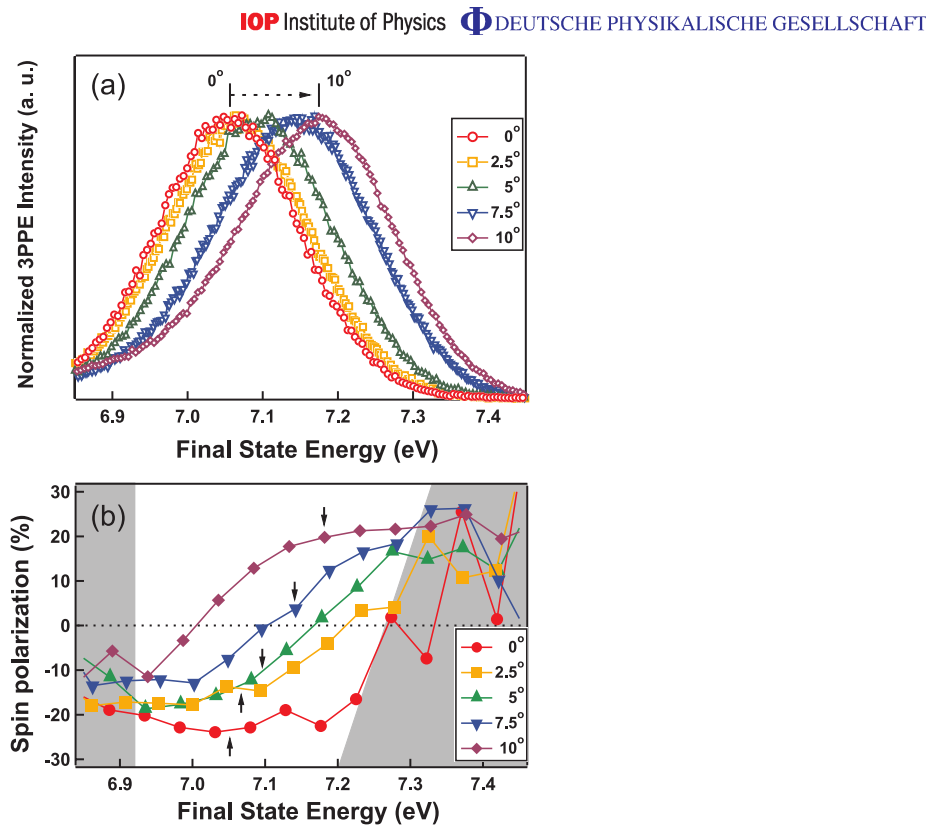


Figure 5. (a) Spin-integrated 3PPE spectra recorded at emission angle 0° – 10° relative to the surface normal with 3.11 eV photon energy. The spectra are normalized to their maximum to allow for a better comparison. (b) Spin-polarization spectra as a function of the emission angle for RCP excitation. The arrows point to the corresponding IP maximum intensity as deduced from (a). The error bar of spin polarization near the 3PPE resonance peak is within $\pm 2\%$. In the grey area, the error bars are larger than $\pm 3\%$.

a variable-energy intermediate level which can couple with either of both SO-split initial state bands (compare with figure 1(c)). Despite the apparent similarity with respect to the previous method, several differences are expected. In order to achieve a variation in the IP state energy, it is necessary to measure the spectra under off-normal conditions, yet at a value of k_{\parallel} for which the two-photon coupling between d -bands and IP state is still significant. This implies that also the initial d -band states will not be located along the ΓX line, so that their symmetry character and SO splitting can in principle differ with respect to the normal emission case (this is also symbolized by the slightly changed initial states in figure 1(c)).

In figure 5(a), we report a set of spin-integrated 3PPE spectra in the IP energy region measured with $h\nu = 3.11$ eV photon energy as a function of the off-normal emission angle θ . At $\theta = 10^\circ$ the 3PPE peak shifts upward by ~ 0.15 eV from 7.05 to nearly 7.2 eV, an energy shift of the order of ΔE_{so} . At $h\nu = 3.11$ eV and normal emission conditions, the IP state is resonantly coupled with the lower-energy branch of the SO-split d -bands at approximately -2.2 eV energy.

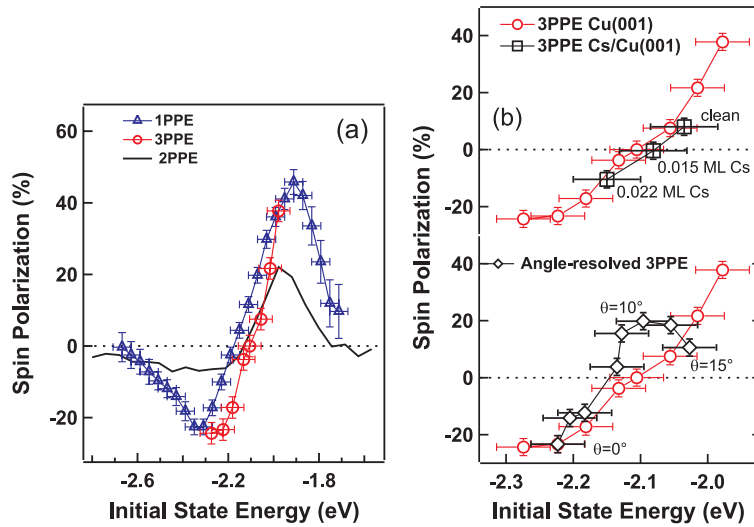


Figure 6. (a) Spin polarization as a function of initial state energy deduced by 1PPE (triangles) and 3PPE (circles). The results are adapted from [10, 11]. Black line: spin polarization as a function of initial state energy deduced by two-photon photoemission (2PPE) from Cs/Cu(001). (b, top) Spin polarization as a function of initial state energy for $h\nu = 3.05$ eV deduced from Cs coverage experiments (squares). The circles are 3PPE data from panel (a) reported for reference. (b, bottom) Spin polarization as a function of initial state energy for $h\nu = 3.11$ eV deduced from angle-dependent photoemission measurements. The circles are 3PPE data from panel (a) for reference.

For an increasing IP state energy level, the resonant coupling conditions will be met for initial states having also a correspondingly higher energy, so we expect to couple to the Δ_6 d -band, which is higher in energy. The spin polarization corresponding to each of these measurements is shown in figure 5(b), where the arrows point to the 3PPE peak position as deduced from figure 5(a). The 3PPE spin polarization at the peak maximum starts from -23% at $\theta = 0^\circ$, passes through zero at $\theta = 7.5^\circ$, and reaches the opposite sign of $+18\%$ at $\theta = 10^\circ$ emission angle, in general agreement with our schematic picture.

Again, we notice that the spin-polarization spectra show significant variation in their overall shape as a function of the excitation condition.

4. Discussion

In this section, we will address two aspects of the data. Firstly, this concerns the comparison of the spin polarization values reported in this investigation with reference data measured by angle-resolved one-photon photoemission (1PPE) [10] and with values obtained by photon-energy-dependent 3PPE [11]. Secondly, we assess the role of resonant excitation pathways in determining the full spin-polarization spectra in our multi-photon scheme.

In figure 6 (top panel), we plot the spin polarization of electrons photoemitted at normal emission from the SO-split Cu d -bands, as a function of their initial state energy measured in

1PPE (triangles) with $h\nu = 11$ eV excitation [10]. The spin polarization versus the initial state energy (deduced by subtracting from the final state energy the energy supplied by the photon excitation) reaches maximum values of +45 and -25% at -1.9 and -2.3 eV below the Fermi level, respectively. The circles in figure 6(a) represent the initial-state spin polarization deduced from the *resonant* IP state polarization in 3PPE experiments on clean Cu(001), measured by tuning the exciting photon energy $h\nu$ from 3.00 to 3.14 eV [11]. Here, the initial state energy was deduced from the final state energy by subtracting the energy supplied by the multi-photon (3PPE) excitation while considering the value corresponding to the *maximum IP state intensity* as the correct one for the spin polarization. Following this procedure, the 3PPE resonant spin polarization agrees well with 1PPE data in the region accessible by our experiments.

In the top part of figure 6(b), we report (black empty squares) the spin polarization as a function of the initial state energy deduced from the Cs-coverage-dependent measurements performed with $h\nu = 3.05$ eV excitation along with the reference 3PPE data from the clean surface (circles). The broadening and reduction of the IP state peak with Cs adsorption restrict the amount of Cs coverage that allows us to observe the resonant 3PPE [26, 30], thereby limiting the accessible initial-state range. Nevertheless, the spin polarizations in the initial state deduced via the two methods agree very well, as demonstrated by their strong overlap. This confirms that the physical picture underlying the idea of tuning the spin polarization in the IP state by shifting its energy level is essentially correct.

The spin polarization measured in the angle-dependent photoemission experiments reported in section 3.2 is shown in the bottom section of figure 6(b) for emission angles ranging from $\theta = 0^\circ$ to $\theta = 15^\circ$. Again, reference 3PPE data are reported for comparison. For small θ , the spin polarization is quantitatively similar to the reference normal-emission 3PPE result. The more the emission angle is increased, the more the discrepancies between the two sets of data increase. The spin polarization deduced via angle-resolved measurements reaches a maximum for $\theta \approx 10^\circ$ and then decreases for larger angles, and exhibits significantly different absolute values. These differences can be accounted for on the basis of a variety of phenomena taking place in off-normal emission geometry. Firstly, as mentioned previously, the *d*-band initial states for off-normal photoemission differ with respect to the ones at the $\bar{\Gamma}$ point shown in figure 3. The spin polarization measured in the experiment is accordingly determined by both the splitting and the exact binding energy of each SO split band as a function of k_{\parallel} . Whereas in the close proximity of the $\bar{\Gamma}$ point (small emission angle θ) we can safely assume minor changes, this assumption might not hold for the large θ case. Secondly, moving out from the normal emission case by an angle θ , the incidence angle of the circularly polarized laser beam gradually increases as $42^\circ + \theta$. Due to the different transmission coefficients of *p*-polarized and *s*-polarized light, the degree of ellipticity of the light (ϵ) in the interior of the material changes as a function of the incidence angle, decreasing from 0.64 at 42° incidence angle to 0.41 at 57° ($\epsilon = 1$ in vacuum) [31, 32]. The corresponding ratio of RCP to LCP components in light intensity is approximately 78 : 1 and 20 : 1 for 42° and 57° incident angle, respectively, possibly yielding a reduction in the electron spin polarization that can be quantified at 5% at the largest incidence angle. Finally, keeping a constant orientation of the detection direction in the spin detector will lead to a change to the measured spin polarization. In the absence of in-plane spin-polarization components, we expect a reduction in the spin polarization proportional to the cosine of the emission angle θ ; therefore, this might be a minor effect in the θ range addressed here. All these effects are, by definition, irrelevant at normal emission, whereas their contribution gradually increases with increasing emission angle. This thereby justifies the observation that

the spin polarization measured by angle-resolved measurements agrees with reference data for normal emission and deviates from the expected behaviour the more the emission angle is increased.

The second point we address is the apparent change in the shape of the spin-polarization spectra as a function of the change in the $d \rightarrow$ IP resonance conditions induced by the tuning of the IP state energy. We focus on the Cs-dependent measurements. It is obvious that, when trying to deduce the initial-state spin polarization from each separate spectrum, ambiguous results will be found, whereas conclusions in agreement with the reference 1PPE spin-polarization data are obtained when considering the spin polarization in accordance with the maximum intensity of the IP peak (i.e. at resonance). This behaviour can be explained taking into account the characteristic resonant behaviour of the $d \rightarrow$ IP excitation pathway. A specific photon energy and IP state level determine the initial d -band energy levels from which the spin-polarized electrons observed at the final state energy may originate. For the Cs-dependent measurements, the central photon energy of $h\nu = 3.05$ eV was chosen to favour the excitation of electrons from the upper Δ_7^5 band at the clean surface, leading to a positive spin polarization at resonance (compare figures 1(a) and (b) above with figures 3 and 4 in [11]). By moving the IP state energy level to lower values under Cs adsorption, the relevant initial d -band level in the two-photon resonance to the IP state is moved accordingly also to lower values. Under continued Cs adsorption and for the same central photon energy, this eventually tunes the resonance to the lower Δ_6^5 states, from which electrons of the opposite spin polarization are preferentially excited. In this way, the spin-polarized electrons excited to the final state energy at the resonance peak are selected in turn from the upper Δ_7^5 to the lower Δ_6^5 states, as would be the case in nonresonant 1PPE measurements with three times the photon energy used for 3PPE. Away from the resonance peak, which defines a dominating excitation pathway, the interpretation of the measured spin polarization is more complicated because of the presence of several excitation pathways that are off-resonant to varying degrees. As we have shown before, both the Δ_7^5 and the Δ_6^5 d -bands can be two-photon-coupled to the IP state by different photon energies [18]. In addition to the resonance favoured at the central photon energy $h\nu = 3.05$ eV employed for the Cs-dependent measurements, a second resonance is possible for higher photon energies. This additional higher-energy resonance would excite spin-polarized electrons from the lower Δ_6^5 d -band states to higher final state energies, whereas the electrons from the higher Δ_7^5 band will appear at lower final states for the lower-energy resonance (compare with figures 1(a)). This means that, in contrast to the conditions in the 1PPE measurements, the spin polarization observed in the final states off-resonance in 3PPE cannot be pictured as a simple linear translation from the initial states upwards by the photon energy. Due to the finite excitation bandwidth (170 meV at $h\nu = 3.07$ eV) of the laser pulses, we will have a mixture of two types of spin-polarized contributions as we move away from the resonance peak: the first contribution is related to off-resonant excitation from the upper Δ_7^5 d -band (lower photon energies in the pulse, ω_2 in figure 1(a)), and the second contribution originates from off-resonant excitation from the lower Δ_6^5 d -band by the alternative resonance for higher photon energies (ω_1 in figure 1(a)). According to this interpretation, the additional off-resonant contribution of the ω_1 pathway at the clean surface and low Cs coverages should be reduced with increasing Cs coverage because tuning the IP state to lower energies will tend to suppress any higher photon energy resonance with the lower Δ_6^5 states. This is supported by the observation that the shape of the spin-polarization spectrum off-resonance in the lower panel of figure 4 is beginning to look more similar to the 1PPE curve shown in figure 6(a). In higher-resolution 3PPE experiments [18], the

separate resonances of the IP state with each SO-split initial state are manifest as a clear splitting in the 3PPE IP state peak. In the present investigation, the lower energy resolution necessary to increase the count rate for spin-resolved detection does not allow us to resolve the IP peak fine structure, yet the peculiar signatures of the resonant and off-resonant behaviour are observable in the spin-polarized measurements. The additional information carried by the electron spins therefore provides information about the electron excitation pathways involved that would not be available in the non-spin resolved spectra.

We point out that it is in principle possible, in the Cu(001) system, to also access the *d*-band spin polarization via a multi-photon excitation process that is nonresonant via the IP state. After deposition of a larger amount of ≈ 0.09 ML Cs on the surface, the workfunction decreases enough to allow the direct observation of the *d*-band states near the X point in 2PPE [33]. The spin polarization spectrum as a function of the initial state energy deduced by a single 2PPE measurement under these conditions is reported as the solid black line in figure 6(a) ($h\nu = 3.14$ eV, $T = 120$ K). The data, besides a total reduction that is ascribable to an unpolarized background, match the spectral structure of the 1PPE results well. This occurs because the 2PPE excitation pathway on Cs/Cu(001) does not provide the very *k*-selective resonant conditions that occur in 3PPE through the IP state. We can expect only a spectrally smooth contribution to the observed transitions caused by the unoccupied *sp*-bands. Such conditions cannot emphasize the contribution of one of the SO-split initial bands like in the resonant 3PPE transitions. This accounts for the overall good agreement of the spin-resolved 2PPE data from Cs/Cu(001) with the (non-resonant) 1PPE data.

5. Summary

In summary, we have investigated different mechanisms of modifying the spin polarization of photoemitted electrons that were optically excited via unoccupied states on the Cu(001) surface. We exploited the coupling of the unoccupied IP states to the occupied SO-split *d*-bands via circularly polarized multi-photon excitation. We addressed the effects of a controlled modification of the energy levels involved in the multi-photon process. This was achieved either by Cs deposition to lower the vacuum level relevant to the IP or by exploiting the k_{\parallel} dispersion of the states involved. The deposition of a small amount of Cs on Cu(001) has been observed to induce a sign reversal of the spin polarization of the $n = 1$ IP state mediated by the decrease in its energy level, whereas the variation in spin polarization for off-normal photoemission is ascribed to the superimposed contribution of electronic effects and of the measurement geometry.

In addition, our results highlight the important differences between resonant and nonresonant excitation pathways in determining the resulting spin polarization. Furthermore, our investigation illustrates the usefulness of the spin degree of freedom of excited electrons to obtain information about the buildup and decay of excited electron populations on nonmagnetic surfaces.

Acknowledgments

The authors acknowledge F Helbig for valuable technical assistance. W-CL acknowledges support from the National Science Council of Taiwan under grant numbers NSC 96-2112-M-003-015-MY3.

References

- [1] Johnson P D 1997 Spin-polarized photoemission *Rep. Prog. Phys.* **60** 1217–304 doi:10.1088/0034-4885/60/11/002
- [2] Dil J H 2009 Spin and angle resolved photoemission on non-magnetic low-dimensional systems *J. Phys.: Condens. Matter* **21** 403001 doi:10.1088/0953-8984/21/40/403001
- [3] Eyers A, Schäfers F, Schönhense G, Heinzmann U, Oepen H P, Hünlich K, Kirschner J and Borstel G 1984 Characterization of symmetry properties of Pt(111) electron bands by means of angle-, energy-, and spin-resolved photoemission with circularly polarized synchrotron radiation *Phys. Rev. Lett.* **52** 1559–62 doi:10.1103/PhysRevLett.52.1559
- [4] Oepen H P, Hünlich K, Kirschner J, Eyers A, Schafers F, Schönhense G and Heinzmann U 1985 Experimental symmetry analysis of energy bands near critical points in Pt using spin- and momentum-resolved photoemission *Phys. Rev. B* **31** 6846–8 doi:10.1103/PhysRevB.31.6846
- [5] Garbe J, Venus D, Suga S, Schneider C and Kirschner J 1986 Spin-polarized angle-resolved photoemission from the (110) surface of platinum *Surf. Sci.* **178** 342–8 doi:10.1016/0039-6028(86)90310-9
- [6] Müller N, Kessler B, Schmiedeskamp B, Schönhense G and Heinzmann U 1987 Spin-resolved photoemission from Ir(111): transitions into a secondary band and energetic position of the final state bands *Solid State Commun.* **61** 187–92 doi:10.1016/0038-1098(87)90027-5
- [7] Heinzmann U 1987 Angle-, energy- and spin-resolved photoelectron emission using circularly polarized synchrotron radiation *Phys. Scr.* **T17** 77–88 doi:10.1088/0031-8949/1987/T17/009
- [8] Garbe J and Kirschner J 1989 Spin-dependent photoemission intensities from platinum (111) *Phys. Rev. B* **39** 9859–64 doi:10.1103/PhysRevB.39.9859
- [9] Schneider C M, Garbe J, Bethke K and Kirschner J 1989 Symmetry-dependent alignment of the electron-spin polarization vector due to electronic band hybridization observed in photoemission from Ag(100) *Phys. Rev. B* **39** 1031–5 doi:10.1103/PhysRevB.39.1031
- [10] Schneider C M, Demiguel J J, Bressler P, Schuster P, Miranda R and Kirschner J 1990 Spin- and angle-resolved photoemission from single crystals and epitaxial films using circularly polarized synchrotron radiation *J. Electron. Spectrosc. Relat. Phenom.* **51** 263–74 doi:10.1016/0368-2048(90)80157-6
- [11] Winkelmann A, Bisio F, Ocana R, Lin W-C, Nývlt M, Petek H and Kirschner J 2007 Ultrafast optical spin injection into image-potential states of Cu(001) *Phys. Rev. Lett.* **98** 226601 doi:10.1103/PhysRevLett.98.226601
- [12] Winkelmann A, Lin W-C, Bisio F, Petek H and Kirschner J 2008 Interferometric control of spin-polarized electron populations at a metal surface observed by multiphoton photoemission *Phys. Rev. Lett.* **100** 206601 doi:10.1103/PhysRevLett.100.206601
- [13] Aeschlimann M, Bauer M, Pawlik S, Weber W, Burgermeister R, Oberli D and Siegmann H C 1997 Ultrafast spin-dependent electron dynamics in fcc Co. *Phys. Rev. Lett.* **79** 5158–61 doi:10.1103/PhysRevLett.79.5158
- [14] Schmidt A B, Pickel M, Wiemhofer M, Donath M and Weinelt M 2005 Spin-dependent electron dynamics in front of a ferromagnetic surface *Phys. Rev. Lett.* **95** 107402 doi:10.1103/PhysRevLett.95.107402
- [15] Weinelt M, Schmidt A B, Pickel M and Donath M 2007 Spin-polarized image-potential-state electrons as ultrafast magnetic sensors in front of ferromagnetic surfaces *Prog. Surf. Sci.* **82** 388–406 doi:10.1016/j.progsurf.2007.03.010
- [16] Bisio F, Nývlt M, Franta J, Petek H and Kirschner J 2006 Mechanisms of high-order perturbative photoemission from Cu(001) *Phys. Rev. Lett.* **96** 087601 doi:10.1103/PhysRevLett.96.087601
- [17] Winkelmann A, Hartung D, Engelhard H, Chiang C-T and Kirschner J 2008 High efficiency electron spin polarization analyzer based on exchange scattering at Fe/W(001) *Rev. Sci. Instrum.* **79** 083303 doi:10.1063/1.2949877
- [18] Winkelmann A, Lin W-C, Chiang C-T, Bisio F, Petek H and Kirschner J 2009 Resonant coherent three-photon photoemission from Cu(001) *Phys. Rev. B* **80** 155128 doi:10.1103/PhysRevB.80.155128

- [19] Eckardt H, Fritsche L and Noffke J 1984 Self-consistent relativistic band structure of the noble metals *J. Phys. F: Met. Phys.* **14** 97–112 doi:10.1088/0305-4608/14/1/013
- [20] Weinelt M 2002 Time-resolved two-photon photoemission from metal surfaces *J. Phys.: Condens. Matter* **14** R1099–141 doi:10.1088/0953-8984/14/43/202
- [21] Thörner G, Borstel G, Dose V and Rogozik J 1985 Unoccupied electronic surface resonance at Cu(001) *Surf. Sci.* **157** L379–83 doi:10.1016/0039-6028(85)90667-3
- [22] Kuch W and Schneider C M 2001 Magnetic dichroism in valence band photoemission *Rep. Prog. Phys.* **64** 147–204 doi:10.1088/0034-4885/64/2/201
- [23] Hanuschkin A, Wortmann D and Blügel S 2007 Image potential and field states at Ag(100) and Fe(110) surfaces *Phys. Rev. B* **76** 165417 doi:10.1103/PhysRevB.76.165417
- [24] Echenique P M and Pendry J B 1978 The existence and detection of Rydberg states at surfaces *J. Phys. C: Solid State Phys.* **11** 2065–75 doi:10.1088/0022-3719/11/10/017
- [25] Papageorgopoulos C A 1982 Studies of separate adsorption and coadsorption of Cs and O₂ on Cu(100) *Phys. Rev. B* **25** 3740–9 doi:10.1103/PhysRevB.25.3740
- [26] Arena D A, Curti F G and Bartynski R A 1997 Unoccupied electronic states of the Cs/Cu(100) and Cs/Cu(111) adsorption systems *Phys. Rev. B* **56** 15404–11 doi:10.1103/PhysRevB.56.15404
- [27] Lang N D and Kohn W 1973 Theory of metal surfaces: induced surface charge and image potential *Phys. Rev. B* **7** 3541–50 doi:10.1103/PhysRevB.7.3541
- [28] Soukiassian P, Riwan R, Lecante J, Wimmer E, Chubb S R and Freeman A J 1985 Adsorbate-induced shifts of electronic surface states: Cs on the (100) faces of tungsten, molybdenum and tantalum *Phys. Rev. B* **31** 4911–23 doi:10.1103/PhysRevB.31.4911
- [29] Binnig G, Frank K H, Fuchs H, Garcia N, Reihl B, Rohrer H, Salvan F and Williams A R 1985 Tunneling spectroscopy and inverse photoemission: image and field states *Phys. Rev. Lett.* **55** 991–4 doi:10.1103/PhysRevLett.55.991
- [30] Bisio F, Winkelmann A, Lin W-C, Chiang C-T, Nývlt M, Petek H and Kirschner J 2009 Band structure effects in surface second harmonic generation: the case of Cu(001) *Phys. Rev. B* **80** 125432 doi:10.1103/PhysRevB.80.125432
- [31] Palik E D (ed) 1991 *Handbook of Optical Constants of Solids I* (New York: Academic)
- [32] Azzam R M A and Bashara N M 1992 *Ellipsometry and Polarized Light* 3rd ed. (Amsterdam: North-Holland)
- [33] Petek H, Nagano H and Ogawa S 1999 Hole decoherence of d bands in copper *Phys. Rev. Lett.* **83** 832 doi:10.1103/PhysRevLett.83.832

PHYSICAL REVIEW B 79, 245428 (2009)



Unconventional spin topology in surface alloys with Rashba-type spin splitting

H. Mirhosseini, J. Henk,* A. Ernst, S. Ostanin, C.-T. Chiang, P. Yu, A. Winkelmann, and J. Kirschner
Max-Planck-Institut für Mikrostrukturphysik, Weinberg 2, D-06120 Halle (Saale), Germany

(Received 4 May 2009; published 24 June 2009)

The spins of a pair of spin-orbit split surface states at a metal surface are usually antiparallely aligned, in accord with the Rashba model for a two-dimensional electron gas. By first-principles calculations and two-photon photoemission experiments we provide evidence that in the surface alloy Bi/Cu(111) the spins of an unoccupied pair of surface states are parallelly aligned. This unconventional spin polarization, which is not consistent with that imposed by the Rashba model, is explained by hybridization of surface states with different orbital character and is attributed to the spin-orbit interaction. Since hybridization is a fundamental effect our findings are relevant for spin electronics in general.

DOI: [10.1103/PhysRevB.79.245428](https://doi.org/10.1103/PhysRevB.79.245428)

PACS number(s): 73.20.At, 71.70.Ej, 79.60.Dp

I. INTRODUCTION

In the emerging field of spin electronics, proposals for device applications often utilize the Rashba effect in a two-dimensional electron gas (2DEG),¹ thereby relying on the spin topology of the 2DEG's electronic states (e.g., Refs. 2–6). The structural inversion asymmetry, that is, the asymmetric confinement of the 2DEG, leads via spin-orbit (SO) interaction to a splitting in the dispersion relation of the free electrons,

$$\epsilon_{\pm}(\mathbf{k}) = \epsilon_0 + \frac{\hbar^2 \mathbf{k}^2}{2m^*} \pm \alpha |\mathbf{k}|, \quad \mathbf{k} = (k_x, k_y), \quad (1)$$

where m^* is the effective mass. The Rashba parameter α comprises the strength of the atomic SO interaction and of the gradient of the confining potential in the z direction.^{7,8} The splitting, quantified by the displacement $\Delta k = 2|\alpha m^*|/\hbar^2$ of the band extrema in reciprocal space, shows up as two concentric circles in the momentum distribution. The spins of the two electronic states at energy ϵ are (i) oppositely aligned, are (ii) lying within the xy plane, and are (iii) normal to the wave vector \mathbf{k} .⁹ The spin polarization can therefore be written as $\mathbf{P}_{\pm}(\mathbf{k}) = \pm (k_y, -k_x, 0)/|\mathbf{k}|$, implying also $|\mathbf{P}| = 100\%$ [Fig. 1(a)].¹⁰

The above paradigmatic spin topology is found to a large extent in semiconductor heterojunctions¹¹ and in surface states at (111) surfaces of noble metals, in particular in Au(111).^{12,13} The surface states in surface alloys such as Bi/Ag(111) (Refs. 14–16) or Pb/Ag(111) (Refs. 16–18) show an unmatched spin splitting (large Rashba parameter α), which is caused by an additional in-plane gradient of the potential;¹⁹ the sp_z surface states in these alloys show the conventional topology of the Rashba model as well but with minor deviations (e.g., a nonzero but small P_z due to the in-plane gradient).

From the experimental and theoretical findings available so far one is lead to conclude that the spin topology imposed by the Rashba model shows up in a large number of systems, if not in all systems. In this paper, we show by first-principles calculations and two-photon photoemission (2PPE) experiments for the surface alloy Bi/Cu(111) that this topology cannot be taken for granted. Instead of the conven-

tional topology with oppositely rotating spins [Fig. 1(a)], we find momentum distributions with identical spin-rotation directions [Fig. 1(b)]. The origin of this effect is explained by the hybridization of surface states with different orbital character mediated by the spin-orbit interaction.

Our findings differ qualitatively from those in conventional Rashba systems. The momentum distribution of the latter comprises spin topologies with identical rotation direction as well but these are restricted to the low-density regime⁶ (or region I in Ref. 20), i.e., to energies between ϵ_0 and the band extrema. This regime extends over 0.015 eV for the sp_z surface states in Bi/Cu(111).²¹ But we find such topology in a 0.7 eV wide window in the high-density regime of the $p_x p_y$ surface states. Note that the present findings are similar to those for topological metals and insulators.^{22,23}

Previous studies of the Rashba effect at metal surfaces focused on occupied surface states since these can be accessed by angle-resolved photoelectron spectroscopy (ARPES).²⁴ These states are mainly of sp_z orbital character and thus agree with those of a 2DEG [see Ref. 10 for Au(111)]. As a consequence, their spin topology is consistent with that of the Rashba model [Fig. 1(a)].

In the Bi/Ag(111) and Pb/Ag(111) surface alloys, the adatoms induce also sp_z states but with larger splitting [as compared to Au(111)] and negative dispersion (effective mass $m^* < 0$).¹⁶ Further, there are indications for another mainly

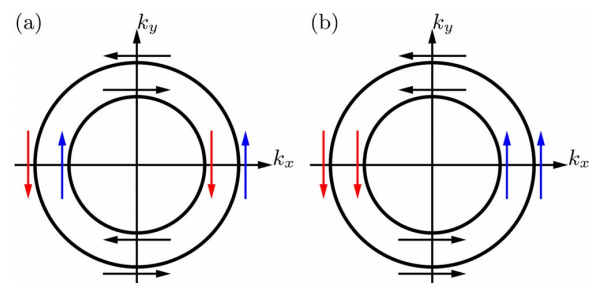


FIG. 1. (Color online) Spin topologies in a spin-orbit split 2DEG (schematic): (a) Conventional Rashba-type and (b) unconventional spin topology in the momentum distribution. The spin polarization of the “inner” and the “outer” state is represented by arrows.

MIRHOSSEINI *et al.*

PHYSICAL REVIEW B 79, 245428 (2009)

unoccupied set of bands. Since these bands cross at energies ϵ_0 above the Fermi energy E_F , their splitting Δk could only be extrapolated from their occupied “tails.” First-principles calculations show that these states are of $p_x p_y$ orbital character (i.e., oriented within the surface plane). Their occupied tails display the same spin topology as the sp_z states [Fig. 1(a)].

In the present work we focus on Bi/Cu(111) which shows a $\sqrt{3} \times \sqrt{3}$ -R30° surface geometry,²⁵ such as Bi/Ag(111) and Pb/Ag(111). Consequently, the surface electronic structure of Bi/Cu(111) consists also of two sets of Rashba-split surface states, namely, the sp_z and the $p_x p_y$ branch. As found by ARPES and scanning tunneling microscopy experiments,^{21,26} the partially occupied sp_z branch extends to about $E_F + 0.23$ eV and shows a Rashba splitting of $\Delta k \approx 0.035$ Bohr⁻¹.

II. EXPERIMENTAL FINDINGS

In contrast to ARPES which maps the *occupied* states, we can additionally access the *unoccupied* states by angle-dependent 2PPE. Experimental details are as described in Ref. 27. The single-photon energy used in the 2PPE measurements was 3.1 eV, using off-normal-incident p -polarized light. Bi was deposited by thermal evaporation on the Cu(111) substrate kept at 500 K. The formation of the $\sqrt{3} \times \sqrt{3}$ -R30° structure was checked by low-energy electron diffraction.

Angle-dependent 2PPE spectra were measured by rotating the sample around the axis perpendicular to the optical plane. The sample was oriented so that k_{\parallel} was measured in the plane containing the [111] and [11 $\bar{2}$] directions. The resulting experimental 2PPE intensity map is shown in Fig. 2. After the deposition of Bi, a reduction in the work function from about 4.9 eV for clean Cu(111) to below 4.4 eV is observed, as judged from the low-energy cutoff of the 2PPE spectrum at $k_{\parallel}=0$ in Fig. 2. This makes possible the observation of additional unoccupied intermediate states in the energy region below 1.8 eV which cannot be excited above the work function on clean Cu(111) using 3.1 eV photons.

In the lower half of Fig. 2, at about 4.5 eV final-state energy, a pair of split bands is clearly visible. These bands belong to unoccupied states located one photon energy (3.1 eV) below the final-state energy; as will become clear from the comparison with theory, these bands originate from the $p_x p_y$ surface states. They cross at $\bar{\Gamma}$ at about $E_F + (1.38 \pm 0.05)$ eV, and their maxima are shifted symmetrically from $\bar{\Gamma}$ by about (0.06 ± 0.01) Bohr⁻¹ [$\Delta k \approx (0.12 \pm 0.02)$ Bohr⁻¹] (Fig. 3).

In addition to the unoccupied states, the 2PPE experiment measures also the occupied states of sp_z character (see Fig. 4), which are excited by two photons to final-state energies near 6.2 eV in the upper half of Fig. 2. We note that a slightly increased intensity is also observed in the region extending to about 0.5 eV above the crossing point of the unoccupied split bands in Fig. 2. While no clearly dispersing bands can be observed experimentally, this intensity is consistent with the theoretical bands in Fig. 4 above 1.5 eV; their weak ex-

perimental intensity correlates with a comparably small theoretical spectral density.

The 2PPE intensity depends strongly on the emission angle, as can be seen by the pronounced intensity maximum at about 4.5 eV final-state energy and +5° emission angle (red spot in Fig. 2; note the comparably small intensity at -5°). Such features also appear also in the conventional (one-photon) photoemission from these surface alloys and can be explained by the transition matrix elements.

III. THEORETICAL FINDINGS

To elucidate the dispersion and especially the spin topology of the unoccupied bands we performed first-principles electronic-structure calculations, in close analogy to our previous investigations on surface alloys (e.g., Ref. 16). The interatomic distances at the surface are obtained from total-energy minimization using the Vienna *Ab initio* Simulation Package.²⁸ Due to the much smaller lattice constant of Cu as compared to Ag ($d_{\text{Cu-Cu}}=4.83$ Bohr and $d_{\text{Ag-Ag}}=5.40$ Bohr), the Bi atoms are more relaxed outward (by 38% of the bulk interlayer distance of Cu, $d_{\perp}=3.94$ Bohr) than in Bi/Ag(111). The optimum surface geometry serves as input for Korringa-Kohn-Rostoker (KKR) calculations. The electronic structure is analyzed in detail by means of the spectral density $n(E, \mathbf{k})$, which is computed from the Green's function in the relativistic layer-KKR method. $n(E, \mathbf{k})$ is resolved with respect to site, spin, and angular momentum.

The spin-averaged spectral density of a Bi site shows the split sp_z and $p_x p_y$ surface states (Fig. 4). Each branch comprises an “inner” band (with smaller $|\mathbf{k}|$) and an “outer” band (with larger $|\mathbf{k}|$). The sp_z bands cross at $E_F + 0.1$ eV; their Rashba splitting is $\Delta k = 0.10$ Bohr⁻¹ (Bi/Ag(111): $\Delta k = 0.14$ Bohr⁻¹). The $p_x p_y$ bands cross at $E_F + 1.4$ eV [experiment: $E_F + (1.38 \pm 0.05)$ eV], with $\Delta k = 0.08$ Bohr⁻¹ [experiment: $\Delta k = (0.12 \pm 0.02)$ Bohr⁻¹]. The theoretical results are thus consistent with the experimental findings and identify the split bands in experiment (Fig. 3) with the $p_x p_y$ surface states. The spectral density becomes blurred in regions in which the surface states hybridize with Cu-bulk states. The dispersion of the two branches follows closely that imposed by the Rashba model [Eq. (1) with negative effective mass m^*]. An exception, however, might be a “kink” in the inner $p_x p_y$ band at $(E, k) \approx (E_F + 0.6$ eV, ± 0.12 Bohr⁻¹) (marked in Fig. 4).

The spin topology of the surface states is visualized by the difference $n(E, \mathbf{k})_{\uparrow} - n(E, \mathbf{k})_{\downarrow}$ of the spectral densities, where \uparrow and \downarrow indicate the projection of the in-plane spin-polarization component normal to \mathbf{k} (Fig. 5; this \mathbf{P} component is prescribed by the Rashba model and is by far dominating). For the sp_z branch we find the expected conventional spin topology which is imposed by the Rashba model; the opposite spin-rotation direction of the two bands shows up at energies below the crossing at $\bar{\Gamma}$ as a red-blue-red-blue color coding with increasing wave number [line a in Fig. 5; cf. Fig. 1(a)]. In contrast, the $p_x p_y$ branch shows a red-red-blue-blue coding at, say, $E_F + 1.0$ eV (line b in Fig. 5); thus these surface states have identical rotation direction [cf. Fig. 1(b)]. This finding is not consistent with the Rashba model: It

UNCONVENTIONAL SPIN TOPOLOGY IN SURFACE...

PHYSICAL REVIEW B 79, 245428 (2009)

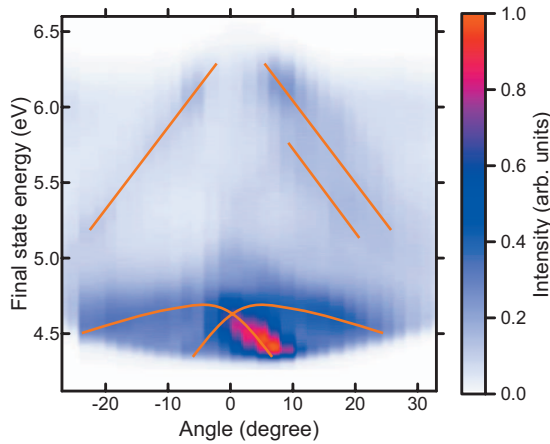


FIG. 2. (Color) Two-photon photoemission from Bi/Cu(111). The intensity for given final-state energy and emission angle is shown as color scale. The unoccupied $p_x p_y$ surface states appear at about 4.5 eV. To guide the eye, orange lines highlight the dispersion of the electronic states.

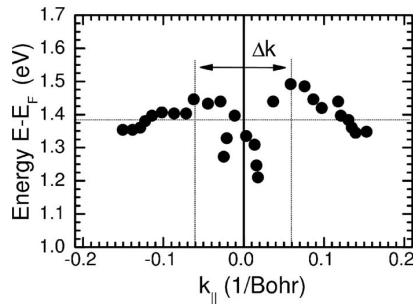


FIG. 3. Rashba splitting Δk in the unoccupied $p_x p_y$ surface states of Bi/Cu(111), as obtained from two-photon photoemission experiments (Fig. 2).

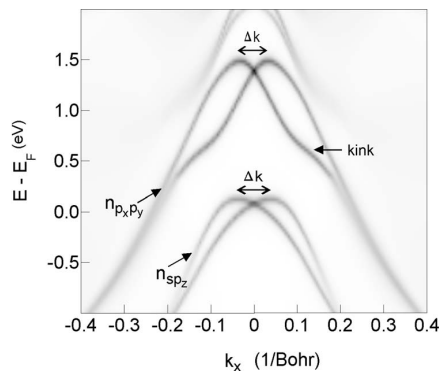


FIG. 4. Surface electronic structure of Bi/Cu(111) as obtained from first-principles calculations. The spectral density $n(E, \mathbf{k})$ for a Bi site is depicted as gray scale (white=zero). The sp_z and the $p_x p_y$ surface-state branches are indicated.

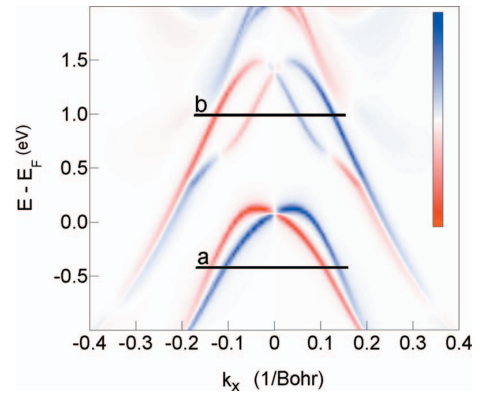


FIG. 5. (Color) Spin-resolved electronic structure of Bi/Cu(111) as obtained by first-principles calculations. The difference $n(E, \mathbf{k})|_{\uparrow} - n(E, \mathbf{k})|_{\downarrow}$ of the spin-projected spectral densities for a Bi site is depicted as color scale (red=negative, white=zero, and blue=positive). The spin projection is in-plane and perpendicular to the wave vector. Horizontal lines are guides to the conventional (line a) and unconventional (line b) spin topology of the sp_z and the $p_x p_y$ states, respectively.

appears that the spin polarization of the inner $p_x p_y$ state is reversed in comparison to that of the inner sp_z state. It is important to note that at energies below the kink the spin polarization of this band has changed sign, e.g., at $E_F + 0.2$ eV, and the conventional spin topology is restored; in other (E, \mathbf{k}) regions its absolute value is as large as 90%.

Deviations from a smooth dispersion, as seen at the kink (Fig. 4), indicate hybridization of electronic states. A group-theoretical analysis shows that wave functions can be represented either as^{29,30}

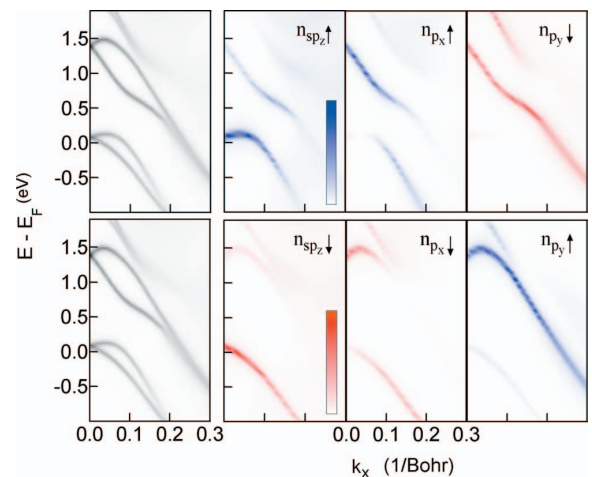


FIG. 6. (Color) Hybridization of surface states in Bi/Cu(111). The orbital- and spin-resolved spectral densities at a Bi site are depicted as color scales. The top [bottom] panels comprise contributions according to Eq. (2) [Eq. (3)]. All data share the same color scale, with white=zero and dark red (dark blue)=maximum spectral density (70 states/Hartree). The left panels display the total spectral density for comparison (in gray scale; cf. Fig. 4).

MIRHOSSEINI *et al.*PHYSICAL REVIEW B **79**, 245428 (2009)

$$|\psi\rangle = |sp_z\uparrow\rangle + |p_x\uparrow\rangle + |p_y\downarrow\rangle \quad (2)$$

or as

$$|\psi\rangle = |sp_z\downarrow\rangle + |p_x\downarrow\rangle + |p_y\uparrow\rangle. \quad (3)$$

The spinors $|\uparrow\rangle$ and $|\downarrow\rangle$ are quantized with respect to the y axis. Both the outer sp_z band and the inner p_xp_y state belong to the representation of Eq. (2) and hence are allowed to hybridize. Thus, if the usually dominating $|p_y\downarrow\rangle$ component of the inner p_xp_y state is surpassed by the $|p_x\uparrow\rangle$ component, the spin polarization of this state changes sign. That this is indeed the case is seen by the $|p_x\uparrow\rangle$ contribution to $n(E, \mathbf{k})$, which increases with energy (top row in Fig. 6). At the kink, where the inner p_xp_y band and outer sp_z band approach, both the $|sp_z\uparrow\rangle$ and the $|p_y\downarrow\rangle$ orbitals show a significant spectral density; the kink shape is thus attributed to the hybridization of these two bands. The inner sp_z and the outer p_xp_y states belong to the representation of Eq. (3) and hybridize as well but less due to their larger (E, \mathbf{k}) “distance” (bottom row in Fig. 6).

Note that hybridization of orbitals with opposite spin is brought about only by SO coupling.³¹ Further, the effect is not described by first-order perturbation theory in the SO interaction because this order would produce the spin splitting but not the hybridization.

The Dresselhaus effect could in principle produce a deviation from the Rashba-type spin topology.³² A closer analysis, however, shows that it vanishes in the present case. Therefore, hybridization as a result of the spin-orbit interaction remains as the sole reason for the unconventional spin topology in Bi/Cu(111).

An important ingredient for the unmatched splitting found in these surface alloys is the in-plane gradient of the potential.^{15,19} As the gradient perpendicular to the surface (along z) produces the in-plane spin polarization (P_x and P_y),

the in-plane gradient gives rise to a nonzero P_z . A p_xp_y surface state is expectedly more susceptible to the in-plane gradient than a sp_z surface state. Consequently, its P_z should be larger. Indeed, P_z of the p_xp_y states is negligibly for small $|\mathbf{k}|$ but reaches 20% in absolute value for larger wave vectors ($|\mathbf{k}| > 0.15 \text{ Bohr}^{-1}$). In contrast, the sp_z states have no significant P_z .

The demonstrated mechanism for changing the spin topology of the surface states in surface alloys is also present in Bi/Ag(111), as we have investigated theoretically as well (results not shown here). In comparison with Bi/Cu(111), the effect is less pronounced because hybridization of the sp_z and p_xp_y branches is decreased by the smaller outward relaxation of Bi.¹⁸ Another aspect is that the surface states hybridize with Ag bulk states in a large (E, \mathbf{k}) region due to projected bulk-band structure of Ag. As a consequence, they show no clear kink.

IV. CONCLUDING REMARKS

In summary, there is more to the spin-resolved electronic structure of surface states in surface alloys than first imagined. Although the basic properties are described by the standard Rashba model, additional effects (e.g., hybridization and the in-plane potential gradient) can change important features of the electronic states and their spin topology. In turn, there is the possibility to exploit these mechanisms in new spintronics devices and in new effects (e.g., Refs. 6 and 23).

Since hybridization is a general mechanism, the present effect can be important also in other systems, possibly at other high-symmetry points in the two-dimensional Brillouin zone or at other energies. It is therefore desirable to carry out spin-resolving experiments on the spin-orbit splitting of surface states.

*Corresponding author; henk@mpi-halle.de

¹Y. A. Bychkov and E. I. Rashba, *J. Phys. C* **17**, 6039 (1984).

²S. Datta and B. Das, *Appl. Phys. Lett.* **56**, 665 (1990).

³T. Koga, J. Nitta, H. Takayanagi, and S. Datta, *Phys. Rev. Lett.* **88**, 126601 (2002).

⁴J. Sinova, D. Culcer, Q. Niu, N. A. Sinitsyn, T. Jungwirth, and A. H. MacDonald, *Phys. Rev. Lett.* **92**, 126603 (2004).

⁵J.-i. Ohe, M. Yamamoto, T. Ohtsuki, and J. Nitta, *Phys. Rev. B* **72**, 041308(R) (2005).

⁶E. Cappelluti, C. Grimaldi, and F. Marsiglio, *Phys. Rev. Lett.* **98**, 167002 (2007).

⁷L. Petersen and P. Hedegård, *Surf. Sci.* **459**, 49 (2000).

⁸Y. M. Koroteev, G. Bihlmayer, J. E. Gayone, E. V. Chulkov, S. Blügel, P. M. Echenique, and P. Hofmann, *Phys. Rev. Lett.* **93**, 046403 (2004).

⁹R. Winkler, *Spin-Orbit Coupling Effects in Two-Dimensional Electron and Hole Systems* (Springer, Berlin, 2003).

¹⁰J. Henk, M. Hoesch, J. Osterwalder, A. Ernst, and P. Bruno, *J. Phys.: Condens. Matter* **16**, 7581 (2004).

¹¹J. Nitta, T. Akazaki, H. Takayanagi, and T. Enoki, *Phys. Rev. Lett.* **78**, 1335 (1997).

¹²S. LaShell, B. A. McDougall, and E. Jensen, *Phys. Rev. Lett.* **77**, 3419 (1996).

¹³F. Reinert, *J. Phys.: Condens. Matter* **15**, S693 (2003).

¹⁴T. Hirahara, T. Nagao, I. Matsuda, G. Bihlmayer, E. V. Chulkov, Y. M. Koroteev, P. M. Echenique, M. Saito, and S. Hasegawa, *Phys. Rev. Lett.* **97**, 146803 (2006).

¹⁵C. R. Ast, J. Henk, A. Ernst, L. Moreschini, M. C. Falub, D. Pacilé, P. Bruno, K. Kern, and M. Grioni, *Phys. Rev. Lett.* **98**, 186807 (2007).

¹⁶C. R. Ast *et al.*, *Phys. Rev. B* **77**, 081407(R) (2008).

¹⁷D. Pacilé, C. R. Ast, M. Papagno, C. Da Silva, L. Moreschini, M. Falub, A. P. Seitsonen, and M. Grioni, *Phys. Rev. B* **73**, 245429 (2006).

¹⁸G. Bihlmayer, S. Blügel, and E. V. Chulkov, *Phys. Rev. B* **75**, 195414 (2007).

¹⁹J. Prempfer, M. Trautmann, J. Henk, and P. Bruno, *Phys. Rev. B* **76**, 073310 (2007).

²⁰C. R. Ast, G. Wittich, P. Wahl, R. Vogelgesang, D. Pacilé, M. C. Falub, L. Moreschini, M. Papagno, M. Grioni, and K. Kern,

UNCONVENTIONAL SPIN TOPOLOGY IN SURFACE...

PHYSICAL REVIEW B **79**, 245428 (2009)

- Phys. Rev. B **75**, 201401(R) (2007).
- ²¹L. Moreschini, A. Bendounan, H. Bentmann, M. Assig, F. Reinert, C. R. Ast, M. Gioni, and J. Henk (unpublished).
- ²²J. W. Wells *et al.*, Phys. Rev. Lett. **102**, 096802 (2009).
- ²³D. Hsieh *et al.*, Science **323**, 919 (2009).
- ²⁴F. Reinert, G. Nicolay, S. Schmidt, D. Ehm, and S. Hüfner, Phys. Rev. B **63**, 115415 (2001).
- ²⁵D. Kaminski, P. Poodt, E. Aret, N. Radenovic, and E. Vlieg, Surf. Sci. **575**, 233 (2005).
- ²⁶H. Bentmann, F. Forster, L. Moreschini, M. Gioni, and F. Reinert (unpublished).
- ²⁷F. Bisio, M. Nyvlt, J. Franta, H. Petek, and J. Kirschner, Phys. Rev. Lett. **96**, 087601 (2006).
- ²⁸G. Kresse and J. Furthmüller, Phys. Rev. B **54**, 11169 (1996).
- ²⁹T. Inui, Y. Tanabe, and Y. Onodera, *Group Theory and Its Applications in Physics*, Springer Series in Solid State Sciences Vol. 78 (Springer, Berlin, 1990).
- ³⁰T. Oguchi and T. Shishidou, J. Phys. Condens. Matter **21**, 092001 (2009).
- ³¹That SO coupling is the origin of the kink was checked by scaling the SO strength following Ref. 33: With vanishing SO coupling, the kink disappears.
- ³²G. Dresselhaus, Phys. Rev. **100**, 580 (1955).
- ³³H. Ebert, H. Freyer, and M. Deng, Phys. Rev. B **56**, 9454 (1997).

Magnetic Dichroism from Optically Excited Quantum Well States

Cheng-Tien Chiang, Aimo Winkelmann,* Ping Yu, and Jürgen Kirschner

Max-Planck-Institut für Mikrostrukturphysik, Weinberg 2, D-06120 Halle(Saale), Germany

(Received 16 March 2009; published 11 August 2009)

We demonstrate magnetic dichroism from optically excited states in two-photon photoemission. Using ultrathin cobalt films grown on Cu(001), we observe unoccupied quantum well states which give rise to a sizable intensity change in photoemission under magnetization reversal. The simultaneous comparison of both circular and linear magnetic dichroism in the same system permits us to check fundamental symmetry requirements and allows us to explicitly elucidate the common origin of both effects. Based on our observations we argue that the observed effect is related to spin-orbit coupling in the intermediate quantum well states.

DOI: 10.1103/PhysRevLett.103.077601

PACS numbers: 79.60.-i, 73.21.Fg, 75.70.Rf

The relativistic coupling between spin and orbital angular momentum of electrons is an essential mechanism in the physics of ultrafast magnetism [1], spintronics, and quantum information processing [2]. Besides its fundamental role in the interplay of spin, electronic and lattice degrees of freedom, a unique capability of spin-orbit coupling is to provide an access to the electron spin via purely optical excitation. In a magnetic system, the optical transition rates can be strongly influenced by spin-orbit interaction, leading to element-specific dichroism in optical absorption [3] and photoemission [4,5]. When combined with ultrashort laser pulses, magnetic dichroism allows us to analyze the dynamics of spin and orbital angular momentum down to the femtosecond time scale [6,7], providing key insights into long-standing issues of nonequilibrium magnetism triggered by the optical excitation [8]. Since excited states play a central role in optically driven processes, it is of great interest to characterize their intrinsic spin-orbit coupling strength, with potential implications for optical control of spin and magnetism on ultrashort time scales.

In order to probe the spin-orbit interaction in excited states, decisive spectroscopic measurements are required, which can be obtained when the excited electronic states act as intermediate levels in a two-photon-photoemission (2PPE) process [9,10]. In combination with magnetic dichroism, 2PPE thus can offer a direct grasp on spin-orbit coupling in the optically excited, initially unoccupied electronic states. Recently, magnetic linear [11] and circular [12] dichroism were indeed observed in 2PPE experiments. Nevertheless, in both cases the dichroic signal could not be correlated to specific excited states: In the first case, Pickel *et al.* [11] observed dichroic signals of up to 20% which were associated with intensively spin-orbit influenced regions in the occupied band structure of cobalt. In the second case, Hild *et al.* [12] carried out nonspectroscopic 2PPE total yield measurements from Heusler alloys, not allowing identification of the intermediate states, and accompanied with a maximum signal of 0.35%.

In this Letter, we demonstrate the effect of magnetic dichroism by specific intermediate optically excited states. Well-characterized unoccupied quantum well states in ultrathin ferromagnetic cobalt films on Cu(001) [13,14] serve as the intermediate levels in a two-photon-photoemission experiment. By control over the incident polarization of

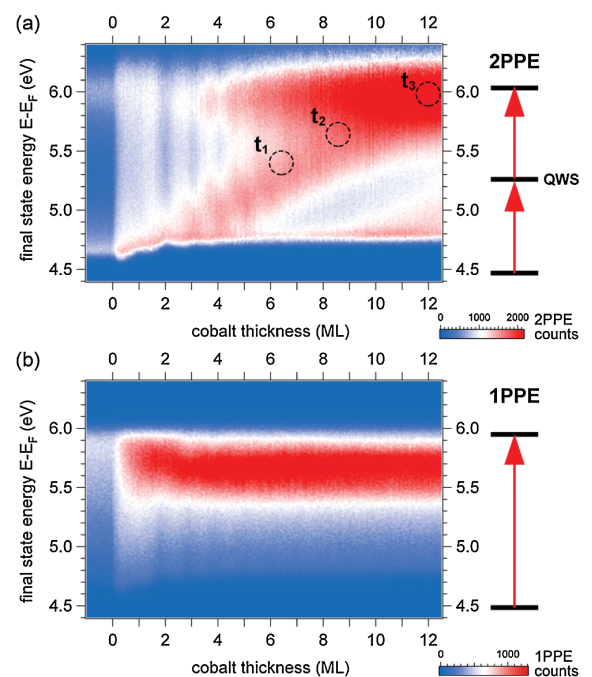


FIG. 1 (color). (a) Thickness dependent 2PPE spectra ($h\nu = 3.1$ eV) measured in normal emission during the deposition of a Co film on Cu(001). Three selected positions of the quantum well state are marked by $t_{1...3}$ (see text). (b) Equivalent experiment as in (a) but with one-photon photoemission (1PPE, $h\nu = 6.0$ eV). The excitation light is p polarized in both cases. General energy level schemes for 2PPE and 1PPE are shown on the side.

light, we experimentally demonstrate the common principle that governs both magnetic circular and linear dichroism: the interference between optical transitions coupled by mutually orthogonal electric field components. Taking into account the available experimental and theoretical data on the initial, intermediate, and final state electronic structure relevant to our system, we attribute the observed dichroism to spin-orbit coupling in the intermediate quantum well states.

The experimental setup has been described before [15]. Deposition and photoemission measurements are performed at 300 K in an ultrahigh vacuum chamber with base pressure lower than 1×10^{-10} mbar. The ultrathin films were grown by electron-beam evaporation from a Co rod. Simultaneously with the Co film growth, we measured thickness dependent normal-emission 2PPE and one-photon photoemission (1PPE) spectra which are shown in Fig. 1. Beginning with initial double layer growth [16], both 2PPE and 1PPE show intensity oscillations with monolayer (ML) periodicity, which we ascribe to additional scattering centers in incomplete layers. Comparison of the 2PPE and 1PPE spectra allows us to immediately identify a contribution from an intermediate state in the 2PPE data, as shown in Fig. 1. The final state energy of this feature disperses characteristically as a function of cobalt thickness and is compatible with unoccupied quantum well (QW) states derived from the sp band of the cobalt film [13,14]. The increased intensity at around 6.0 and 5.8 eV in 2PPE and 1PPE is attributed to the occupied Co d band near the Fermi level.

To examine a possible magnetic dichroism in 2PPE, we employed the experimental geometry shown in Figs. 2(a) and 2(b) for measurements with circularly and linearly polarized light. The sample magnetization M is in the optical plane, with $\pm M$ parallel and antiparallel to the Co [110] magnetic easy-axis. We note that the geometry of Fig. 2(b) is not the standard magnetic linear dichroism setup, where M is usually taken perpendicular to the optical plane [17]. Our setup instead allows us to systematically investigate the effects of light polarization on dichroism with the magnetization in the optical plane. The plane of linear polarization can be continuously rotated by an angle α relative to the optical plane OP [Fig. 2(b), p : $\alpha = 0^\circ$, s : $\alpha = 90^\circ$]. The photoelectrons are detected in normal emission. Photoemission through the quantum well state and from the Fermi level is indicated by $E_{\text{QW}} + h\nu$ and $E_F + 2h\nu$, respectively. The normalized intensity change under magnetization reversal A (dichroic asymmetry) is determined from the magnetization dependent 2PPE intensities $I_{\pm M}$ for circularly (A_{MCD}) and linearly polarized light (A_{MLD}) according to $A_{\text{MCD,MLD}} = (I_{+M} - I_{-M}) / (I_{+M} + I_{-M})$.

The 2PPE spectra observed using circularly polarized light are shown in the upper panel of Fig. 2(c), and the derived A_{MCD} curves for right- as well as for left-circularly polarized light (σ^- , σ^+) are shown in the lower panel.

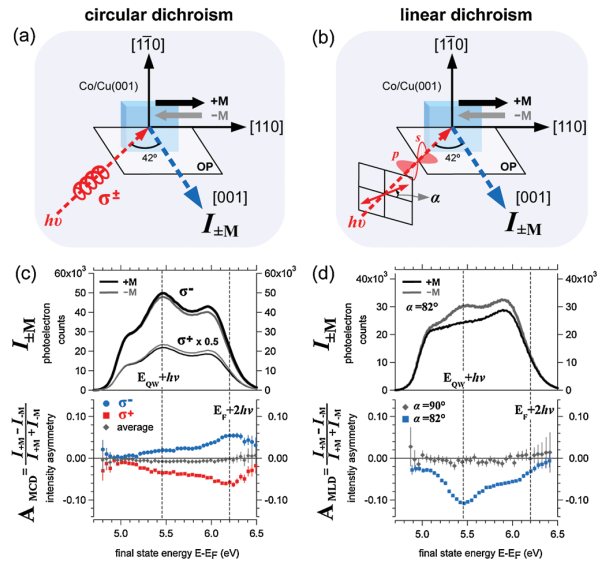


FIG. 2 (color). (a) and (b) Experimental geometry. OP denotes the optical plane, and the angle of the linear polarization plane is α . (c) upper panel: 2PPE spectra measured for opposite sample magnetizations $\pm M$ using right- (σ^-) and left-circularly polarized light (σ^+); lower panel: dichroic asymmetry A_{MCD} for σ^- (blue circles) and σ^+ (red squares), and their average (gray diamonds). (d) upper panel: 2PPE spectra measured for $\pm M$ using linear polarized light at $\alpha = 82^\circ$; lower panel: dichroic asymmetry A_{MLD} for s -polarized light ($\alpha = 90^\circ$, gray diamonds) and for $\alpha = 82^\circ$ (blue squares). The Co film thickness was 6 ML.

Looking at A_{MCD} , we observe a large dichroism of 5% originating from the occupied states near the Fermi level [11,18]. More importantly, a signal of about 3% is observed at the position $E_{\text{QW}} + h\nu$ of the unoccupied QW state.

While we cannot observe any dichroic asymmetry within our detection limit for nominally p - and s -polarized light, magnetic dichroism appears for a tilted polarization plane ($\alpha \neq 0^\circ, \pm 90^\circ, 180^\circ$), in agreement with symmetry requirements [17]. For $\alpha = 82^\circ$, we observe a very large dichroic signal of 10% at $E_{\text{QW}} + h\nu$, and a small signal of 2% at $E_F + 2h\nu$, as is shown in Fig. 2(d). In order to verify the intrinsic connection of the dichroic feature at $E_{\text{QW}} + h\nu$ to the QW state, we measured the thickness dependence of the dichroism as shown in Fig. 3 for films of 6, 8, and 12 ML thickness. There we see in the lower panel that the maximum dichroic signal in A_{MLD} moves consistently with the dispersion of the QW state feature in the thickness dependent 2PPE spectra shown in Fig. 1(a). The behavior of the circular dichroism A_{MCD} in the upper panel of Fig. 3 is less obvious due to the overlap of the relatively small contribution from the QW state at $E_{\text{QW}} + h\nu$ with a larger signal from $E_F + 2h\nu$, but a consistent shift of the partial contribution from the QW state can still be identified.

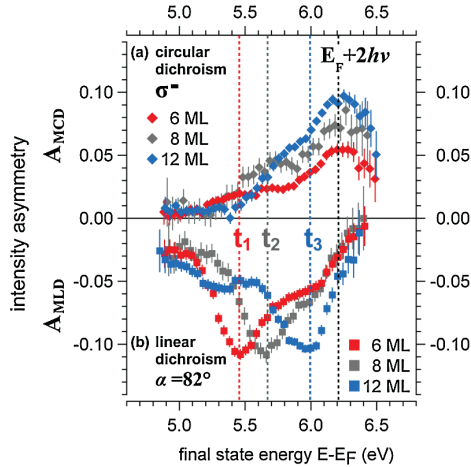


FIG. 3 (color). Thickness dependence of magnetic circular and linear dichroism (MCD and MLD) from Co/Cu(001). MCD obtained with σ^- light and MLD with $\alpha = 82^\circ$ are shown in the upper and lower panel, respectively. The positions of the QW state $E_{QW} + h\nu$ for three different thicknesses are marked by $t_{1...3}$ (see also Fig. 1). 2PPE from near the Fermi level is indicated at $E_F + 2h\nu$.

Using systematic measurements of linear and circular dichroism, we can check general symmetry relations that are expected to hold in the experimental geometry. For circular dichroism, reversal of the light helicity combined with a reversal of the sample magnetization should not change the photoemission intensity in our setup [17,19]. The average of A_{MCD} from σ^- and σ^+ light, shown in Fig. 2(c) (lower panel, gray diamonds), would thus give zero in the ideal case. We ascribe the remaining experimental average of below 1% to the apparatus asymmetry. Furthermore, since the photoemission intensity is a current in the optical plane OP, it must be invariant under the mirror operation (m_{OP}), whereas the magnetization M , the helicity of circularly polarized light σ and the angle α of linearly polarized light are reversed by m_{OP} . This implies the relations [17,19,20]: $I_{\pm M}(\sigma^+) \stackrel{m_{OP}}{=} I_{\mp M}(\sigma^-)$ and $I_{\pm M}(\alpha) \stackrel{m_{OP}}{=} I_{\mp M}(-\alpha)$. From these relations we can trace the cause of circular and linear dichroism back to the difference in photoexcitation between the σ^+/σ^- and $+\alpha/-\alpha$ settings, respectively. For both cases, it is the sign of the s -polarized component that is reversed when applying the mirror operation. This can be followed by looking at Fig. 2(b) where we explicitly indicate the p - and s -polarized components of the incident electric field. The difference between circular and linear dichroism is only the switch in phase difference between s and p components, which is $+90^\circ/-90^\circ$ between σ^+ and σ^- , and $0^\circ/180^\circ$ between α and $-\alpha$. We checked these expectations experimentally by measuring the 2PPE intensities I_{+M} and I_{-M} at $E_{QW} + h\nu$ as a function of the polarization plane angle α . In the upper panel of Fig. 4, the experimental data are fitted under the assumption of a

constant contribution I_s plus a contribution varying with angle and sign of magnetization as $I_p \cos^2(\alpha \pm \Delta\alpha/2)$. Very good agreement can be reached assuming a constant shift angle $\Delta\alpha = 5^\circ$ (solid lines). In the lower panel, we show the experimental dichroic asymmetry $A_{MLD}(\alpha)$ together with a curve resulting from the fit in the upper panel. As one can clearly see, the predicted symmetry property $A_{MLD}(\alpha) = -A_{MLD}(-\alpha)$ is convincingly fulfilled by the experimental data. The assumptions of the model fit in Fig. 4 are derived from the common interpretation of linear dichroism in terms of interference of photoemission pathways where $\Delta\alpha$ is related to the product of transition matrix elements coupled to the components of the electric field which are perpendicular and parallel to the surface [19,20]. Such interference is provided by states of mixed spatial symmetries in the presence of spin-orbit coupling. The good agreement of the model with the experimental data strongly supports the interference mechanism behind the observed magnetic dichroism.

So far, we have shown that our observations are consistent with general symmetry requirements, independent of the details of the 2PPE process. Now we will discuss where spin-orbit coupling influences 2PPE in our magnetic system, involving initial, intermediate, and final states. In the 2PPE study of Co/Cu(001) by Pickel *et al.* [11], the relativistically calculated band structure of fcc Co shows several spin-orbit hybridization points, one of them located at about 1.3 eV above the Fermi level along the Δ direction, hybridizing unoccupied Co d -band states with the sp band from which the quantum well states are derived. This specific hybridization point is lower in energy than the intermediate quantum well state we measured in Fig. 3 at 2.4 to 2.9 eV above E_F . In this case, the phase difference between spin-orbit coupled bands of different spatial symmetry does not have a sign change in the energy range observed by us. This gives rise to a single-signed magnetic dichroism in both A_{MCD} and A_{MLD} [21]. These qualitative considerations are corroborated by theoretical calculations of photoemission from quantum well states in tetragonally distorted Co films, which indeed show spin-orbit hybridization and corresponding dichroic effects that are consistent with our experimental observations [22]. The Co initial states which are relevant for excitation of the QW state in Fig. 3 show a spin-orbit hybridization point of Δ_5 and Δ_1 majority bands near $E_F - 0.6$ eV [23] and a minority Δ_1 surface resonance is present at $E_F - 0.4$ eV [23]. A significant influence of these initial states on the observed dichroism does not seem compatible with the fact that the dichroic signal of the dispersing QW state feature for linearly polarized light shows almost no variation in Fig. 3 while the relevant initial states move through the strongly variable region of the band structure between $E_F - 0.7$ eV and $E_F - 0.2$ eV. Concerning the final states, which are required to have Δ_1 symmetry for normal emission, we can exclude final state diffraction [24,25] and surface transmission [21,26] effects because they are for-

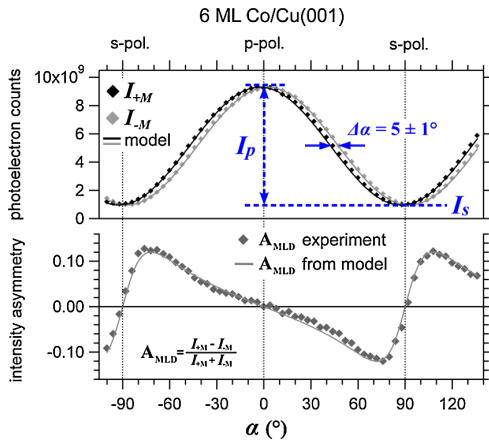


FIG. 4 (color online). Upper panel: Intensity $I_{\pm M}(\alpha)$ as a function of the polarization plane angle, measured at the quantum well state feature on a 6 ML cobalt film ($E_{QW} + h\nu = 5.45 \pm 0.05$ eV). A shift angle $\Delta\alpha = 5 \pm 1^\circ$ is measured. Lower panel: The MLD asymmetry $A_{MLD}(\alpha)$ derived from the experimental data (gray diamonds). Solid curves in both panels are based on the model: $I_{\pm M}(\alpha) = I_s + I_p \cos^2(\alpha \pm \Delta\alpha/2)$ with $\Delta\alpha = 5^\circ$.

bidden in our normal-emission geometry with magnetization and optical plane along a high symmetry crystal direction [25,26]. Additionally, a possible contribution of magneto-optical effects on photoemission [27] is contradicted by the α -independent shift angle $\Delta\alpha$ in A_{MLD} (Fig. 4), which is also much too large for a linear magneto-optical rotation as estimated from known magneto-optical constants ($\theta_{Kerr} \leq 0.5^\circ$ at $h\nu = 3$ eV [28]).

To summarize, we demonstrated both circular and linear magnetic dichroism in two-photon photoemission via optically excited states. Our observations are well explained by the interference between spin-orbit influenced photoemission pathways and indicate the presence of spin-orbit interaction in the unoccupied quantum well states. Our experiments provide a starting point for future pump-probe dichroic studies on femtosecond dynamics of optically excited magnetic systems, allowing extended insights into the relativistic unoccupied band structure at surfaces [17] and spatial imaging of magnetization and spin dynamics [29]. The identification of spin-orbit coupling in intermediate states in a 2PPE process would also be a first step towards the analysis and control of quantum interference effects [30] via multiple spin-dependent excitation pathways at surfaces, enabling for instance the steering of spin-polarized surface currents [31,32] by optical pulses.

We gratefully acknowledge discussions with J. Henk as well as technical assistance by F. Helbig.

*winkelm@mpi-halle.de

- [1] C.D. Stanciu, F. Hansteen, A.V. Kimel, A. Kirilyuk, A. Tsukamoto, A. Itoh, and T. Rasing, Phys. Rev. Lett. **99**, 047601 (2007).
- [2] I. Zutic, J. Fabian, and S.D. Sarma, Rev. Mod. Phys. **76**, 323 (2004).
- [3] G. Schütz, W. Wagner, W. Wilhelm, P. Kienle, R. Zeller, R. Frahm, and G. Materlik, Phys. Rev. Lett. **58**, 737 (1987).
- [4] L. Baumgarten, C.M. Schneider, H. Petersen, F. Schäfers, and J. Kirschner, Phys. Rev. Lett. **65**, 492 (1990).
- [5] C. Roth, F.U. Hillebrecht, H. Rose, and E. Kisker, Phys. Rev. Lett. **70**, 3479 (1993).
- [6] C. Stamm *et al.*, Nature Mater. **6**, 740 (2007).
- [7] L. Braicovich and G. van der Laan, Phys. Rev. B **78**, 174421 (2008).
- [8] E. Beaupaire, J.C. Merle, A. Daunois, and J.Y. Bigot, Phys. Rev. Lett. **76**, 4250 (1996).
- [9] H. Petek and S. Ogawa, Prog. Surf. Sci. **56**, 239 (1997).
- [10] M. Weinelt, J. Phys. Condens. Matter **14**, R1099 (2002).
- [11] M. Pickel, A.B. Schmidt, F. Giesen, J. Braun, J. Minar, H. Ebert, M. Donath, and M. Weinelt, Phys. Rev. Lett. **101**, 066402 (2008).
- [12] K. Hild, J. Maul, G. Schönhense, H.J. Elmers, M. Amft, and P.M. Oppeneer, Phys. Rev. Lett. **102**, 057207 (2009).
- [13] D.H. Yu, M. Donath, J. Braun, and G. Rangelov, Phys. Rev. B **68**, 155415 (2003).
- [14] J.E. Ortega, F.J. Himpsel, G.J. Mankey, and R.F. Willis, Phys. Rev. B **47**, 1540 (1993).
- [15] F. Bisio, M. Nyvlt, J. Franta, H. Petek, and J. Kirschner, Phys. Rev. Lett. **96**, 087601 (2006).
- [16] A.K. Schmid and J. Kirschner, Ultramicroscopy **42–44**, 483 (1992).
- [17] W. Kuch and C.M. Schneider, Rep. Prog. Phys. **64**, 147 (2001).
- [18] T. Nakagawa and T. Yokoyama, Phys. Rev. Lett. **96**, 237402 (2006).
- [19] J. Henk, T. Scheunemann, S.V. Halilov, and R. Feder, J. Phys. Condens. Matter **8**, 47 (1996).
- [20] D. Venus, Phys. Rev. B **49**, 8821 (1994).
- [21] D. Venus, J. Magn. Magn. Mater. **170**, 29 (1997).
- [22] J. Henk *et al.* (to be published).
- [23] A.B. Schmidt, M. Pickel, T. Allmers, M. Budke, J. Braun, M. Weinelt, and M. Donath, J. Phys. D **41**, 164003 (2008).
- [24] C. Westphal, A.P. Kaduwela, C.S. Fadley, and M.A. Van Hove, Phys. Rev. B **50**, 6203 (1994).
- [25] F.U. Hillebrecht, H.B. Rose, T. Kinoshita, Y.U. Idzerda, G. van der Laan, R. Denecke, and L. Ley, Phys. Rev. Lett. **75**, 2883 (1995).
- [26] H.P. Oepen, K. Hünlich, and J. Kirschner, Phys. Rev. Lett. **56**, 496 (1986).
- [27] G.K.L. Marx, H.J. Elmers, and G. Schönhense, Phys. Rev. Lett. **84**, 5888 (2000).
- [28] D. Weller, G.R. Harp, R.F.C. Farrow, A. Cebollada, and J. Sticht, Phys. Rev. Lett. **72**, 2097 (1994).
- [29] C.M. Schneider and G. Schönhense, Rep. Prog. Phys. **65**, R1785 (2002).
- [30] U. Höfer, I.L. Shumay, C. Reuss, U. Thomann, W. Wallauer, and T. Fauster, Science **277**, 1480 (1997).
- [31] J. Hübner, W.W. Rühle, M. Klude, D. Hommel, R.D.R. Bhat, J.E. Sipe, and H.M. van Driel, Phys. Rev. Lett. **90**, 216601 (2003).
- [32] J. Güdde, M. Rohleder, T. Meier, S.W. Koch, and U. Höfer, Science **318**, 1287 (2007).

PHYSICAL REVIEW B **81**, 115130 (2010)**Spin-orbit coupling in unoccupied quantum well states: Experiment and theory for Co/Cu(001)**

Cheng-Tien Chiang, Aimo Winkelmann, Ping Yu, Jürgen Kirschner, and Jürgen Henk

Max-Planck-Institut für Mikrostrukturphysik, Weinberg 2, D-06120 Halle (Saale), Germany

(Received 21 December 2009; revised manuscript received 9 February 2010; published 19 March 2010)

The influence of spin-orbit coupling in the unoccupied sp_z quantum well states in ultrathin Co films is investigated by two-photon photoemission spectroscopy with linearly polarized light. The asymmetry of the experimental two-photon photoemission intensities upon magnetization reversal is as large as 10%, which is in striking contrast to expectations based on the weakness of spin-orbit coupling in the observed quantum well states. The magnetic dichroic signal depends strongly on the polarization of the incident light as well as on the spin polarization of the quantum well states. These findings are explained by detailed electronic structure calculations and one-photon photoemission calculations. Our conclusions are supported by analytical considerations. In this way, a detailed picture of spin-orbit coupling in the unoccupied Co/Cu(001) quantum well states is provided.

DOI: [10.1103/PhysRevB.81.115130](https://doi.org/10.1103/PhysRevB.81.115130)

PACS number(s): 79.60.-i, 73.21.Fg, 71.70.Ej

I. INTRODUCTION

The coupling between spin and orbital angular momentum in the relativistic electronic structure is essential in the interplay between the electronic and lattice degrees of freedom with the electron spin in solid state systems, including their dynamical properties. In particular, the mechanism of spin-orbit coupling (SOC) can be exploited to provide access to the electron spin via purely optical excitation,¹ which is relevant in investigations of the relativistic band structure of nonmagnetic and magnetic solids by photoemission,^{2,3} in laser-based ultrafast magnetism,⁴ and in optically controlled spintronics.⁵ In a magnetic system, the optical transition rates between electronic states can be strongly influenced by the spin-orbit interaction. This leads to element-specific dichroism in optical absorption⁶ and photoemission^{7,8} and gives access to magnetic properties of materials without an experimentally more demanding external spin analysis.^{3,9} Powerful applications of magnetic dichroism include the element-specific imaging of magnetic domains in photoemission electron microscopy,¹⁰ the determination of spin and orbital magnetic moments and their anisotropy by core-level x-ray magnetic circular dichroism (XMCD),¹¹ and the study of the hybridization of occupied electronic states by angle-resolved photoemission spectroscopy (ARPES).^{2,12-14} Moreover, by exploiting the time resolution given by ultrashort laser pulses, magnetic dichroism can provide access also to the dynamics of spin and orbital angular momentum down to the femtosecond regime.^{15,16}

Since excited states naturally play a key role in optically driven processes, it is important to characterize to which degree these states are influenced by spin-orbit coupling. For this purpose, investigations of magnetic dichroism have to be extended to the unoccupied states with energies between the Fermi and the vacuum level. Inaccessible by conventional ARPES experiments based on one-photon photoemission (1PPE), these states can be approached by two-photon photoemission (2PPE) using lasers with photon energies in the order of a few electron volts.^{17,18} In such 2PPE experiments, magnetic linear¹⁹ and circular²⁰ dichroism were recently observed. In these investigations, however, the dichroic signal

was not related to specific unoccupied states. In another 2PPE investigation, we have demonstrated magnetic dichroism from unoccupied states for the well understood and characterized Co films on Cu(001).²¹ These experiments addressed the dispersion of unoccupied quantum well states in the Co film in connection with magnetic circular dichroism (MCD) and magnetic linear dichroism (MLD). The sizable MLD, with a maximum intensity asymmetry under magnetization reversal of about 10%, is particularly astonishing since it is common knowledge that MLD is large in band structure regions where electronic states hybridize strongly due to spin-orbit coupling; see, for example, Ref. 13 for Fe(110). The unoccupied Co quantum well states on Cu(001), however, are derived from the exchange-split sp_z bands²² which are thought to be negligibly affected by spin-orbit coupling but are found to show considerable MLD at energies far away from hybridization regions. Apparently, this finding questions the interpretation of magnetic dichroism studies performed so far. It thus seems necessary to establish whether the experimentally observed MLD can indeed be attributed to the unoccupied quantum well states. Because not only the unoccupied intermediate states but also the occupied initial states and the final outgoing photoelectron states are involved in the 2PPE process, we have to take into account the possible contributions from the occupied Co states²³ or even the final state²⁴ as origins of magnetic dichroism in the 2PPE experiments from Co/Cu(001). We will show that the established interpretation of MLD is still valid. In fact, we will demonstrate that MLD in 2PPE is a suitable tool for investigating even marginal hybridizations, which are mediated by spin-orbit coupling, provided an appropriate setup is chosen.

The above questions can hardly be answered by experiments alone. Thus, there is need for a joint experimental and theoretical investigation of Co/Cu(001) on which we report in this paper. The major issues to be addressed are: how large is the spin-orbit induced hybridization in the unoccupied Co quantum well states? If it is tiny, as expected, is it nevertheless large enough to produce the significant MLD found in experiment? How crucial is the choice of the setup, in particular the polarization of the excitation light and its incidence angle, for obtaining large asymmetries? A detailed pic-

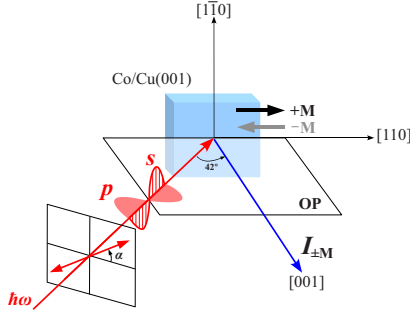


FIG. 1. (Color online) Setup for magnetic linear dichroism in 2PPE from Co/Cu(001). The 2PPE intensities $I_{\pm M}$ are detected in normal emission (blue arrow along [001]), with the in-plane magnetizations along [110] (+ M) or $[\bar{1}\bar{1}0]$ ($-M$). The optical plane (OP) is spanned by the surface normal and the incidence direction of the linearly polarized light (red arrow; polar angle 42°). The electric field vector (red double arrow) is rotated by an angle α out of the OP and can be tuned continuously between s and p polarization.

ture of the unoccupied quantum well states is obtained by relating results of 2PPE experiments, first-principles electronic structure calculations, 1PPE calculations, and analytical considerations.

The paper is organized as follows. Methodical aspects of both experiment and theory are addressed in Sec. II. Results are discussed in Sec. III, and conclusions are given in Sec. IV.

II. METHODOLOGICAL ASPECTS

A. Experimental

The experiments were performed at 300 K in an ultrahigh vacuum chamber with base pressure lower than 1×10^{-10} mbar. Ultrashort laser pulses with photon energy $\hbar\omega = 3.1$ eV served as the excitation light source for two-photon photoemission. The pulse width was about 20 fs, with an energy per pulse of about 1 nJ. The repetition rate was 81 MHz. The linear polarization of the incident light was controlled by an achromatic $\lambda/2$ waveplate, which tuned the electric field vector \mathbf{E} to any angle α with respect to the optical plane (Fig. 1). The latter is spanned by the incident direction (polar angle fixed to 42°) and the sample surface normal, parallel to a $(1\bar{1}0)$ plane containing the magnetic easy axis of the Co films. The photoelectrons were collected in normal emission by an electrostatic cylindrical sector energy analyzer (CSA 300, Focus GmbH). The energy resolution was about 100 meV, as was estimated from the vacuum cutoff at the low energy edge of the photoemission spectra.

Before growing the Co films, the Cu(001) substrate was cleaned by 2 keV Ar ion sputtering, followed by annealing up to 900 K in order to recover a smooth surface morphology. After cooling down to room temperature, the cleanliness and crystalline structure of the surface were confirmed by the clean Cu Auger electron spectrum and sharp low energy electron diffraction spots. Subsequently, Co films with a

thickness of several atomic layers were deposited on the well-prepared Cu(001) single crystal by an electron beam evaporator (EFM 3, Omicron) from a cobalt rod of 99.995% purity.

We measured 2PPE spectra continuously during film growth. The thickness-dependent intensity modulations with a period of one monolayer (ML) served as a self-calibrated indication of film thickness.²¹ Moreover, we observed the characteristic features of 2PPE through unoccupied quantum well states in the Co film and their evolution as a function of film thickness.²¹ For the magnetic dichroism measurements, the Co films are magnetized along the crystalline [110] (+ M) and $[\bar{1}\bar{1}0]$ ($-M$) directions by a magnetic field pulse generated from a copper coil (Fig. 1). 2PPE intensities $I_{\pm M}$ were then measured for $\pm M$.

B. Computational

The first-principles electronic structure calculations rely on the local spin-density approximation to density-functional theory. The computations were performed with our scalar-relativistic and fully relativistic multiple-scattering codes [Korringa-Kohn-Rostoker (KKR) (Ref. 25) and layer KKR (Ref. 26)], using the Perdew-Wang exchange-correlation functional.²⁷

The 1PPE calculations were performed with our relativistic layer-KKR code in which spin-orbit coupling and magnetism are treated on equal footing (Dirac equation). The spin-density matrix of the photoelectrons is computed within the relativistic one-step model of photoemission,^{26,28} using the potentials from the self-consistent electronic structure calculations as input. For photon energies in the optical region, as in this work, it is essential to include the dielectric response of the system by means of Fresnel's equations.

The systems comprise a semi-infinite face-centered cubic Cu(001) substrate, n monolayers of face-centered tetragonal Co layers ($n=1, \dots, 12$), and a semi-infinite vacuum region. The latter is modeled by so-called empty muffin-tin spheres. The Co films are assumed to continue epitaxially the Cu(001) substrate, with identical in-plane lattice constant (2.65 Å). A lattice contraction in perpendicular direction of 2% is assumed homogenous within the entire Co film, in reasonable agreement with crystallographic structure analyses (e.g., Refs. 29 and 30).

C. Setup and magnetic linear dichroism

Magnetic dichroism is the change in the photocurrent I upon reversal of the magnetization, $\mathbf{M} \rightarrow -\mathbf{M}$. It is quantified by the asymmetry A of the two intensities $I_{\pm M}$,

$$A \equiv \frac{I_{+M} - I_{-M}}{I_{+M} + I_{-M}}. \quad (1)$$

Our setup (Fig. 1) differs from the standard setup for MLD,³¹ in which the magnetization is normal to the optical plane and p -polarized light is commonly chosen. To observe MLD in the present setup, the electric field vector \mathbf{E} of the light has to be rotated out of the optical plane by an angle α : For $\alpha=0^\circ$ or $\pm 90^\circ$, one has p -polarized (\mathbf{E} within optical

plane) or s -polarized light (\mathbf{E} normal to optical plane), respectively: $\mathbf{E}(\alpha) = E_p \cos \alpha + E_s \sin \alpha$. In accordance with previous analytical and numerical considerations,³² there is no MLD for $\alpha = 0^\circ$ and $\pm 90^\circ$.

The present setup is rather similar to the standard setup for MCD in which the helicity vector and the magnetization are parallel or antiparallel (or are at least coplanar).³³ One might think that, because of the complex dielectric constant, the incident linearly polarized light produces elliptically polarized light in the sample and consequently the magnetic *linear* dichroism is close to magnetic *circular* dichroism. It has been shown theoretically for Ni(001), however, that this assumption does not hold.³² Experimental evidence is provided further by the different shapes of the asymmetries of MLD and MCD in 2PPE from Co/Cu(001); confer Fig. 3 in Ref. 21.

To analyze the dichroic intensities in more detail, the calculated electronic states are decomposed into the basis functions of the single-group representations Δ_i of the point group $4mm$ (C_{4v} in Schönflies notation; $i=1, 2, 2',$ and 5 ; $\Delta_{1'}$ contributions show up for f states³⁴ and are thus considered irrelevant in this work, which focuses on s , p , and d states). Due to the dipole selection rules, s -polarized light excites the Δ_5 part into the Δ_1 part of the electronic states, whereas p -polarized light excites both the Δ_1 and Δ_5 parts into the Δ_1 part.³⁵ According to the acknowledged picture,³¹ MLD is expected to be large for electronic states in which sizable Δ_1 and Δ_5 contributions are simultaneously present. We will show below that the Δ_1 and Δ_5 contributions hybridize only marginally in the unoccupied quantum well states of the Co films.

In two-photon photoemission, three types of electronic states are involved: the occupied initial state, the intermediate state, and the final state, all of which can in principle contribute to the magnetic dichroism. To pinpoint that the experimentally observed MLD is indeed due to the intermediate Co quantum well states we compare the experimental MLD in 2PPE with calculated MLD in 1PPE. On the one hand we consider 1PPE from the quantum well states into the same final state as in the 2PPE experiment, with photon energy $\hbar\omega = 3.1$ eV. Here, the quantum well states are assumed to be equally populated, which might not be true in 2PPE. With respect to these approximations we expect at least qualitative agreement of the theoretical 1PPE and the experimental 2PPE spectra. On the other hand we consider 1PPE from the occupied states of the 2PPE experiment into the final state, with photon energy $\hbar\omega = 6.2$ eV; thus the Co quantum well states are not involved in this process.

The comparison of experimental 2PPE and theoretical 1PPE motivated above assumes that 2PPE via an intermediate state (i.e., a quantum well state) can be treated as two independent sequential one-photon transitions: First, a one-photon transition from the initial state to the intermediate state and, second, one from the intermediate state to the final state. Within this approximation, the contribution in 2PPE that is solely due to the polarization from the coherent superposition of initial and final state is neglected; it does not involve the population of the intermediate state. Consequently, we are only concerned with the dichroic signal from the transition from the intermediate to the final state. As will

be shown in the following, this conveys information on spin-orbit coupling in the quantum well state and is in agreement with the experimental 2PPE results.

III. RESULTS AND DISCUSSION

A. Spin-orbit coupling in unoccupied Co quantum well states

First, we address the formation of the unoccupied quantum well states in Co films on Cu(001) (Fig. 2). These states are derived from the strongly dispersive and exchange-split sp_z bands of fct Co. Without spin-orbit coupling these belong at $\bar{\Gamma}$ (i. e. $k_{\parallel} = 0$) to the representation Δ_1 . They are confined on the vacuum side of the film by the image-potential barrier (surface barrier) and on the substrate side by a gap in the Δ_1 bands of the Cu band structure along Γ - Δ - X . Such a band gap shows up at energies higher than the maximum of the sp_z band, that is at $E > E_F + 1.63$ eV (horizontal arrow in Fig. 2). Consequently, majority quantum well states can exist from this energy up to the maximum of the Co majority sp_z band at $E_F + 2.85$ eV [dark gray area in Fig. 2(b)]. Likewise, minority quantum well states appear at energies up to $E_F + 3.04$ eV [light gray area in Fig. 2(b)].

In both the Cu and Co band structure, several band gaps appear as a consequence of the spin-orbit interaction.¹⁹ In particular if majority and minority states of Co hybridize, their spin-polarization changes sign (confer the bands turning from blue to red or vice versa in Fig. 2(b); note that spin is not a good quantum number due to spin-orbit coupling). The spin-orbit induced gaps appear mainly in the regime of the weakly dispersive d bands. In contrast, the strongly dispersive sp_z bands do not show any signature of spin-orbit coupling in the regions of the unoccupied quantum well states. Consequently, the associated Bloch states should be almost exclusively of Δ_1 character. That this is indeed the case is shown by displaying the relative weights of the single-group representations for each band (Fig. 3).

As addressed in Sec. II C, the relevant representations for the present photoemission setup are Δ_1 and Δ_5 whose weights are displayed in Figs. 3(a) and 3(b). The exchange-split sp_z bands hybridize with the minority Δ_5 band at about $E \approx 1.0$ eV and $k_{\perp} \approx 0.8(\Gamma$ - Δ - $X)$ [this region is marked by circles in (a) and (b)]. As a result, a minority Δ_5 contribution is mixed into the sp_z states [Fig. 3(b)]; and, vice versa, Δ_1 contributions are mixed into the minority Δ_5 band [Fig. 3(a)]. Both additional contributions, however, decrease rapidly when leaving the hybridization region. To be more specific, the Δ_5 contribution to the sp_z bands is less than 1% in the regime of the quantum well states [gray areas in Fig. 3(b)]. We also performed a symmetry analysis of the Bloch spectral functions of the quantum well states in $\text{Co}_n/\text{Cu}(001)$; it fully confirms the picture derived from the bulk-band structure of fct Co, namely, that the quantum well states are marginally affected by hybridization and are almost of pure Δ_1 type.

Summarizing at this point, we find that the effect of spin-orbit coupling is very weak in the energy regime of the unoccupied Co sp_z quantum well states. Since hybridization due to the spin-orbit interaction is a prerequisite for MLD, this finding calls into question that the MLD observed in the

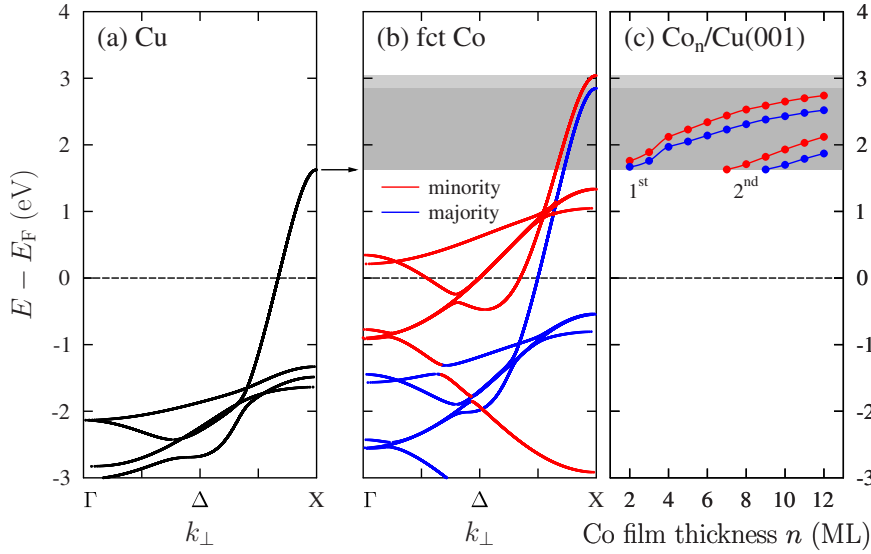


FIG. 2. (Color online) Formation of unoccupied quantum well states in Co/Cu(001). (a, b) Relativistic band structures of Cu (a) and fct Co (b) for the Γ - Δ -X direction. (c) Theoretical dispersion of unoccupied quantum well states in fct Co films on Cu(001) with thickness n from 2 to 12 ML. The two branches of states are labeled 1st and 2nd. The region in which unoccupied quantum well states can exist is highlighted by gray stripes in b and c. The horizontal arrow at the top of the Cu sp band marks the minimum energy for the unoccupied quantum well states. For Co, majority and minority spin orientations are indicated by blue and red symbols, respectively.

2PPE experiments can be attributed to the quantum well states.

B. Dispersion of the unoccupied Co quantum well states

To show that the exchange-split Co quantum well states are well described by the theory we address now their dispersion, that is the dependence of their energies on the Co film thickness n . The energy positions were obtained from

the maxima in the layer- and spin-resolved Bloch spectral function (Fig. 4).

A first set of bands is already present in the “window of quantum well states” [gray area in Fig. 2(c)] at 2 ML thickness (labeled “1st”). A parabolic dispersion, however, is obtained at thicknesses larger than about 3 to 4 ML, in agreement with experiment. A second set (“2nd”) shows up at 7 ML (minority spin) and 9 ML (majority spin), which is in agreement with experiment as well.²¹ Note that the exchange

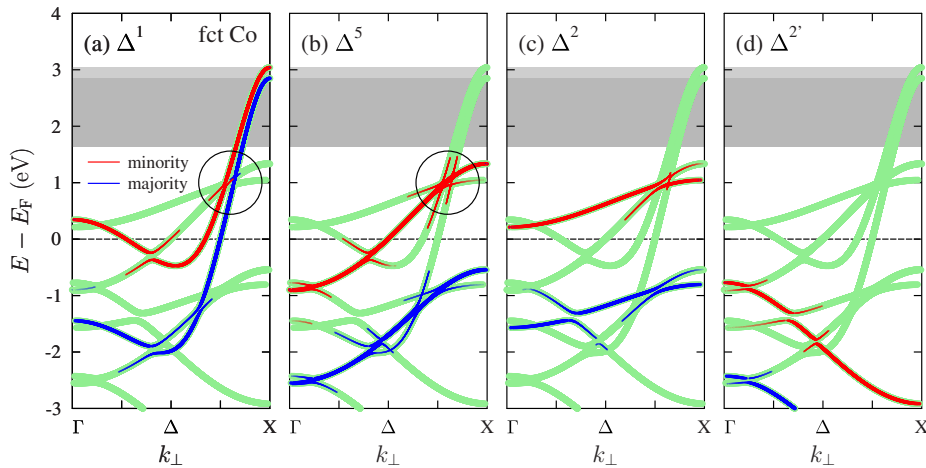


FIG. 3. (Color online) Relativistic band structure of fct Co along Γ - Δ -X, decomposed into representations Δ_1 (a), Δ_5 (b), Δ_2 (c), and Δ_2' (d) of the single-group 4 mm. Blue and red lines indicate majority and minority spin orientation, respectively. The line width is proportional to the relative weight of the representation of the associated Bloch state. The minimum weight shown is 1%. For clarity, the band structure itself is represented by green lines with fixed width. The region in which unoccupied quantum well states in fct Co/Cu(001) can exist is highlighted by gray stripes, as in Fig. 2(b). The circles in (a) and (b) guide to hybridization regions, which are discussed in the text.

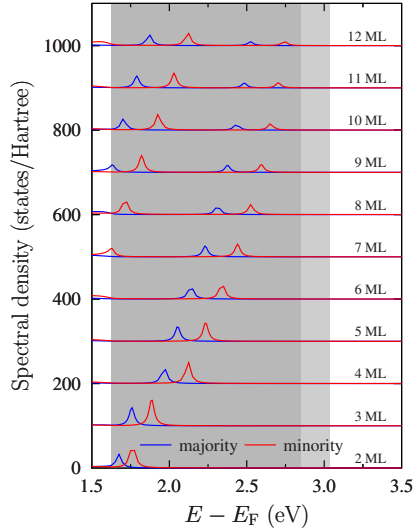


FIG. 4. (Color online) Bloch spectral function of the surface Co layer in $\text{Co}_n/\text{Cu}(001)$. Blue and red lines indicate majority and minority spin orientation, respectively. The Co film thickness n is given at the right of each data set; the spectra are offset vertically by 100 states/Hartree for clarity. The region in which unoccupied quantum well states can exist is highlighted by gray stripes, as in Fig. 2(b).

splitting increases with n . The dispersions for $n > 3$ ML can be well approximated by parabolae, indicating that the Co sp_z electrons can be regarded as nearly free.

The agreement between the theoretical dispersions and their experimental counterparts is addressed in Fig. 5. In our 2PPE experiments, electrons are selectively pumped into the

majority quantum well states, due to the majority character of the relevant initial states. This scheme is supported by the agreement of the experimental dispersion obtained from 2PPE and the calculated results for the first majority branch 1st in Fig. 5(a)]. The dispersions determined from spin-integrated inverse photoemission (Ortega *et al.*, Ref. 36) support our findings for the first branch. Spin-resolved inverse photoemission data (Yu *et al.*, Ref. 22) show also the second branches, which have higher energies than those in our calculations and, in particular for the thin Co films, lie outside the theoretically calculated region of quantum well states (confer the gray stripes in Fig. 2).

C. Magnetic linear dichroism in the unoccupied Co quantum well states

We now address the question whether the Δ_5 contribution, which is mixed into the Δ_1 quantum well states (Sec. III A), is sufficient to produce a significant MLD. It is important to stress that not only the weight of these contributions in the wave function is important but also the transition matrix elements; the latter enter explicitly the analytical expression for the photocurrent (Appendix).

Taking advantage of the dipole selection rules, we can disentangle the hybridized Δ_1 and Δ_5 components of the quantum well states by tilting the electric field vector \mathbf{E} of the incident light by an angle α out of the optical plane (cf. Sec. II C, Appendix, and Fig. 1). We have experimentally investigated the α -dependence of the quantum well states at film thicknesses 3.5 ML, 6 ML, and 16 ML; because all spectra show the same qualitative behavior we focus in the following on 6 ML as a representative (Fig. 6).

The experimental 2PPE intensities are maximum at $\alpha = 0^\circ$, that is for p -polarized light. Here, only the Δ_1 contri-

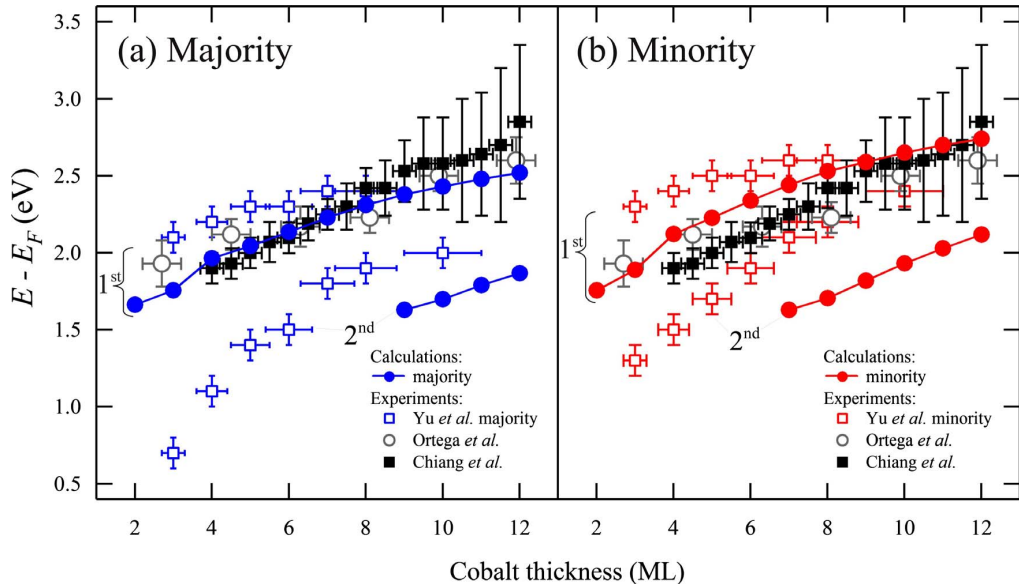


FIG. 5. (Color online) Dispersions of the unoccupied majority (a) and minority (b) quantum well states in $\text{Co}/\text{Cu}(001)$. Experimental data are extracted from inverse photoemission [Yu *et al.* (Ref. 22) and Ortega *et al.* (Ref. 36)] and 2PPE (Chiang *et al.*, Ref. 21). Theoretical data are taken from Fig. 2(c). The two sets of quantum well states are labeled by 1st and 2nd.

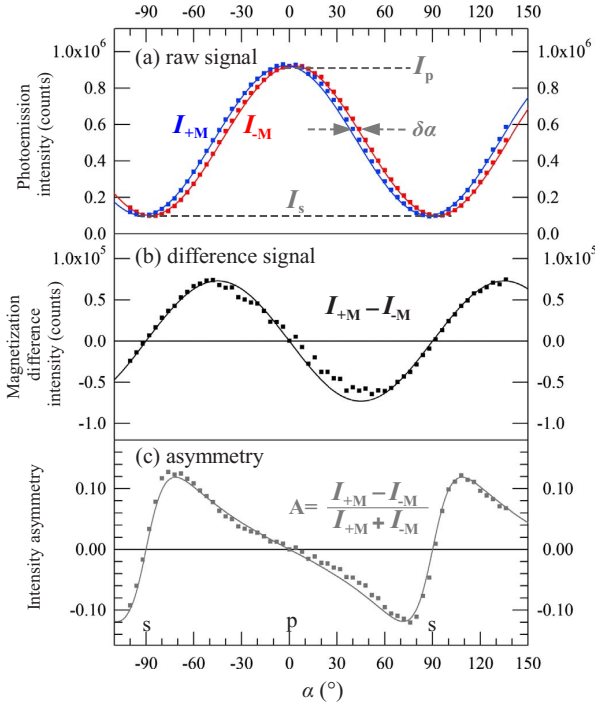
CHIANG *et al.*PHYSICAL REVIEW B **81**, 115130 (2010)

FIG. 6. (Color online) Magnetic linear dichroism in 2PPE experiments from the majority quantum well state in (6 ± 0.5) ML Co/Cu(001) with energy $E = E_F + (2.35 \pm 0.05)$ eV. The tilt angle α of the electric field vector of the incident light is defined in Fig. 1. (a) Photoemission intensities $I_{\pm M}$ for opposite magnetization directions $\pm M$ (Please note the corrected photoemission intensity compared to Fig. 4 in Ref. 21). (b and c) Difference $I_{+M} - I_{-M}$, and asymmetry derived from the raw intensities in (a). The photon energy $\hbar\omega$ is 3.1 eV. Solid lines display the α -dependence of the phenomenological model [cf. Appendix and Eq. (2)] with $\delta\alpha = 5^\circ$; I_s and I_p label the intensities for s - and p -polarized light [dashed lines in (a)].

bution to the quantum well state is probed. In contrast, the intensities are minimal for $\pm 90^\circ$ (s -polarized light) for which the Δ_5 contribution is probed. Neglecting for a moment matrix elements effects, this finding supports nicely the orbital character derived theoretically (Sec. III A): a strong Δ_1 but a weak Δ_5 contribution.

The intensities show a cosine dependence on the tilt angle α [Fig. 6(a)]. Further, the intensity difference $I_{+M} - I_{-M}$ is largest (in absolute value) at $\pm 45^\circ$ [Fig. 6(b)] whereas the asymmetry is largest at $\pm 75^\circ$ [Fig. 6(c)]. As will become clear from what follows, the position of the asymmetry extrema reflects the ratio of the dipole transition matrix elements that are related to excitations from the Δ_1 and the Δ_5 contributions of the quantum well state.

The α -dependence of the dichroic intensities is phenomenologically modeled as (Appendix)

$$I_{\pm M}(\alpha) = I_s \sin^2(\alpha \pm \delta\alpha/2) + I_p \cos^2(\alpha \pm \delta\alpha/2), \quad (2)$$

with I_s and I_p defined in Fig. 6(a). A fit to the experimental data gives $\delta\alpha = (5 \pm 1)^\circ$. The asymmetry defined in Eq. (1) can thus be approximated as

$$A(\alpha) = \frac{I_p - I_s}{2} \frac{\sin(2\alpha) \sin \delta\alpha}{I_s \sin^2 \alpha + I_p \cos^2 \alpha}. \quad (3)$$

The first term in the above expression determines mainly the amplitude of the asymmetry. The second term relates the tilt angle α_{\max} for which the asymmetry becomes extremal to the ratio of the intensities I_s and I_p for s and p polarization. Ignoring again the transition matrix elements, it reflects the Δ_5 and Δ_1 contributions to the quantum well state. From Sec. III A, we know already that the Δ_5 contribution (equivalent to a small I_s) is very small. Consequently, to obtain roughly similar weights of the two contributions, α_{\max} must be close to $\pm 90^\circ$, as is confirmed by its numerical values of $\pm 75^\circ$ (see also Appendix). This analysis supports the experimental value of $\delta\alpha$ of about 5° and rules out effects due to the magneto-optical Kerr effect since typical Kerr rotation angles are significantly smaller.

In the following, we provide theoretical evidence that the experimental findings are related to the unoccupied quantum well states and not to the occupied initial states. For this purpose, we calculated 1PPE spectra for which the quantum well states are assumed to be occupied, as is motivated in Sec. II C. The magnetic linear dichroism shows (in absolute value) largest numerical values at about $\alpha_{\max} = \pm 76^\circ$, with about 6% peak value [Fig. 7(c)]. The α dependence as well as the maximum asymmetry agree astonishingly well with those found in the 2PPE experiments (Fig. 6). Since occupied Co states are not involved in this 1PPE calculation, our finding corroborates that either the unoccupied Co quantum well states or, rather unlikely, the final states produce the sizable MLD.

The optical response of the system is taken into account by Fresnel's equations. With a dielectric constant $\epsilon = 1$, the linearly polarized light in the vacuum is transferred unaltered into the solid; with a complex dielectric constant ($\sqrt{\epsilon} = 1.61 + 3.05i$ for Co at $\hbar\omega = 3.0$ eV; Ref. 37), however, the incident light turns into a superposition of linearly and circularly polarized light within the solid. As a consequence, one observes in the former case a purely magnetic *linear* dichroism, whereas in the latter case one is concerned with superimposed *linear* and *circular* dichroisms.

Since the circular dichroism produces no α -dependence at all, the dependence on the tilt angle α can be solely ascribed to linear dichroism; this finding is evident from the asymmetries for $\epsilon \neq 1$ and $\epsilon = 1$ [Fig. 7(c)], which display identical shapes and, in particular, identical positions of the extrema. The asymmetry for $\epsilon \neq 1$ is, however, sizably larger than that for $\epsilon = 1$ [note the scale factor of 20 in Fig. 7(c)]. Thus, the *magnitude* of the effect is influenced by the additional circular dichroism introduced by the optical response, while the *position* of the asymmetry extrema is determined by the linear dichroism. This important effect of the optical response can be understood from Eq. (A2), where the two terms involving real and imaginary parts of $\sin \theta' E'_\parallel E'_\perp^*$ will correspond to purely linear (Re term) and circular dichroism (Im term) only in the limit of vanishing optical response ($\epsilon = 1$). With $\epsilon \neq 1$, both terms contribute to the magnetic dichroism.³²

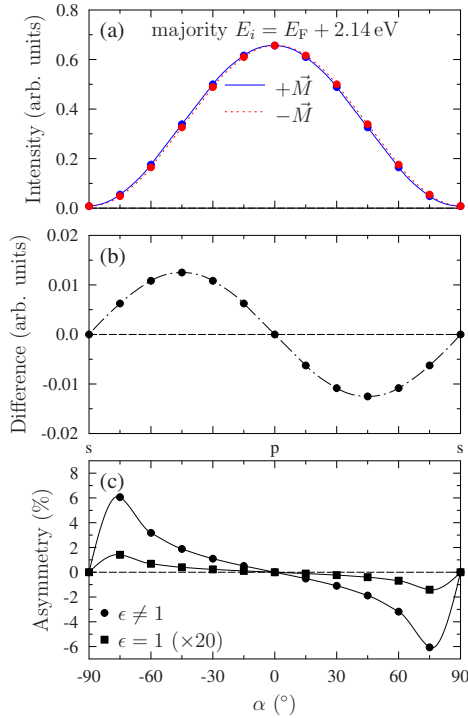


FIG. 7. (Color online) Theoretical magnetic linear dichroism in 1PPE from the unoccupied majority quantum well state in 6ML Co/Cu(001) with energy $E_F + 2.14$ eV (cf. Figure 2(c)). (a) Intensities $I_{\pm M}$ for magnetization direction $+\vec{M}$ (blue, solid) and $-\vec{M}$ (red, dotted) versus tilt angle α of the incident light. (b) Difference of $I_{\pm M}$. (c) Asymmetries derived from intensities that have been computed with optical response ($\epsilon \neq 1$; filled circles; shown in a) and without optical response ($\epsilon = 1$; filled squares, scaled by a factor of 20; intensities not shown). $\alpha = \pm 90^\circ$ correspond to s -polarized light, $\alpha = 0^\circ$ to p -polarized light. The photon energy $\hbar\omega$ is 3.1 eV.

These observations emphasize that the optical response is essential for quantitatively understanding the magnetic dichroism. We note in passing that the intensities from the minority quantum well state with energy $E_F + 2.35$ eV are very similar to those from the majority state. Its opposite spin polarization, however, manifests itself in an opposite sign of the asymmetry.

To rule out the final states of the photoemission process as origin of the magnetic linear dichroism we calculated 1PPE spectra for 6.2 eV photon energy, using the same final states as for $\hbar\omega = 3.1$ eV. Here, the unoccupied Co quantum well states are not involved but the occupied Co states serve as initial states. The theoretical spectra (not shown) reveal a cosine-dependence on α as well but an α_{\max} close to $\pm 45^\circ$ follows from almost equally large I_s and I_p . This finding clearly contrasts the experimental 2PPE observation. Assuming 2PPE as two sequential one-photon excitation processes, it supports that the Δ_1 and the Δ_5 parts of the quantum well states become probably equally populated in 2PPE by the initial excitation process; we note that the final state in photoemission (i.e., the photoelectron's wave function) belongs to the Δ_1 representation,³⁸ as do the unoccupied quantum

well states except for the tiny Δ_5 contribution mixed in by spin-orbit coupling. In conclusion, the agreement of the calculations for 1PPE from the unoccupied quantum well states and the disagreement of similar calculations from the occupied Co states with the 2PPE experiment, supports that the origin of the MLD in 2PPE are the unoccupied quantum well states.

IV. SUMMARY AND CONCLUSIONS

In summary, by relating results of 2PPE experiments, electronic structure and photoemission calculations, as well as analytical considerations, we have derived a more complete picture of the unoccupied quantum well states in Co films on Cu(001). The magnetic linear dichroism in 2PPE, here in a nonstandard setup, is found to be a valuable tool for the investigation of spin-orbit coupling in unoccupied states. Although the spin-orbit mediated hybridization is very weak, we showed that it can be clearly probed in 2PPE experiments when the excitation conditions are chosen properly.

Besides demonstrating the characterization of spin-orbit coupling in unoccupied states via magnetic linear dichroism in 2PPE, our results should be directly relevant for PEEM imaging of magnetization dynamics down to the fs-time scales provided by ultrashort laser pulses.^{39,40} In addition to the magnetization contrast provided by initial states near the Fermi level in threshold photoemission,^{41,42} the magnetic dichroism from the unoccupied Co quantum well states provides enhanced analytical potential because it is element-specific and it is sensitive to the film thickness.

ACKNOWLEDGMENTS

We gratefully acknowledge very fruitful discussions with A. Ernst and the technical support from F. Helbig.

APPENDIX: ANALYTICAL DESCRIPTION OF MAGNETIC LINEAR DICHROISM

In order to better understand the mechanism behind the observed dichroism, we use an analytical model, in addition to the numerical results presented in Sec. III C, to extract different contributions to the magnetic dichroism.

The electric field vector of the incident light is decomposed into components perpendicular to (subscript \perp) and within (subscript \parallel) the optical plane, respectively. The field inside the solid (quantities within the solid are marked by a prime) is given by Fresnel's formulas,

$$E'_{\perp} = 2E_0 \frac{\cos \theta \sin \alpha}{\cos \theta + \sqrt{\epsilon' - \sin^2 \theta}}, \quad (\text{A1a})$$

$$E'_{\parallel} = 2E_0 \frac{n' \cos \theta \cos \alpha}{\epsilon' \cos \theta + \sqrt{\epsilon' - \sin^2 \theta}}, \quad (\text{A1b})$$

where ϵ' is the complex dielectric constant and $n' = \sqrt{\epsilon'}$. θ and α are the polar angle of incidence and the tilt angle of the electric field vector with respect to the optical plane, respectively.

CHIANG *et al.*PHYSICAL REVIEW B **81**, 115130 (2010)

According to the analytical analysis of Ref. 32, the dichroic photoemission intensity can be written schematically as

$$I_{\pm M} = (|E'_{\perp}|^2 + |\sin \theta'|^2 |E'_{\parallel}|^2) A_{(1,5)} + |\cos \theta'|^2 |E'_{\parallel}|^2 B_{(5)} \\ \pm 2 \operatorname{Re}(\sin \theta' E'_{\parallel} E'_{\perp}{}^*) \operatorname{Im} C_{(1,5)} \\ \pm 2 \operatorname{Im}(\sin \theta' E'_{\parallel} E'_{\perp}{}^*) \operatorname{Re} C_{(1,5)}. \quad (\text{A2})$$

$A_{(1,5)}$ abbreviates an expression, which comprises terms of transition matrix elements for excitation from the Δ_1 and Δ_5 parts of the initial state; it is even under magnetization reversal. Likewise, the even $B_{(5)}$ is for excitations from the Δ_5 part. On the contrary, $C_{(1,5)}$ is odd under magnetization reversal; thus the magnetic linear dichroism is described by the last two terms in Eq. (A2), with an angular dependence given by $\sin \theta' E'_{\parallel} E'_{\perp}{}^*$ (Section II.C in Ref. 32; note that the subscript “(1,5)” reflects that hybridization among Δ_1 and Δ_5 parts is necessary for magnetic dichroism in our experimental geometry).

According to Snell’s law, $n' \sin \theta' = \sin \theta$ and $n' \cos \theta' = -\sqrt{\epsilon' - \sin^2 \theta}$, the internal polar angle θ' does not depend on the tilt angle α . Thus, the α -dependence of the dichroism is solely due to E'_{\perp} and E'_{\parallel} in $\sin \theta' E'_{\parallel} E'_{\perp}{}^*$, which with Eq. (A1) yields $\sin \alpha \cos \alpha$ or equivalently $\sin(2\alpha)/2$. Its maxima at $\alpha = \pm 45^\circ$ [orange and cyan in Fig. 8(a)] agree with the experimental and computational findings [Figs. 6(c) and 7(b)]. Consequently, we can condense Eq. (A2) further to

$$I = A \cos^2 \alpha + B \sin^2 \alpha \pm C \sin(2\alpha). \quad (\text{A3})$$

In contrast to the intensity difference, the experimental and theoretical asymmetries are maximum at about $\alpha = \pm 75^\circ$ [Fig. 6(d) and Fig. 7(c)], which is explained by the transition matrix elements. The emission from the Δ_1 part of the initial-state wave function, which is represented by A in Eq. (A3) is sizably stronger than that from the Δ_5 part, which is given by B in Eq. (A3), an argument that is supported by the group theoretical analysis given in Sec. III A. The experimental α -dependence is roughly reproduced by assuming $A \approx 9$, $B \approx 1$, and $C \approx 0.35$ [Fig. 8(b) and 8(c)]. Note that the dichroic intensities appear mutually shifted by a small angle $\delta\alpha$. Indeed, Eq. (A3) can be rewritten approximately as in Eq. (2),

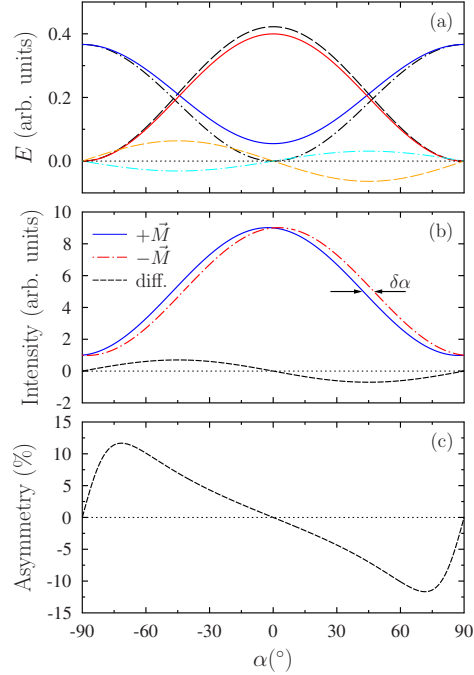


FIG. 8. (Color online) Analytical magnetic linear dichroism in 1PPE versus tilt angle α of the incident light. (a) Angular-dependent prefactors of the photoemission intensity Eq. (A2). Black: E'_{\perp} dash-dotted and E'_{\parallel} dashed, from eq. (a). Color: $|E'_{\perp}|^2 + |\sin \theta'|^2 |E'_{\parallel}|^2$ blue, $|\cos \theta'|^2 |E'_{\parallel}|^2$ red, $\operatorname{Re}(\sin \theta' E'_{\parallel} E'_{\perp}{}^*)$ orange dashed, and $\operatorname{Im}(\sin \theta' E'_{\parallel} E'_{\perp}{}^*)$ cyan dash-dotted. The photon energy, the dielectric constant of Co, and the polar angle of incidence are 3.1 eV, $\epsilon' = 1.61 + 3.05i$, and $\theta = 42^\circ$, respectively. (b) Photoemission intensities for $+M$ (blue) and $-M$ (red dash-dotted), calculated according to Eq. (A3). Their difference is shown as dashed line. The matrix element expressions that appear in Eq. (A3) are chosen to reproduce roughly the experimental results ($A/B/C = 9/1/0.35$). The angular shift $\delta\alpha = 5.5^\circ$ in Eq. (2) is indicated. (c) Asymmetry of the intensities shown in (b).

keeping terms up to first order in $\delta\alpha$. From Fig. 8(b), we obtain $\delta\alpha \approx 5.5^\circ$, which agrees nicely with the $(5 \pm 1)^\circ$ deduced from experiment.

¹M. Wöhlecke and G. Borstel, in *Optical Orientation*, edited by F. Meier and B. P. Zakharchenya (North-Holland, Amsterdam, 1984).

²W. Kuch and C. M. Schneider, *Rep. Prog. Phys.* **64**, 147 (2001).

³J. H. Dil, *J. Phys.: Condens. Matter* **40**, 403301 (2009).

⁴C. D. Stanciu, F. Hansteen, A. V. Kimel, A. Kirilyuk, A. Tsukamoto, A. Itoh, and T. Rasing, *Phys. Rev. Lett.* **99**, 047601 (2007).

⁵I. Žutić, J. Fabian, and S. Das Sarma, *Rev. Mod. Phys.* **76**, 323 (2004).

⁶G. Schütz, W. Wagner, W. Wilhelm, P. Kienle, R. Zeller, R.

Frahm, and G. Materlik, *Phys. Rev. Lett.* **58**, 737 (1987).

⁷L. Baumgarten, C. M. Schneider, H. Petersen, F. Schäfers, and J. Kirschner, *Phys. Rev. Lett.* **65**, 492 (1990).

⁸C. Roth, F. U. Hillebrecht, H. B. Rose, and E. Kisker, *Phys. Rev. Lett.* **70**, 3479 (1993).

⁹P. D. Johnson, *Rep. Prog. Phys.* **60**, 1217 (1997).

¹⁰C. M. Schneider, Z. Celinski, M. Neuber, C. Wilde, M. Grunze, K. Meinel, and J. Kirschner, *J. Phys.: Condens. Matter* **6**, 1177 (1994).

¹¹J. Stöhr, *J. Magn. Magn. Mater.* **200**, 470 (1999).

¹²A. Fanelsa, E. Kisker, J. Henk, and R. Feder, *Phys. Rev. B* **54**,

SPIN-ORBIT COUPLING IN UNOCCUPIED QUANTUM...

PHYSICAL REVIEW B **81**, 115130 (2010)

- 2922 (1996).
- ¹³A. Rampe, G. Güntherodt, D. Hartmann, J. Henk, T. Scheunemann, and R. Feder, *Phys. Rev. B* **57**, 14370 (1998).
- ¹⁴J. Bansmann, L. Lu, M. Getzlaff, M. Fluchtmann, J. Braun, and K. H. Meiwes-Broer, *J. Magn. Magn. Mater.* **185**, 94 (1998).
- ¹⁵C. Stamm, *et al.*, *Nature Mater.* **6**, 740 (2007).
- ¹⁶L. Braicovich and G. van der Laan, *Phys. Rev. B* **78**, 174421 (2008).
- ¹⁷M. Weinelt, *J. Phys.: Condens. Matter* **14**, R1099 (2002).
- ¹⁸H. Petek and S. Ogawa, *Prog. Surf. Sci.* **56**, 239 (1997).
- ¹⁹M. Pickel, A. B. Schmidt, F. Giesen, J. Braun, J. Minár, H. Ebert, M. Donath, and M. Weinelt, *Phys. Rev. Lett.* **101**, 066402 (2008).
- ²⁰K. Hild, J. Maul, G. Schönhense, H. J. Elmers, M. Amft, and P. M. Oppeneer, *Phys. Rev. Lett.* **102**, 057207 (2009).
- ²¹C.-T. Chiang, A. Winkelmann, P. Yu, and J. Kirschner, *Phys. Rev. Lett.* **103**, 077601 (2009).
- ²²D. H. Yu, M. Donath, J. Braun, and G. Rangelov, *Phys. Rev. B* **68**, 155415 (2003).
- ²³A. B. Schmidt, M. Pickel, T. Allmers, M. Budke, J. Braun, M. Weinelt, and M. Donath, *J. Phys. D* **41**, 164003 (2008).
- ²⁴X. Gao, A. N. Koveshnikov, R. H. Madjoe, R. L. Stockbauer, and R. L. Kurtz, *Phys. Rev. Lett.* **90**, 037603 (2003).
- ²⁵*Electron Scattering in Solid Matter*, edited by J. Zabloudil, R. Hammerling, L. Szunyogh, and P. Weinberger (Springer, Berlin, 2005).
- ²⁶J. Henk, in *Handbook of Thin Film Materials*, edited by H. S. Nalwa (Academic Press, San Diego, 2001), Vol. 2, Chap. 10, p. 479.
- ²⁷J. P. Perdew and Y. Wang, *Phys. Rev. B* **45**, 13244 (1992).
- ²⁸J. Braun, *Rep. Prog. Phys.* **59**, 1267 (1996).
- ²⁹E. Navas, P. Schuster, C. Schneider, J. Kirschner, A. Cebollada, C. Ocal, R. Miranda, J. Cerdá, and P. de Andrés, *J. Magn. Magn. Mater.* **121**, 65 (1993).
- ³⁰O. Heckmann, H. Magnan, P. le Fevre, D. Chandesris, and J. J. Rehr, *Surf. Sci.* **312**, 62 (1994).
- ³¹R. Feder and J. Henk, in *Spin-Orbit Influenced Spectroscopies of Magnetic Solids*, edited by H. Ebert and G. Schütz, *Lecture Notes in Physics* Vol. 466 (Springer, Berlin, 1996), p. 85.
- ³²J. Henk and R. Feder, *Phys. Rev. B* **55**, 11476 (1997).
- ³³W. Kuch, A. Dittschar, K. Meinel, M. Zharnikov, C. M. Schneider, J. Kirschner, J. Henk, and R. Feder, *Phys. Rev. B* **53**, 11621 (1996).
- ³⁴T. Inui, Y. Tanabe, and Y. Onodera, *Group Theory and Its Applications in Physics, Springer Series in Solid State Sciences* Vol. 78 (Springer, Berlin, 1990).
- ³⁵J. Henk, T. Scheunemann, S. V. Halilov, and R. Feder, *J. Phys.: Condens. Matter* **8**, 47 (1996).
- ³⁶J. E. Ortega, F. J. Himpsel, G. J. Mankey, and R. F. Willis, *Phys. Rev. B* **47**, 1540 (1993).
- ³⁷P. B. Johnson and R. W. Christy, *Phys. Rev. B* **9**, 5056 (1974).
- ³⁸J. Hermanson, *Solid State Commun.* **22**, 9 (1977).
- ³⁹C. M. Schneider and G. Schönhense, *Rep. Prog. Phys.* **65**, 1785 (2002).
- ⁴⁰T. Nakagawa, K. Watanabe, Y. Matsumoto, and T. Yokoyama, *J. Phys.: Condens. Matter* **21**, 314010 (2009).
- ⁴¹T. Nakagawa and T. Yokoyama, *Phys. Rev. Lett.* **96**, 237402 (2006).
- ⁴²T. Nakagawa, I. Yamamoto, Y. Takagi, K. Watanabe, Y. Matsumoto, and T. Yokoyama, *Phys. Rev. B* **79**, 172404 (2009).

Lebenslauf

Dr. Aimo Winkelmann
Max-Planck-Institut für Mikrostrukturphysik
Weinberg 2
06120 Halle (Saale)

Geburtsdatum: 24. März 1973
Geburtsort: Waren(Müritz)

Wissenschaftlicher Werdegang:

- 1996-2000: Studium der Physik mit Abschluss Diplom-Physiker,
Friedrich-Schiller-Universität Jena
Thema der Diplomarbeit:
"Photoelektronenbeugung an Halbleiteroberflächen"
(Fakultätspreis der Physikalisch-Astronomischen Fakultät)
Arbeitsgruppe: Prof. W. Richter
- 2000-2003: Dr. rer. nat. , Friedrich-Schiller-Universität Jena
Thema der Dissertation:
"Elektronenbeugungsmethoden zur Strukturanalyse epitaktischer
Siliziumkarbidschichten"
Arbeitsgruppe: Prof. W. Richter
- seit 2004: Wissenschaftlicher Mitarbeiter
Max-Planck-Institut für Mikrostrukturphysik, Halle (Saale)
Abteilung Prof. J. Kirschner
- 2005: Forschungsaufenthalt, University of Pittsburgh, USA
Arbeitsgruppe Prof. H. Petek
- Mai 2009: Forschungsaufenthalt, Australian National University,
Research School of Physics and Engineering
Canberra, Australien
Arbeitsgruppe Dr. M. Vos

Halle, den 12. September 2011

Erklärung an Eides statt

Ich erkläre hiermit, die vorliegende Habilitationsschrift

Nichtlineare Photoemission an Metalloberflächen unter Einfluss der Spin-Bahn-Kopplung

selbständig und ohne fremde Hilfe verfasst und keine anderen als die von mir angegebenen Quellen und Hilfsmittel benutzt zu haben. Die den benutzten Werken wörtlich oder inhaltlich entnommenen Stellen sind als solche kenntlich gemacht.

Halle(Saale), den 12. September 2011